Proceedings of the 20th ICSMGE-State of the Art and Invited Lectures– Rahman and Jaksa (Eds)

State of the Art: MICP soil improvement and its application to liquefaction hazard mitigation

Etat de l'art : Amélioration de sols par biocalcification (MICP) et applications pour la prévention des risques de liquéfaction

Jason T. DeJong
Civil and Environmental Engineering, University of California, Davis, CA, USA, jdejong@ucdavis.edu

Michael G. Gomez
Civil and Environmental Engineering, University of Washington, Seattle, WA, USA, mggomez@uw.edu

Alexandra C.M. San Pablo
Civil and Environmental Engineering, University of California, Davis, CA, USA

Charles M.R. Graddy & Douglas C. Nelson
Microbiology and Molecular Genetics, University of California, Davis, CA, USA

Minyong Lee
Civil and Environmental Engineering, University of Washington, Seattle, WA, USA

Katerina Ziotopoulou & Maya El Kortbawi
Civil and Environmental Engineering, University of California, Davis, CA, USA

Brina Montoya
Civil, Construction, and Environmental Engineering, North Carolina State University, Raleigh, NC, USA

Tae-Hyuk Kwon
Korea Advanced Institute of Science and Technology, Daejeon 34141, Republic of Korea

ABSTRACT: The field of biogeotechnics has emerged from the realization that processes intrinsic to natural systems can provide new approaches and inspiration through which the efficiency, sustainability, and functionality of geotechnical systems can be improved. Of these processes, microbially induced calcite precipitation (MICP) has advanced the most rapidly with the use of ureolytic microbial activity providing an opportunity to control the precipitation of calcium carbonate minerals throughout a soil matrix, thereby significantly improving soil engineering behaviors. The process affords increases in soil stiffness, strength, and dilatancy, with utility across a breadth of geotechnical and geoenvironmental applications, including mitigation of earthquake-induced soil liquefaction. This state of the art paper first covers: (1) enabling scientific processes, (2) treatment methods, and (3) monitoring techniques, which are broadly useful for different engineering applications. The second part focuses on how MICP can: (1) improve engineering behaviors at the element scale, (2) be modeled at the particle- and continuum-scales, (3) be applied at the field-scale, and (4) improve the resistance to liquefaction triggering and reduce the consequences when it does occur.

RÉSUMÉ : La biogéotechnique a émergé de la prise de conscience que des processus intrinsèques du vivant peuvent apporter de nouvelles approches et inspirations grâce auxquelles l'efficacité, la durabilité et la fonctionnalité de procédés géotechniques peuvent être améliorées. Parmi eux, la précipitation de calcite induite par voie biologique (MICP) basée sur la voie uréolytique a progressé très vite pour contrôler la précipitation de carbonate de calcium dans une matrice de sol et améliorer ainsi ses propriétés. Le procédé permet d'augmenter la rigidité, la résistance et la dilatance du sol, pour une grande diversité d'applications géotechniques et géoenvironnementales, dont la réduction des risques de liquéfaction de sol sous séisme. Cet état de l'art couvre dans un premier temps (1) les principes fondateurs scientifiques, (2) les méthodes de traitement et (3) les techniques de contrôle, utilisés largement pour différentes applications de traitement de sol. La seconde partie se concentre sur la façon dont la biocalcification peut (1) améliorer les comportements du sol à l'échelle élémentaire, (2) être modélisée à l'échelle des particules et du continuum, (3) être appliquée sur site, et (4) améliorer le seuil de déclenchement de la liquéfaction et en réduire les conséquences le cas échéant.

KEYWORDS: biogeotechnics, microbially induced calcite precipitation, ground improvement, biocementation

biogéotechnique, précipitation de calcite induite par voie biologique, amélioration de sol, biocimentation

1 INTRODUCTION

Biogeotechnics, specifically biomediated and bioinspired geotechnical engineering, has matured rapidly over the past two decades, becoming one of the fastest growing subdisciplines within geotechnical engineering. Academics and practitioners exploring this field are motivated in part by the notion that natural processes have been optimized to some degree to address biological constraints including limited material and energy resources and can thereby yield new insights regarding how geotechnical processes may be accomplished in a more efficient and sustainable manner. The natural world provides endless opportunities to identify alternative resources and inspire innovation in the geotechnical engineering community. This is a contrast to current practices for which geotechnologies have been almost exclusively inspired by human ingenuity with practical constructability constraints, capital cost considerations, and public safety being of highest priority. As new technologies developed, energy and material resource limitations as well as environmental quality were largely not considered, and broader issues related to climate change and sustainability remained outside the profession. Consequently, our profession seeks new opportunities to realize a more sustainable, less impactful, geotechnical engineering practice in the future with biogeotechnical solutions providing one path forward to realize this vision.

1.1 *Biomediated & bioinspired geotechnics*

The envisioned opportunities for biogeotechnics are broad, as discussed by several researchers (DeJong et al. 2013, Pacheco-Torgal & Labrincha 2013, Mujah et al. 2016, Baveye et al. 2018, El Mountassir et al. 2018, Terzis & Laloui 2019, Almajed et al. 2021, Lai et al. 2021, Martinez et al. 2021, Assadi-Langroudi et al. 2022), with engineering applications spanning across the geotechnical, environmental, water, transportation, and energy sequestration sectors. Geotechnical specific applications identified include, but are not limited to, liquefaction mitigation, building settlement reduction, dam and levee safety, tunneling, foundations and anchorage systems, bluff and slope stabilization, impermeable and reactive barriers, drilling technologies, and site characterization and monitoring tools (DeJong et al. 2013, DeJong 2020, Martinez et al. 2021).

1.1.1 *Biomediated geotechnologies*

A generalized workflow for biomediated geotechnologies is shown in Figure 1. In these technologies, geochemical reactions in the soil are most frequently controlled by biological processes which determine the timing, rate, and distribution of some realized change oftentimes consisting of modification of soil pore fluids, generation of inorganic minerals, or production of organic polymers. Such changes can be tracked using various process monitoring tools including compression and shear wave propagation, electrical conductivity, and measurements of solution species, with changes to mechanical properties oftentimes varying several orders of magnitude. Such processes can be further refined to achieve specific performance objectives (i.e., predictable increase in improvement per treatment) through modification of implementation details. Finally, upscaling of the treatment methodology to field-scale must address treatment uniformity, material permanence, and byproduct management, with identification of the means by which treatment success and quality can be effectively verified.

Three examples of biomediated technologies on which substantial research has been performed include bio-cementation, bio-gas generation, and bio-film formation in sands (DeJong 2020). Bio-cementation coats soil particles and produces stiff, brittle bonds at particle-particle contacts, which increases initial shear stiffness, peak shear strength, and decreases hydraulic conductivity and compressibility. Such improvements are primarily realized through the binding of particle contacts, densification of soil matrixes due to addition of precipitated solid masses, and increase in particle surface roughness and angularity. A range of different technologies can achieve this end state condition, of which variations in the process may include different biogeochemical pathways (i.e., urea hydrolysis, denitrification, sulfate reduction, iron reduction, carbonic anhydrase), varying precipitated minerals (calcium carbonate, dolomite, ankerite and other amorphous and mixed mineral phases), ranges in treatment times, and use of augmented or stimulated whole cells versus free enzymes (Ciurli et al. 1991, Ferris et al. 1997, Benini et al. 1999, Warthmann et al. 2000, Bachmeier et al. 2002, Roden et al. 2002, Karatas et al. 2008, DeJong et al. 2010, van Paassen et al. 2010b, Chu et al. 2011, Hamdan et al. 2011, Gat et al. 2011, Mortensen et al. 2011, Weaver et al. 2011, Burbank et al. 2011, 2012, Gomez et al. 2014, 2016, Dhami et al. 2017, Graddy et al. 2018, Kavazanjian and Hamdan 2015, Khodadi Tirkolaei et al. 2020, Yu et al. 2021). Of these various approaches, microbially induced calcite precipitation (MICP) via microbial ureolysis is the most technologically mature biomediated soil improvement process and will be the focus of this paper.

Bio-gas generation processes yield gas bubbles in soil pore spaces, typically N_2 or CO_2 gases, which do not alter particle structures, but rather increase pore fluid compressibility. The resulting effect is best realized on loose of critical specimens with increases in monotonic strengths and cyclic resistances to liquefaction under undrained conditions and decreases in soil permeabilities. Perhaps the most prominent of such methods is the generation of nitrogen gases and soil desaturation via denitrification activity commonly referred to as microbial desaturation and precipitation or MIDP (van Paassen et al. 2010a, He & Chu 2014, O'Donnell et al. 2017b, van Paassen et al. 2018, Pham et al. 2018, Hall et al. 2018). While bio-gas is primarily generated, alkalinity generated from this process can also enable carbonate precipitation; however, mineral production rates are orders of magnitude slower than ureolysis.

Bio-film production involves the formation of an agglomeration of microbial cells, extracellular polymeric substances (EPS), and organic and inorganic materials on soil particle surfaces in aqueous environments (Cunningham et al. 1991, Proto et al. 2016). The accumulation of biofilms can be accomplished through the introduction of growth factors which permit the formation of biofilms in the presence of augmented and/or indigenous microbial communities. Hydraulic conductivity reductions exceeding 100-fold can be achieved in saturated sands due to the coating and bridging of adjacent particles, which can be maintained through continued nutrient injections. The permanence of biofilm structures is dependent on both continued nutrient availability and hydraulic conditions, however, and affords the unique advantage of reversibility when reductions are no longer needed (Phradichith et al. 2020, Zamani et al. 2022).

1.1.2 *Bioinspired geotechnologies*

The workflow process for bioinspired geotechnologies can be similarly described. In the bioinspired approach, inspiration from various biological systems can be leveraged in conjunction with current understandings of soil behavior, soil-structure interaction, and system design to yield new technologies (Martinez et al. 2021). The development of bioinspired engineered solutions requires appropriately defining and contextualizing both the engineering problem to be solved and abstracting the forms, behaviors, and principles of the biological analog(s) used for inspiration (DeJong et al. 2017). Hypothesis testing and refinement is performed iteratively throughout this

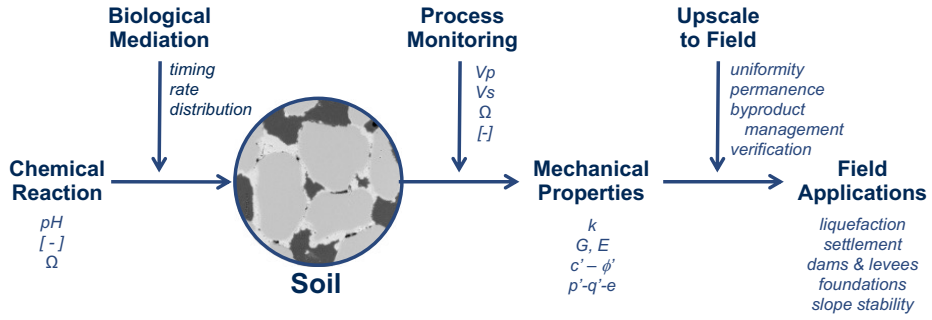

Figure 1. Generalized workflow for biomediated soil improvement geotechnologies.

process with upscaling challenges including physical constraints encountered at both stress and length scales. Although not fully refined, some bioinspired solutions have already been found to afford performances that are orders of magnitude better than existing technologies (e.g., Burrall et al. 2020).

Three examples of bioinspired technologies for which substantial research has been performed include snake-skin inspired anisotropic surfaces, self-burrowing probes, and root-inspired anchorage systems (DeJong 2020, Martinez et al. 2021). Snake-skin inspired anisotropic surfaces, inspired by the ventral scales of snakes, can mobilize directionally-dependent interface friction (Martinez et al. 2019). Such surfaces have potential applications for piles, soil nails, geomembranes, and other interfaces (O'Hara & Martinez 2020, Gray & Lissmann 1950, Marvi et al. 2013, Baum et al. 2014) and have shown promise for upscaling in recent centrifuge testing (Martinez & O'Hara 2021).

Self-penetrating probes, inspired by the burrowing and movement strategies of marine bivalves (i.e., clams), earth worms, and other organisms, may hold significant promise towards improving the energy efficiency and exploration capabilities of current subsurface techniques. Such probes have been investigated through cavity expansion analysis, DEM simulations, and laboratory experiments (Cortes & John 2018, Huang & Tao 2018, 2020, Khosravi et al. 2018, Chen et al. 2020, Martinez et al. 2020, Borela et al. 2021, Vego et al. 2021). Robot prototypes have also been used to study such mechanisms and have been inspired by razor clam locomotion (Tao et al. 2019, Huang et al. 2020) and marine peristaltic body motion (Ortiz et al. 2019), among other processes.

Novel foundation and anchorage systems, inspired by the architecture of tree root systems, have the potential to provide significant increases in stiffness and capacity compared to current foundation systems when normalizing achieved performance by material requirements. Mechanical performance of root and root-inspired systems has been investigated through field pull-out studies of trees (Burrall et al. 2020), laboratory testing of root analogs (Dyson and Rognon 2014, Mickovski et al. 2007, Schwarz et al. 2011), centrifuge testing of root systems and analogs (Liang et al. 2017, Zhang et al. 2022b), numerical modeling (Dupuy et al. 2007, Vego et al. 2021, Yang et al. 2018), and analytical methods (Blackwell et al. 1990, Cohen et al. 2011, Mallett 2019). The bioinspired process provides new opportunities to realize sustainability and performance objectives in a manner that is very different than biomediated technologies but equally important.

1.2 *Sustainability through innovation*

As biogeotechnical technologies mature there is an opportunity to maximize sustainability gains relative to current practices. This opportunity is abundantly clear for biomediated processes, which aim to improve upon existing soil improvement technologies, which are generally highly material and energy intensive (Jefferis 2008, Raymond 2020). A review of the United Nation's 17 sustainability goals (United Nations 2019) indicates that at least 10 of these goals can be directly impacted by geotechnical practices, with the balance oftentimes indirectly affected (DeJong 2020). In recognition of these broader potential impacts, it is increasingly critical to realize the benefits that a given geotechnical technology may afford with respect to sustainability and the role that continued development may have towards furthering such benefits. Biogeotechnical technologies are particularly well suited for such developments with their potential to improve the sustainability of geotechnical practice.

To this end, life cycle sustainability assessments (LCSA) can be used to quantitatively evaluate the impacts of both existing and future technologies. LCSA integrates the three-pillars of sustainably, namely, environmental, economic, and social impacts, through environmental life cycle assessment (LCA), life cycle costing assessment (LCCA), and social life cycle assessment (S-LCA) (Guinée 2016). LCAs provide quantitative, benchmarked evaluations of technologies and their impact on the environment over an entire life cycle. Raymond et al. (2021) recently developed further criteria specifically for geotechnical evaluations. The use of LCA in the geotechnical profession has been limited (Kendall et al. 2018), however, efforts are growing and now include evaluations of existing technologies against which emerging biogeotechnical technologies can be compared, including deep foundations (Misra 2010, Giri & Reddy 2014, Lee & Basu 2018), various soil improvement methods (Spaulding et al. 2008, Pinske 2011, Shillaber et al. 2016, Raymond et al. 2021), and site characterization methods (Purdy et al. 2021). More recently, LCA evaluations have been performed for developing biogeotechnical technologies, including MICP (Raymond et al. 2022) and EICP (Martin et al. 2020, Raymond et al. 2020b). Such individual evaluations can be effective in identifying the primary components contributing to sustainability impacts and therefore prioritizing changes that can be most effective in improving their sustainability. Further, comparative LCSAs can be used to provide early and updated assessments of how beneficial a new technology may be relative to existing practice. Raymond et al. (2020b) outlined an approach by which a technology can be re-evaluated and design considerations re-prioritized during this process in order to guide future field implementation.

The benefits and challenges of performing individual and comparative LCSA evaluations frequently throughout the development of a technology can be captured by considering the "Collingridge dilemma" and the "Gartner hype cycle" paradigms. The Collingridge dilemma (Collingridge 1980), shown in Figure 2a, contrasts the ability for reducing environmental impacts during a technologies development with the increasing cost of realizing those changes as the technology matures. Early in development, when a technology is poorly constrained, there are significant opportunities for change that

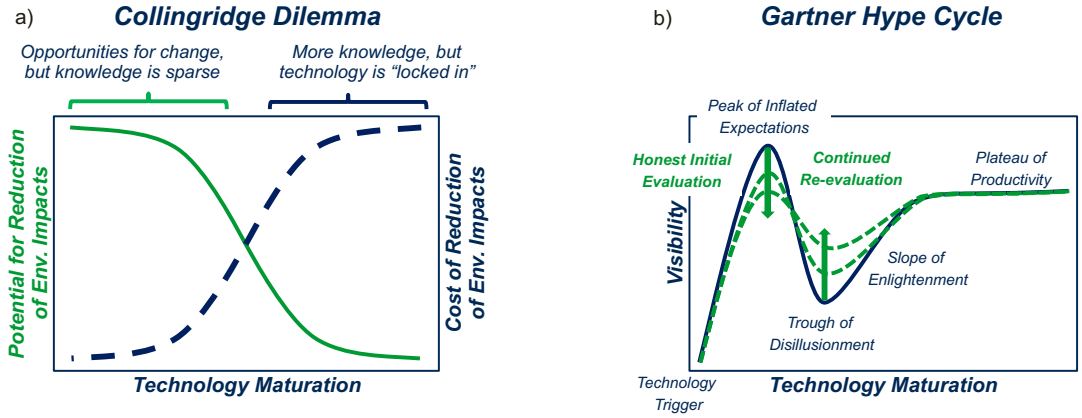

Figure 2. Conceptual schematics illustrating the (a) Collingridge dilemma and (b) Gartner hype cycle paradigms.

inflict minimal additional costs, but for which the current knowledge base may be insufficient to rationally assess the consequences of such decisions. As a technology matures towards implementation, however, available processes and knowledge increase, but at the expense of decreased flexibility with the design becoming increasingly less nimble. Thus, without continued evaluation of a technology during its development, maximum sustainability benefits will almost certainly remain unrealized. The potential benefits of frequent and transparent evaluation can be further considered within the Gartner hype cycle (Gartner 2018), shown in Figure 2b. As shown, oscillations in perceptions commonly observed during technology development, including inflated expectations and subsequent disillusionment, can be tempered through initial and ongoing quantitative evaluations of a technology.

In this context, it is important to understand and examine how biogeotechnical technologies and all related design decisions including treatment solution compositions, realized and desired improvement levels, and implementation details may require continuous evaluation, refinement, and optimization in order to more fully realize the greatest sustainability gains while still meeting financial constraints and holding societal safety paramount.

1.3 *Objectives and scope*

The focus of this paper is microbially induced calcite precipitation (MICP) via microbial ureolysis, the biomediated process that has arguably achieved the greatest academic and industrial interest, research investment, and realized progress to date. While this paper is specifically focused on the applicability of this process towards liquefaction mitigation, the paper is organized in two parts recognizing the broader interest in this particular technology and the applicability of more fundamental insights to other applications.

The first part of this paper is designed to be relevant and applicable to all with interest in the MICP process, regardless of the specific engineering application considered. This portion begins by describing the more fundamental microbiological and biogeochemical processes by which MICP can be achieved, the structure of resulting biocemented materials, and other more fundamental considerations including material permanence. This is followed by detailed coverage of the entire treatment process, from establishment of biological activity through either stimulation of indigenous bacteria or augmentation of non-native strains, to cementation treatments, through byproduct management strategies, and finally consideration of first-order environmental variables. Finally, details and recommendations regarding methods and techniques that can enable process monitoring and verification including those relevant to microbiological aspects, geochemical changes, and mechanical enhancements are further provided to ensure that the treatment technology is occurring as intended and that the final improved condition can meet project requirements.

The second part, building on the previously established base knowledge, advances specifically into how the engineering behaviors of sandy soils can be improved by MICP in the context of behaviors most relevant to liquefaction hazard mitigation. This portion begins at the element scale, addressing how MICP treatment affects low-strain dynamic properties including stiffness degradation and damping, monotonic behaviors, and undrained cyclic responses. Leveraging these experiment understandings, advances in the ability to model such behaviors at the discrete and continuum scales are further addressed. Finally, upscaling of the MICP treatment technology itself for field scale implementation is addressed through large upscaling experiments, centrifuge modeling, and a synthesis of experience and guidance from planned and executed field implementations. Conclusions and priorities for continued maturation of biogeotechnologies, and MICP in particular, are then discussed.

2 MICP TREATMENT PROCESS

2.1 *Chemical reaction network for ureolytic MICP*

Biocementation is enabled by the biological production of carbonate species in the presence of dissolved calcium salts. There are a number of pathways through which carbonate species can be biologically generated (Section 2.2) however the fundamental microbial processes capable of enabling MICP must yield carbonate species, hydroxide ions capable of elevating surrounding solution pH, or both. Urea hydrolysis (ureolysis), the most well-studied pathway through which biocementation has been achieved, involves the hydrolysis of urea, a reaction catalyzed by the enzyme urease, which yields carbonic acid and ammonia (Equation 1). Ammonia, under pH conditions that are representative of most soil systems (pH < 9.5), will have some fraction protonated to form ammonium, leading to a reduction in protons and thus a net increase in pH (Equation 2). The distribution of carbonate species is pH dependent and governed by carbon dioxide equilibria (Equations 3 & 4); therefore, pH increases resulting from the formation of ammonium enables generated carbonic acid to shift increasingly towards bicarbonate and carbonate (Equation 4). Due to the relatively low solubility product (K_{sp}) of calcite and other calcium carbonate ($CaCO_3$) polymorphs, even when small amounts of aqueous carbonate are formed in the presence of sufficient calcium, calcium carbonate mineral precipitation can be favored (Equation 5). The mineralogy and morphology of the generated mineral product can be variable and has been shown to depend on many factors

(Section 2.5). Although generated minerals may include calcite, aragonite, and vaterite, among others, the authors refer to the precipitate resulting from MICP throughout this paper as either calcite or calcium carbonate, and do so interchangeably. This subtlety may be not strictly correct, but is supported by experimentation demonstrating that the predominant mineral in almost all MICP experiments is calcite (Burdalski 2020). The net reaction for ureolytic MICP presented in Equation 6 is simplified to neglect pH-dependent ammonium speciation. During $CaCO_3$ precipitation, free protons are generated as carbonate is consumed, making precipitation an acidogenic process. Thus, without a continuing source of alkalinity, the precipitation would acidify and self-limit, reaching equilibrium without fully utilizing the provided calcium. In the existing literature, it is frequently discussed that MICP requires substantially alkaline conditions to be successful. However, the low solubility of $CaCO_3$ minerals permits substantial pH latitude in order to maintain super-saturation (Section 2.5). For example, only 3.3 pM CO_3^{2-} is needed to supersaturate solutions with respect to calcite when 1 mM Ca^{2+} is present. Indeed, the steady state pH when both urea hydrolysis and carbonate precipitation are occurring in MICP experiments is generally between 7.5 and 7.8 (Gomez et al. 2018b) with only the final pH altered by supplied urea (Figure 3). Thus, while the precipitation can and does occur at more neutral pH, it does require constant hydroxide and carbonate species generation to maintain super-saturation, both of which are provided by ureolysis.

$$CO(NH_2)_2 + 2\,H_2O \xrightarrow{urease} H_2CO_3 + 2NH_3 \quad (1)$$

$$NH_3 + H_2O \overset{pK_a: 9.3}{\longleftrightarrow} NH_4^+ + OH^- \quad (2)$$

$$CO_{2\,(g)} + H_2O \overset{dissolution}{\longleftrightarrow} CO_{2\,(aq)} + H_2O \overset{hydration}{\longleftrightarrow} H_2CO_3 \quad (3)$$

$$H_2CO_3 \overset{pK_a: 6.35}{\longleftrightarrow} HCO_3^- + H^+ \overset{pK_a: 10.33}{\longleftrightarrow} CO_3^{2-} + 2H^+ \quad (4)$$

$$Ca^{2+} + CO_3^{2-} \xrightarrow{K_{sp\ calcite}: 10^{-8.48}} CaCO_{3\,(s)} \quad (5)$$

$$CO(NH_2)_2 + Ca^{2+} + 2\,H_2O \xrightarrow{urease} CaCO_{3\,(s)} + 2NH_4^+ \quad (6)$$

2.2 *Alternate MICP pathways*

Urea hydrolysis by *Sporosarcina pasteurii (S. pasteurii*) has been the most frequently employed biological process and organism combination to drive $CaCO_3$ biocementation. Nonetheless, other biological processes, namely sulfate-reduction, iron-reduction, and denitrification have also been proposed (Castanier et al. 1999, DeJong et al. 2010). In Graddy et al. (2018), kinetic parameters for whole cell urease from 6 MICP isolated *Sporosarcina* strains and the *S. pasteurii* type strain were reported. Furthermore, alkalinity and carbonate generation rates (in CO_2 equivalents) were compared between these ureolytic strains involved in both biostimulated and bioaugmented MICP (Sections 2.3 & 2.4) to rates in the available literature for denitrifying, iron-reducing, and sulfate-reducing bacteria in pure culture. Figure 4 presents the ranges of production rates for *Sporosarcina* strains compared to heterotrophic bacteria respiring anaerobically with alternative electron acceptors. As shown, the *S. pasteurii* type strain produces alkalinity and carbonate species at rates that are roughly 100-fold greater than even the most active of the other proposed

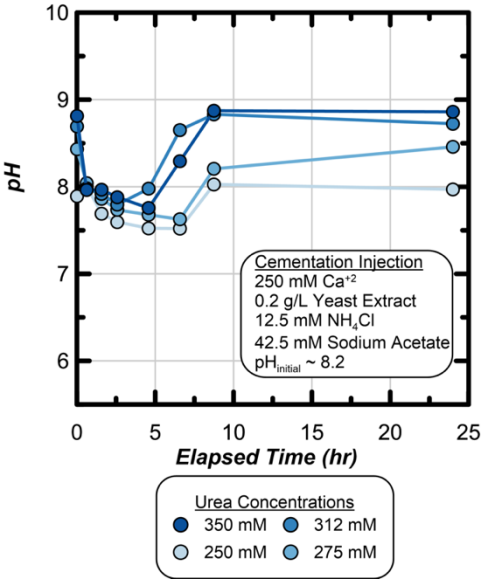

Figure 3. Solution pH in time during a representative cementation injection using solutions with 250 mM calcium show the ability to control final pH by varying urea concentrations (adapted from San Pablo et al. 2022a).

biological processes, as studied in pure cultures. Furthermore, rates for recently isolated ureolytic strains range from approximately 80% down to 1% of the corresponding rate for the *S. pasteurii* type. However, even the lowest measured rates for ureolytic isolates from biostimulated MICP are near the highest known rates for the other metabolic processes. Ureolytic representatives from other genera such as *Bacillus, Lysinibacillus*, and *Alkalibacterium* (Cheng & Cord-Ruwisch 2012, Kang et al. 2016, Cheng et al. 2017b, Gowthaman et al. 2019, Dikshit et al. 2020, Ezzat & Ewida 2021, Mukherjee et al. 2021) have also been used to stabilize soils via MICP.

Of the most promising alternate methods, microbially induced desaturation and precipitation (MIDP) uses denitrification to generate both alkalinity for precipitation as well as dinitrogen gas bubbles, which desaturate soils (DeJong and Kavazanjian 2019). Data from Figure 4 clearly suggest a much slower rate of MICP with denitrification, which was demonstrated by soil column experiments (van Paassen et al. 2010a) wherein achieving a relatively low calcite content (~2% by mass) required 100 days. In comparison, this same amount of biocementation was achieved after 4 daily cementation treatments by both bioaugmented or biostimulated ureolytic MICP (Graddy et al. 2021), and alternate higher concentration treatment formulas could be realized within 48 hours. It should be noted that field implementations of MICP are likely to impose practical time constraints on the treatment frequency and overall duration of projects. To this end, much attention has been given to achieving the highest production rates of carbonate and alkalinity; however, it is unknown what effect, if any, a lower rate of calcite precipitation may have on bio-cemented soil behavior. At a minimum, lower production rates can present an opportunity to improve the spatial uniformity and extent of treatment as discussed later in Section 3.2.3.3 & 7.2.

The use of alternative alkalinity generating processes, however, may present further drawbacks than simply slower precipitation rates. For example, iron-reduction requires the use of insoluble iron (III) compounds and sulfate-reduction can produce toxic hydrogen sulfide gases, both of which would likely present field implementation challenges. A possible advantage for denitrification-driven MICP is that it may not leave remediation-requiring waste products in the soil; however,

comprehensive nitrogen balance studies have not yet been completed for applications of MIDP in natural soils. Thus, the possibility exists that a portion of added nitrate may be instead respired to ammonia by native bacteria, remain unreacted, or be reduced to intermediate phases other than dinitrogen gas (e.g., NO_2^-, N_2O; Rütting et al. 2011).

A number of non-ureolytic bacterial strains or enrichments have been successfully employed in bioaugmented or biostimulated MICP studies, wherein the explanations for the mechanisms by which alkalinity and carbonate are generated are sometimes unclear. The common feature of most of the systems is the alkalinization deriving from organic acid uptake. That is, any time a metabolizable weak organic acid is added as a salt, e.g., sodium formate (pKa = 3.74) or sodium lactate (pKa = 3.88), bacterial utilization of that substrate as an uncharged molecule, for subsequent respiration or incorporation, will include uptake of protons, thereby rendering the medium more alkaline. This mechanism is explicitly recognized as the cause of MICP driven by aerobic formate oxidation (Ganendra et al. 2014). Acetoclastic methanogenesis, which is based on acetate consumption, almost certainly resulted in the alkalinity increase that drove carbonate precipitation in a consortium feed sodium acetate (Su & Yang 2020). Likewise, mechanisms of non-ureolytic MICP observed for aerobic growth of *Bacillus alkalinitrilicus* and *Lysinibacillus* sp. strain YS11 (Nielsen et al. 2020, Lee et al. 2017) strongly implicate growth at the expense of, respectively, lactate or acetate anions. Yet another mechanism for alkalinity generation driving MICP based on deamination of amino acids has also been proposed (Lee et al. 2017).

2.3 *Ureolytic augmentation*

Bioaugmentation is the introduction of non-native microorganisms to soils to initiate some process of interest. Augmentation has been both the first and most commonly employed method for ureolytic MICP. Although other strains can be used, *S. pasteurii* (strain 11859; American Type Culture Collection, ATCC) is the most commonly augmented bacterium. Despite some suggestions in the MICP literature to the contrary, bacterial ureases are typically cytoplasmic, with any apparent extracellular activity resulting from cell lysis (Mobley & Hausinger 1989). The canonical role long assigned to urease, which is active in many types of bacteria, is to alleviate nitrogen starvation by providing assimilable ammonia. However, given

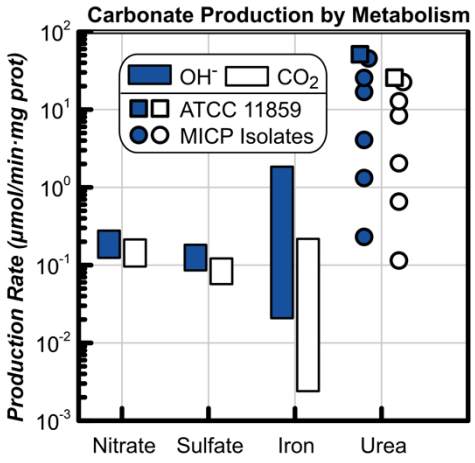

Figure 4. Rates of whole-cell production of CO_2 and alkalinity (expressed as OH^-), i.e. the drivers of carbonate production essential for MICP for denitrification, sulfate reduction, iron reduction and urea hydrolysis. Data and equations used to calculate production rates for CO_2 and OH^- include the contribution of acetate uptake on alkalinity production (adapted from Graddy et al. (2021).

the high ammonium environment that emerges during ureolytic MICP treatments, the constitutive and persistent urease expression suggests it may also play an ecological role in toxifying its environment to achieve a competitive advantage. Additionally, it has been suggested that urea hydrolysis provides cellular energy to *S. pasteurii* adequate to fuel anoxic growth (Cheng et al. 2017a). Because it is a hydrolysis and not an oxidation/reduction reaction or a fermentation, there is no literature precedent for such a reaction playing a sustained role in energy generation by a free-living bacterium. The literature does, however, provide two short-term, biophysical studies that demonstrated urea-driven production of ATP and a proton motive force in *S. pasteurii* and *Ureaplasma urealyticum* (Smith et al. 1993, Jahns 1996).

During the last two decades, literature involving bioaugmented MICP has grown rapidly and pertained to a wide variety of applications. The discussion of the more fundamental factors involving augmentation, however, will be confined to conditions applicable to liquefaction mitigation applications in saturated soils at nominal depths up to 30 meters. Foremost, the preparation of a bulk quantity of cells by growth under well-aerated conditions must occur prior to augmentation. The ATCC recommended medium (2% yeast extract, 75 mM $(NH_4)_2SO_4$, 130 mM Tris, pH 9) or a variety of other formulations found in the literature can be used for cultivation, but minimum requirements include the presence of at least 15 mM NH_4^+, some complex source of amino acids, nucleotides, and other trace nutrients, and an initial pH in the range of 8.0 to 9.0. Urea is not required for bulk cultivation, but if it is present, controlling the pH of the surrounding medium once growth has commenced is largely unnecessary as intrinsic buffering will occur from urease-generated ammonia/ammonium and carbonate species. Following preparation of cells in some medium, the most basic augmentation process involves rinsing and resuspending cells in some medium, injecting cells into soils, initiation of strategies to distribute and retain cells, and proceeding with the subsequent biocementation process. In most studies the cell rinsing and resuspension process has largely been omitted, with grown augmented bacteria introduced into soils in a solution containing urea, ammonium salts, and organic constituents (unconsumed organics and waste products present in spent growth medium and possibly defined additions of yeast extract, nutrient broth, etc.). Variations on this treatment scheme may also include, as examples, providing a fixation solution after augmenting soils, removing generated carbonate species after augmentation using a flush treatment, repeated augmentations during the cementation process, and alternating directions of pumping (van Paassen 2009, Al Qabany & Soga 2013, Gomez et al. 2016, Cheng et al. 2017b, El Mountassir et al. 2018, Zamani et al. 2019b).

Perhaps most fundamental to the augmentation process are the mechanisms controlling successful distribution of injected cells into initially untreated soils. Bacterial cells introduced into porous media as a flowing suspension may adsorb to individual soil particles and/or be subject to colloidal filtration, dependent on soil particle size, the result typically being higher augmented bacterial cell densities adjacent to injection sources, which result in higher reactivity and ultimately greater localization of precipitation at these locations provided that the flow conditions are not exceedingly fast. Whether this phenomenon can be solely attributed to non-uniform augmentation or abiotic precipitation events (resulting from the mixing of high calcium and high carbonate solutions near the injection source) is unclear. Uniformity of cell densities, however, is one critical factor influencing whether or not more uniform cementation can be achieved. In some of the earliest MICP studies, augmented cells supplied to columns filled with sand (Kantzas et al. 1992, Mahawish et al. 2019b) produced highly localized porosity

reductions, indicative of non-uniform augmented cell densities. This non-uniformity was attributed to issues with cell distribution as governed by colloidal filtration and cell retention as governed by electrostatic repulsion.

The impact of colloidal filtration is well exemplified by three studies wherein bacteria were augmented in different sands. In San Pablo et al. (2020), a poorly graded, alluvial sand (D_{10} = 0.23 mm, D_{60} = 1.5 mm, 1% fines) contained in a 3.7 m long column was augmented over a 3 hour period with 1.5 pore volumes (PV) of a dilute *S. pasteurii* culture (density of 9.4 x 10^7 cells/mL). After four daily 1.5 PV injections of a non-nutritive cementation solution, substantial cementation (ΔV_s ~800 m/s) was achieved at a distance of 0.3 m with no improvement detected at more distal locations. A second augmentation injection consisting of 9 PV was applied followed by 5 additional cementation injections with, yet again, more minimal improvement observed at further distances. In contrast, a similar stimulated 3.7 m column, achieved significant improvement at distances exceeding 3.4 m. This study comes closest to highlighting the primary challenges associated with interactions between augmented bacteria and surrounding soils, namely those related to electrostatic interactions and colloidal filtration, as the potential for unintended biostimulation (discussed later in Section 2.3.2) was kept to a minimum by two procedural choices. First, organic constituents that were residual in the bulk culture were diluted approximately 20-fold before augmentation and injected cells were resuspended and injected in a 150 mM NaCl solution. Second, the organics were eluted within 24 hours by the first cementation treatment. In contrast, two other studies (Whiffin et al. 2007, van Paassen et al. 2010b) which showed significant improvements at more than 10 times this distance (4.5 and 7.5 m, respectively) also used a finer poorly-graded sand (D_{10} = 0.110 mm, D_{90} = 0.275 mm, no fines) and augmentation. However, in their treatments, unamended stationary phase cultures were injected and $CaCl_2$ fixation solutions were applied 18 to 24 hours later. While this offers a possible explanation for the observed differences, another important difference in the protocols of these two studies from that of San Pablo et al. (2020) is that augmentation was performed using dense undiluted cultures of *S. pasteurii* with correspondingly higher concentrations of residual nutrients. The residual nutrients in combination with slower pumping rates and longer residence times may have provided between 5 and 15 days for unintended biostimulation to have occurred (Section 2.3.3).

The initial retention of bacteria following augmentation is thought to be substantially controlled by electrostatic forces (El Mountassir et al. 2018). The enhancement of bacterial cell attachment to soil particles requires a reduction of electrostatic repulsion and can be accomplished by providing a solution of sufficient ionic strength, such as synthetic (artificial) groundwater, or by providing urea in augmentation solutions in which augmented cells can generate their own increases in ionic strength. Harkes et al. (2010) provides an early example demonstrating the utility of a fixation solution. In this study, a dense cell culture was applied to a saturated fine sand with higher ionic strength fixation fluids provided to retain cells. Their findings suggested that a fixation solution consisting of 50 mM $CaCl_2$ achieved greater fixation than 150 mM NaCl; however, no cell retention was reported when fixed with deionized water. Variations on similar strategies have been employed in many other successful bioaugmented studies. Furthermore, other more elaborate schemes have been used including applying alternating < 1 PV injections of bacterial suspensions and fixation solutions (Cheng & Cord-Ruwisch 2012, 2014).

2.3.1 *Realized bacterial populations over time*

Studies examining changes in soil bacterial populations in natural soils over time following non-nutritive bioaugmented MICP are currently non-existent. If and when such studies are completed, representative bacterial sampling will remain challenging as recent observations suggest that ~90% of the active bacteria during MICP are not readily sampled as suspended cells (Graddy et al. 2021). This is presumably because such cells may be attached to soil particle surfaces and or embedded in generated $CaCO_3$ minerals. Recent experiments by the authors involving 1.7 m diameter tanks included one specimen that was initially bioaugmented and one that was biostimulated; however, daily cementation treatments included organic nutrients (Gomez et al. 2016). In this study, the added *S. pasteurii* type strain was shown to be outcompeted by enriched native ureolytic strains, as evaluated by cultured strains, high throughput sequencing, and sequencing of full length 16S clones (Graddy et al. 2018, 2021). Thus, in the presence of nutrients, the final composition of each initially augmented bacterial community converged largely to that of the corresponding stimulated one. Furthermore, the augmented type strain, which was dominant on day 5, following inoculation on day 4 as judged by isolates (Figure 5a), was barely detected by day 8 by DNA sequencing (Figure 5c), and not detected by day 12 at experiment's end in either method. These results suggest that, at a minimum, augmented microbial populations may be transient, although it is less clear if similar trends may be observed for augmented soils wherein nutrients are not supplied.

2.3.2 *Unintended biostimulation*

As previously discussed, a clear distinction should be made between augmented experiments wherein nutrients are not supplied with augmented bacteria (deemed "pure" or "non-nutritive" augmentation) and those experiments involving

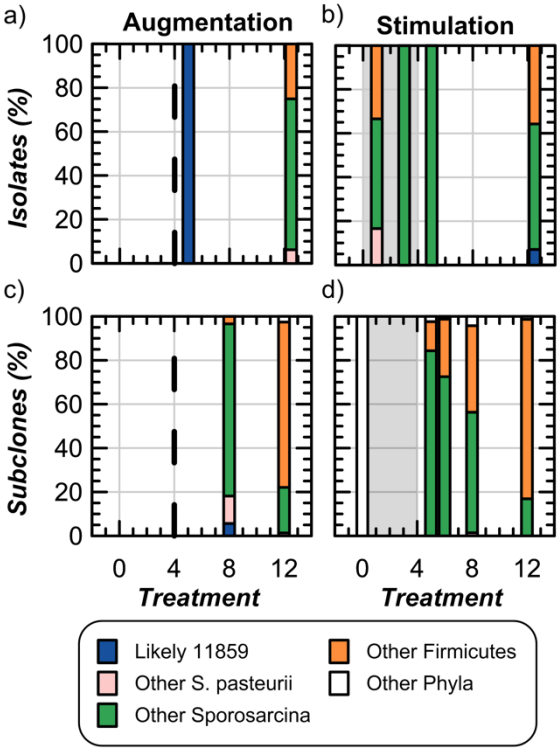

Figure 5. Microbial community estimates based on the (a,b) relative abundance of isolates and (c, d)16S rRNA fragments in (a,c) augmented and (b, d) stimulated soils. Dotted line indicates the augmentation treatment for (a) and (c), and the shaded regions in (b) and (d) represent stimulation treatments. (adapted from Graddy et al. 2018, 2021).

introduction of cells with sufficient nutrients wherein the potential for stimulation of indigenous bacteria should be acknowledged (deemed "nutritive" augmentation). The use of nutritive augmentation dominates the literature regarding studies of bioaugmented MICP and may result from the often-cited assumption that bacteria grown to a high density for use in MICP enter a stationary phase because all readily available nutrients have been consumed from the medium (Whiffin et al. 2007, Harkes et al. 2010, Mahawish et al. 2019a). Based on this assumption, augmentation cultures are commonly introduced in what is termed "spent" growth medium. If not fully consumed, however, dilute residual organics could stimulate indigenous soil bacteria. In this spent growth medium it is possible that the growth of bacteria in cultures to be augmented may be limited not by nutrient depletion, but rather by the accumulation of toxic metabolites (i.e., waste products) and oxygen transfer limitations. This nutrient exhaustion assumption can be examined by considering the experimental details of Whiffin et al. (2007). In this study, a medium containing 20 g/L of yeast extract, yielded an OD_{600} of 1.6, which translates into about 1 x 10^9 cells/mL based on the authors' best estimates (Figure 32). To estimate the fractional use of yeast extract in producing bacterial cells, the following well accepted assumptions can be made, which are essential and accurate to approximately 10%: (1) the elemental composition of yeast extract and bacterial dry matter are approximately 50% carbon by mass, (2) a single *S. pasteurii* cell contains approximately 3 x 10^{-13} g of organic carbon, and (3) when growing aerobically, a bacterium utilizes organic carbon roughly equally between catabolism (i.e., energy generation) and anabolism (i.e., generation of biomass). From these assumptions, 20 g/L yeast extract would be expected to yield *S. pasteurii* at about 1.7 x 10^{10} cells/mL, 17 times the observed final cell density in Whiffin et al. (2007). This suggests that ~95% of the growth potential provided by yeast extract might still present in "spent" medium; however, to the authors' knowledge this has not yet been tested. To put such concentrations into the context of what is needed for stimulation, it should be noted that a very low yeast extract concentration (0.04 g/L) enabled successful stimulation over meter-scale distances in San Pablo et al. (2020). Thus, even if "spent" medium and bacteria were diluted 20-fold prior to introduction into sand columns, there might still exist ~25 times more yeast extract than was needed for enrichment in these stimulated experiments.

In light of these observations, the authors suggest that earlier augmented studies could be divided into three groups, dependent on the particular augmentation protocols employed. Although exceedingly rare, the first category deemed "pure" or "non-nutritive" augmentation, involves the use of rinsed cell pellets of ureolytic bacteria that are introduced into a soil in strictly inorganic medium with later cementation solutions lacking any added nutrients (e.g., Gollapudi et al. 1995, Ferris et al. 1997, Stocks-Fischer et al. 1999, Peng and Liu 2019, Nafisi et al. 2020b, Ezzat and Ewida 2021, Burdalski 2020, Burdalski & Gomez 2020). In a second group, augmented bacteria are added to soils with nutrients provided at some point, either by suspending cells in fresh or "spent" growth media or providing cementation solutions including organics, thus presenting a possibility for unintended stimulation (e.g., Whiffin et al. 2007, Harkes et al. 2010, Jiang et al. 2017, Jiang & Soga 2017, 2019, Nafisi et al. 2019, Song & Liu 2020, San Pablo et al. 2020, Lee et al. 2021). Importantly, these studies provided relatively short residence times (< 36 hours), however, the time courses observed for urea degradation experiments with sequential enrichments (Figure 20 & 21), suggest that stimulated ureolytic bacteria could have still made some contribution to MICP in these scenarios. A third group allow for organic constituents to be present for several days during the cementation phase and therefore offer a clear opportunity for stimulated MICP to occur (e.g., van Paassen et al. 2010b, Al Qabany et al. 2012, Gomez et al. 2016, Cheshomi & Mansouri 2019, Jiang et al. 2019). One clear example of this potential is highlighted in Mukherjee at al. (2021) where an organic resuspension solution with no added bacteria was mixed into a silty soil column experiment. Their results suggested that this single organic amendment triggered stimulated MICP that achieved nearly 25% of the strength improvement observed in other columns with added organics and bacteria at a cell density of ~10^8 per gram of soil. Whether or not stimulation occurred in past augmented experiments may not be fully known; nonetheless, it is clear that there are important nuances between employed augmentation procedures meriting further consideration and investigation with the boundary between stimulation and augmentation being less clear than perhaps originally thought.

2.4 *Ureolytic stimulation*

Biostimulation is a second approach by which ureolytic cells can be generated to complete the MICP process. Rather than growth and injection of non-native bacteria, stimulation instead involves the injection of a growth medium that imposes selective environmental conditions intended to enrich indigenous ureolytic bacteria in natural soils. Successful stimulation of native ureolytic bacteria requires careful consideration of the needs of the target microorganism and how the growth of competing microorganisms can be minimized. Stimulation approaches have largely involved the application of solutions containing organic carbon, trace nutrients, and urea. Progressive modifications to these formulations have been made to increasingly select for alkali-tolerant and ammonium-tolerant soil microorganisms of which a larger fraction are thought to be ureolytic. A multitude of treatment solution factors may impact enriched microbial communities with our current understanding of individual factors described later in Section 3.2.

Initial attempts at ureolytic stimulation largely involved attempting to stimulate ureolytic activity simply by adding substantial urea to a general growth medium. By supplementing solutions with urea, such efforts presumably hypothesized that ureolytic microorganisms may gain some benefit from urea degradation such as the alleviation of nitrogen limitations. Recognizing that stimulation media typically include nutritionally complex ingredients like nutrient broth or yeast extract that are rich in amino nitrogen and are supplemented with ammonium (both of which satisfy the nitrogen requirements of growing bacteria), it is unlikely that such a benefit may be related to increased nitrogen availability. More recent experiments, discussed below, suggest that the bacteria selected for are closely related to *S. pasteurii*, and may share its capacity for urea hydrolysis linked ATP synthesis (Jahns 1996). Although stimulated MICP was originally investigated by Ferris et al. (1997), a multitude of other studies have contributed toward the development of stimulation techniques and current understandings of the biostimulation process (e.g., Fujita et al. 2008, Tobler et al. 2011, Burbank et al. 2013, Gomez et al. 2014, Gat et al. 2016, Gomez et al. 2016, Dhami et al. 2017). The current understanding of ureolytic enrichment involves the targeted selection for microorganisms in soils with unregulated ureolytic activity and elevated ammonia and pH tolerance. This is accomplished by supplying stimulation solutions with concentrations of ammonia and hydroxide that are tolerated by the targeted microorganisms, but suppress the growth of non-ureolytic bacteria that would otherwise compete for the limiting media components. Stimulation by this approach has always been successful in application to 14 different sands or sites, including repeated trials with a single sand tested 7 times over an

8-year span and one site tested at three different depths ranging from 2 to 12 m (Gomez et al. 2014, Gomez et al. 2016, Gomez & DeJong 2017, Gomez et al. 2018a, b, Lee et al. 2019a, b, San Pablo et al. 2020, Graddy et al. 2021, San Pablo et al. 2022a, Yanez et al. 2022). Although it may be possible that certain soils have an uncooperative natural population of bacteria that stymies efforts to stimulate, no such circumstances have been encountered thus far.

From a practical perspective, stimulation offers the ability to avoid previously discussed challenges related to colloidal filtration of injected cells by enriching microorganisms that are already present. This differentiation can yield important benefits with respect to improving cementation spatial uniformity and control through the elimination of issues related to the localization of cells near injection locations and poor distribution of ureolytic activity and reactants over large treatment distances. For field scale applications, such advantages may be a decisive factor allowing for the MICP process to become practically superior to other technologies, allowing for treatment of soils over large injection distances, including those potentially needed when addressing existing infrastructure, as well as permitting associated reductions in treatment implementation costs. Additional benefits of stimulation include the elimination of the need for sterile cultivation and transportation of dense cell suspensions to project sites and the reduction in environmental and soil ecological impacts that follow. From a treatment efficacy standpoint, stimulation also yields a persistent ureolytic microbial community that requires minimal additional inputs to maintain ureolytic capacity. In effect, this precludes activity losses associated with cell death and entombment, thereby avoiding the periodic need for reintroduction of augmented ureolytic cells. The stimulation process does have some different requirements, however. In particular, biostimulation requires repeated applications of a selective growth medium to soils and incubation thereafter in order to achieve sufficient ureolytic activity. This might involve the addition of several days to a given treatment program before cementation and improvement of soils can commence. Given the significant practical performance benefits that stimulation affords including its high rate of success and ease of application, however, the authors almost exclusively employ stimulated MICP with specific techniques described later in Section 3.

2.4.1 *Stimulated microbial communities*

The stimulation treatment method (Section 3.2) is strongly selective for a narrow group of closely related microorganisms (Figure 5b, d). Nevertheless, within this clade, there is also a surprising amount of diversity given the repeated application of stimulation solutions, which impose stringent selection. Recent findings suggest that enrichment techniques used in the authors' studies yield at least 96% Firmicutes at the end of stimulation when solutions are applied with artificial ground water (AGW) or deionized water as the solution base (Figure 6a-c), 93% when using stimulation solutions with natural seawater (NSW) as a base (Figure 6d, e), or 90% using a combination of 40% NSW and 60% AGW (Figure 6f), of which 85%, 92%, and 89%, respectively, were of the genus *Sporosarcina*. Similar selection appears in both freshwater alluvial sands (Concrete Sand) and marine sands (Beach Sand) when applying solutions with either artificial ground water or natural sea water, indicating that this selection is robust and the requisite bacteria are ubiquitously distributed. While enrichment for Firmicutes is not surprising, given that they include a number of halo- and alkali-tolerant bacteria, the consistent and stringent selection for a single genus is remarkable.

Sporosarcina are an example of such haloalkalitolerant bacteria, but are also known for their preference for urea-nitrogen, constitutive ureolytic activity, and ammonia tolerance

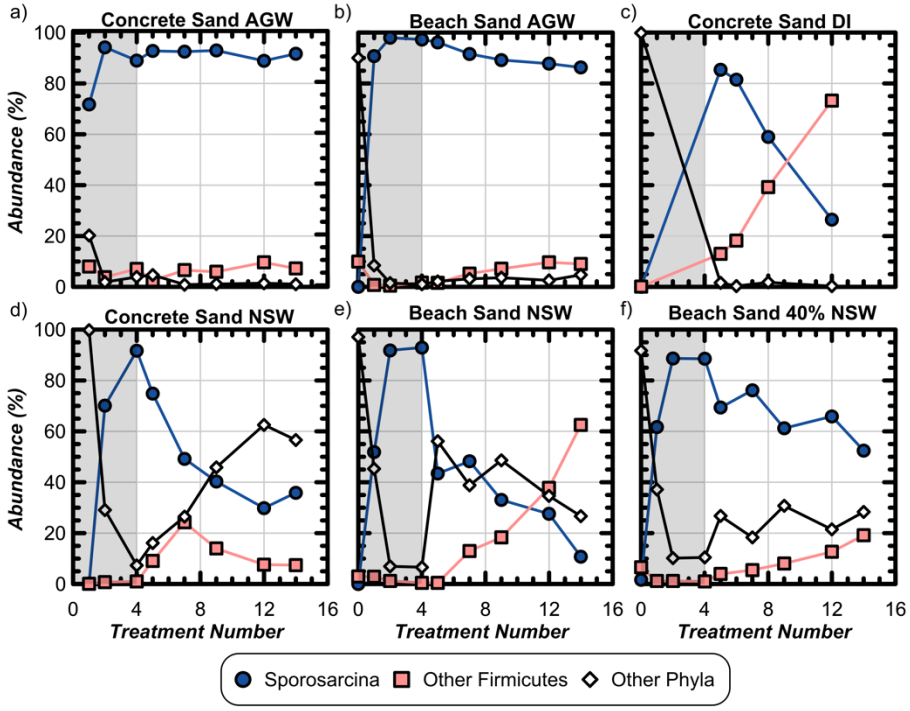

Figure 6. Microbial community composition by 16S rRNA analysis of (a, c, d) alluvial Concrete Sand or (b, e, f) Beach Sand using treatment solutions based in (a,b) artificial ground water (AGW; Ferris et al. 2004), (d,e) natural seawater (NSW), (c) deionized water (from Graddy et al. 2021), or (f) a 40% mixture of NSW with 60% AGW. Biostimulation treatments were 350 mM urea, 100 mM ammonium chloride, 42.5 mM sodium acetate, 0.2 g/L yeast extract, pH 9 and the cementation treatments were 350 mM urea, 250 mM calcium chloride, 12.5 mM ammonium chloride, 42.5 mM sodium acetate, 0.2 g/L yeast extract, at an incidental pH of around 8.3 in all but (c), where the treatments were the same save 12.5 mM ammonium, 0.1 g/L yeast extract with no pH adjustment throughout. Shaded regions indicate stimulation treatments. Data are missing for the initial microbial communities in (a) and (d) (adapted from Yanez et al. 2022).

(Mörsdorf & Kaltwasser 1989, Leejeerajumneanet al. 2000, Trujillo et al. 2015). These stimulated species are therefore presumably strongly selected for on the basis of ionic strength, pH, and urea-hydrolysis end products. It remains unknown if they are the best suited for these conditions or simply the first to dominate these enrichments and, if given enough time, more efficient but more slowly growing bacteria may displace them from this niche. If their success and competitive edge is the result of more rapid growth, increasing treatment application frequency may maintain selection for fast growing organisms through the repeated elution of resident bacteria. Given these repeated growth and elution cycles (analogous to a traditional serial enrichment), it is rather surprising that 7 species of *Sporosarcina* appear to be present at significant abundance (> 10%) in these environments (Graddy et al. 2021). This outcome further suggests that a number of *Sporosarcina* species are frequently present in natural soils and capable of contributing to the function of stimulated MICP, rendering stimulation success less susceptible to the presence or absence of a particular species in any given soil. This diversity also suggests that there may be niches present for each of these species, perhaps at different points during a treatment cycle.

The relative abundance of *Sporosarcina* has been found to range from remaining steady to decreasing substantially over the course of repeated stimulated MICP treatments. In one instance, *Sporosarcina* was found to be partially displaced by *Lysinibacillus* (Figure 5d "Other Firmicutes", Graddy et al. 2021). In this case, frequent pore fluid sampling over the course of the experiment likely desaturated portions of the column and increased oxygen availability to the microbial community. The appearance of *Lysinibacillus* was not seen in other analogous sub-culturing (Graddy et al. 2018) or comparable AGW based enrichments independent of the parent material; better control of desaturation maintained strict selection for *Sporosarcina* using both freshwater alluvial sand and marine sand (Figure 6a, b). Therefore, increased oxygen availability was thought to have enabled the shift in microbial community composition, though no apparent decrease in ureolytic activity was observed, despite *Lysinibacillus* isolates not manifesting clear ureolytic activity (Graddy et al. 2021). When treated with natural seawater, substantial diversity was observed following the transition from stimulation to cementation treatments. This was partly attributed to the use of natural seawater that provided a consistent source of exogenous bacteria with each solution injection as well as the reduction in selective conditions employed in cementation treatments (reduced initial pH and reduced added ammonium). This may also be partially due to the fact that marine bacteria are naturally more salt and alkalitolerant than freshwater soil bacteria, making the primary mechanism for negative selection the presence of ammonia. The selectivity of total ammonium additions in turn is largely attenuated by the decreased pH experienced during cementation relative to stimulation. Regardless of these distinct community differences, there was no correlation between this increase in diversity and a decrease in ureolytic rate or achieved engineering performance, as discussed later in Sections 3.2.3.4 and 3.7.3 (Figures 23 & 30).

2.5 *$CaCO_3$ mineralogy & morphology*

Microbially-induced calcite precipitation is commonly referred to as generating calcite minerals, however, the generated calcium carbonate ($CaCO_3$) may exist as a variety of different mineral polymorphs, each with identical elemental compositions but important differences in crystalline structures and physical properties (Bladh et al. 2001, APHA 2005). $CaCO_3$ polymorphs generated during ureolytic biocementation include vaterite ($K_{sp} = 10^{-7.91}$), aragonite ($K_{sp} = 10^{-8.34}$), and calcite ($K_{sp} = 10^{-8.48}$), presented here in order of decreasing solubility in water at 20º C (Plummer & Busenberg 1982, Gal et al. 1996, APHA 2005). $CaCO_3$ can also exist in an amorphous phase with no definitive structure and as a result with varying solubilities and morphologies. The solubilities of these three primary polymorphs vary significantly and govern the $CaCO_3$ minerals that can be formed under different aqueous conditions. It is helpful to consider expected differences in mineral formation from the perspective of abiotic mineral stability although biogenic mineral formation oftentimes cannot be fully captured using thermodynamics alone due to the ability of microorganisms to overcome abiotic reaction activation energies. For a given solution condition, the thermodynamic favorability for a given mineral phase to either precipitate or dissolve can be expressed using saturation state (Ω) as shown in Equation 7, wherein K_{sp} is the solubility product of a given mineral polymorph, (Ca^{2+}) is the activity of calcium in solution, and (CO_3^{2-}) is the activity of carbonate in solution. The product of (Ca^{2+}) and (CO_3^{2-}) is commonly referred to as the ion activity product (IAP) and represents the availability of these species in solution to participate in reactions that either form or dissolve minerals.

$$\Omega = \frac{(Ca^{2+})(CO_3^{2-})}{K_{sp}} = \frac{IAP}{K_{sp}} \quad (7)$$

When Ω >1, solutions are supersaturated with respect to a given mineral phase and precipitation is favored. When Ω <1, solutions are undersaturated with respect to a given mineral and dissolution is favored. Lastly, when Ω =1, solutions are in equilibrium and neither dissolution nor precipitation would be expected. For the same geochemical conditions (i.e., aqueous Ca^{2+} and CO_3^{2-} activities) solutions may be either undersaturated or supersaturated, depending on the solubility of the $CaCO_3$ polymorph. Activity ratio diagrams, such as that shown in Figure 7 can be used to compare existing solution conditions to the mineral solubilities of different $CaCO_3$ polymorphs expected during MICP. In this diagram, solution Ca^{2+} and CO_3^{2-} activities can be compared to equilibrium lines (Ω =1) for common $CaCO_3$ polymorphs to determine conditions under which mineral precipitation or dissolution would be expected. Solution activities plotting above respective lines indicate supersaturation and a tendency for the solution to precipitate a given $CaCO_3$ polymorph with values plotting below lines indicative of undersaturation and a tendency for dissolution. As shown for the

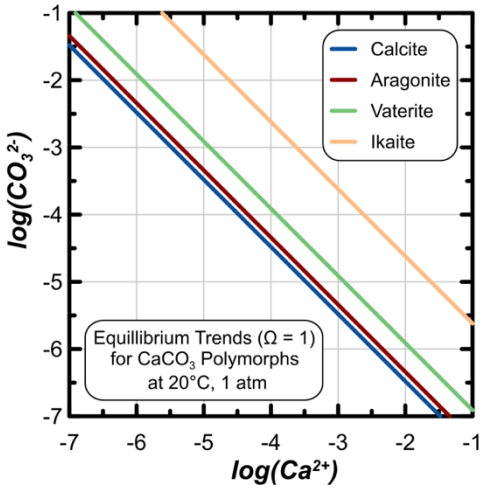

Figure 7. Activity ratio diagram illustrating differences in equilibrium lines (Ω = 1) between $CaCO_3$ polymorphs (at 20°C and 1 atm) resulting from differences in mineral solubility products (K_{sp} values) (adapted from Burdalski 2020).

three $CaCO_3$ polymorphs considered, solution conditions can exist wherein values can remain supersaturated with respect to lower solubility polymorphs (e.g., calcite) yet simultaneously undersaturated with respect to higher solubility phases (e.g., vaterite). Thus, the tendency for various $CaCO_3$ polymorphs to form during MICP is governed by aqueous geochemical conditions present during and after precipitation.

Differences between $CaCO_3$ polymorphs extend beyond their chemical solubilities and include important morphological differences. For example, calcite crystals most frequently exhibit a trigonal (rhombohedral) lattice structure, aragonite exhibits an orthorhombic crystal structure, and vaterite has a hexagonal crystal structure and often appears in a spherical form (Bladh et al. 2001). Although perhaps less relevant to MICP applications, at temperatures near freezing, $CaCO_3$ can also exist as ikaite, a polymorph with a monoclinic crystal structure and a spike-like morphology. Amorphous calcium carbonate has no definitive crystalline structure and thus can exhibit even larger differences in morphology. Although many researchers have characterized the mineralogy of ureolytic biocementation generated under specific experimental conditions, a clear understanding of how differences in achieved minerals may translate to changes in soil mechanical behaviors has remained limited. Nonetheless, these morphological differences and their spatial distribution have important implications with respect to the engineering behavior of biocemented soils with anticipated effects with respect to interparticle friction, volumetric responses, and initial shear stiffnesses, among other critical behaviors.

2.5.1 *Reaction progression*

The realized biocementation mineralogy will be influenced by the extent of reactions that occur during treatment injections as well as by the treatment solutions and subsurface environmental factors. In particular, recent studies have shown that while higher solubility $CaCO_3$ polymorphs (e.g., aragonite and vaterite) may precipitate initially during biocementation in the presence of higher IAP values, such minerals may subsequently dissolve and reprecipitate later in the treatment process as activities of involved species (Ca^{2+}, CO_3^{2-}) decrease below that needed to maintain supersaturation for these higher solubility polymorphs. This process, more formally known as Ostwald ripening, is not unique to MICP and suggests that the mineralogy and structure of MICP may be transient during the treatment process, influenced by not only reaction geochemical conditions but also reaction progression. Wang et al. (2019) captured this phenomenon visually using microfluidic experiments wherein the ripening of spherical vaterite-like crystals to rhombohedral calcite-like crystals was observed during stop-flow treatment residence periods as reagent concentrations were consumed (Figure 8). Similarly, they also observed the appearance of smaller and presumably more soluble crystals early during injections with later dissolution and recrystallization of these minerals to form larger more thermodynamically stable crystals. Burdalski (2020) performed small volume plate experiments that were destructively sampled at various points during the biocementation process to examine changes in mineralogy with reaction extent using semi-quantitative x-ray diffraction analyses (XRD). In experiments involving relatively high reactant concentrations (1250 mM urea and Ca^{2+}), the formation of significant quantities of vaterite were observed early during reactions with progressive reductions in vaterite and associated increases in calcite fractions as the treatment process proceeded (Figure 9). Zambare et al. (2020) performed MICP droplet experiments and noted similar transitions in mineralogy and morphology in time during reactions, with the appearance of poorly-structured amorphous calcium carbonate as a precursor to vaterite and some limited amounts of calcite. Collectively, these studies suggest that the mineralogy of biocementation is significantly influenced by both chemical conditions during and after precipitation with the potential for ripening of more soluble mineral phases towards more stable $CaCO_3$ polymorphs in time when reactions are allowed to proceed to completion and water remains present.

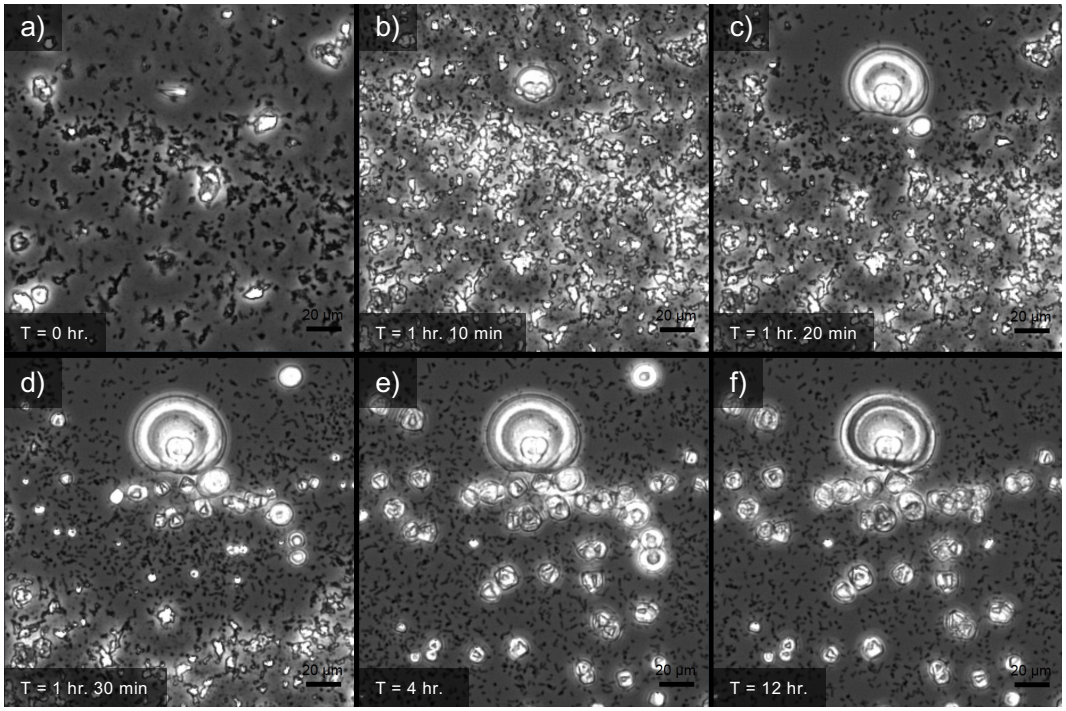

Figure 8. Microscope images (a) 0 hr., (b) 1 hr. 10 min, (c) 1 hr. 20 min, (d) 1 hr. 30 min, (e) 4 hr., and (f) 12 hr. after injections show the initial appearance and dissolution of spherical vaterite-like $CaCO_3$ crystals with the appearance of rhombohedral calcite-like $CaCO_3$ crystals later in time (adapted from Wang et al. 2019).

2.5.2 *Treatment solution composition*

Although researchers have considered a wide variety of reactant concentrations, chemical additives, and bacterial densities in biocementation treatments, the relationship between these formulations and resulting mineralogy has not been systematically examined. This has primarily resulted from differences in treatment formulations, soil materials, and treatment application methods between researchers which have prevented attributing specific mineralogical differences to isolated variables. Depending on the particular study, cementation solution urea and calcium concentrations can vary by orders of magnitude with specific additives such as sodium bicarbonate, ammonium chloride, and various growth factors frequently included or excluded. "Legacy" treatment formulations have persisted likely out of concern for unintended consequences if formulations are modified. Nonetheless, it is clear that the decision to modify applied reactant concentrations and include or omit specific additives should be carefully considered within the context of the minerals that are being generated. Burdalski (2020) aimed to further improve understanding of these relationships and examined the impact of isolated factors including applied urea and Ca^{2+} concentrations, augmented cell densities, and common treatment solution additives (e.g., NH_4Cl, $NaHCO_3$) on biocementation mineralogy and morphology in high-throughput plate experiments. These investigations yielded important insights regarding how treatment formulation changes can have significant consequences on the produced mineral phases. For example, in experiments wherein augmented *Sporosarcina pasteurii* cell densities were varied by over one order of magnitude, large differences in urea hydrolysis reaction rates were observed, but only small differences in mineralogy and morphology resulted (Figure 10). In contrast, when growth factors (i.e., yeast extract, nutrient broth) were supplied to treatment solutions with a *Sporosarcina pasteurii* cell density of ~7.5 x 10^7 cells/mL dramatic differences in mineralogy and morphology were observed with increasing quantities of more soluble vaterite minerals detected with increases in growth factor concentrations (Burdalski et al. 2022c). Interestingly, both increases in augmented cell densities and growth factor concentrations have been used in past studies to achieve faster reaction rates, and therefore these results suggest that such changes may have had significant consequences for the produced minerals.

2.5.3 *Environmental conditions*

Treatment solutions can impose specific geochemical conditions during MICP, however, remaining uncertainties include unavoidable environmental conditions including soil types, trace ions, pH, and other factors, which may alter geochemical conditions present during biocementation. While differences in environmental conditions present nearly endless possibilities with respect to the geochemical conditions, experiments by Burdalski et al. (2022a) have examined a limited range of environmental factors expected to be of importance for practical field applications. In these experiments, notable differences in biocementation mineralogy and morphology were observed in the presence of seawater ions with magnesium concentrations found to significantly inhibit ureolytic activity. When variations in parent soils were considered, including different natural poorly-graded sands and clay minerals, large differences in reaction kinetics were observed. This was likely due to differences in exchangeable soil ions, however, large mineralogical differences were not observed, with calcite remaining the predominant mineral polymorph (Figure 11). While questions remain regarding a multitude of factors, similar high-throughput experiments may allow for the impact of site-specific environmental conditions to be more readily examined, quantified, and understood. Finally, although the impact of mineralogical and morphological differences on soil mechanical responses and permanence have yet to be fully understood, it is clear that such differences will likely have important practical implications and thus require more extensive characterization moving forward.

2.6 *Microstructure & microscale properties*

While the microstructure of MICP is inherently linked to the treatment processes used to generate such cementation, the

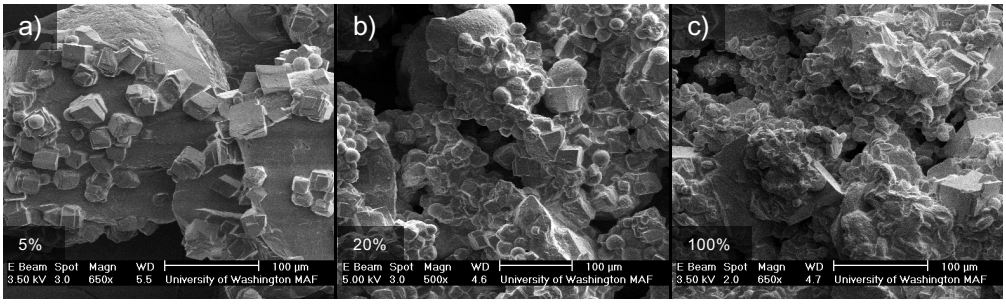

Figure 9. SEM images of biocemented specimens from 1250 mM urea and Ca^{2+} plate experiments after (a) 5, (b) 20, and (c) 100% reaction completion show the appearance of significant vaterite early on during reactions with progressive dissolution of vaterite and reprecipitation as calcite in time as conditions approached equilibrium (adapted from Burdalski et al. 2022b).

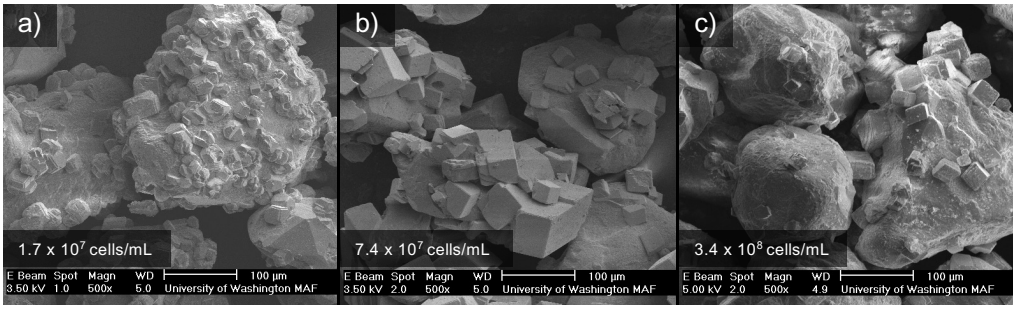

Figure 10. SEM images of biocemented specimens from 250 mM urea and Ca^{2+} plate experiments with augmented *Sporosarcina pasteurii* at cell densities of (a) 1.7 x 10^7, (b) 7.4 x 10^7, and (c) 3.4 x 10^8 cells/mL (adapted from Burdalski et al. 2022c).

effects of $CaCO_3$ precipitation can be considered to more broadly include the following primary microstructural changes: (1) the bonding of adjacent particles through cohesive cementation bridges that generate tensile capacities and cohesive forces, (2) the coating of particle surfaces with $CaCO_3$ crystals that alter surface roughness, angularity, and interparticle friction, and (3) the densification of soil particle matrices through the filling of voids with solid mineral phases. As a direct outcome of more microbiological and geochemical fundamental processes discussed earlier in Section 2, Figure 12 presents examples of SEM images of biocemented sand particles for which noticeable differences in cementation morphologies and distributions can be observed. Even without knowledge of their mechanical behaviors, such differences would be expected to manifest as differences in engineering responses dependent on not only the magnitude of cementation, but also its distribution at the particle-scale, crystal morphology, and association with particle surfaces and contacts.

Further characterizations including those presented in Figure 13**,** which involved the impregnation of cemented sand samples with epoxy, cross-sectioning, and subsequent polishing before imaging, clearly show the coating of soil particle surfaces with generated $CaCO_3$ and the resulting reductions in void ratios (DeJong et al. 2006). DeJong et al. (2010) conceptualized the cementation distribution and expected failure mechanisms, considering the proportional distribution of cementation at particle-particle contacts and on open surfaces and whether breakage would occur within the cementation precipitate or at the particle-precipitate interface. Subsequent studies have refined these hypotheses and have provided quantitative evaluations. For

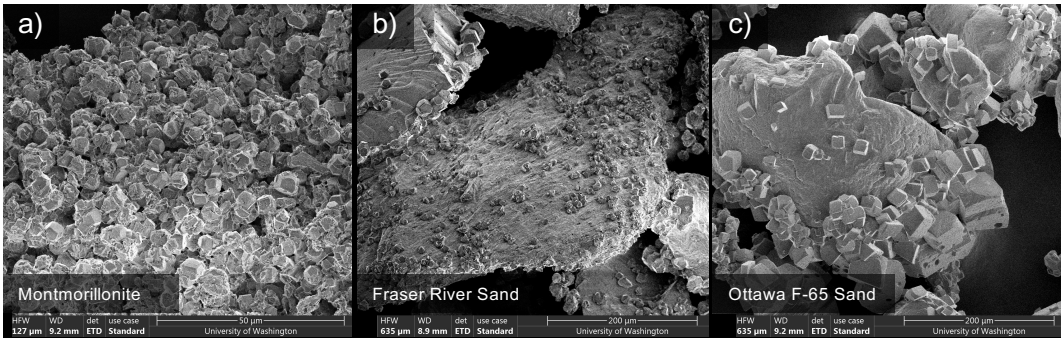

Figure 11. SEM images of biocemented specimens from 250 mM urea and Ca^{2+} plate experiments involving (a) montmorillonite, (b) Fraser River Sand, and (c) Ottawa F-65 sand materials (adapted from Burdalski et al. 2022a).

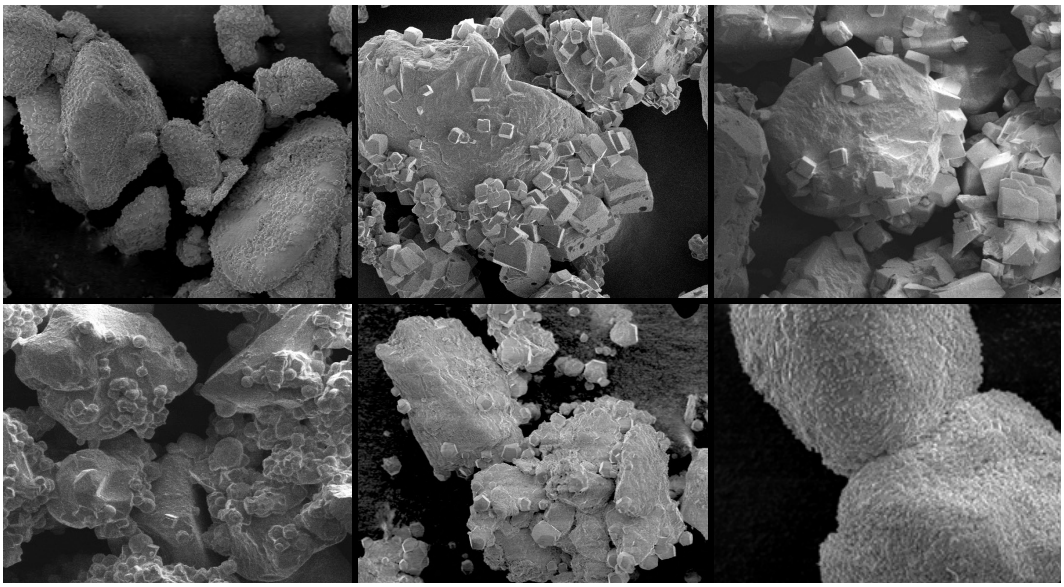

Figure 12. SEM images from the authors' experiments involving both stimulation and augmentation as well as varying treatment techniques highlight the breadth of possible microstructures that can result from the MICP process.

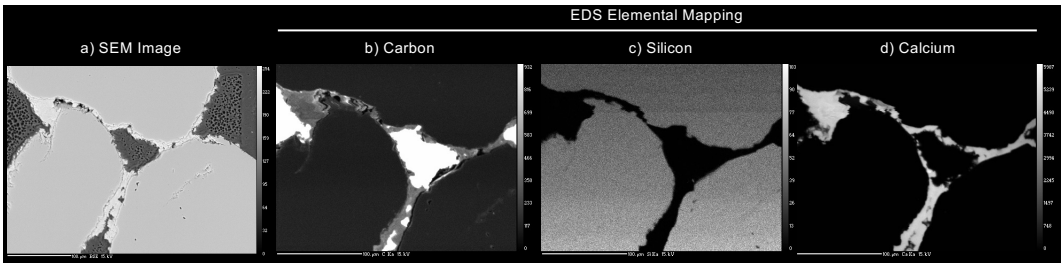

Figure 13. SEM images and EDS elemental mapping of a cross-section of biocemented sand with elemental concentrations of carbon silicon, and calcium shown (adapted from DeJong et al. 2006). It is noted that the carbon map reflects some influence of the carbon mounting tape.

example, further study is still necessary to confirm that preferential cementation occurs at contact locations; while it is clear that cementation preferentially forms near bacterial cells (wherein carbonate species are generated) and that bacterial cells are oftentimes attached to soil particle surfaces, the extent to which flow stagnation zones and colloidal filtration may concentrate cells near particle-particle contacts (El Mountassir et al. 2018) is still debated.

2.6.1 *Mechanisms of improvement*

How the primary mechanisms of improvement, (1) cohesive bonds, (2) particle angularity and surface roughness changes, and (3) bulk densification of soils through the filling of void volumes, alter the engineering behaviors of soils, depends on the applied loading. The presence of interparticle bonds in biocemented soils has been established through a variety of means including the direct measurement of particle contact tensile capacities to the qualitative imaging of particle bonds. These particle bonds provide cohesive forces between particles, however, brittleness results in improvements observed at smaller shear strains (< ~0.5%) being diminished at higher strains due to bond fracturing. This is most easily observed in specimens treated to low levels of cementation wherein initial stiffnesses and peak strengths are improved, with more minimal improvement post-peak (Section 5).

The coating of soil particle surfaces inevitably results in soil particles with apparent increases in shape and surface roughness. Recent imaging of Ottawa F-65 sands at varying cementation levels (Figure 14a) clearly shows the progression of these changes. Image analysis and quantitative evaluation of roundness (Wadell 1932, 1933, 1935) and sphericity (S = length/width) following Zheng and Hryciw (2015) show that roundness can capture such changes, particularly when comparing untreated particles to particles cemented to 5% calcite by mass, while sphericity shows no strong correlation (Figure 14b). These shape and surface roughness increases would be expected to influence behaviors after cemented bonds have fractured and the frictional resistance and volumetric behaviors of the soil are mobilized (shear strains > ~0.5%). At larger strains, it is expected that sufficient cementation may also alter critical state behaviors via increases in constant volume friction angles.

The addition of precipitate solids further densifies soils, which can also alter volumetric behaviors. The addition of mineral masses would be expected to alter shearing behaviors primary at strains corresponding to peak strength and beyond where the volumetric tendencies of a soil are mobilized (shear strains > ~0.5%). While the density of calcite mineral is similar to that of quartz ($G_S \sim 2.71$), the volume occupied by cementation may be larger due to the presence of voids and imperfections. Thus, progressive crushing of cementation during mechanical loadings, may further alter the volume occupied by $CaCO_3$ during shearing, thereby resulting in cemented soils becoming less dilatant at higher shear strains. Aside from mechanical behaviors, the addition of mineral solids may also alter important hydraulic characteristics as discussed later in Section 4.

2.6.2 *Mechanical testing of single particle contacts*

In an effort to better understand the mechanisms of enhancement at the particle level, researchers have examined the behavior of single particle contacts to characterize the strength and stiffness of such bonds, their modes of failure, and inform input parameters for the modeling of cemented materials using discrete elements. Ham et al. (2022) examined the response of cemented glass beads in tension and shear (Figure 15). Results showed the failure of cemented bonds to depend on cementation level, with the internal fracturing of bonds observed at high cementation, and the debonding of bonds and particles as well as combined failures exhibited at lower cementation levels. The tensile capacity of such bonds appeared to exceed the shear capacity of similar bonds by a factor of two. Interestingly, debonding failure mechanisms also appear to achieve the largest tensile and shear strength when compared to internal and combined failure mechanisms.

2.6.3 *Characterization of cemented soil matrices*

X-ray computed tomography (X-ray CT) has been used to non-destructively visualize spatial distributions of generated cementation (DeJong et al. 2008, Terzis & Laloui 2018, Baek et al. 2022) and quantify the microstructure of cemented soil matrices including bond frequencies, orientations, and how such characterizations may inform predictions of mechanical and hydraulic behaviors (Roy 2021), These CT images are similar to that shown in Figure 16, which presents cross-sections through poorly graded soils with D_{50} values of 0.18, 0.51, 1.39, and 2.74 mm which have been treated to approximately 20% calcite by mass.

2.6.4 *Distribution of contact-level cementation and effects on macroscale responses*

Improved understandings regarding cementation distributions and contact mechanics have been investigated by comparing anticipated behaviors from simplified models to experimental

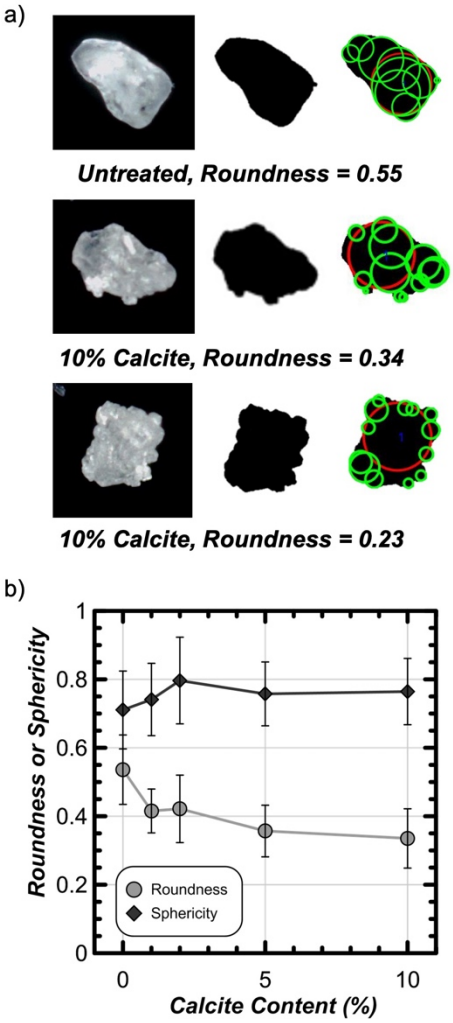

Figure 14. (a) Particle images of Ottawa F-65 sand comparing an untreated soil grain and a specimen treated with 10% calcite content and (b) roundness and sphericity for particles at varying cementation levels calculated using parameters from Zheng and Hryciw (2015).

data sets. For example, Lin et al. (2020) examined how differences in shear and compression wave velocities of biocemented sands from the literature compared to expectations from models which assumed either (1) localization of cementation on contacts, (2) uniform coating of grains with cementation, or (3) void infilling by cementation with no particle associations. Figure 17 presents an example of the model and experimental data comparisons for shear wave velocity measurements. Their results suggested that experimental trends were best approximated by considering a combination of particle coating and void infilling mechanisms.

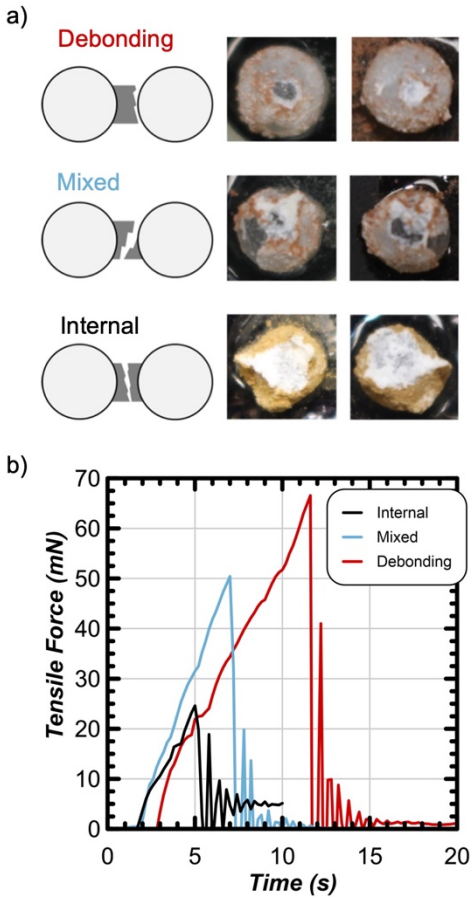

Figure 15. (a) Conceptual schematics and images of debonding, mixed, and internal bond failure mechanisms, (b) tensile force responses for example cemented particle tests involving the three different failure mechanisms (adapted from Ham et al. 2022).

2.7 *Permanence & reversibility*

The resilience of biocemented soils to extreme mechanical and chemical stressors, including acid rain exposure (Cheng et al. 2013, Liu et al. 2019, Chen & Achal 2020), freeze-thaw cycles (Cheng et al. 2013, Liu et al. 2019), wet/dry cycles (Liu et al. 2019), and unloading/reloading events (Porter et al. 2018) have yielded practical insights regarding specific scenarios, but broader understandings regarding the long-term permanence of biocementation under conditions more representative of liquefaction mitigation applications (i.e., saturated natural sand deposits) has remained limited. As biocementation advances towards field-scale deployment, estimating the permanence of biocemented soils will be critical to identify favorable field applications, quantify life-cycle environmental impacts, and predict long-term in situ mechanical performances. Although few studies have examined the dissolution of $CaCO_3$-based biocementation specifically (Ribeiro & Gomez 2022a, Ribeiro & Gomez 2022b), other studies considering the dissolution behavior of naturally-occurring and abiotically-generated $CaCO_3$ minerals (Sjöberg 1978, Morse and Arvidson 2002, Cubillas et al. 2005, Gehlen et al. 2005, Colombani 2016, and others) have yielded important insights regarding the factors that control $CaCO_3$ mineral stability, including their dissolution rates, magnitudes, and how such phenomena can be captured using geochemical kinetic frameworks. Although the chemical stability of biocementation is still being investigated, recent insights and preliminary results from ongoing studies are presented here.

2.7.1 *Tendency for dissolution*

The tendency for minerals to dissolve over time is controlled by the chemical composition of the pore fluid. More specifically, the stability of existing $CaCO_3$ biocementation is primarily controlled by the activity product (IAP) of carbonate and calcium ions in solution, and its relation to the solubility product (K_{sp}) of the particular $CaCO_3$ mineral(s) present. The state of this system is described using the saturation ratio (Ω) introduced earlier in Section 2.5. When solutions contain low concentrations of aqueous carbonate and calcium, the saturation ratio can be less than 1, suggesting that dissolution is favored. The greater the undersaturation, the closer the saturation ratio will be to zero, and

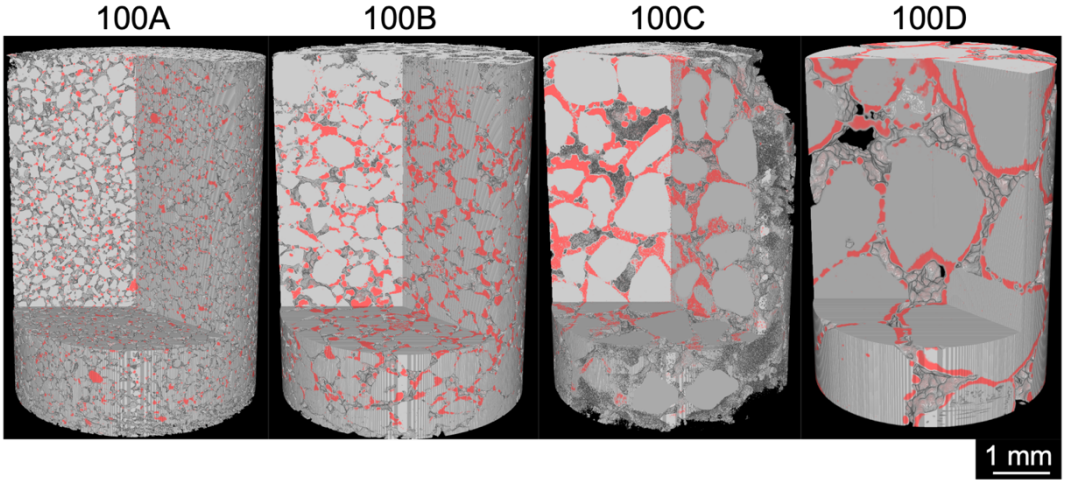

Figure 16. Example of X-ray CT images of a cemented soil volume wherein various volumes have been removed with distinctions between sand particles (red), pore fluids (blue), cementing $CaCO_3$ minerals (green) (adapted from Baek et al. 2022).

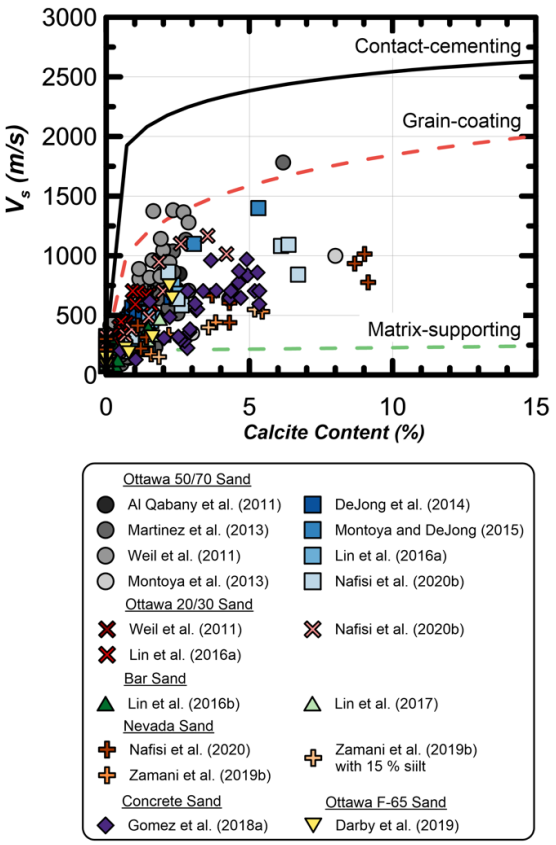

Figure 17. Comparison between an extensive set of shear wave velocity measurements from biocemented sands in the literature and model expectations for simplified cementation distributions shows best agreement between the experimental data and matrix-supporting and grain-coating models (adapted from Lin et al. 2020).

the more $CaCO_3$ mass that must be dissolved to achieve equilibrium. Since the solubility of different $CaCO_3$ minerals can vary by orders of magnitude, both the biocementation mineralogy and pore fluid chemistry directly determine which minerals dissolve most readily and the magnitudes of dissolution needed to achieve equilibrium. Although biocementation dissolution can be intuitively assessed under some conditions, such as in the presence of aggressive groundwater or acid mine drainage, in many cases where the groundwater may be slightly undersaturated and/or near equilibrium, accurate characterization of solution chemistry may be critical towards assessing stability and predicting longevity over years or decades. While accurate prediction of dissolution may be of high priority for some projects and sites, it should be recognized that dissolution may also not occur at some sites. For example, typical surface seawater includes ~10 mM calcium and ~2 mM bicarbonate with a pH near 8.1, resulting in saturation states ranging between ~2 and 7 (Dickson and Goyet 1994). Under these conditions representative of coastal locations, supersaturation of solutions with respect to $CaCO_3$ may exist, suggesting the favorability for subsequent precipitation events after MICP treatments. Therefore, dissolution may not be of primary concern if aqueous conditions are initially characterized and deemed favorable. Even when conditions are undersaturated, if the groundwater is not readily exchanged, the low solubility of $CaCO_3$ minerals may require only minimal mass losses to achieve equilibrium and maintain further stability. Although questions regarding biocementation dissolution and long-term stability will always remain site-specific, the frameworks for assessing mineral stability are available today and can be used, requiring only collection and characterization of site groundwater samples and evaluation of generated $CaCO_3$ mineralogy.

2.7.2 *Rate of dissolution*

Predicting how biocementation will dissolve over time is complicated by the temporal progression of dissolution. That is, even when solutions are undersaturated, dissolution will not occur instantaneously, but instead a slow kinetic process will occur with rates dependent on many variables including the physical properties of the minerals and groundwater. In this context, biocementation dissolution is a reactive transport problem, governed by the transport of groundwater through biocemented soils and its interactions with mineral surfaces, the mineralogy of biocementation and its specific surface area among other characteristics, the rate at which ions can be exchanged between mineral surfaces and undersaturated solutions, and other aspects related to the groundwater chemistry. While the dissolution behavior of biocementation has only been recently investigated (Ribeiro & Gomez 2022a), past studies regarding $CaCO_3$ minerals have suggested that rates may be strongly correlated to surrounding solution chemistry and in particular the solution pH and temperature (Sjöberg & Rickard 1984). Sjöberg & Rickard (1984) showed that when the pH of surrounding solutions exceeded ~5.5, $CaCO_3$ dissolution rates were saturation-controlled with dissolution rates being proportional to the solution's saturation index (Equation 8). In contrast, under more acidic conditions where pH values were near and below 4, $CaCO_3$ dissolution rates were increasingly diffusion-controlled due to limitations in how fast ions can exchange at mineral surfaces with dissolution rates primarily dependent on the pH of solutions (Equation 9). Equation 8 presents the saturation-controlled dissolution kinetic equation, wherein r_c is the dissolution rate, k_c is a dissolution rate constant, A_c is the mineral specific surface area, n is the reaction order, K_{sp} is the solubility product of the mineral, and (Ca^{2+}) and (CO_3^{2-}) are the activities of calcium and carbonate ions, respectively (Morse & Berner 1972). Equation 9 presents the diffusion-controlled kinetic equation, wherein r_c, k_c, n, and A_c are similar to Equation 8 and (H^+) is the activity of hydrogen ions (Sjöberg & Rickard 1984). Although understanding of biocementation dissolution remains somewhat limited, these studies have provided key insights and suggest that the surrounding solution chemistry is an important factor altering dissolution rates and our ability to model and predict such processes.

$$r_c = k_c A_c \left(1 - \frac{(Ca^{2+})(CO_3^{2-})}{K_{sp}}\right)^n \quad (8)$$

$$r_c = k_c A_c (H^+)^n \quad (9)$$

2.7.3 *Current understanding of dissolution*

Recent studies have provided new insights regarding biocementation dissolution rates, the spatial and temporal progression of biocementation degradation when exposed to undersaturated solutions, and the ability of existing kinetic frameworks to capture such processes. Ribeiro and Gomez (2022a) completed a series of batch experiments where biocemented poorly-graded sands were subjected to different acidic solutions to investigate the magnitude and rate of $CaCO_3$ dissolution as a function of acid type, concentration, initial pH, and other factors. The results suggested that although acid type and concentration can alter dissolution patterns, such trends can be captured using existing saturation-controlled kinetic models, especially when surrounding solutions are strongly buffered. Figure 18 presents an example of dissolution batch experiment results where biocemented samples were subjected to 50 mM acetic acid with and without 100 mM acetate, with both solution

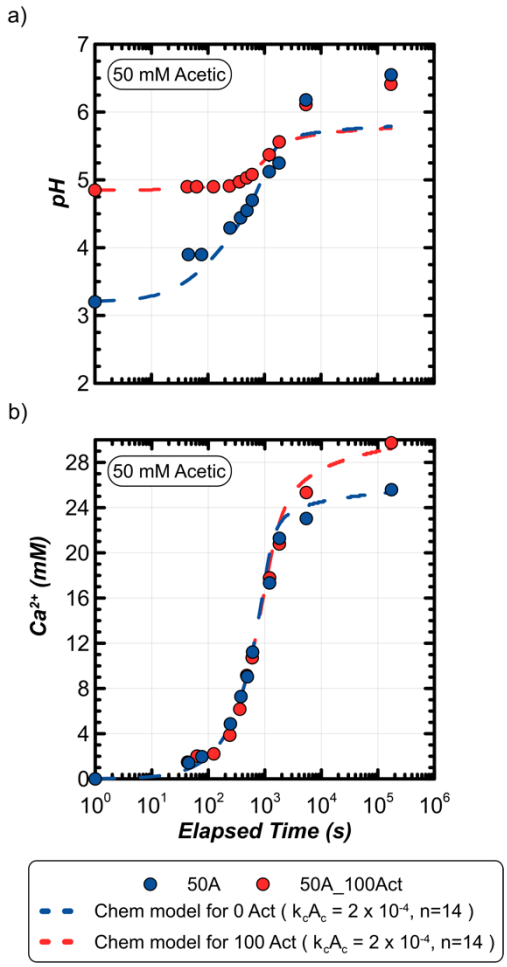

Figure 18. Progression of (a) solution pH and (b) calcium concentration changes in time during biocementation dissolution batch experiments involving biocemented sand samples subjected to 50 mM acetic acid solutions with 100 mM acetate (50A_100Act) and without acetate additions (50A). Trends were further captured using the model presented in Equation 2.8 following calibration of k_cA_c and n (adapted following Ribeiro & Gomez 2022a).

calcium and pH changes monitored in time to assess dissolution progression. A kinetic model was fit to the achieved data following Equation 8 by varying unknown parameters k_cA_c and n. As $CaCO_3$ dissolves, calcium ions are released into solution, resulting in increasing calcium concentrations and more alkaline solution pH due to the release of carbonate ions and their speciation as other carbonate species (i.e., bicarbonate) in accordance with solution pH. Following calibration, dissolution kinetic frameworks can be implemented in reactive transport models to capture spatial and temporal changes in soil biocementation when subjected to undersaturated solutions. Preliminary results from Ribeiro and Gomez (2022b) demonstrate the potential of such approaches to capture dissolution progression at the element scale. Figure 19 presents measured soil $CaCO_3$ contents during progressive dissolution injections applied to soil column experiments along with modeled distributions from a calibrated reactive transport model. As evident, such calibrated models can reasonably predict dissolution induced changes and could be used to forward predict dissolution for field-scale applications for more complicated flow regimes and biocementation distributions. While still being refined, it is likely that either site specific column or batch testing will be necessary to calibrate dissolution frameworks to enable the use of more advanced reactive transport programs (e.g., PHT3D, COMSOL) for forward prediction of biocementation

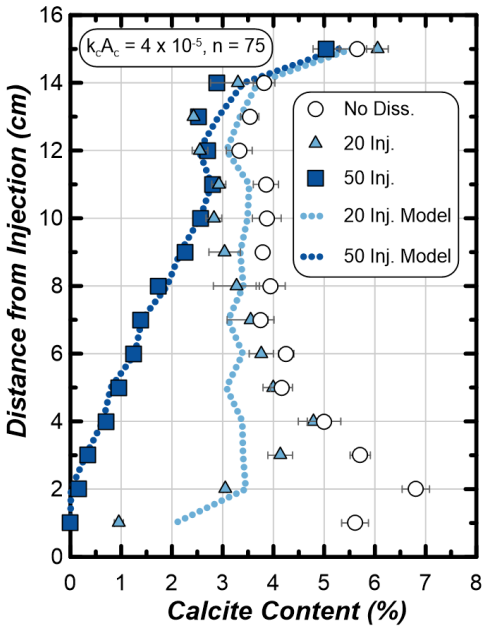

Figure 19. Progression of biocementation dissolution during experiments wherein repeated dissolution injections were applied over time to biocemented soil columns and specimens were analyzed after 0, 20, and 50 dissolution injections. Trends were further captured using the model presented in Equation 2.8 following calibration of k_cA_c and n (adapted following Ribeiro & Gomez 2022b).

longevity and spatial and temporal changes following initial implementation. As the technology achieves more widespread application, project sites may also provide further opportunities to calibrate models to field data when permanence is monitored over time.

3 MICP TREATMENT METHOD

3.1 *Development of augmentation approaches*

Bioaugmentation, the injection of specialized non-native microbial strains to complete some process of engineering interest, has been leveraged in the literature for a variety of different environmental applications, of which perhaps bioremediation of contaminated soils and pore fluids has been most notable (Ellis et al. 2000, Nzila et al. 2016, Cycoń et al. 2017). With respect to biocementation, augmentation has been the method of choice for almost all prior literature, with *Sporosarcina pasteurii* ATCC strain 11859, a constitutively ureolytic bacterium with high specific activity, being the most commonly augmented microorganism. In this process, ureolytic microorganisms are prepared using sterile culturing techniques, quantified, and injected into soils to enable urea hydrolysis and the biocementation process. This process in the context of MICP has been extensively investigated in numerous past studies, which have been comprehensively reviewed in prior works (El Mountassir et al. 2018, Rahman et al. 2020, Bhutange & Latkar 2020, Tang et al. 2020); therefore, this section provides a brief synopsis of the augmentation process and primary considerations when employing the technique.

3.1.1 *History of augmentation approaches*

Although microorganisms have been used to reduce borehole hydraulic conductivity since the early 1980's (Updegraff et al. 1983, Finnerty & Singer 1983, Jenneman et al. 1984), specific use of *S. pasteurii* (formerly *Bacillus pasteurii*) to catalyze what is now called augmented MICP appeared nearly one decade later

(Kantzas et al. 1992). Shortly thereafter, *S. pasteurii* was further used to drive $CaCO_3$ precipitation to enable hydraulic conductivity reductions for sandy soils (Gollapudi et al. 1995, Ferris et al. 1997, Stocks-Fischer et al. 1999). These studies represent an early stage in the use of what is now broadly recognized as augmented MICP to alter soil engineering properties. They are also among the very few examples of "pure" augmented MICP, as they involved no carryover of residual organic compounds from cultured growth media, which could have unintentionally enriched other native ureolytic strains (Section 2.3.2). In its most pure form, the augmentation process involves growth of *S. pasteurii* in some growth medium, commonly ATCC 1376 medium [yeast extract 20g/L, $(NH_4)_2SO_4$ 10g/L, 0.13 M Tris buffer, pH= 9.0], harvesting cells by centrifugation, washing cells to remove most medium constituents, resuspending in some alternative medium, injecting cell-dense suspensions, sometimes also introducing other high ionic strength constituents into soils to facilitate improved attachment and retention, and subsequently providing sequential injections containing urea and calcium to permit $CaCO_3$ biocementation. In the literature, such processes oftentimes include supplying cells in a resuspending medium that contains significant nutrients, whether intentionally added or as carryover from growth medium, that could enable enrichment of indigenous bacteria. Indeed, this consideration, along with others, may hinder our ability to understand the true distribution of augmented bacteria from the majority of past augmented MICP experiments (Section 2.3.1). That being said, it is clear that augmented microorganisms can be used as an approach to achieve ureolytic activity particularly over smaller length scales wherein other physical limitations can be largely overcome. While augmentation is not the authors' suggested approach for field applications requiring the improvement of large soil volumes, when relying on augmented microbes for either field or lab applications, the following specific considerations should be made.

3.1.2 *Specific considerations for augmentation*

The application of non-native cell suspensions to soils during augmented MICP presents some unique physical challenges including ensuring that cells (1) remain the primary catalyst of MICP, (2) can be effectively transported through porous media, which can act to filter out and concentrate cells spatially, and (3) can successfully attach to soil particles following initial introduction. Although not exhaustive, such considerations are mentioned briefly below with reference to studies by a multitude of authors who have examined such mechanisms comprehensively.

3.1.2.1 *Augmented culture validation*

Efforts should be made to ensure that the bacterium to be augmented remains uncontaminated and true to its nomenclature and genetic profile. Cell lines that are broadly available ought to be used where possible to facilitate reproducibility. For example, the most frequently used *S. pasteurii* strain is available through the American Type Culture Collection as strain 11859, but the same strain is available in other culture collections and databases under other designations including DSM 33, NCTC 4822, CCM 2056, NCIB 8841, etc. New cell lines require initial characterization to generate a familiarization with their appearance and behavior such that deviations, which represent possible contamination or mutation, can be detected. Thus, its recommended to carefully note colony morphology, liquid culture description, growth rate, and specific activity of newly acquired cell lines to serve as a reference. Frozen glycerol stocks should be prepared from new cell lines and returned to at the start of a new round of experiments or when any changed behavior is observed in a culture to guard against genetic drift or contamination. Details of specific methods, while beyond the scope of this paper, may be readily found in a volume on microbiological methods (e.g., Gerhardt et al. 1994).

3.1.2.2 *Non-nutritive augmentation*

As discussed earlier, the potential for unintended enrichment of native ureolytic microorganisms and/or contaminants remains when augmented microorganisms are supplied with added nutrients. These considerations and their implications for current and past studies were further discussed in Sections 2.1.1 and 2.3.2. It should be mentioned that in future applications, care should be taken to minimize carryover nutrients and establish sterile controls if observed phenomena are intended to be attributable to specific augmented strains. For some applications, such efforts may not be critical nor desired, and thus the potential for enrichment of alterative communities should be explicitly acknowledged. While other approaches can be used, most pure augmented experiments have involved culturing of *S. pasteurii* in a sterile ATCC medium, rinsing of cells through multiple cycles with sterile saline (9 g/L NaCl), and final resuspension in similar sterile saline solutions, which can then be injected into heat (or otherwise) sterilized soils. Specific procedures may be critical to this effort and are further outlined later in Section 3.6.1.

3.1.2.3 *Colloidal filtration*

When introduced into soil systems, the distribution of augmented bacterial cells can be significantly altered by interactions with surrounding soil particles including electrostatic repulsion/attraction and colloidal filtration. The net effect is that the successful distribution of bacterial cells in porous media depends on the properties of the provided medium, the surrounding soil surfaces, and the filtration attributes of the porous media (e.g., pore size and pore distributions). When developing augmentation protocols, such interactions should be considered and may require more formal investigation of the effects of augmentation media on bacterial cell and soil mineral surface charges through more involved measurements (i.e., zeta potential) or other means (Tominaga et al. 2009). Similarly, differences in injection volume, flow, and cell density should be considered, which can promote improved cell uniformity and delivery over larger injection distances even when filtration challenges are present. Although the authors refrain from recommending specific augmentation protocols here, such details are more comprehensively described elsewhere (El Mountassir et al. 2018). Interactions should be carefully considered if pure augmentation protocols are used for field applications. For laboratory applications involving centimeter-scale specimens, however, more uniform distributions and retention of cells can be accomplished through brute-force strategies wherein large, augmented volumes are injected in multiple directions and cycled to promote uniformity. The authors' own protocols (e.g., Darby et al. 2019, Lee et al. 2021, San Pablo et al. 2022b) have used similar injection techniques and may be admittedly suboptimal in comparison to others (Section 2.3) who have been more dedicated in their investigation of such processes. Furthermore, practical soil treatability concerns applicable to augmented cells are discussed later in Section 3.7, with specific examples illustrating the considerable challenges presented by colloidal filtration processes discussed earlier in Section 2.3.

3.1.2.4 *Cell fixation*

Following the introduction of augmented cells into porous media, fixation solutions have been used to promote attachment and retention of supplied cells (Harkes et al. 2010, Cheng &

Cord-Ruwisch 2012, 2014). The primary mechanism of such fixation solutions is thought to provide sufficient ionic strength that net attractive interactions between largely negatively-charged soil minerals and bacterial cells can be achieved. While an understanding of these resultant forces requires more involved analysis of surface ion interactions in these systems (e.g., DLVO theory; Hermansson 1999), numerous researchers have demonstrated the merit of such process (Section 2.3). While these other researchers favor use of $CaCl_2$, in the authors' current approach to augmentation, similar increases in ionic strength have occurred via introduction of saline, urea, NH_4Cl, or other salts with augmented cells; however, such additions have been less than intentional from a fixation standpoint, but rather have instead attempted to mitigate cell osmotic stress. Although the importance of this effect is hard to separate in such experimentation, at a minimum, the authors agree that prolonged retention periods for augmentation solutions can improve cell retention during subsequent cementation injections, an outcome which may result from improved attachment via electrostatic effects or other means.

3.2 *Development of stimulation approaches*

Similar to bioaugmentation, biostimulation, the enrichment of indigenous microorganisms with particular enzymatic or metabolic capabilities to complete a process of interest, was originally investigated for bioremediation applications. With respect to biocementation applications, the process has been intentionally investigated by researchers (Fujita et al. 2008, Tobler et al. 2011, Burbank et al. 2013, Gomez et al. 2014, Gat et al. 2016, Gomez et al. 2016, Dhami et al. 2017) and perhaps unintentionally involved in a considerable fraction of experiments that are mistakenly deemed augmented. The fundamental science behind the stimulation process as it pertains to MICP is covered in detail in Section 2; however, the development of the recommended approach and considerations for stimulation treatments are summarized here.

3.2.1 *History of stimulation approaches*

Ferris et al. (1997) provided the first attempt of ureolytic stimulation wherein an enrichment medium [333 mM urea, 187 mM ammonium chloride, 25 mM sodium bicarbonate, and 3 g/L nutrient broth, at a pH of 6] was supplied to a sandy soil and incubated anaerobically for several weeks. Such efforts achieved minimal ureolytic activity and precipitation as monitored indirectly by soil hydraulic conductivity changes. While hydraulic conductivity is an insensitive measure of ureolytic enrichment, the success of this approach likely suffered from protracted anoxic incubation, limited selection due to the use of a single enrichment treatment, and off-target enrichment resulting from initially low pH conditions. Later, Fujita et al. (2008) achieved successful ureolytic stimulation during a field trial involving treatment of an aquifer sand layer for the purpose of strontium sequestration. In their study, a 50-fold increase over baseline ureolytic activity was observed in the characterized community, which, while notable, was approximately six orders of magnitude less than what can be currently achieved with more modern biostimulation approaches. An opportunity to apply the technique for fracture sealing and geotechnical applications was later recognized by Tobler et al. (2011) and Burbank et al. (2011), respectively. The former demonstrated enrichment success using groundwater collected from a sandstone aquifer and the latter demonstrated detectable $CaCO_3$ and increases in the genetic potential of urease by 2.5 orders of magnitude (as measured by *ureC* copy number) in experiments involving natural alluvial sands. While similar studies followed (Gat et al. 2016, Dhami et al. 2017), the authors' intentional stimulated experimentation started with Gomez et al. (2014) wherein ten successive stimulation treatments were applied to soil column experiments containing eight different poorly-graded natural sands. The use of successive treatments differed from past work and ensured more vigorous enrichment for ureolysis by compounding the selection within each treatment. Further experimentation demonstrated similar enrichments at meter-scale (Gomez et al. 2016, Graddy et al 2018) and the repeatability of such processes in a variety of materials (Gomez & DeJong 2017). Recognizing that enrichment selectivity could be improved, significant stimulation solution enhancements were demonstrated in Gomez et al. (2018b), which included adjustment of initial solution pH to more alkaline values and increases in solution initial ammonium concentrations, the fundamental mechanisms for which were discussed in Section 2.4. Current formulations have retained similar selective pressures, but have included additional modifications for control of bulk ureolytic rates and reductions in supplied reactant concentrations during stimulation injections, primarily to improve spatial uniformity and material efficiency (San Pablo et al. 2020).

3.2.2 *Recommended stimulation solution composition*

While other stimulation solutions can likely be successful, the authors' current approach involves the application of repeated stimulation solution treatments containing urea, along with ammonium chloride, sodium acetate, and yeast extract concentrations between ~0.04 and 0.2 g/L (San Pablo et al. 2020, Lee et al. 2022). Such injections have proceeded in past experiments on a daily or alternating-day basis (depending on the targeted activity and the potential of the specific soil material) until a desired ureolytic rate was achieved, as assessed by various monitoring methods discussed in Section 4. Key to selecting a particular stimulation protocol is an understanding of the reactive transport problem of interest. This includes identifying the distance over which successful treatment delivery is desired, the hydraulic conductivity and flow regime expected in the treated zone, including the flow rates that can be reasonably achieved in that material, and the impact of supplied nutrients on bulk ureolytic activity for a specific soil and groundwater composition. The recommended stimulation solutions attempt to enforce highly selective conditions for ureolysis (high ammonium, high pH) that are maintained during the entire stimulation period. During these treatments, supplied complex organics (e.g., yeast extract) can be used to control bulk ureolytic rates. When higher ureolysis rates are desired, supplying yeast extract concentrations near 0.2 g/L may be appropriate. Conversely, when slower rates of ureolysis are desired, supplying lower yeast extract concentrations near 0.02 g/L may be needed. Such concentrations are based upon experimental observations; however, it remains likely that lower and/or higher yeast extract concentrations can be used and further modifications in rates achieved accordingly. Other stimulation solution components can be further altered to change the selectivity of a given stimulation solution and/or modify provided carbon and electron acceptors, and current understandings of these factors as they pertain to stimulation success are further described below. However, once successful enrichment and the establishment of sufficient ureolytic activity for MICP have occurred, soils can be transitioned to the cementation phase. In the authors' current approach, supplied cementation solutions include reduced ammonium concentrations, increased urea concentrations, and the addition of calcium when compared to earlier stimulation treatments. This transition is particularly critical and thus specific considerations are also provided in Section 3.2.3.5.

3.2.3 *Specific considerations for stimulation*

A number of factors exist that govern the success and behavior of stimulation approaches. While the success of an enrichment could be judged by the ability to achieve high bulk ureolytic activity, under some conditions, rapid urea degradation may pose additional challenges with regard to spatial control and treatment extent. It is recommended, instead, that stimulation approaches not be generalized, but rather contemplated as part of some particular treatment design, with the requirement that some minimal ureolytic activity be achieved. Important factors that may affect the behavior of a given enrichment as they are currently understood are presented here.

3.2.3.1 *Selectivity of medium*

Generally, stimulation solutions have been designed to maximize the selective pressure for ureolysis, thereby allowing for soils resistant to ureolytic enrichment to have the best opportunity to stimulate. Initial solution pH and ammonium concentrations can effectively serve as the primary mechanisms that enforce this selection process. These factors are thought to stress or kill bacteria intolerant of urea hydrolysis end-products before they utilize provided nutrients for further growth. Added stimulation solution ammonium concentrations between 12.5 mM and 200 mM as well as initial pH increases from 7.0 to 9.0 have been examined and shown to impact selectivity as measured by observed urea hydrolysis magnitudes (Gomez et al. 2018b). Figure 20a and 20b present a subset of these data highlighting the impact of increasing initial pH and added yeast extract, both of which increased bulk ureolytic rates by increasing selectivity for ureolysis and increasing total cell densities, respectively. Figure 20c shows a comparison of urea degradation in similar soil columns receiving stimulation solutions containing varying ammonium (12.5 mM to 200 mM) that were adjusted to an initial pH of 9 as well as the response of a single column receiving a previous stimulation solution formulation that was not pH adjusted and contained 12.5 mM ammonium following solutions similar to that used in Gomez et al. (2016). As shown, urea degradation is observed more rapidly when ammonium concentrations exceed 12.5 mM and increase to 100 mM; however, with no further improvement observed at the higher concentration (200 mM). Following these results, current stimulation solutions have both included an initial pH of 9.0, an ammonium concentration of 100 mM, and have proven successful for a variety of natural soils. For more recalcitrant soils, however, increasing the availability of membrane-permeable ammonia concentrations through an increase in pH (to > 9) or the addition of substantially higher ammonium concentrations could apply greater selective pressure and increase the probability of stimulation success. Such modifications in employed solutions present unavoidable tradeoffs with respect to material use and byproduct production and therefore should be carefully contemplated.

3.2.3.2 *Supplied urea concentrations*

Although somewhat related to the selectivity of the medium, variations in supplied urea concentrations during stimulation may be a critical factor controlling stimulation success. Figure 21 presents results from a series of experiments by San Pablo et al. (2022a) where four soil columns received either 0 mM, 50 mM, or 350 mM urea during stimulation with 350 mM urea during cementation or 350 mM urea during stimulation but only 250 mM urea during cementation. All stimulation solutions contained 100 mM ammonium chloride, 42.5 mM sodium acetate, 0.2 g/L yeast extract, and the $pH_{initial}$ was 9. All cementation solutions contained 250 mM calcium chloride, 12.5 mM ammonium chloride, 42.5 mM sodium acetate, and 0.2 g/L yeast extract with a non-adjusted $pH_{initial}$ of 8.3. The column receiving no urea during stimulation (Figure 21a) exhibited minimal ureolytic activity upon the initial transition to cementation. In contrast, the columns that received 50 mM (Figure 21b) and 350 mM urea (Figure 21c, d) during stimulation both achieved sufficient ureolytic activity to hydrolyze all provided urea in the ~23.5 hour residence of the first and subsequent cementation treatments. A reduction in urea during cementation also appeared to have minimal impacts on ureolytic activity during cementation (Figure 21d). Collectively, these results suggest that even with highly selective stimulation solutions, the addition of some amount of urea during stimulation may be critical to enrichment success. Notably, the response of the column receiving 50 mM during stimulation was similar to the column receiving 350 mM urea during stimulation, suggesting that even low concentrations near 50 mM may be sufficient. Such results have in part provided the basis for reductions in urea during simulation, as demonstrated by San Pablo et al. 2020 and the authors' more recent studies.

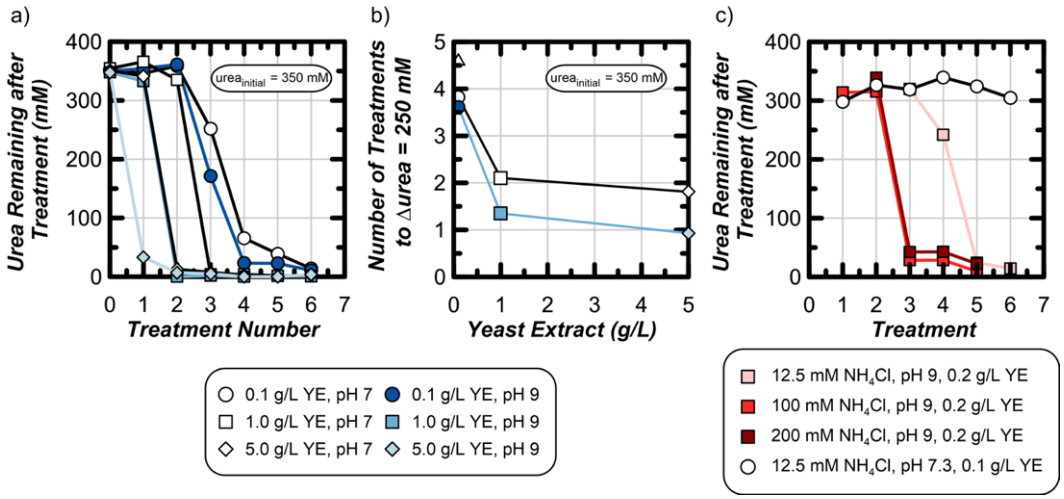

Figure 20. Select data from stimulated soil columns receiving stimulation solutions with (a,b) varying yeast extract and initial pH conditions and (c) varying ammonium concentrations with alkaline pH adjustment highlight the benefits afforded by higher yeast extract additions, alkaline pH adjustment, and higher initial ammonium concentrations. Plots (a) and (c) present residual urea remaining after treatment residence periods versus daily treatment injection number and plot (b) presents numbers of treatments required to achieve 250 mM urea degradation versus yeast extract concentration from the earlier data set present in (a) (adapted from Gomez et al. 2018b).

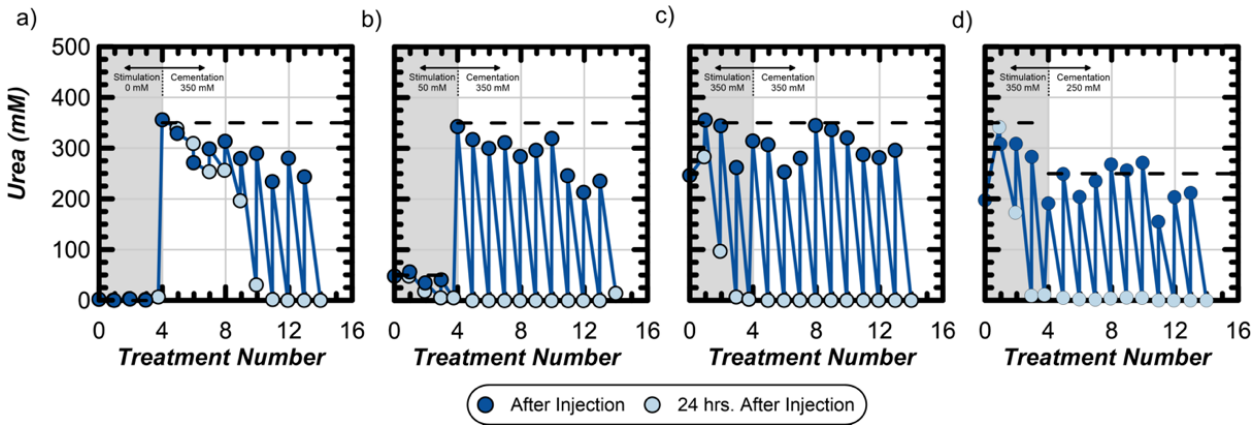

Figure 21. Select data from stimulated soil columns receiving stimulation solutions with varying urea during stimulation and cementation highlighting the impact of added urea concentrations during stimulation on the efficacy of degradation during cementation. Data presents urea concentrations measured at the start and end of each treatment retention period versus treatment number during both stimulation and cementation. Data is from columns receiving (a) 0 mM, (b) 50 mM, and (c) 350 mM urea during stimulation and 350 mM during cementation whereas (d) received 350 mM urea during stimulation but only 250 mM urea during cementation. Injected urea concentrations are indicated by dashed lines and stimulation treatments are indicated by shading. (adapted from San Pablo et al. 2022a).

3.2.3.3 *Supplied organic carbon*

Organic carbon serves two essential functions in biological systems, providing both an energy source and a source of carbon needed for biosynthesis. It is suggested that non-fermentable sources of organic carbon be provided in stimulation solutions to minimize the potential for acidogenesis and the reversal of generated biocementation. While glucose and other sugars are prototypical sources of organic carbon in microbial media, under anoxic conditions such additions can be readily fermented by a host of soil microbes to furnish organic acids, which decrease solution pH. Many other carbohydrates can likewise be fermented to produce organic acids. Molasses, as an example, is a relatively inexpensive carbon source that has seen frequent application for stimulated MICP. Molasses is composed of approximately 96% sugar by effective dry mass (Clarke 2003, USDA ARS 2021), giving it substantial fermentative potential if not used sparingly. Acetate is often provided as a non-fermentable carbon source, though lactate is an alternative with comparable geomicrobiological significance. When supplied in stimulation solutions, only 125 µM acetate is needed to consume the 250 µM dissolved oxygen concentration measured in atmosphere-equilibrated media, rendering them anoxic. However, given that a substantial portion of acetate is likely to be used for biosynthesis rather than energy, suppling millimolar quantities are likely more than sufficient for efficient aerobic growth. The proposed stimulation solutions provide acetate at a concentration of 42.5 mM, which may be in 1.5-2 orders of magnitude in excess of what is strictly required for aerobic growth. While perhaps in excess, aside from the added material cost, this excess is unlikely to be detrimental and may or may not merit further optimization.

In addition to acetate, other complex sources of organic carbon are provided in stimulation solutions, of which the preferred form is presently yeast extract. Complex sources of organic carbon are preparations unable to be chemically defined that are used to provide a broad array of organic molecules for uptake and utilization. Classically, these complex carbon additions can satisfy the growth requirements of all but the most fastidious organisms ensuring that the medium satisfies fundamental macro and micronutrient requirements. If media were to be provided with defined organic carbon alone (e.g., acetate), enriched microorganisms in natural soils would be subject to rapid limitations by nitrogen, sulfur, phosphorous, or other essential nutrients. The addition of yeast extract in solutions alleviates those limitations and allows for increased rates and magnitudes of growth, which assist in the generation of bulk microbial activity. By the same token, reducing the complex carbon in stimulation solutions can impose limits to microbial growth and, by extension, can regulate achieved bulk ureolytic activity. Recent experiments have shown that increases in supplied yeast extract can increase the speed at which ureolytic activity is achieved in biostimulated soils, decreasing the time and number of treatments required to achieve sufficient enrichment (Figure 20a, b). Conversely, decreases in supplied yeast extract have been shown to reduce bulk ureolytic activity (Figure 22) and may help reduce non-uniformity that emerges from reactions during transport (San Pablo et al. 2020, Lee et al. 2022). The spectrum of yeast extract concentrations ranging from a lower bound that may be soil- and condition-specific to ~0.2 g/L provides the greatest latitude with respect to ureolytic rate control. As previously mentioned, and more fully discussed in Section 7.2, the impact of ureolytic rate on biocementation distribution is substantial so the types and amounts of organics used may be of primary importance.

3.2.3.4 *Supplied electron acceptors*

As described earlier, the proposed stimulation protocols have attempted to minimize the use of fermentable carbon sources to avoid the potential for acid formation. The direct outcome being that the stimulation protocols are strongly dependent upon the energy generated from respiration. The authors' current stimulation solutions also do not explicitly include alternate electron acceptors, and therefore it is presumed that they rely heavily upon equilibrium oxygen dissolved concentrations to enable energy generation. It should be acknowledged, however, that small quantities of such acceptors can be found in the complex organic source provided, although they are likely at negligible concentrations. It may then be essential to ensure atmospheric equilibration of stimulation solutions prior to injection to maximize the oxygen available for cellular growth and utilization of the supplied growth medium. This is especially important for saturated soils where oxygen diffusion is limited and dissolved oxygen will rapidly become limiting. When and if dissolved oxygen requirements prove limiting, alternate electron acceptors may need to be considered to maintain respiration and energy generation after oxygen has been depleted. It remains unclear, however, if ureolytic bacteria that are enriched using our currently recommended solutions, which do not contain additional electron acceptors, have the respiratory machinery to

utilize other electron acceptors in order to extend their growth in the absence of oxygen. A recent study employing varying percentages of natural seawater as the treatment solvent (Yanez et al. 2022) suggests that ureolytic enrichment was not substantially affected by the presence of up to ~28 mM sulfate in the applied media (Figure 23), suggesting that the utility of other alternative electron acceptors may be less than clear. Furthermore, the small but consistent decrease in ureolytic activity observed with increasing seawater concentrations may be indicative of other inhibitory species present in seawater (e.g., Mg^{2+}) which have been noted in purely augmented MICP experiments (Burdalski 2020).

3.2.3.5 *Cementation processes following stimulation*

Upon the transition from stimulation to cementation, special considerations must be made to enable the continued selection and growth of a select subset of soil bacteria. Aside from allowing for generation of $CaCO_3$, cementation solutions applied following stimulation must provide conditions that allow for microbial growth to replace cells lost during precipitation and washed out during subsequent injections, while also ensuring that the achieved microbial community maintains sufficient ureolytic activity. Cementation solutions, then, attempt to maintain similar conditions experienced during stimulation treatments, but include enough calcium and urea to achieve efficient $CaCO_3$ precipitation. That said, some additional changes are merited to meet the different requirements of the cementation process. It is thought that less selective pressure is required for maintenance of established stimulated ureolytic populations than that required to initially convert and develop the ureolytic microbial community. Thus, the proposed cementation solutions, as discussed in Section 3.3, typically use less organics in comparison to stimulation solutions, as they are intended to maintain a steady-state biomass rather than fuel substantial growth. Additionally, since ammonium is readily generated upon introduction of cementation treatments due to hydrolysis of the supplied urea, cementation solutions similarly include reduced initial concentrations of ammonium and reduced initial pH with the assumption that ureolytic activity during the treatment residence period will increase selectivity in time. Cementation solutions, then, apply reduced selective pressure by lessening the ammonium additions and foregoing pH adjustment and furthermore achieve more minimal pH rise during the treatment period due to simultaneous carbonate consumption during $CaCO_3$ precipitation. This can be controlled in part by varying the urea concentration supplied during cementation. As shown in Figure 24, when urea concentrations were varied between 250 mM and 350 mM and exceeded the concentration of supplied calcium (which was constant at 250 mM), increases in final pH values could be achieved during the cementation process. While final pH values during cementation are clearly reduced from values observed during stimulation, which approach 9.5, excess urea concentration variations provided the opportunity to vary final pH values between 8 and 9 and accordingly apply more selective pressure for ureolysis. Although not encountered in the authors' experiments (e.g., Figure 21d), if insufficient selective pressure were to be provided during cementation, it is possible that a microbial community could shift and undesirable reductions in ureolytic activity and incomplete precipitation could occur, thus urea concentrations may provide a means by which this outcome could be mitigated. Additionally, as discussed in Section 3.3.2.5, the transition from biostimulation to cementation typically includes a flush treatment intended to mitigate abiotic calcium carbonate precipitation during the introduction of high calcium. This flush almost certainly reduces

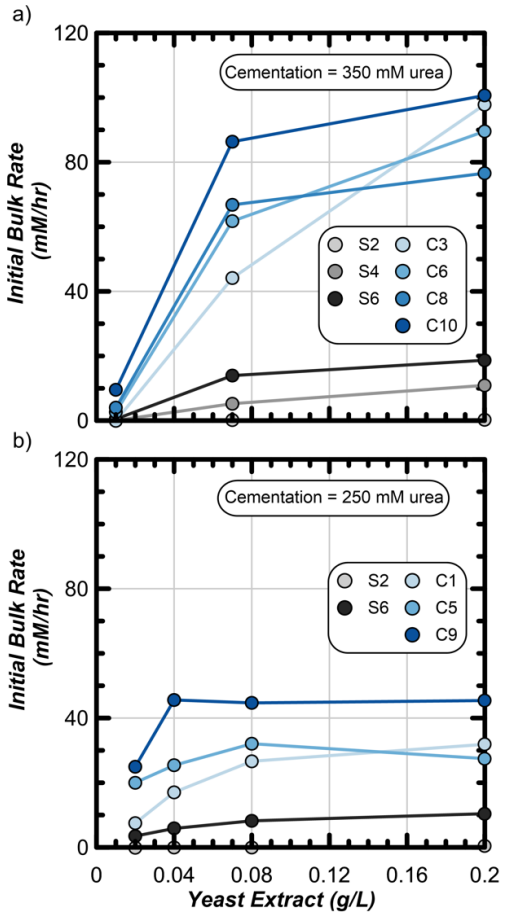

Figure 22. Initial bulk rates determined from columns receiving stimulation treatments (S) containing 50 mM urea and varying yeast extract concentrations and cementation treatments (C) containing similar yeast extract concentrations with either (a) 350 mM or (b) 250 mM urea. Provided letters and numbers refer to treatment type and injection numbers, respectively. Initial rates were determined from first-order fitting of urea degradation curves (data from Lee et al. 2022).

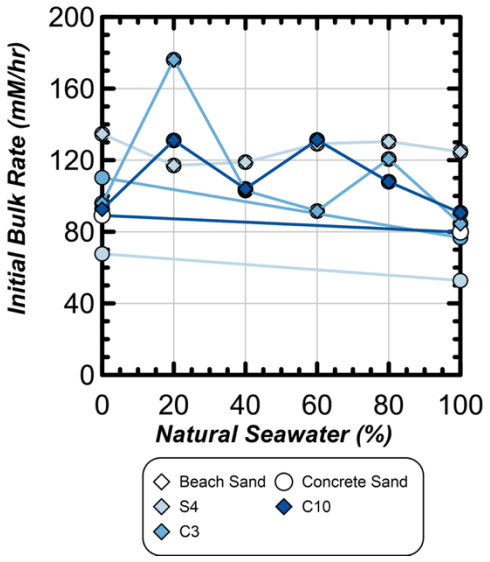

Figure 23. Initial bulk urea hydrolysis rates obtained from experiments performed on Beach Sand (BS) and an alluvial Concrete Sand (CS) receiving stimulation and augmentation treatments of varying seawater compositions. Initial rates were determined from first-order fitting of urea degradation curves. As shown, minimal decreases in ureolysis rates were observed with increasing seawater concentrations (adapted from Yanez et al. 2022).

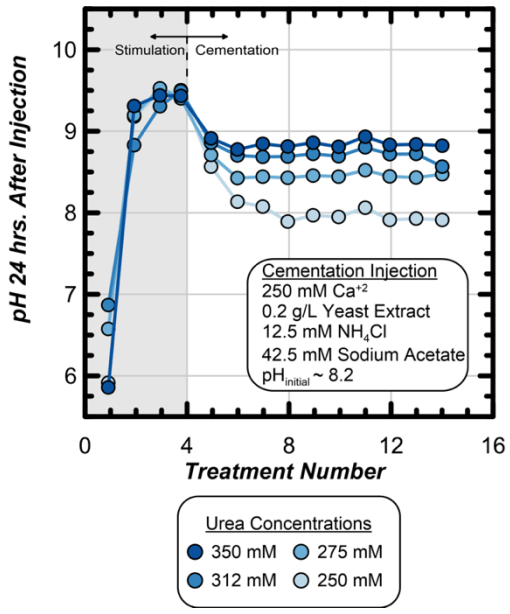

Figure 24. Select data from stimulated soil columns receiving stimulation solutions with 50 mM urea and cementation solutions with urea varying between 250 mM and 350 mM and calcium at 250 mM (constant), highlight the impact of urea concentrations during cementation on final pH conditions (adapted from San Pablo et al. 2022a).

the established microbial densities by eluting some portion of the resident bacterial population. While this may render the system more vulnerable to secondary, competitive enrichment, wherein there has been detectable ureolytic activity established following stimulation, issues regarding the transition from stimulation to cementation have not been encountered. Instead, while a reduction in ureolytic activity has been observed immediately after the flush treatment, this activity generally rebounds during cementation to exceed what was observed during the final stimulation treatments. Nevertheless, the transition from stimulation to cementation treatments has the potential to be perilous and it is recommended to maintain similar selective pressures during cementation as were present during stimulation, with modifications made only once the stability of a given ureolytic population enriched in some soil material is better understood.

3.3 *Development of cementation approaches*

Through over two decades of development MICP treatment solutions have been progressively modified to enhance cementation mineral products, improve control of the geochemical process, and minimize energy, materials, and environmental impacts among other objectives. While one would be hard pressed to suggest that "optimal" cementation solutions and techniques exist, continuous advances with respect to the collective understanding of the MICP process have manifested in a variety of modifications to the way researchers perform biocementation, including those pertaining to differences in treatment injection sequences, cementation solution formulations, and even the types of microorganisms used to hydrolyze urea and catalyze the biocementation process. In some cases, these modifications have been driven by improved understandings of the fundamental science behind the MICP process including those pertaining to precipitation saturation state. In other cases, researchers may not have been able to clearly state the mechanisms responsible for specific differences, but have provided empirical evidence supporting hypotheses and their preferred treatment techniques. Rather than provide a fully inclusive summary of all past treatment solutions, in this section, the authors instead provide a brief history of cementation solution formulations, followed by a discussion of the modifications made to their treatment processes including the rationale for these changes and recommendations for cementation treatment solution formulations. Lastly, some more poorly understood factors will be discussed along with recent results that highlight the unexpected impact of solution changes.

3.3.1 *History of cementation approaches*

Although the first cementation formulations were proposed by Ferris et al. (1997), applied solutions have been continuously modified by researchers who have changed urea to calcium concentrations, added and removed treatment additives, and shifted the types of microorganisms used and requiring sustainment during the process. Perspective on cementation solution formulation evolution is evident in Table 1, which includes the original MICP cementation formulation developed by Ferris et al. (1997) and subsequently used by Stocks-Fischer et al. (1999) and others, three other formulations showing how such treatments solutions have been further modified, and two more recent formulations currently used by the authors for most of their research (Gomez et al. 2016, San Pablo et al. 2020). As shown, early formulations (Stocks-Fischer et al. 1999, Bang et al. 2001, DeJong et al. 2006) remained relatively unchanged from Ferris et al. (1997) with a transition to cementation solutions consisting of purely urea and calcium salts at generally much higher concentrations by Whiffin et al. (2007), van Paassen et al. (2010b), Chu et al. (2012), and others. As time progressed, cementation formulations appear to generally fall into two camps: (1) modification of the Ferris et al. (1997) formulation and (2) modification of pure urea and calcium formulations similar to that by Whiffin et al. (2007). Formulas by Martinez et al. (2013) and Montoya and DeJong (2015) represent minor departures from Ferris et al. (1997) while those by other researchers including Tobler et al. (2018) remain similar to the Whiffin et al. (2007) formulation. Perhaps the most significant departure from both formulations has occurred as the result of the transition to stimulation. Although stimulation of MICP was first intentionally investigated by Ferris et al. (1997) and later successfully demonstrated by Fujita et al. (2008) and others for strontium immobilization, similar strategies for geotechnical applications resulted in treatment formulations that started deviating most significantly following Burbank et al. (2011), who proposed a cementation formulation similar to Ferris et al. (1997) but included additional substrates likely intended to maintain enriched ureolytic cell populations throughout the cementation process. Building from these formulations, modifications by the authors presented in Gomez et al. (2014, 2017, 2018b) and others have led to further optimization of these cementation solutions for both enhanced material-efficiency, retention of ureolytic activity during the cementation period, and improved control of precipitation location. Eventually, this has led to the authors' most recent formulations presented in San Pablo et al. (2020), which will be discussed in greater detail in Section 7.2.

As cementation solution formulations have been modified, so too has an understanding of the role of specific additives. For example, while early formulations include the addition of sodium bicarbonate with the intention for such additions to serve as a pH buffer, the addition of bicarbonate also increases the potential for abiotic precipitation by eliminating the ability of urea hydrolysis to solely control carbonate generation. Similarly, ammonium chloride has been included at high concentrations, as it was perceived to slow urea hydrolysis reaction rates through product inhibition. While such concentrations were shown to inhibit free enzymes dramatically (Fidaleo & Lavecchia 2003), in other

Table 1. Progression of cementation solution development.

Year	Reference	Augmentation or Stimulation	Cementation Solution Formulation	Commentary
1997	Ferris et al.	Augmented with *Sporosarcina pasteurii*	333 mM of Urea; 25.2 mM Calcium Chloride; 187 mM NH_4Cl; 25 mM Sodium Bicarbonate; 3 g/L Nutrient Broth	-
1999	Stocks-Fischer et al.	Augmented with *Sporosarcina pasteurii*	333 mM of Urea; 25.2 mM Calcium Chloride; 187 mM NH_4Cl; 25 mM Sodium Bicarbonate; 3 g/L Nutrient Broth	Identical to Ferris et al.
2007	Whiffin et al.	Augmented with *Sporosarcina pasteurii*	1100 mM Urea; 1100 mM Calcium Chloride	Removal of Additives; Use of Higher Concentrations
2010b	van Paassen et al.	Augmented with *Sporosarcina pasteurii*	1000 mM Urea; 1000 mM Calcium Chloride	Removal of Additives; Use of Higher Concentrations
2013	Martinez et al.	Augmented with *Sporosarcina pasteurii*	333 mM Urea; 100 mM Calcium Chloride; 374 mM NH_4Cl; 25.2 mM Sodium Bicarbonate	Similar to Ferris et al.; Modification of Urea-to-Calcium Ratios & Additive Concentrations
2017	Gomez et al.	Stimulation	350 mM Urea; 250 mM Calcium Chloride; 12.5 mM NH_4Cl; 42.5 mM Sodium Acetate; 0.1 g/L Yeast Extract	Transition to Stimulation; Addition of Growth Factors and Modification of Urea-to-Calcium Ratios
2020	San Pablo et al.	Stimulation	250 mM Urea; 250 mM Calcium Chloride; 12.5 mM NH_4Cl; 42.5 mM Sodium Acetate; 0.2 g/L Yeast Extract	Further Optimization of Growth Factors and Urea-to-Calcium Ratios

studies involving whole cells, such effects appear to be much more minimal (Lauchnor et al. 2015). Thus, from a cementation perspective, increasing ammonium chloride concentrations may only increase generated byproducts, albeit with some potentially significant impacts on the activity of augmented and stimulated ureolytic bacteria (Section 2). Similar to cementation solutions proposed by Whiffin et al. (2007), the only essential components of a cementation solution are sufficient urea and calcium. Of course, urea is necessary to enable the generation of carbonate species and calcium is an essential component of calcium carbonate precipitation. While the other additions early on were primarily intended to control reaction speed and pH, it is the authors' opinion that for purely augmented experiments, many of these additives could have been removed with little consequence. This is clear in the works of Whiffin et al. (2007), van Paassen et al. (2010b), Chu et al. (2012), and many others who demonstrated successful cementation using simple solutions following augmentation with ureolytic bacteria. When considering the formation of cementation, the addition of calcium carbonate forming reagents is key, but so too is the viability of the ureolytic cells completing the process. This was recognized by Ferris et al. (1997) and others who included various components such as nutrient broth and yeast extract likely intended to maintain or increase densities of augmented cells. Interestingly, such additives may have also unintentionally led to stimulation of indigenous bacteria (Section 2.3.2). As the potential of enriched native ureolytic bacteria to complete this process has been increasingly recognized, these additives have started to play a more critical role during the cementation process, to both provide nutrients needed to maintain these populations but also poise the system such that enriched bacteria can remain dominant in otherwise mixed bacterial cultures. It is the authors' opinion that this aspect is where most of the novelty regarding cementation solutions has occurred and has led to the primary differences proposed in the solution recommendations discussed later.

While the understanding of the cementation process is continuously evolving, the authors have made several significant departures from even their own past treatments techniques in recent years. These choices have been made for several main reasons: (1) the transition from the use of pure augmentation to almost solely stimulated microbial communities to complete precipitation reactions, (2) the desire to remove superfluous additives and reagents to minimize environmental impacts, financial costs, and byproduct concentrations, and (3) the desire to enhance spatial uniformity and control of the process. The most significant differences can be summarized as follows: (1) reductions in calcium and urea concentrations, (2) reductions in urea-to-calcium ratios, (3) addition of nutrients and trace growth factors in cementation treatments and the elimination of augmentation, (4) elimination of additives including sodium bicarbonate and reductions in ammonium chloride, and finally (5) the addition of "flush" injections to avoid spontaneous abiotic precipitation events. Each of is described briefly below, along with the justification for why such decisions were made.

3.3.2 *Specific considerations for cementation*

As presented above, specific factors were considered in the development of the current cementation solutions used. While cementation treatment formulations are presented largely in the context of stimulated MICP, specific considerations for and modifications to cementation solutions have occurred over time and the authors' understanding of these factors are described briefly below.

3.3.2.1 *Urea and calcium concentrations*

The selection of urea and calcium concentrations, although rarely explained, is an aspect of the cementation solution meriting careful consideration. Concentrations of urea approximately 333 mM have long persisted in cementation solutions most likely out of deference to those first used by Ferris et al. (1997). At the higher end of the spectrum, concentrations at and above 1 M urea and calcium similar to those used by Whiffin et al. (2007) are

also commonly found in the literature. Beyond preference, researchers using higher concentrations have likely done so to achieve higher magnitudes of cementation per injection, thus potentially minimizing implementation costs and reducing treatment time. Alternatively, higher concentrations can also result in more unpredictable urea hydrolysis behavior due to at least two competing effects. Ureolytic rates increase with increases in urea concentration based on the K_M values of *S. pasteurii* and commonly enriched species (Graddy et al. 2018, Lauchnor et al. 2015). But at very high concentrations, the resultant ammonia may be inhibitory or cytotoxic and result in reduced ureolytic activity. For example, only *S. pasteurii* and one other strain among the 26 Gram positive bacterial species tested grew at 1.4 M total ammonium (Leejeerajumnean et al. 2000), though the upper limit for maintaining ureolytic activity for *S. pasteurii* or other stimulated strains has not yet been determined. Aside from impacts on ureolysis, higher calcium concentrations can also increase precipitation rates, which are oftentimes assumed to be proportional to saturation states. Although the authors admit the lower concentrations used in their formulations (~250 mM urea and calcium) have been selected primarily out of experience, higher concentrations present the possibility of inhibiting enriched microbial growth, altering urea hydrolysis and calcite precipitation kinetics thus impacting spatial control, generating effluent with elevated by-product concentrations, and even influence of the mineralogy and morphology of achieved precipitates with more soluble phases including amorphous $CaCO_3$ and vaterite becoming increasingly possible at higher reagent concentrations. Although the impacts of altering such concentrations may be specific to the formulations employed, the use of higher concentrations (> 500 mM urea and calcium) may present more risks than benefits.

3.3.2.2 *Reductions in urea to calcium ratios*

The notion is pervasive throughout MICP literature that pH rise is needed in order for $CaCO_3$ precipitation to occur. Following the discussion in Section 2, however, it should be clear that this is not needed, but rather the product of the activities of calcium and carbonate simply must exceed the solubility product of some $CaCO_3$ mineral phase. Through extensive modeling of the MICP reaction network and physical experimentation, it can be concluded that providing urea at concentrations exceeding that of calcium provides almost no measurable benefit with respect to precipitate formation provided that the supplied urea is fully hydrolyzed. The authors have tended to use solutions with concentrations of urea exceeding calcium particularly when performing stimulated experiments in order to maintain higher pH and ammonium concentrations during cementation and therefore maintain selective pressure favoring ureolytic microorganisms. Recent experiments suggest, however, that excess urea may not be needed and communities can seemingly remain stable over 10 daily cementation treatments even when large pH rises do not occur (Figure 21d, 24). It is the authors' opinion that equimolar concentrations of urea and calcium be used to minimize byproduct production and urea consumption, and that the lack of excess urea has minimal impacts on bulk ureolytic activity and precipitate magnitudes. There are special conditions, however, where excess urea could be advantageous including: (1) acidic soils requiring greater alkalinity generation to make sufficient concentrations of carbonate available, (2) conditions where pH spikes indicative of Ca^{2+} consumption may be favorable for process monitoring (Section 4), and (3) when additional selective pressure is needed to ensure that stimulated ureolytic microorganisms remain dominant.

3.3.2.3 *Addition of nutrients & elimination of augmentation*

While early formulations by Ferris et al. (1997) and others recognized the need to include growth factors to maintain augmented cell populations throughout the cementation process if re-augmentation is to be avoided, the recent use of indigenous ureolytic microorganisms has only further solidified the need to include such factors in cementation solutions. While the specific organic additives used have changed over time (e.g., yeast extract versus nutrient broth, the addition of sodium acetate), the more fundamental objective has remained the same – to allow for sustained microbial activity throughout the cementation process. It seems intuitive that in the absence of organic substrate renewal, ureolytic activity will decrease over time, due to an inability of cells to meet their metabolic needs and the precipitation of $CaCO_3$, which can encapsulate and stress cells over progressive injections. Thus, treatment additives such as yeast extract and sodium acetate have been included during the cementation process to maintain ureolytic activities generated in the enrichment period. When modified during cementation treatments involving enriched microorganisms, however, the literature has only begun to understand the utility of such concentrations to control ureolytic cell densities and alter reaction rates. From this context, the concentrations of organic carbon, energy sources, and growth factors should be carefully selected to target some ureolytic activity that will be reached once the system approaches a steady condition. Additionally, when such nutrients are provided in gross excess, the potential for fermentation of supplied carbohydrates may become a significant possibility, thereby potentially reversing generated precipitates through acid-driven dissolution. While there is much to understand about the potential of such substrates in the stimulation process, it is clear that this treatment decision may have important implications with respect to both maintaining ureolytic activity process and altering the spatial control of the process (Section 3.2.3.3).

3.3.2.4 *Removal of sodium bicarbonate and high ammonium chloride*

Although many different treatment additives exist, two of the most consistent additions to cementation solutions are sodium bicarbonate and ammonium chloride. Sodium bicarbonate, although included by some researchers to act as a pH buffer (Ferris et al. 1997, Stocks-Fischer et al. 1999, Al Qabany & Soga 2013), does have the potential to undermine biological mediation of the MICP process due its abiotic reactivity with added calcium resulting in abiotic precipitation. This could limit distribution of reactants during injections among other potential issues such as injection source clogging. Secondarily, the addition of sodium bicarbonate likely provides very little additional buffering as such solutions will undoubtedly become dominated by much higher ammonium and carbonate concentrations produced during urea hydrolysis, although it is acknowledged that such additions could play some microbiological role. However, given these additional limitations and added material costs, bicarbonate additions may be largely superfluous. In addition to sodium bicarbonate, ammonium chloride is also commonly provided in cementation solutions. While the authors believe that concentrations exceeding 150 mM such as those provided by Ferris et al. (1997) and others may be excessive, such concentrations likely do play a critical role in applying selective pressure for ureolysis and may be critical toward maintaining ureolytic activity. Given that ammonium is generated as a by-product of urea hydrolysis, the authors have shown that supplied ammonium chloride concentrations may need to be higher initially to maintain greater selection for ureolysis, but may be reduced to values of 12.5 mM or below once sufficient ureolytic activity is observed and the enrichment becomes more stable.

Since ammonium byproducts are undesirable from an environmental perspective, any reductions in ammonium chloride concentrations in treatment solution may be beneficial and aid in the post-treatment rinsing and waste-management processes.

3.3.2.5 *Addition of flush treatments*

The application of urea-rich solutions during stimulation results in the enrichment of native ureolytic bacteria with the production of alkaline ammonium- and carbonate- rich effluent. This presents problems with the application of the first cementation treatment wherein calcium is first introduced into an otherwise calcium-limited system. If not mitigated, cementation solution injections will react with carbonate-rich stimulation effluent upon mixing, leading to substantial abiotic calcium carbonate precipitation. This precipitation oftentimes occurs in free solution thereby blocking soil pore spaces and well filters, among other problems, and results in a decrease of soluble calcium that may reduce cementation at further distances. Although not strictly related to the cementation solution itself, transitional treatment solutions, termed "flush" solutions, have been employed to preclude these behaviors. First employed in Gomez et al. (2016) and later used in Gomez et al. (2018b) and San Pablo et al. (2020), flush treatment solutions are similar to the composition of cementation solutions but lack calcium (and sometimes other amendments). These solutions are applied immediately after stimulation and just before applying cementation solutions to remove high aqueous carbonate species present following the end of stimulation. Figure 25 illustrates the impact of the flush treatment on solution carbonate as indicated in an activity ratio diagram (Gomez et al. 2019) highlighting the reduction in carbonate activities and saturation states achieved with a flush injection, thereby minimizing the potential for abiotic precipitation. When augmentation is performed using urea-containing cell suspensions, similar flush solutions can be employed prior to cementation to avoid practical issues related to clogging and losses in cementation from spontaneous precipitation of $CaCO_3$ upon the introduction of calcium.

3.3.2.6 *Recommended cementation solution composition*

While decisions regarding treatment solution formulations should be made with reference to the specific applications considered, the authors do have several primary treatment formulations that have been identified following the advancements described earlier. It should also be mentioned that certainly other treatment solution formulations can and have been used with success and such recommended formulations are specific to stimulated treatment techniques. Table 2 presents the composition of the authors' baseline cementation solution formulation along with comments regarding the potential modifications that researchers may want to consider with respect to this composition. As shown, the main decision points may include: (1) the modification of yeast extract concentrations to target terminal ureolytic rates optimal for some treatment application (i.e. flow rate, treatment residence period, desired cementation distribution), (2) the modification of urea and calcium concentrations to higher values while still maintaining urea to calcium ratios near 1, and (3) potential increases in ammonium chloride concentrations when the potential for enrichment failure is high (e.g., when cell densities of competing microorganisms are high and threaten to undermine the enrichment for ureolysis). Past research suggests that the most dynamic changes in these behaviors may be observed when yeast extract is varied between ~0.02 and 0.2 g/L and ammonium chloride is varied between ~12.5 mM and 100 mM, while further recommending that care should be taken when using urea and calcium concentrations in excess of 500 mM to prevent potential inhibition by high concentrations and unintended consequences with respect to biological function and mineral products (i.e., mineralogical and morphological differences).

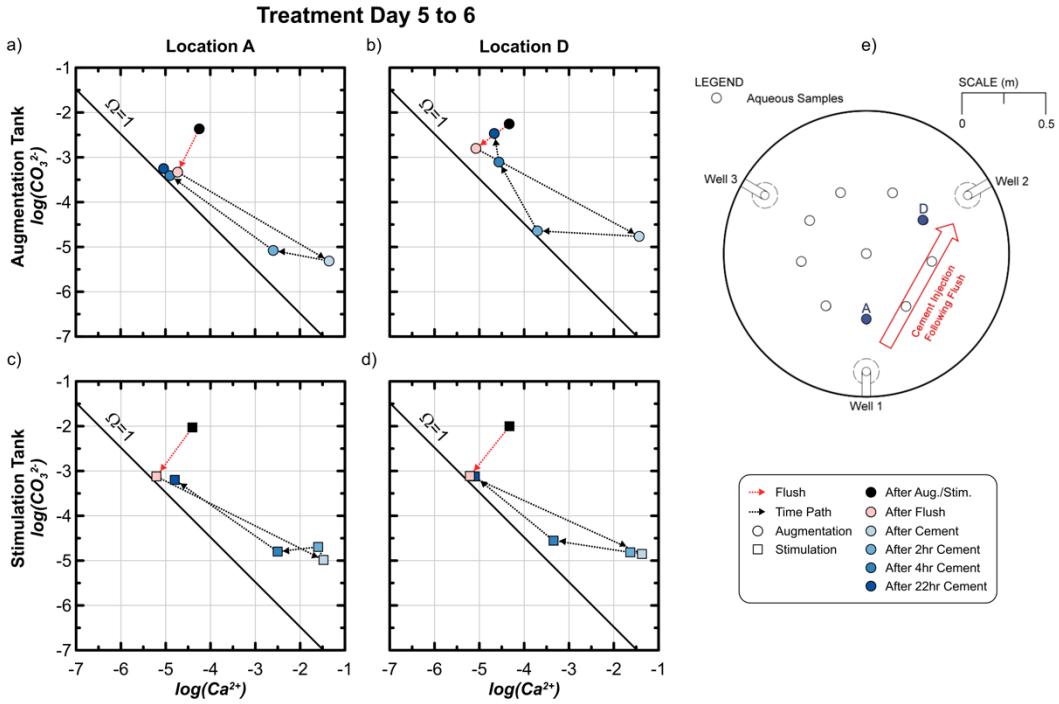

Figure 25. Example of solution carbonate and calcium activity changes following stimulation/augmentation, a single flush treatment, and a single cementation treatment as monitored at various locations in a large meter-scale tank experiments. As shown, at locations receiving concentrated solutions (Locations A, D) in both the augmented and stimulated tanks, aqueous carbonate activities were reduced substantially after flushing (adapted from Gomez et al. 2018a).

Table 2. Baseline cementation following stimulation (summarized from San Pablo et al. 2020).

Solution	Baseline Cementation
Urea (mM)	250 [1]
Calcium Chloride (mM)	250 [1]
Ammonium Chloride (mM)	12.5 [2]
Sodium Acetate (mM)	42.5 [3]
Yeast Extract (g/L)	0.2 [4]

[1] Urea and calcium magnitudes may be increased to values near 500 mM, however, urea-to-calcium ratios near 1.0 remain

[2] Increases in ammonium chloride concentrations may be considered when there is a potential for instability of the enrichment (i.e., conditions where other microorganisms may outcompete ureolytic bacteria for supplied nutrients).

[3] Recent results suggest that the addition of sodium acetate may not be critical.

[4] Yeast extract concentrations can be modified to control ureolytic rates (higher concentration = higher cell densities = higher ureolytic rates).

3.4 *Ammonium byproduct management and removal*

The produced ammonium resulting from microbial urea hydrolysis may present serious human health and environmental impacts if left untreated in subsurface soils (DeJong et al. 2013, Gat et al. 2017). Although few researchers have investigated ammonium removal following MICP, it has been proposed that generated ammonium may be removed through a variety of processes including subsequent biological transformations of generated nitrogen species in situ and removal of ammonium-rich solutions using post-treatment injections with later remediation of extracted ammonium occurring ex situ. Numerous past studies have shown that generated ammonium concentrations following MICP are approximately twice that of the applied urea in accordance with reaction stoichiometry. Such concentrations may surpass values above 500 mM, which far exceed expected groundwater concentrations and some regulatory limits. Although total ammonium limits have not been established for drinking water in the U.S., the U.S. Environmental Protection Agency recommends maximum ammonium concentrations for aquatic life of ~1 mM and ~0.1 mM at a pH of 7.0 for acute (1 hour) and chronic (30-day) exposure, respectively (EPA 2013). Furthermore, the European Union recommends maximum ammonium concentrations for drinking water of ~0.03 mM (European Union 2020). These regulations are both location and application specific and reflect the potential impacts of ammonium concentrations on human health and environmental quality. For example, in some locations maximum concentrations are pH-dependent due to differences in the inherent toxicity of ammonium when speciated as charge-neutral ammonia. For example, the B.C. Contaminated Sites Registry (British Columbia Contaminated Sites Regulation 2020) suggests that acceptable total ammonium levels may be higher under more acidic conditions (pH < 8.5) due to the increased speciation of total ammonium as ammonia. While such regulations limit concentrations of aqueous ammonium, it should also be mentioned that positively charged ammonium ions can sorb to negatively-charged soil surfaces. Thus, post-treatment ammonium removal following MICP may require careful monitoring of both aqueous and adsorbed concentrations. Adsorbed ammonium concentrations may pose long-term management challenges due to the potential for desorption over time when such quantities are not preemptively addressed and monitored during the removal process.

Recent studies have considered injecting cation-amended solutions to remove ammonium-rich MICP effluent from previously biocemented soils via solution advective transport and cation-exchange with adsorbed ammonium ions. In this process, cations are provided to exchange with ammonium ions at soil surfaces, thereby reducing adsorbed ammonium concentrations present following the MICP process and accelerating aqueous ammonium transport out of treated zones. Results from Lee et al. (2019a) suggested that interactions between positively charged ammonium ions and negatively charged, poorly-graded sand surfaces may result in significant retardation of ammonium transport when compared to passive ions (Figure 26). In addition, a significant fraction of injected ammonium was retained within columns suggesting that such surfaces may retain sorbed ammonium. It was expected that such phenomena would likely be influenced by both surrounding pore

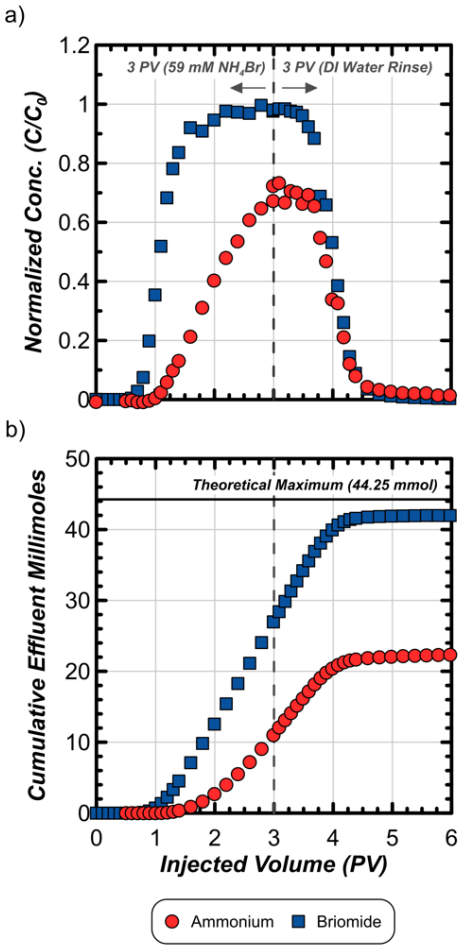

Figure 26. Breakthrough curves during ammonium bromide injections in soil column experiments suggest that the transport of ammonium is inhibited relative to passive ions such as bromide due to interactions with soil mineral surfaces. Limited appearance of ammonium at column outlets, suggested that appreciable sorption of ammonium occurred in the considered clean sand material (adapted from Lee et al. 2019a).

fluid conditions as well as the cation exchange capacities of treated soils. Lee et al. (2019a) further demonstrated that the addition of calcium ions to rinse solutions and adjustment of rinse solution pH to more alkaline values may result in enhanced ammonium removal likely due to both improved cation exchange and increased speciation of residing ammonium as charge-neutral ammonia while also limiting the potential for $CaCO_3$ dissolution. Although such techniques have been largely developed at the centimeter bench-scale, recent studies have demonstrated the effectiveness of post-treatment rinsing processes at meter-scale under more practically-relevant treatment conditions. Lee et al. (2019b) characterized ammonium removal during post-treatment rinse injections with a single 12 PV continuous injection in five 3.7-meter-long columns containing different poorly-graded sands (San Pablo et al. 2020). The results suggest appreciable adsorbed ammonium may persist after rinse injections and may require careful characterization following field-scale applications. More recent experiments by Lee & Gomez (2022a) have examined the impact of changes in supplied cations within rinse solutions as well as injection sequencing. These experiments suggest that while deionized water rinse injections can remove similar magnitudes of aqueous ammonium as other rinse solutions containing added cations; adsorbed ammonium removal is significantly reduced when cations are not supplied. Potassium (K^+), sodium (Na^+), and Ca^{2+} cation additions were explored at varying concentrations within rinse solutions with select results for biocemented columns receiving a single 12 PV continuous rinse injection with different rinse solutions (200 mM of Na^+, K^+, Ca^{2+} added rinse solutions and deionized water) presented in Figure 27. Interestingly, K^+ ions appeared to enhance aqueous and sorbed ammonium removal when compared to other ions at similar concentrations. The improved performance of K^+ ions relative to other ions suggests it may be favorable for exchange with adsorbed ammonium. Additionally, deionized water rinses were shown to perform poorly on the basis of reducing sorbed ammonium, clearly indicating the advantages afforded by suppling cations during rinsing. Although not shown, staged injections wherein 1 PV was applied for twelve daily injections as opposed to a single 12 PV injection were also shown to improve both aqueous and adsorbed ammonium removal likely due to increased cation exchange during residence periods.

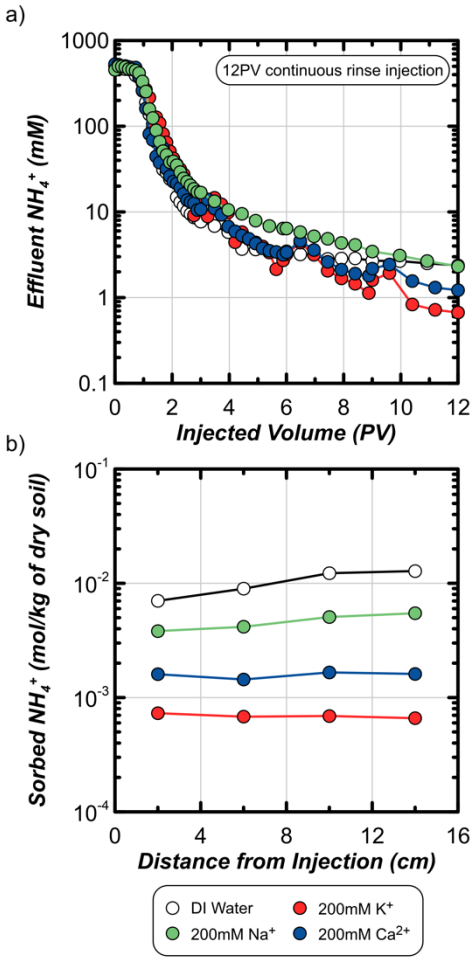

Figure 27. (a) Effluent aqueous ammonium concentrations in time during continuous 12 PV injections of alkaline cation-amended solutions in small columns show ammonium removal during rinsing with greater than 97% aqueous ammonium removed after completing injections. (b) Normalized sorbed ammonium masses along soil column lengths obtained from soil samples after rinse treatment completion (adapted from Lee & Gomez 2022a).

The above advancements have improved understanding of post-treatment ammonium removal. However, further investigation of these techniques remains needed. It is recommended that several aspects be monitored related to both the progression of ammonium removal and the potential for detrimental impacts with respect to post-treatment cementation integrity. For example, ammonium concentrations from both the aqueous and adsorbed phases should be monitored using both fluid and soil samples to assess removal success. Ammonium concentrations in pore fluid samples can be measured using colorimetric assays similar to that described in Krom (1980). Furthermore, soil samples should be preserved at a free-draining water content and soil ammonium extraction should be performed following procedures similar to Keeney & Nelson (1983) and Lee et al. (2019b) with subsequent aqueous ammonium measurements completed to account for the presence of ammonium masses in residual pore fluids. Although pH measurements may not provide significant insights, it is also recommended that such measurements be completed to examine the impact of soil solution buffering during rinsing and other unintended reactions resulting from rinse solution cation additions. Finally, measurements of both soil shear wave velocities and aqueous calcium concentrations can provide the opportunity to examine changes in cementation integrity during rinsing which may reduce shear wave velocity values and release measurable calcium when such injections are dissolving $CaCO_3$ minerals. While not exhaustive, such measures have been used in previous studies (Lee et al. 2019b) and may provide the opportunity to quantify and compare ammonium removal success, thereby accelerating further developments with respect to these techniques. Although the effectiveness of cation-amended rinse solution injections for post-treatment ammonium removal has been demonstrated, knowledge gaps still exist regarding a variety of aspects. For example, optimization of rinse techniques within the context of life-cycle sustainability analyses (LCSA) is needed to identify the impacts of specific cation additives and identify the breakpoint at which increasing the injected volume will increase overall impacts due to more limited ammonium removal near the end of rinse injections. It is anticipated that ammonium removal will remain a key aspect of the MICP treatment process, which may accelerate more widespread implementation of the technology. From this perspective, further investigation of approaches which leverage biological transformations of produced nitrogen may afford new opportunities to enhance post-treatment remediation using processes beyond those currently examined.

3.5 *Injection scheme*

The treatment injection scheme employed in the laboratory or field is a balance between achieving treatment spatial control and implementation simplicity, the latter being particularly challenging and expensive when scaled to field-scale applications (Section 7). Achieving spatial control of cementation is primarily dependent on the ureolytic reaction rate relative to the treatment solution transport rate. Ideally, treatment solutions would be injected into soils without any reactions occurring thus allowing for full solution concentrations to be delivered into the treatment zone with perfectly spatial uniformity achieved by allowing solutions to react in place over some retention period. While this is not practically possible, a given treatment strategy can be designed to minimize precipitation during treatment injections thereby achieving improved uniformity (San Pablo et al. 2020).

The authors' preferred injection strategy for treatment uniformity is a stopped flow injection sequence where the treatment injection time is a small fraction of the total time required for substantial ureolysis of the injected urea concentration (and associated consumption of calcium), followed by a retention time period that meets or exceeds the required reaction time (Barkouki et al. 2011). In laboratory tests on ~125 cm^3 columns treated with 1.25 pore volumes using a peristaltic pump, such treatment injections can oftentimes be completed in under 20 minutes. This is followed by a retention period that exceeds the expected time required for cell growth, urea hydrolysis, and/or precipitation dependent on the treatment stage with treatment intervals oftentimes being once every 24 or 48 hours, with adaptations possible as reaction activities increase or decrease. Following stimulation, the authors' stimulated soil column experiments suggest that consumption of 250 mM urea and calcium can be completed between ~3 and 48 hours, dependent on targeted reaction activity. Ideally, injections should be performed over time periods that exceed no more than 10% of the total time required for full hydrolysis. Aside from more obvious benefits with respect to uniformity, mineralogical transformations over time observed and discussed in Section 2 clearly suggest that ripening of precipitate phases toward more stable calcium carbonate polymorphs may occur over time with longer treatment residence periods perhaps affording benefits with respect to material permanence. While continuous injection schemes can also be implemented, their use will almost surely result in large cementation gradients when injection rates are too slow (and large amounts of reactants are consumed during injections) and poor chemical utilization efficiency (when injection rates are too fast and reactants are transported out of the treatment zone without being fully consumed). Depending on particular site conditions field treatments may involve some combination of both, with stop-flow treatments used to introduce reagents and existing groundwater gradients moving injected solutions over time yielding a predictable flow regime but perhaps much more complicated reactive transport conditions.

Beyond these considerations, altering the flow direction between subsequent treatment injections has also been explored to improve treatment uniformity. This was attempted particularly in earlier studies where augmentation was used and the stop-flow methodology had yet to be fully explored and refined. Nevertheless, such an approach can be useful when treatment distances are relatively large and stop-flow conditions may not be successful due to other practical limitations (i.e., exceeding low soil hydraulic conductivities). Martinez et al. (2013) demonstrated specifically how alternating injections can improve the spatial distribution of augmented cells and its impact on the subsequent distribution of precipitated calcite. Additional consideration should be given when attempting to introduce alternating injections of treatment solutions with excess urea to calcium (urea to calcium ratios > 1), as the introduction of high calcium at a previous effluent location upon flow reversal can lead to significant abiotic precipitation and localized clogging of injection sources and surrounding soils.

3.6 *Generalized treatment approaches*

Although the authors have experience with both augmented and stimulated MICP, considerations of cost, scalability, environmental impacts, and treatment process benefits have led to primary use of stimulation in the authors' most recent experimentation. Still, augmented MICP can prove useful for more controlled experimentation wherein more fundamental effects are to be elucidated. Two brief examples of treatment protocols are provided below for either augmentation or stimulation.

3.6.1 *Augmentation treatment approach*

The suggested best practices for "pure" bioaugmented MICP as differentiated earlier in Section 2.3.2 is described in the below steps. It should be mentioned that other approaches have and can be used with success, however. Thus, these recommendations provide solely the authors' suggested approach with implementation recommendations made as appropriate.

- Step 1: Grow the desired ureolytic bacteria under aseptic conditions in recommended growth medium to a predetermined optical density (OD_{600}) that represents late exponential phase of growth, as judged by a previously determined growth curve. Cell densities corresponding to the target OD_{600} should be predetermined as outlined in Section 4.1.1 and reported in publications. The primary objective of this step is to obtain a culture that is as dense as possible without substantial death or a reduction in specific ureolytic activity. Actual achievable cell densities will be limited by rate of oxygen transfer, build-up of toxic waste products, and other factors under the selected growth regime.
- Step 2: Cell densities targeted for the final added cell suspension should be determined based upon project objectives, with special emphasis on colloidal filtration properties of the specific soil and whether or not pure augmentation is intended. The potential for unintended stimulation described earlier in Section 2 should be considered and mitigated if specific outcomes are to be attributed to augmented cells alone.
- Step 3: An inert saturation solution should be applied to soil specimens (e.g., artificial groundwater) followed by the injection of prepared cell suspensions when laboratory tests are to be performed. Cell suspensions for pure augmentation should be prepared with rinsed and pelleted cells and resuspended in some medium of sufficient ionic strength to mitigate cell osmotic stress and potentially enhance cell attachment. In some cases, this suspension may contain added urea to generate ionic strength during the augmentation process and enable monitoring of urea degradation activity. Recirculation of augmented cell suspensions can further promote more uniform distribution of cells along the length of a soil column specimen. This will be specific to the advective-dispersive and filtration properties of the porous media, however, augmented cell breakthrough curves may be used to help aid in this determination (i.e., monitoring of injected cells at some outlet location to determine extent and densities transported in the aqueous phase).
- Step 4: Urease activity should be determined with distance from the cell suspension injection source location when possible. If researchers wish additionally to monitor density

of suspended cells, total direct cell counts (Section 4) are recommended over OD_{600} measures, which have been used for this purpose occasionally by others, but can be compromised by suspended fines released from the treated soil. Depending on the time frame needed for bulk ureolytic activity determinations, aqueous total ammonium appearance and/or urea disappearance can be monitored. Urea degradation is the preferred approach due to the volatility of ammonium species at high pH and their soil surface interactions at low pH.

- Step 5: Cementation injections proceed once the specimen is ready for cementation, as judged by sufficient and uniform urease activity. When urea is included in augmentation solutions, a flush injection of artificial ground water or other solution is advisable to remove much of the carbonate species and alkalinity generated from urea hydrolysis prior to cementation. Such methods can help mitigate abiotic $CaCO_3$ precipitation upon the introduction of high calcium as discussed earlier in Section 3.
- Step 6: Flush treatments, when used, should be followed in rapid succession by the injection of a cementation solution that is near equimolar in $CaCl_2$ and urea to begin the cementation process. Cementation solutions should be applied successively once such reactants are deemed to have been fully utilized during a given residence period. Treatments should proceed until some target treatment level is achieved. The authors recommend that improvement be non-destructively monitored during treatments using shear wave velocities and other geophysical and geochemical methods as discussed later in Section 4. During this phase, modifications in injection schemes may be used to further control cementation extent and distribution.
- Step 7: Soil and pore fluid samples may be destructively obtained for further analysis of achieved microbial communities following all augmentation and cementation treatments. Alternately, rinse injections should be applied to remove soluble salts prior to destructive mechanical testing.

3.6.2 *Stimulation treatment approach*

The authors' suggested best practices are summarized below. It should be mentioned that stimulation treatment schemes are nuanced and therefore the authors refrain from providing universal formulations. Instead, stimulation protocols should be designed with consideration of the specific soil materials, site environmental factors, and reactive transport conditions present, among other important factors. These recommendations provide an outline for such protocols, with more specific implementation recommendations provided only where generalization may be appropriate.

- Step 1: Care should be taken to collect soil samples aseptically when stimulation is to be evaluated and attributed to a given soil material ex situ. This can be achieved through a variety of different approaches, which include but are not limited to collection with sterilized split-spoon samplers, sonic drilling, and/or other methods. During and following soil collection, similar efforts shall be made to minimize contamination, though such procedures may never fully eliminate the potential for contamination. Furthermore, sterilized glass bead control specimens can be subject to similar procedures to evaluate and control for unexpected contamination. Gomez et al. (2018b) provides some examples of such efforts.
- Step 2: Minimize the potential for contamination when preparing soils in particular experiments for a laboratory test program. Efforts should include sterilization of soil containment devices (e.g., columns), tubing, soil placement tools, and all items which may be in contact with soils. Sterilization is ideally accomplished using wet or dry heat in an autoclave or oven respectively, though chemical agents (e.g., bleach, ethanol) or a number of other methods may also be appropriate.
- Step 3: Apply an inert saturation solution (e.g., artificial groundwater) or stimulation treatment solution following initial soil preparation. For in situ treatments, however, such processes may not be necessary. Stimulation solutions should be designed in consideration of the soil material and surrounding environmental conditions as described earlier in Sections 2 and 3 in order to successfully enrich native ureolytic bacteria. This includes consideration of selective factors such as provided ammonium concentrations and initial pH as well as provided nutrients and growth factors. Solutions should at a minimum include some amount of ammonium, urea, and organic carbon and nutrients for cell growth and maintenance. For a given treatment scheme, both the flow regime employed (i.e., flow rates) and the targeted reaction rates (i.e., bulk ureolytic activity) should be considered together to identify supplied organics. Cell growth, and by association bulk ureolytic rates, can significantly alter treatment extent and uniformity. Thus, specific treatment solutions may vary in composition depending on the desired treatment uniformity, treatment level, and financial and sustainability constraints. Finally, for applications wherein evaluating and attributing stimulation potential to specific soil materials is of highest priority, stimulation solutions shall be prepared aseptically. This may require filter sterilization (i.e., use of 0.2-micron filters) of prepared solutions but could involve other sterilization methods. Autoclaving may not be a suitable method for sterile solution preparation, however, given the heat labile nature of urea.
- Step 4: Monitoring of ureolytic activity shall be completed during stimulation solution treatment residence periods to quantify urea degradation. With knowledge of urea utilization, appropriate treatment frequencies can be identified. In the authors' experiments stimulation injections have been provided on a daily or alternating-day basis and have consisted of sufficient volume to fully replace the pore volume of a given sample (~1.5 PV but dependent on soil advective-dispersive transport characteristics). Aseptic protocols should be maintained throughout the stimulation process, however, such precautions may be most impactful at the beginning of the stimulation period during which indigenous communities may be most susceptible to contamination. At all points during the stimulation and cementation process methods described in Section 4 may be employed to characterize enriched communities and associated microbiological and geochemical changes in time during the treatment process.
- Step 5: Treatments can be transitioned to cementation following successful stimulation, as identified by achieving some desired ureolytic capacity (e.g., degradation of enough urea in 12 hours to efficiently precipitate the calcium salts to be employed during cementation). During this transition a flush treatment should be applied immediately prior to initiating the cementation process. The flush solution may be similar to the composition of the stimulation solution or more inert. For example, similar solutions lacking urea and pH adjustment have been used (San Pablo et al. 2020). This flush treatment, however, will elute stimulated cells, thus monitoring of ureolytic activity following this transitional period may be important.

- Step 6: Cementation injections can proceed once flushing has been performed, with repeated cementation injections continuing until some target treatment level is achieved. The authors' recommendation would be to assess this improvement non-destructively during treatments using shear wave velocities and other geophysical and geochemical methods as discussed later in Section 4. During this phase, modifications in injection schemes may be used to further control cementation extent and distribution. Additionally, during the cementation process it is recommended that solution compositions not differ dramatically from those used during stimulation to maintain selective pressure for ureolysis. However, in the authors' experiences, initial ammonium chloride concentrations and pH can be reduced due to the production of ammonium from urea hydrolysis directly and strong buffering of pH by carbonate and ammonium species during cementation treatments regardless of initial conditions.
- Step 7: Soil and pore fluid samples may be destructively obtained for further analysis of achieved microbial communities following all augmentation and cementation treatments. Alternatively, rinse injections should be applied to remove soluble salts prior to destructive mechanical testing.

3.7 *Soil & environmental considerations*

Methods regarding the activation of microbial ureolytic capacity through applied stimulation treatments, the precipitation of $CaCO_3$ through applied cementation treatments, and the removal of ammonium byproducts resulting from MICP through applied rinse injections was largely described throughout Section 3 for poorly-graded silica sands under saturated freshwater conditions. Such methods are also robust and effective across a much broader range of soil and environmental conditions. This section surveys the broad treatment effectiveness demonstrated to date across variations in soil gradations and mineralogy as well as environmental conditions.

3.7.1 *Soil gradation*

MICP treatment effectiveness is primarily governed by the: (1) ability of stimulation and augmentation procedures to develop a robust microbial community to facilitate $CaCO_3$ precipitation, (2) ability of treatment methods to deliver stimulation, cementation, and byproduct constituents through a targeted treatment zone within a time period compatible with achieved microbial reaction rates, and (3) magnitude and spatial distribution of $CaCO_3$ precipitation generated at particle contacts and on open particle surfaces.

Analysis of the spatial compatibility between microbes and soil particle sizes (Mitchell & Santamarina 2005, DeJong et al. 2010) identified probable limits for in situ augmentation of soils using whole bacterial cells and hypothesized lower bound particle size limits for which the effectiveness of such treatments may be significantly less probable. Rebata-Landa & Santamarina (2006) further investigated microbe viability in fine-grained soils as a function of applied overburden stress, and identified conditions for which microbial viability limits likely exist.

The breadth of microbes that can be used to facilitate MICP are now more fully characterized in part due to the transition from augmentation to stimulation. The *S. pasteurii* strain (ATCC 11859) typically used in bioaugmentation is a rod shape with a typical length of 1.3 to 4 μm with a diameter of 0.5 to 1.2 μm. Bacterial species identified in stimulated soils (*S. pasteurii, S. soli, S. saromensis, S. aquamarina, S. luteola, S. koreensis*) are all rod-shaped and have published diameters of 0.5 to 1.2 μm and lengths of 2 to 3.5 μm (Tominaga et al. 2009), which are consistent with direct measurements of MICP isolates of these species. Injection of microbes of this size into soil becomes a limiting factor due to their ability to move through pore throats and consequently influences cementation uniformity. Colloidal filtration of the microbes during injection typically produces a log-linear decrease in population with distance under 1D flow conditions (Li et al. 2004) though variations in pumping techniques can produce some improvements (Martinez et al. 2013). Nonetheless, severe filtration/straining of the bacteria is likely when the D_{10} of the soil is less than about 10 times the microbe length, and effects of filtration may persist when the D_{10} of soil is up to 50 times the microbe length. Hence, filtration is expected when the D_{10} of the soil is less than about 50 μm. An alternative augmentation approach wherein freeze-dried spores (typically spherical, diameter ~0.5 to 1.0 μm) are resuspended in some treatment solution and are injected (Dadda et al. 2017, Terzis & Laloui 2018, Pungrasmi et al. 2019, and others), may be slightly more effective in treating finer-grained soils. Additionally, spores of close relatives of *Sporosarcina* have demonstrated viability in soils stored for hundreds of years in a dry state (Sneath 1962). Thus, it remains possible that such spores may contribute to the success of stimulated MICP in natural soils, including those which would be expected to have limiting particle sizes.

The use of stimulation approaches may extend the limit of soils amenable to MICP at smaller particle sizes by requiring only the transport of aqueous chemical concentrations to native ureolytic cells and/or spores already present within soil materials. By avoiding the physical constraints related to cell transport in porous media, treatability for stimulation is largely governed by the rate at which a given treatment solution is transported through the soil (i.e., governed by soil hydraulic conductivity) relative to the rate at which biologically-mediated chemical reactions can occur (i.e. governed by microbial populations, activity, and reactant availability). As, discussed earlier in Section 3, these considerations have been the primary motivation for developing new treatment techniques by which stimulated bulk ureolytic rates can be controlled.

Mechanical mixing methods have also been used for treatment of fine-grained soils for which hydraulic conductivity limitations prevent advective transport and solution injections. For example, the treatment of clayey soils has been explored via ex situ mixing of ureolytic bacteria and treatment solutions with soils followed by placement and compaction (Li 2015, Cheng & Shahin 2015, Jiang et al. 2017). Others have attempted mixing solely treatment solutions with soils to stimulate indigenous bacteria (Islam et al. 2020, Asghari et al. 2021, Mukherjee et al. 2021), however, such results have varied. In particular, the role of changes in solution chemistry on clay mineral electrochemical interactions can remain unclear when not controlled for. Therefore, it is the authors' recommendation that careful controls be performed for such studies in order to be able to separate the effects of cementation from other clay-ion interactions. MICP treatment of organic soils, such as peat, have also been explored using high water content slurry mixtures and stimulation of indigenous bacteria (Phang et al. 2019, Safdar et al. 2021). While not strictly MICP, Duggan et al. (2017) achieved stabilization of peat via abiotic carbonation wherein peat was oxidized, releasing CO_2 in the presence of calcium ions in the pore fluid, and calcium carbonate precipitation occurred. Although in this instance peat specimens achieved some level of mechanical improvement, it should be noted that carbonation reduces the pH of surrounding pore fluids and could lead to degradation of generated $CaCO_3$ if not carefully controlled.

The upper bound particle size limit for MICP treatments in coarse-grained soils is unconstrained. However, more practical size limits can be thought of as being reflective of treatment

efficiency considerations as opposed to physical flow and transport constraints. While coordination number in a poorly graded soil matrix is independent of particle size, the number of contacts per unit volume decreases with particle size, resulting in each particle-particle contact being subjected to a higher contact stress. Assuming that the proportional distribution of $CaCO_3$ precipitation between open surfaces and at contacts is independent of particle size, for a given $CaCO_3$ content the effectiveness of cementation toward improving mechanical responses would be expected to reduce with particle size increases. This is because with larger particles and thus larger interparticle forces, the role of interparticle friction is greater and accordingly the impact of added cohesive forces from cementation on soil mechanical responses becomes smaller. However, there is some indication that the distribution of $CaCO_3$ precipitation between open particle surfaces and particle contacts does not remain constant as particle sizes increase. In addition, in more well-graded natural soils the coefficient of uniformity ($C_u = D_{60}/D_{10}$) tends to increase with average particle size (D_{50}), in which case the number of particle contacts per unit volume would increase relative to more finer and poorly-graded soils, thus reducing interparticle contact stresses and perhaps making MICP improvement more effective. Thus, the true impact of particle size differences may be difficult to generalize and instead specific to the treatment techniques employed (i.e., distribution of cementation) in addition to differences in soil material particle sizes and gradations.

MICP has been shown to effectively improve a broad range of silica-based granular soils and some silts using both stimulation and augmentation approaches. Documentation regarding suitable soils for such treatments is therefore extensive in this respect as most publications provide details about tested soil material gradations. Figure 28 presents a representative sampling of the range of quartz-based soils that have been successfully treated using MICP using direct treatment injections (exclusive of mixing), with differences in the reported biological approach (augmentation versus stimulation) and USCS soil classification (SP, SM, SW, GP) distinguished. Although the majority of past MICP studies have reported the use of augmentation, it remains unknown what fraction of these studies may have been inadvertently stimulated due to a carbon source being included in treatment solutions (Section 2.3.2). Thus, such differentiations here are less clear and are only intended to highlight the breadth of treatment processes and soil gradations that can be successfully improved. As shown, the successful treatment range has spanned from a D_{50} of 0.12 to 10.0 mm and

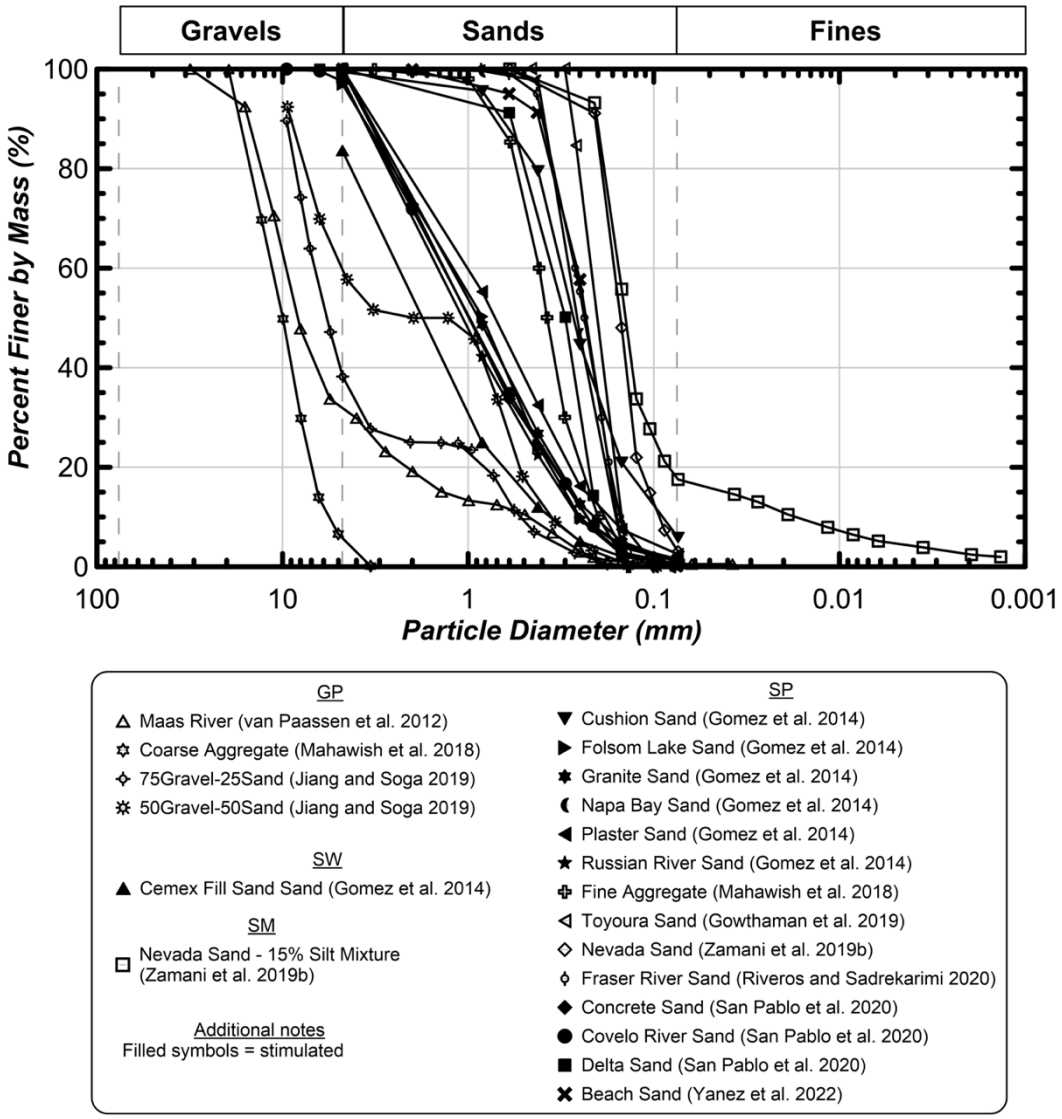

Figure 28. Grain size distribution of select MICP research studies illustrates the range of quartz-based soils that have been successfully tested and are categorized in their respective USCS group symbol.

a D_{10} of 0.02 to 5.64 mm. Both poorly- and well-graded soils have been effectively treated, with C_u values ranging from 2.0 to 8.4. It should be noted that treatment effectiveness does not appear to be directly driven by geologic deposition, but rather this is an indirect factor in determining soil gradation. Further extension of treatment success into sand and silt mixtures is clear, however, success in pure silts is not reported likely due to the low hydraulic conductivity of these soils. The upper bound particle size treatment range, however, is unconstrained and as shown is only reflective of the geotechnical interests of such studies and can extend even into treatment of isolated rock fractures (Minto et al. 2016).

3.7.2 *Soil mineralogy*

Extension of MICP treatments from silica-based soils into other geomaterials with significantly different mineralogical compositions has been largely successful. The presence of other minerals may influence MICP treatment effectiveness if the (1) particle surface charge and/or surface roughness differs from largely quartz-based sands and influences bacteria attachment, (2) presence of additional dissolved chemical species and surface minerals alters precipitation nucleation, growth, morphology, and mineralogy, and (3) availability of additional minerals catalyzes unanticipated parallel chemical reaction pathways.

To date natural sands with high concentrations of carbonate minerals (Xiao et al. 2018, Zhang et al. 2020, Yanez 2022) and iron oxides (Mortensen et al. 2011) as well as anthropogenically produced materials including fly ash (Montoya et al. 2019, Safavizadeh et al. 2019), and iron and gold tailings (Liang et al. 2014, Liu 2021, O'Toole et al. 2022) have been effectively treated. The range of gradations of these different soil materials is provided in Figure 29.

MICP treatment effectiveness in soils consisting of human-induced process waste products, including fly ash, tailings, and other waste rocks have shown promise. For example, Montoya et al. (2019) demonstrated MICP effectiveness in fly ash by testing two different coal ash materials which contained aluminum silicate, silicon oxide, aluminum oxide, and iron oxide. Treatment of these fine-grained materials (D_{50} = 19.9 and 31.6 µm) in modified oedometer tests showed an increased in soil stiffness and resilience of such materials to repeated stress loading and unloading cycles as the cementation levels increased. Safavizadeh et al. (2019) tested the same coal ash material as Montoya et al. (2019) in addition to one other coal ash. This additional coal ash material, however, was not effectively cemented with MICP and may have resulted from inhibitory concentrations of metals and other dissolved species in these materials.

Researchers have also investigated the effectiveness of MICP in tailings materials wherein it can be used to accelerate consolidation (Liang et al. 2015, Liu & Montoya 2020, Liu & Montoya 2021, Liu 2021) and enable strength improvement for applications including liquefaction mitigation (Gui et al. 2018, O'Toole et al. 2022). Results from Liu and Montoya (2021) showed that MICP can accelerate sedimentation in oil sand tailings by increasing soil particle sizes with resulting densification of the material and a reduction in reclamation time. The same effect was observed in mature fine tailings by Liang et al. (2015). Liu (2021) observed that MICP could achieve an appreciable increase in shear wave velocity (from 50 m/s to 325 m/s) indicating the development of a stiffer cemented soil matrix. Lastly, O'Toole et al. (2022) treated iron and gold mine tailings and observed undrained shear strength increases up to 4.5 times following MICP treatments when compared to untreated controls.

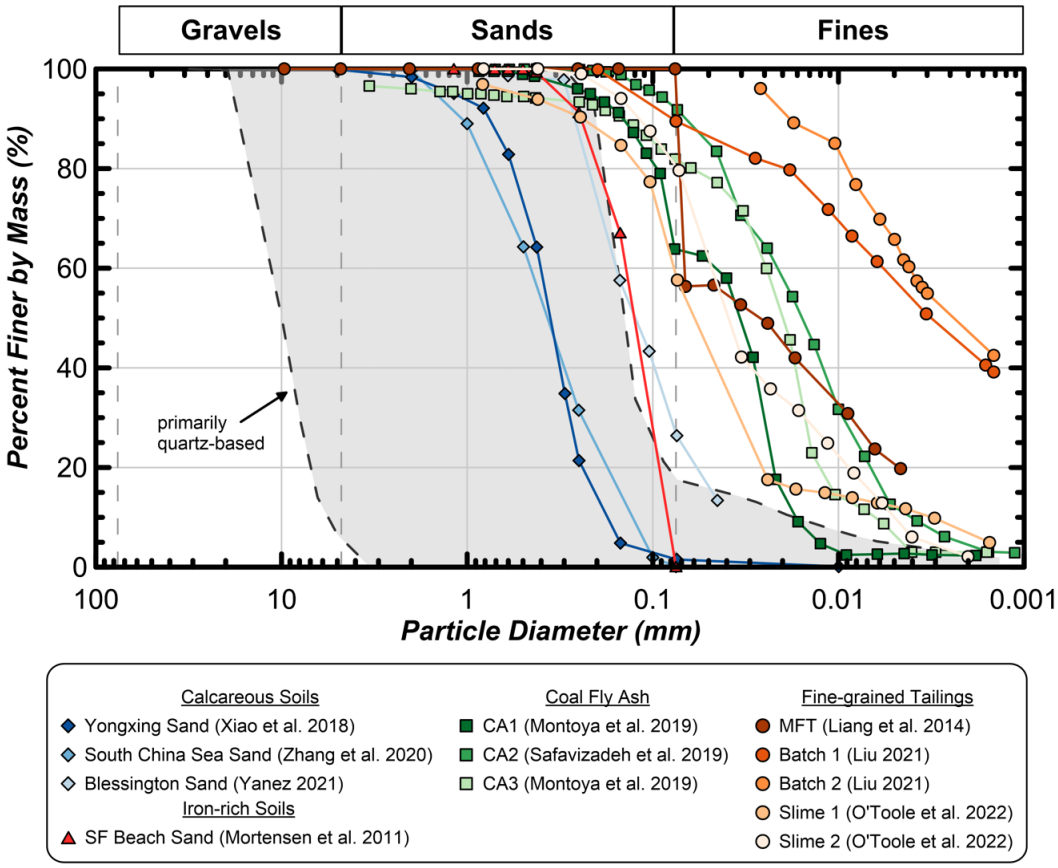

Figure 29. Grain size distribution of select MICP research studies involving different soil mineralogies. Band of primarily quartz-based soils tested with MICP is also shown for reference (Figure 28).

MICP treatment of anthropogenically generated coarser soils, such as waste rock and base aggregate, have also been successful. Jiang and Soga (2019) investigated the effectiveness of MICP treated gravel-sand mixtures for erosion resistance via one-dimensional internal erosion tests. This study highlighted the importance of soil gradation, overburden stress, and MICP treatment method in mitigating internal erosion issues. Furthermore, Mahawish et al. (2018) performed a suite of tests on coarse and fine aggregate soil mixtures in order to investigate the effect of particle size distribution and its contribution to unconfined compressive strength values. The addition of 25% fine aggregates into a coarse soil matrix led to a measurable improvement in strength (i.e., UCS increase of 575 kPa), however, higher fines contents above 25% did not provide additional improvement.

3.7.3 *Environmental conditions*

MICP treatment effectiveness not only depends on the largely physical constraints posed by different soil materials but also highly depends on surrounding geochemical conditions, the presence of pore fluids, and other site dependent factors. Of the infinite possible environmental variations, some variables that have been explicitly examined to date include changes in water salinity, surrounding temperatures, specific ion additions, and partial saturation.

MICP soil improvement feasibility in coastal environments where either seawater or brackish pore fluids are present has been shown to be feasible. For example, studies by Mortensen et al. (2011) and Cheng et al. (2014) examined treatments in saline water conditions. Recent experiments by the authors' (Yanez et al. 2022) considered a broader range of seawater mixtures and similarly demonstrated treatment effectiveness using stimulation. Figure 30 presents a subset of these results obtained in experiments involving applications of MICP treatments applied in various combinations of natural seawater and fresh water (100% AGW to 100% NSW) to an alluvial (Concrete Sand) and marine (Beach Sand) sand. As shown, stimulation was effective towards achieving sufficient urea hydrolysis activity in all experiments (Figure 30a) with uniform calcite contents near 5.2% achieved after cementation (Figure 30b) and average unconfined compressive strengths for all soils near 840 kPa.

The in situ temperature of soils at depths below 2 m in most environments is between about 8 and 11ºC. However, the vast majority of MICP research is performed in the laboratory where the temperature is about 20ºC. Bacterial activity typically reduces by a factor of 2 to 3 per 10ºC decrease in temperature, as bacteria processes typically have a Q_{10} temperature coefficient of 2 to 3 in ideal conditions where growth and other factors are ignored. De Muynck et al. (2013) performed batch experiments with *S. pasteurii* under various temperatures (10, 20, 28, 37°C) and observed varying rates of urea degradation in the absence of any added nutrients. Their results showed expected increases in rates between 10ºC and 20ºC specimens with the 20ºC specimen achieving roughly twice the ureolysis rate of the 10ºC specimen for three different pure cultures (i.e., *Sporosarcina psychrophila, Sporosarcina pasteurii, Bacillus sphaericus)*. Conversely, as temperatures increased from 28°C to 37°C, minimal effects were observed. van Paassen (2009) reported an increase in urease activity near a factor of 3.4 for every 10°C increase. Whiffin (2004) further observed stable urease activity from 15°C to 25°C and a linear increase of 0.04 mM urea hydrolyzed/min/OD from 25°C to 60°C. Consequently, the kinetics governing the MICP reaction network are expected to slow, perhaps significantly, when comparing responses observed in lab experiments to that observed in the field. This decline in reaction rates may be acceptable and manageable for certain projects, but in other cases, particularly when such effects are not anticipated, may necessitate unfavorably long retention and reaction periods between treatment injections. Compensation for this shift in environmental conditions can be addressed in part by modification of the treatment formulation (Section 3.1). For example, a decrease in single-cell activity due to temperature reductions encountered in the field could be conceptually compensated for by increasing the stimulated microbial cell population, resulting in a comparable bulk ureolytic rate to that achievable in the laboratory. Although not discussed here, changes in ionic strength and specific inhibitory solution species (such as magnesium ions and other metals) may further alter achieved bulk ureolytic activities. While the authors' will refrain from discussing all of these effects, characterization of soluble species present in soil material pore fluids and testing of site soils in tandem with other more well characterized soils which can serve as a control, may allow for such effects to be identified early during the treatment design process. As with temperature, reductions in bulk ureolytic rates resulting from such inhibitory concentrations could be compensated for through greater cell densities in theory, however, the success of this approach is less

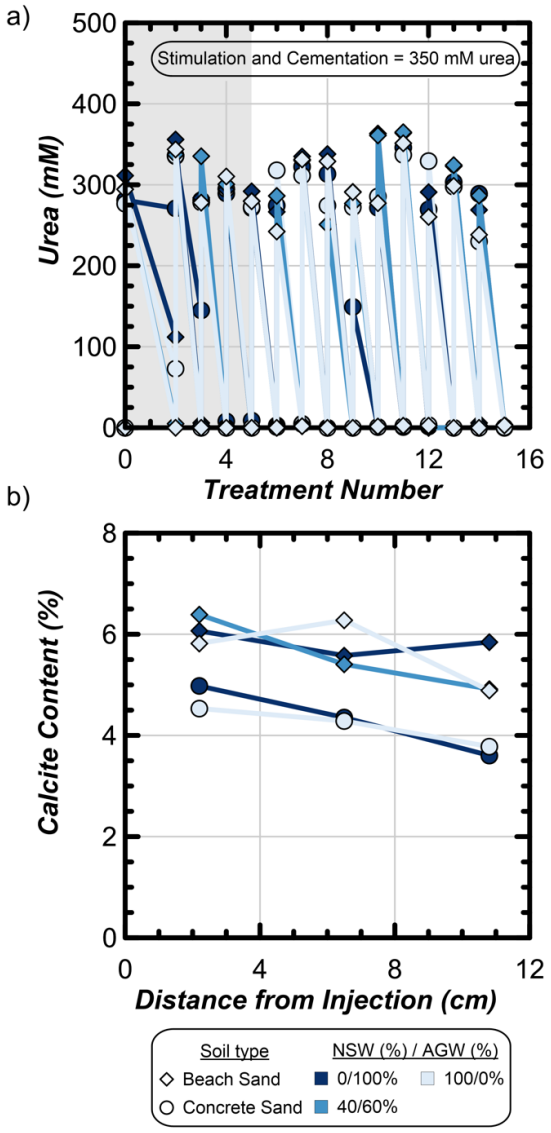

Figure 30. (a) urea degradation and (b) calcite contents from stimulated column tests involving two sands and solutions of varying salinity. Full urea degradation is observed after 3 stimulation treatments with sustained activity after 10 cementation treatments (adapted from Yanez et al. 2022).

certain due to the varying impact of such concentrations on cell growth which would merit more specific testing.

The vast majority of MICP work to date has been performed using saturated soils, and this remains the focus herein as it directly applies to liquefaction mitigation. However, MICP treatment of free-draining soils susceptible to liquefaction could be performed if temporary dewatering was implemented. Conceptually, soil treatment under freely draining conditions would be expected to be comparably, or more effective, than the fully saturated counterpart condition if more specific challenges related to treatment uniformity and implementation are not considered. Free-draining treatments could in theory provide some benefits as it requires a smaller treatment solution volume (~0.25 to 0.5 of the pore volume) and would allow for localization of retained solutions at solution menisci existing at particle-particle contacts where precipitation can be most effective towards improving soil mechanical properties. Cheng & Cord-Ruwisch (2012) and Cheng et al. (2013) demonstrated this effect and showed that treatments applied under partially saturated conditions can be more effective than treatments applied under saturated conditions when comparing specimens at similar cementation levels.

3.7.4 *Reagent purity*

While the majority of laboratory experiments have been performed with research-grade chemicals, such sources will in many cases be cost prohibitive when applied to field-scale. Therefore, it will likely be necessary to source chemicals from other commercial sources. The use of such sources will require compromise with respect to product purity and particular impurities may be important to recognize and quantify prior to use. It is the authors' recommendation that some amount of testing be performed to evaluate the performance of these feedstocks relative to other more well characterized reagent grade sources. Specifically, the authors' suggest that caution be taken when selecting urea sources, as some commercial fertilizer products intentionally contain urease inhibitors to promote the gradual release of ammonium nitrogen for agricultural applications. When reflecting on past up-scaling experiments, the authors' believe that such chemical grade differences may have played some role in the limited success of a high concentration MICP field trial plot performed for surface stabilization as described in Gomez et al. (2013). Therefore, this aspect among many other considerations should be contemplated when selecting these commercial chemical sources.

3.8 *Additional considerations*

Implementation of MICP in the laboratory or field requires additional process and design considerations, including the sterility conditions and stress changes during and after treatment. A summary of these important considerations is provided below, while acknowledging that other important considerations may exist for a particular application and/or experimental program.

3.8.1 *Sterility during testing*

Preparation of soils and MICP treatment solutions in past studies have ranged from fully sterile laboratory tests designed to definitively demonstrate the biogeochemical basis of the technology to field scale implementation where construction-scale equipment is used for preparation and injection of treatments into natural, non-sterile subsurface conditions. As alluded to in Section 2, fully sterile laboratory tests where augmentation has been applied using non-nutritive solutions (and perhaps even sterilized soils) have clearly defined the science of MICP. In such tests, augmented *S. pasteurii* was the primary microbe performing ureolysis and facilitating precipitation of calcite, enabling measurements specific to the *S. pasteurii* strain to be made.

However, recognizing that eventual implementation of MICP as a soil improvement technology in the field would inevitably be under non-sterile conditions and that stimulation of native microbes in the natural environment would be preferrable to augmentation, research efforts shifted focus towards verifying robustness of the stimulated MICP process under non-sterile conditions. Acknowledgement of non-sterile field conditions and the need for treatment robustness led to the refinements in the stimulation formula that produce temporary environmental stressors, which are favorable for ureolytic bacteria to thrive and outcompete other bacteria (Section 2). One example of the effect soil sterility can have on stimulation success is shown in Figure 31, which presents urea degradation across multiple treatment cycles applied to a fully sterile glass bead soil and a natural sand material (Concrete Sand) both treated with non-sterile solutions. As shown, the sterile control does not exhibit any detectable ureolytic activity over seven different treatment cycles, indicating that minimal activity resulted from use of non-sterile solutions. In contrast, the natural sand is readily stimulated and begins degrading urea in the third cycle of treatment with increasing activity over time.

The efficacy of MICP treatment using stimulation in natural soils under non-sterile conditions has been sufficiently established in both laboratory and field conditions. Nonetheless, in the laboratory thorough cleaning and sterilization of treatment solutions and testing equipment is still recommended to minimize the likelihood of sequential transfer of microbes and contamination from one test series to the next. Otherwise, it may be incorrectly concluded that a specific soil may support stimulated MICP, when the true source of activity was instead some contaminant. In the field thorough cleaning of mixing and pumping equipment is also recommended prior to use, particularly if the equipment was previously used for implementation of a different soil improvement method or environmental remediation technology.

3.8.2 *Stress conditions during MICP*

The MICP cementation formed is brittle, and susceptible to disturbance from stress and strain perturbations, especially at cementation levels below about 5% calcite content by mass. This susceptibility requires consideration and management of the

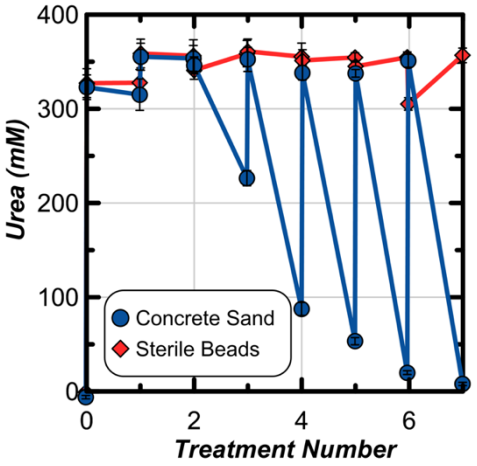

Figure 31. Comparison of ureolytic activity generated by non-sterile stimulation medium treatments of a sterile soil analog, 0.25-0.42 mm glass beads, with one composed of a natural alluvial sand. The soil analog was oven-sterilized for 72 hours at 180°C prior to application of the same stimulation treatments. Urea concentrations were measured at the start and end of each treatment. Error bars represent one standard deviation of triplicate urea quantifications (adapted from Graddy et al. 2021).

confining stress applied to specimens during treatment and subsequently during some applied loading. In the laboratory, this is relevant when stresses are relaxed (or entirely) released as specimens are transferred from a treatment cell to some other testing apparatus. In the field, this is relevant when considering the in situ stress during treatment in comparison to the lower or higher stresses that may be applied during some project's service life (e.g., due to earthquake or infrastructure loadings).

Differences in confining stresses between those applied during treatments and those applied during subsequent loading can be differentiated as the treatment stress, σ'_{treat}, and the operational stress, σ'_{oper}. Conceptually, calcite precipitation forms brittle cemented bonds between particles (Section 2.4) while particle-particle contacts experience contact forces dependent on the σ'_{treat}, particle size, and mineral-specific compressibility, which can be approximately understood using Hertzian contact theory. Following cementation, deviations from the σ'_{treat} can result in elastic loading or unloading of the contact forces, which will produce changes in compressive or tensile stresses acting at the precipitated contacts. The susceptibility of damage to this loading and unloading is dependent on the amount of precipitation and the magnitude of stress change, however, all other factors equal, the susceptibility of a cemented soil to this disturbance decreases with cementation level increases and as stress changes are minimized. Montoya et al. (2013) documented how cementation integrity (as measured using shear wave velocities) can systematically degrade with unloading and reloading cycles for specimens treated to low cementation levels, but can remain relatively intact when similar stress cycles are applied to higher cementation levels. This can be explained in part by the fact that as cementation levels increase, shear modulus values becomes increasingly stress invariant, exhibiting behaviors more similar to intact rock. Such behaviors are further described in Section 5.

Changes between the σ'_{treat} and σ'_{oper} are important to recognize as such variations can affect the subsequent engineering behaviors of MICP-treated soils, particularly at low cementation levels. This typically manifests as a decrease in stiffness, peak strength, and changes in dilative tendencies. The magnitude of this influence can range from complete degradation to the corresponding uncemented state to more minor effects with the magnitude being dependent on the cementation level, the magnitude of $(\sigma'_{treat} - \sigma'_{oper})$, and other unquantifiable handling disturbances. Per the above discussion, the impact of such disturbances will decrease as the cementation level increases due to decreased stress dependence. The effect of the stress difference induced, $(\sigma'_{treat} - \sigma'_{oper})$, depends on whether or not the operational stress exceeds or is less than the treatment stress. Laboratory results show that unloading from σ'_{treat} to a lower σ'_{oper} induces less, sometimes minimal, damage relative to increasing to a higher σ'_{oper}. This can be explained by a smaller elastic deformation being recovered upon unloading and both plastic and elastic deformation occurring when loading to higher stresses never experienced by the sample. However, given these complexities, the effects of stress changes are not necessarily predictable and there are no existing empirical corrections to account for the change in engineering behaviors induced by stress changes from σ'_{treat} to σ'_{oper}.

MICP treated specimens prepared in soil columns, particularly at lower cementation levels, are often even more susceptible to damage due to the strains imparted on the specimen during extrusion, movement, handling, and remounting of specimens between a treatment cell and a testing device. Again, the magnitude of damage is inconsistent and cannot be reliably corrected for. Thus, treatment of laboratory test specimens following placement in some testing device (e.g., triaxial, simple shear) is preferred whenever possible.

The consequence of handling-induced damages on the subsequently measured engineering behavior is often substantial and contributes significantly to exceptionally large variations in measurements reported in the literature. This is most evident in reported unconfined compression test strength (UCS) values. For this specific test, the large variations can be primarily attributed to the damage induced during extraction of the specimens from treatment molds, setup of the specimens in the test device, and end cap imperfections, with treatment formulations and injection methods having likely only secondary effects. For this reason, UCS values could be appropriate as a more qualitative metric by which improvement can be said to have been achieved. However, it likely that the actual strength gain achieved is larger (possibly substantially) than that measured with UCS. Consequently, it is recommended that more advanced strength tests be performed using processes where the specimens can be treated at a stress state that is maintained through shearing (i.e., $\sigma'_{treat} = \sigma'_{oper}$).

4 PROCESS MONITORING & QA/QC

The following section describes a series of methods for monitoring of ureolytic MICP. This includes methods for determination of microbial activity and abundances, geochemical changes, the mineralogy and composition of achieved cementation, and other methods aimed at furthering understanding of microstructural and mechanical changes afforded by the presence of cementation.

4.1 *Microbiological process monitoring*

Several methods have been used for quantifying densities of bacteria used in MICP. Some of these methods come with significant potential pitfalls, and the most rigorous methods are typically not the most readily implemented ones.

4.1.1 *Cell quantification approaches*

Although many methods exist by which total cells can be quantified, the following sections outline the primary methods for cell enumeration in MICP experiments with a discussion of specific considerations.

4.1.1.1 *Optical density measurements*

Quantifying the initial density of *S. pasteurii* or other bacteria to be added to soil column or flask experiments is most often accomplished using a spectrophotometer to measure optical density at some standard wavelength, 600 nm being typical (OD_{600}). Bacterial suspensions, which impact optical density in a fundamentally different way than colored solutions, do so by scattering (not absorbing) light. Data collected on six different randomly selected spectrophotometer models are presented (Figure 32) and show that the same *S. pasteurii* suspensions scatter light very differently on the various instruments based, presumably, on different internal geometries and other factors. As shown, an OD_{600} of 1.0, near the middle of this range, corresponds to a 4-fold range in cell densities of approximately 1.8 to 7.8 x 10^8 cells/mL. When considering the extremely low value of 0.8 x 10^8 cells/mL, which was derived from the oft-used standard equation of Ramachandran et al. (2001), that equation is found to be largely inconsistent with observed trends and the range of cell densities expands to 10-fold. The use of uncalibrated optical density measurements therefore should be confined only to assuring that different experiments within a single laboratory are performed at equivalent cell densities. This approach also requires appropriate pre-measurement dilutions to remain within the linear range of the instrument, which can be quite different for various instruments (Figure 32). Only after a specific spectrophotometer has been accurately calibrated, such as by measuring total bacterial protein or total direct counts and

relating these to OD_{600} values, can the data produced be relied upon to accurately measure and report absolute cell densities. Key to reproducing any type of experimental work by another researcher is ensuring that such values are transparent and universally understood. Thus, it is recommended that cell densities be reported in the literature only after accurate conversion from optical density and that raw OD_{600} values not be reported in isolation.

4.1.1.2 *Total bacterial protein (TBP)*

Total protein comprises approximately 50% of bacterial dry weight (Luria 1960, Ingraham et al. 1983) and is, therefore, an excellent surrogate for bacterial abundance (Figure 33a). To convert from protein/mL to cell densities (cells/mL), the following additional conversions can be employed: (1) the wet density of whole bacteria is nearly constant at 1.05 g/cm^3, and (2) the ratio of dry weight to wet weight for bacterial cells is approximately 0.30 (Bakken & Olsen 1983). Thus, one can readily convert total bacterial protein/mL to wet biomass/mL and finally to actual cells/mL, if the shape and average dimensions of the bacterium under the employed conditions are known. The Coomassie brilliant blue method of Bradford (1976), has long been employed; representative details for measuring total cellular protein (soluble + membrane associated) can be found in Nelson & Jannasch (1983). A second widely used dye-binding method employs bicinchoninic acid (Smith et al. 1985). Commercial kits are available for both and include advice on specific protein standards.

4.1.1.3 *Total direct counts (TDC)*

Initially devised for enumeration of dilute bacterioplankton in marine environments, the epifluorescence microscopy method of Hobbie et al. (1977), which makes individual bacteria visible by brightly staining their nucleic acid, has been adapted to quantifying densities of appropriately diluted pure cultures that have been concentrated, post-staining, into a single focal plane on a counterstained membrane filter. This method was initially called the acridine orange direct counting (AODC) method. Another method (Porter & Feig 1980) employs the less toxic/mutagenic DAPI (4-6-diamidino-2-phenylindole). Regardless of the fluorochrome used, the result is direct microscopic counting of cell densities that can be used to generate a standard curve relating TDC to OD_{600} values obtained spectrophotometrically for the same cell suspensions. Access to a high-quality epifluorescence microscope, equipped with one or the other filter set, is likely available at most research universities, and only periodic calibration of an OD_{600} versus cell density curve is required.

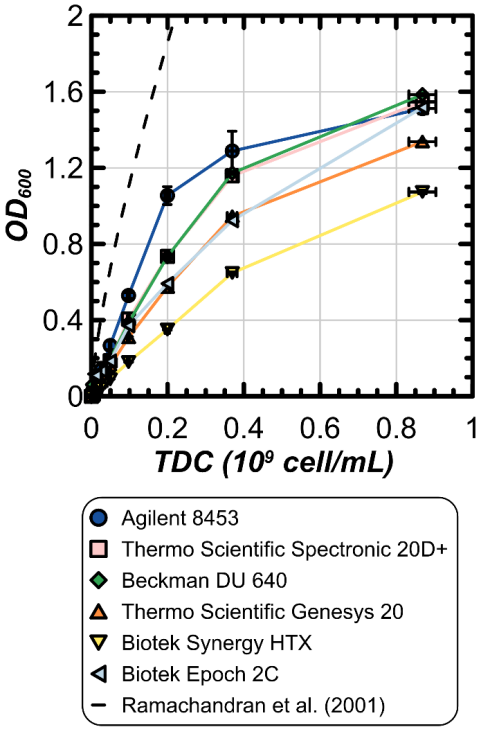

Figure 32. Spectrophotometric response of a set of washed *S. pasteurii* suspensions on a series of spectrophotometers. Total direct counts (TDC) were performed using acridine orange epifluorescence method. Cell counts estimated from the measured OD_{600} using the relationship from Ramachandran et al. (2001) are plotted for comparison. Error bars are standard errors of triplicate suspensions for OD_{600} and 10 microscopic field counts for TDC.

4.1.1.4 *Viable plate counts (VPC)*

If the bacterium under study, when serially diluted in sterile diluent and spread on plates of appropriate agar-gelled medium, produces colonies whose density corresponds to that measured by TDC or TBP, then such counts can be used as another way to calibrate and periodically check an OD_{600} to total cell density conversions factor, independent of access to an epifluorescence scope. Unfortunately, for the type strain of *S. pasteurii*, different types of plate count medium can yield very different recoveries for the same cell suspension. Especially on ATCC 1376 Medium (Stocks-Fischer et al. 1999), which was used to calibrate an equation relating OD_{600} to cell density (Ramachandran et al. 2001), recovery was poor and variable (Figure 33a, b) compared with recovery on BHI (brain heart infusion) agar with urea (75 mM), pH 8 (Figure 33c). Unknown factors, including how long the ATCC 1376 medium was autoclaved, how long plates of medium were aged prior to serial dilution, and culture condition appear to contribute to its highly variable recovery. In the authors' experience, BHI gives by far the most reproducible and accurate results for *S. pasteurii* as shown by the agreement between the BHI calibration OD_{600} with the measured TDC on two separate cultures (Figure 33a, b). It is therefore exceedingly important, if reported VPC results are to be an accurate measure of that cell densities, that they be calibrated ultimately and regularly against either TDC or TBP.

4.1.2 *Ureolytic rate determination approaches*

The following sections outline the primary methods by which ureolytic activity can be quantified in MICP experiments. This includes methods for determination of ureolytic activity per cell (termed specific ureolytic activities) as well as the determination of the collective ureolytic activity of enriched microbial communities (termed bulk ureolytic rates). Finally, methods by which these rates can be modelled are further discussed. Measurements of urea hydrolytic activity are important in the design, implementation, and analysis of both biostimulated and bioaugmented ureolytic MICP implementations. These determinations are applied in vitro to pure culture suspensions of bacteria, frequently but not exclusively to *S. pasteurii*, to, for example, validate and dose the bioaugmentation inoculation or to evaluate the potential utility of a microbial strain for MICP. In situ measurements are made on pore fluid samples obtained from soils during treatments to monitor the progress of urea hydrolysis in the soil, to determine when enough time has elapsed to apply a subsequent treatment, as well as to evaluate the efficacy and uniformity of stimulation or augmentation inoculation. Measurements of urea hydrolysis can be made either from the disappearance of urea directly or through the appearance of reaction products (e.g., total ammonium). While measurements of the appearance of end-products is indirect, it is typically a more sensitive means of detecting small changes in urea concentration, especially at the start of reactions where the

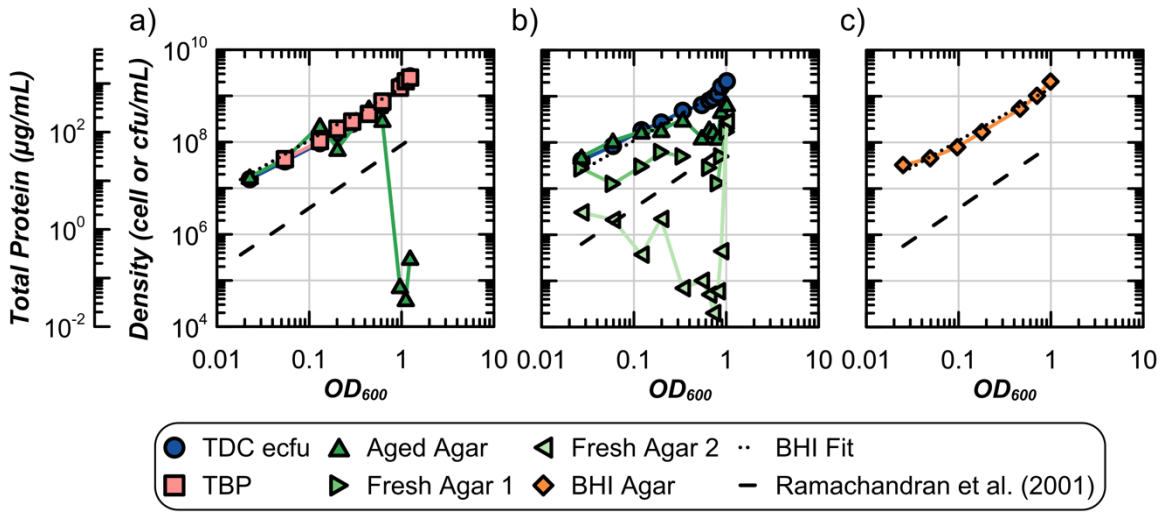

Figure 33. *S. pasteurii* quantification methods and agar efficiency. Three exponential growth curves of *S. pasteurii* in ATCC medium 1376 (28°C, 150 rpm) measured by OD_{600} and total direct counts in effective colony forming units (TDC ecfu; i.e., attached cells or cell clusters count for one ecfu) in (a) and (b), total bacterial protein (TBP) in (a), viable plate counts on ATCC 1376 agar aged one week (aged agar) in (a) and (b), viable plate counts of two separate batches of one day old ATCC 1376 agar (fresh agar) in (b), and viable plate counts on BHI agar in (c). The relationship between OD_{600} and cfu from Ramachandran et al. (2001) is used to estimate culture density from the OD_{600} measures in all panels, while a power fit of the BHI data in (c) is to estimate culture densities in (a) and (b).

relative change in product concentration is large compared to substrate. This is especially important for short duration assays required for accurate specific ureolytic activity determinations but may be accordingly less important for longer duration soil element measurements.

4.1.2.1 *Specific ureolytic activity*

The most sensitive and quantitative method for measuring ureolytic activity in vitro uses the colorimetric Berthelot method of ammonia determination (Weatherburn 1967, Krom 1980, Section 3.4.1), though other ammonia methods, frequently enzymatic, exist (Kaltwasser & Schlegel 1966) and are discussed elsewhere (Mobley & Hausinger 1989). The Berthelot method, however, is relatively slow and uses somewhat hazardous chemicals (e.g., phenol, nitroprusside, bleach), leading to other, less involved measures of end-product accumulation being preferred for some applications. The most prominent alternative utilizes the generation of charged end-products from the neutral urea product, allowing a solution's electrical conductivity to serve as a measure of urea degradation (Lawrence 1971). Colorimetric change of pH indicator has also been suggested to estimate urea degradation from medium alkalinization, though the method's sensitivity, both of the method overall and the buffering capacity of the chosen medium, may preclude accurate quantification of specific activity (Cui et al. 2022). As discussed below, accurate measures of specific activity must be done on short timescales in which the chemical environment of the solutions remains effectively unchanged. Thus, direct measurements of urea disappearance are typically not appropriate for this application, where a detectable decrease in the enzyme substrate is likely to affect the interpreted instantaneous rate of hydrolysis.

Measures of activity are best reported on a repeatable and transferrable biomass basis. Optical density as a proxy for turbidity is not a quantitative, transferrable measure of cell density and should instead be calibrated internally and presented on a cell or total protein basis, as discussed previously. Additionally, the specific ureolytic activity of a suspension of cells is subject to substantial change based on the growth phase in which they were harvested and the duration and conditions under which they are held. Even for bacteria that express urease constitutively, stress-induced global metabolic regulation, such as might be found in a starving or toxified late exponential/stationary phase culture, could lead to substantial reduction in the cellular urease concentration. Similarly, the average cell size of a culture elongates as it exits exponential growth, which can affect measures of per-cell, if not per-biomass, activity. Thus, for the most repeatable results, cells should be harvested during exponential growth after a minimum of 4 to 6 doublings to ensure consistent, vigorous cell state, and used promptly. If late stationary or long-resting cells are to be used, more variability should be expected.

Finally, caution is urged to identify the contribution to total ureolytic activity of free urease that may exist in the solution. As cultures proceed, they can accumulate a population of dead cells. Due to the nature of exponential growth, this effect becomes much more significant during the later phases of growth, and is especially prominent during the stationary and the appropriately named death phase. During this stage, dead cells' membranes disintegrate and their cytoplasm is released into free solution, liberating urease. Free urease has five fold higher activity than equivalent whole-cell urease which has an activity that is seemingly limited by membrane diffusion (Larson & Kallio 1954). Thus, it is the authors' recommendation that cultures be used soon after growth (ideally within a few hours) with storage at 4°C. Longer storage may substantially increase variability and soluble urease concentration. In addition, the activity of media filtered and/or centrifuged to remove bacteria should be at a minimum occasionally checked to quantify the impact of free urease.

4.1.2.2 *Bulk ureolytic activity*

The determination of bulk ureolytic activity in treated soils can be achieved through pore fluid sampling and chemical analysis of the in situ conditions over time. Such measurements are typically obtained over a period of hours during which chemical compositional changes are expected. The desired outcome primarily being to either describe the ureolytic behavior of some treated soil over a treatment residence period or merely to assess urea concentrations at a particular point during treatments. Direct colorimetric urea assays on pore fluid samples (Knorst et al. 1997) are typically used for such measurements, when substantial urea is expected to degrade during the sampling time course. If instantaneous ureolytic rates are instead desired,

caution should be employed before assaying pore fluid samples in vitro, as a substantial amount of ureolytic activity appears to be unable to be sampled by simply extracting pore fluids and monitoring this fluid's activity in isolation (Graddy et al. 2021). In this case, assaying washed soil/cell pellets from soil samples could better capture this activity and allow for more stringent control over assay conditions, however, obtaining such samples would likely require significant specimen disturbance.

4.1.2.3 *Kinetic models for ureolysis*

For some applications, it can be desirable to model the kinetic process by which ureolytic activity degrades supplied urea in a given system. This can be accomplished by fitting appropriate kinetic models which can approximate experimentally observed urea degradation trends. Three kinetic models are commonly employed to fit observed urea degradation trends, and include zero-order, first-order, and Michaelis-Menten, each of which have specific difficulties and limitations.

First-order reactions have reaction rates that change linearly as a function of a single reactant concentration (e.g., urea). This is typical of the degradation of single species, with radioactive decay being the canonical example. Trends are primarily captured by first-order rate coefficients which describe the proportion of a reactant that is degraded per unit time. The integrated first-order rate equation is presented in Equation 10 and is related to the current substrate concentration, $[S]_t$, as well as the initial substrate concentration, $[S]_0$, rate coefficient, k, and time, t.

$$[S]_t = [S]_0 e^{-kt} \tag{10}$$

Zero-order kinetics describe reactions where the reaction rate is constant, independent of reactant concentration. For enzyme mediated reactions, if a substate is present at sufficient concentrations, the active sites of the enzymes that are present can remain occupied, and therefore the reaction can only proceed as fast as the enzymes can complete these reactions, leaving the rate dependent upon the concentration and efficiency of the enzyme. The integrated zero-order rate equation (Equation 11) is linear, with a slope of –k. As shown, the zero-order rate coefficient is in units of concentration per time and the equation includes the initial substrate concentration, $[S]_0$.

$$[S]_t = -k\,t + [S]_0 \tag{11}$$

Most reactions only transiently operate under zero-order conditions, as eventually one of the reactants is consumed to the point at which the catalyst begins to desaturate or become less than fully occupied. At this point, the behavior may transition toward first- or higher-order kinetics as other reactants are subsequently consumed. This can limit the utility of zero-order fitting to relatively narrow ranges of concentrations and or times over which the reaction rate is approximately constant. To that end, zero-order kinetics are frequently used to estimate an instantaneous rate of a first or higher order reaction under a given set of conditions by measuring the reaction rate for a very short period after initiation. In this initial rate approximation, the short duration does not afford much deviation from the initial reaction conditions, so the rate is largely constant and zero-order fitting of the pseudolinear portion of the data is typically a reasonable descriptor of the behavior.

Michaelis-Menten kinetics were developed to better describe enzyme-substrate interactions and can better approximate the transition from a zero-order to first-order kinetic regime, as occurs upon catalyst desaturation. It takes the form seen in Equation 12, where the reaction rate or velocity, V, is related to the substrate concentration, [S], the Michaelis-Menten half-saturation constant, K_M, and the maximum reaction velocity, V_{max}, which in turn is the product of enzyme concentration, [E] and the catalytic turnover number of the enzyme, $k_{cat.}$

$$v = \frac{-V_{max}\cdot[S]}{K_M+[S]} \tag{12}$$

At [S] >K_M, the denominator approximates [S] and the reaction rate approaches V_{max}. Since enzymes are catalytic and not consumed in a reaction, V_{max} remains a constant. In other words, at high substrate concentrations, the reaction rate is independent of substrate concentration and is effectively described by zero-order kinetics. At [S] <K_M the denominator instead approximates K_M, allowing V_{max} and K_M to be collected into a rate coefficient, k, yielding v = k[S]. At this point, the reaction rate is linearly dependent on [S] and thus is best described by first-order kinetics. The K_M parameter describes the concentration at which the model transitions between kinetic regimes. From a biological perspective, K_M describes the binding affinity of a given enzyme and its substrate. The more effective the binding, the lower the K_M, and the lower the concentration at which the enzyme becomes saturated and the kinetic behavior transitions.

Michaelis-Menten kinetics are therefore applicable over a large range of substrate concentrations and are uniquely suited to describe kinetic behaviors around the transition from zero- to first-order kinetics. This utility, however, is somewhat offset by the unwieldy integrated form (Equation 13, Beal 1982, Schnell & Mendoza 1997), which requires the use of the Lambert W function.

$$[S]_t = K_M W\left(\frac{[S]_0}{K_M} e^{\frac{-V_{max}t+[S]_0}{K_M}}\right) \tag{13}$$

4.1.2.4 *Ureolytic rate modeling*

In the context of describing the behavior of ureolytic MICP, kinetic properties typically have two primary purposes: allowing for ureolytic rate determinations of cell suspensions in vitro or allowing for bulk ureolytic rate determinations and predictions in situ. In both circumstances, rate determinations are being made for intact whole bacterial cells, and thus yield apparent whole cell ureolytic rates. Nearly all of the pertinent organisms and communities have apparent whole cell K_M values in excess of 50 mM, with the *S. pasteurii* type strain having a K_M exceeding 300 mM (Lauchnor et al. 2015, Graddy et al. 2018). Thus, for most MICP applications and applied urea concentrations, the concentration-dependence of ureolytic rates is an important consideration.

In vitro measurements are typically relatively short, perhaps several minutes, which satisfies the preconditions for the initial rate approximation. The result being that zero-order fitting can do a reasonable job of describing the initial rate (Figure 34a); however, the linearity of these urea concentration reductions will be dependent upon the activity and whole cell K_M of the active cells. Similarly, it should be mentioned that the apparent rate will be sensitive to the initial urea concentration when urea concentrations are not in significant excess of the K_M.

For bulk activity measurements, relatively uniform sampling over the entire retention period allows for characterization of behaviors over larger substrate concentration changes. For these instances, zero-order fits may not be appropriate unless the apparent K_M is uncharacteristically small. Some researchers have fit zero-order models to data observed at the start of in situ urea degradation curves, with the result being an average rate over the interval fit (Figure 34b). However, these estimates are sensitive to the subjective definition of the linear range, which will vary over the course of an experiment with the bulk ureolytic rate. For

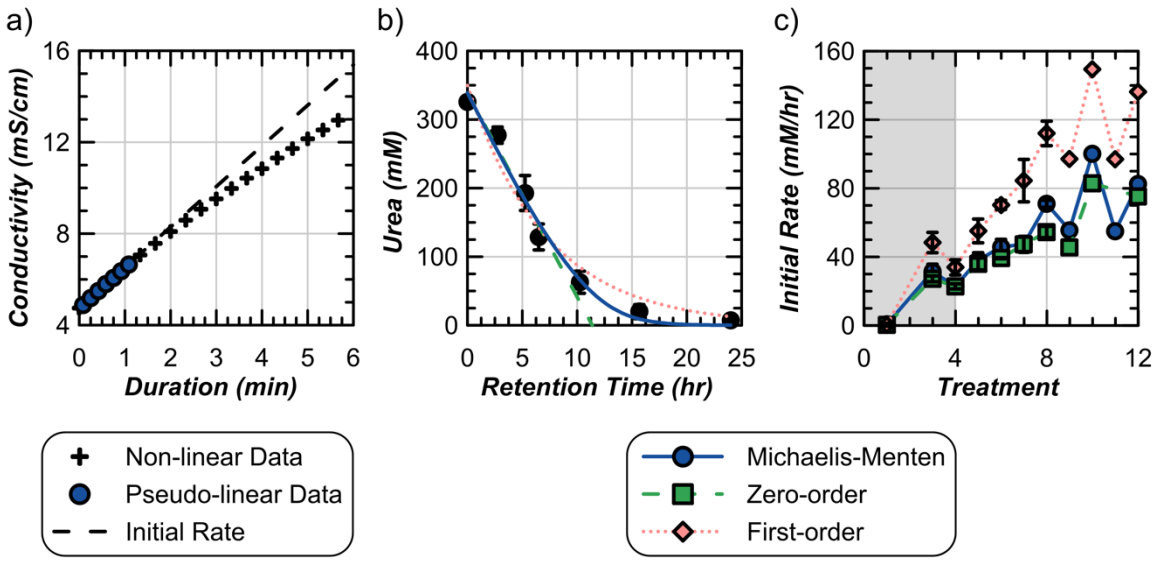

Figure 34. Examples of ureolytic rate analysis. Initial rates approximation of in vitro *S. pasteurii* ureolytic activity in (a), where the data are initially reasonably linear, but quickly deviate based on changing reaction conditions. Comparison of the three primary urea degradation models in a single MICP treatment (b) and estimating the initial rate for each treatment over the course of a whole MICP implementation (c). The shaded region in (c) represents stimulation treatments. Error bars are triplicate standard deviations in (b) and treatments 1-5 in (c), with duplicates in treatments 6-8 (adapted from Graddy et al. (2021).

these cases, fitting may be improved through more frequent sampling at the start of urea degradation time courses. In contrast, first-order fitting of these bulk ureolytic degradation curves does not require subjective determination of data inclusion and can reasonably apply over the entire times series. Such fits may work best for degradation time courses where the apparent K_M is high relative to the initial urea concentration, and therefore the degradation trend closely follows a first-order trend. These conditions are generally encountered during ureolytic MICP. The first-order rate coefficients determined, however, have less direct, inherent meaning than an initial linear fit can provide, however, instantaneous rates can be calculated as the product of the rate constant and substrate concentration. Lastly, a Michaelis-Menten fit is the most physically appropriate model but is also the most computationally challenging. In particular, fitting can be difficult if the achieved data density is low at concentrations near the K_M. However, the model can well capture the behavior of ureolysis during MICP over larger time periods, affording useful kinetic parameters that represent the aggregate behavior of all microorganisms present.

The performance of all three models is presented for a single urea degradation time course in Figure 34b, where all models do a reasonable job describing the urea degradation curve, though the Michaelis-Menten fit seems to better maintain accuracy over an entire residence. The derived initial ureolytic rate for all three models from simulated soil columns from Graddy et al. (2021) shows they all perform reasonably in describing relative initial rate behavior over an MICP experiment, though the first-order model tends to overestimate initial ureolytic rates (Figure 34c).

Importantly, none of these models directly account for the impact of cell growth that is happening concurrent with urea degradation. The models reasonably approximate this behavior without the need to specifically attend to changes in cell growth. Additionally, a Monod term could have been included but would require calibration of additional parameters which would be difficult to determine. Finally, product inhibition via generated total ammonium has largely been ignored in this discussion of ureolytic kinetics. However, it has been shown that whole cell ureolytic activity is largely insensitive to ammonium and pH product inhibition in *S. pasteurii* (Lauchnor et al. 2015), likely due to the homeostatic efforts of the host cell, a feature thought to be shared by other *Sporosarcina.* Nevertheless, the incorporation of inhibition kinetics can be included should it be necessary (Qin & Cabral 1994, Fidaleo & Lavecchia 2003).

4.2 *Cementation process monitoring*

During the MICP treatment process, various aspects of solution geochemistry may be monitored to assess $CaCO_3$ precipitate formation. While a variety of different parameters may be quantified, a summary of several of the most impactful and commonly used monitoring approaches for assessing $CaCO_3$ precipitation are provided below.

4.2.1 *Aqueous calcium measurements*

Measurement of aqueous calcium (Ca^{2+}) concentrations provides an opportunity to characterize cementation progression and dissolution when such processes are of interest. Aqueous calcium, although somewhat infrequently measured in most geotechnical studies, can be easily performed using a variety of approaches including readily available colorimetric assays (e.g., QuantiChrom Calcium Assay; Bioassay Systems Inc.) and other high precision approaches including inductively coupled mass spectrometry (ICP-MS). During the cementation process, such measurements may allow for characterization of $CaCO_3$ precipitation kinetics, assessment of changes in saturation state, and the identification of reaction completion. Practically, such aspects may be of importance for identifying optimal treatment residence periods, enabling temporal and spatial modeling of the precipitation process, and allowing for characterization of site-specific conditions and their potential impact on long-term material permanence, among other aspects. While such concentrations can be routinely measured in most basic analytical laboratories, special care should be taken to ensure that collected samples are indeed representative of pore fluids. In particular, it is recommended that aqueous samples be first filtered to remove any $CaCO_3$ solids that may have been collected during the sampling process and subsequently stabilized samples in strong acid (i.e., hydrochloric acid) to inhibit the potential for both further ureolytic activity and $CaCO_3$ precipitation (see example protocol in Burdalski & Gomez

2020). An example of calcium and urea data obtained during cementation injections involving three different equimolar urea and calcium concentrations is provided in Figure 35. As shown, urea and calcium trends were similar in time, suggesting that the rate of $CaCO_3$ precipitation in these experiments was governed by urea hydrolysis rates. Calcium measurements offer the opportunity to monitor the progression of cementation process directly, without need for further interpretation.

4.2.2 *Solution carbonate analyses*

Measurement of solution aqueous carbonate (CO_3^{2-}) may be equally important in assessing the potential for $CaCO_3$ precipitation. Carbonate species are generated directly from urea hydrolysis as a result of carbonic acid generation with pH rise from ammonia speciation driving the increased availability of carbonate. CO_3^{2-} concentrations play a key role in controlling solution saturation states and can provide important understandings regarding the thermodynamic favorability for precipitation, equilibrium, or dissolution. Aqueous CO_3^{2-} can be assessed through a variety of means including total alkalinity (A_T) measurements and total inorganic carbon analyses. Total alkalinity measurements provide a means by which all proton acceptors in solution including carbonate species can be quantified. Although an example method can be found in ASTM D1067-16, the basic premise of the measurement is the use of a titration procedure wherein strong acid additions are performed in the presence of a pH indicator to determine concentrations of proton acceptors. Proton acceptors are the conjugate bases of

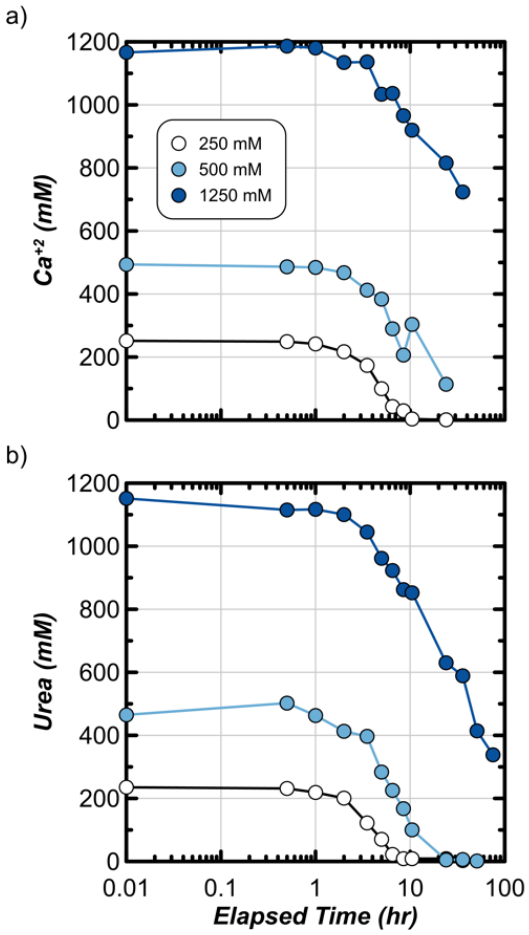

Figure 35. Measurements of (a) calcium and (b) urea concentrations in time during cementation treatments involving three different equimolar urea and calcium concentrations (adapted from Burdalski & Gomez 2020).

weak acids with pKa less than 4.5 in 25°C degree solutions with zero ionic strength. They include HCO_3^-, CO_3^{2-}, OH^-, and NH_3, which must all be accounted for when completing measurements for MICP solutions. When solution pH, total alkalinity, and ammonia (NH_3) concentrations are known, Equations 14, 15, and 16 can be used to determine CO_3^{2-} and HCO_3^- concentrations using the pKa_2 for HCO_3^-/CO_3^{2-} of 10.329. Similarly, total inorganic carbon analyzers can be used to determine HCO_3^- and CO_3^{2-} concentrations. This process works instead by acidifying specimens, therefore speciating carbonate species towards carbon dioxide (CO_2) gas with subsequent capture and quantification of CO_2 using various spectroscopic methods.

$$A_T = [HCO_3^-] + 2[CO_3^{2-}] + [OH^-] + [NH_3] \quad (14)$$

$$[\mathrm{HCO_3^-}] = \frac{[\mathrm{H^+}](\mathrm{A_T} - [\mathrm{OH^-}] + [\mathrm{NH_3}])}{[\mathrm{H^+}] + 2[10^{-pKa_2}]} \quad (15)$$

$$[CO_3^{2-}] = \frac{[10^{-pKa_2}][HCO_3^-]}{[H^+]} \quad (16)$$

4.2.3 *Saturation state determinations*

Knowledge of carbonate and calcium concentrations can be used to determine solution saturation state, however, such calculations should consider other surrounding solution species that will impact activities of carbonate and calcium. Thus, solution activities are considered. Although many different models exist for activity coefficients, model selection generally requires knowledge of solution ionic strength (I) and temperature as well as ion specific parameters including ion size. Under most cases representative of MICP solutions, the Extended Debye-Hückel equation can be used to determine activity coefficients for all samples with I of less than 0.1 M and the Davies equation can be used for samples with I values between 0.1 and 0.7 M. Once concentrations, activity coefficients, and activities of Ca^{2+} and CO_3^{2-} have been determined, the solubility products (K_{sp}) of the specific $CaCO_3$ minerals of concern can be used to determine saturation states. Under most conditions representative of MICP solutions at both atmospheric pressure and near room temperature (25°C), the solubility product of calcite mineral of $10^{-8.48}$ can be used. Equation 17 presents the saturation state (Ω) of solutions with respect to calcite, determined by dividing the ion activity product (IAP), or product of Ca^{2+} and CO_3^{2-} activities (concentrations multiplied by activity coefficients), by the solubility product (K_{sp}) for calcite mineral.

$$\Omega = \frac{IAP}{K_{sp}} = \frac{\gamma_{Ca^{2+}}[Ca^{2+}]\,\gamma_{CO_3^{2-}}[CO_3^{2-}]}{K_{sp}} \quad (17)$$

4.2.4 *Solution electrical conductivity*

Solution electrical conductivity (EC) can be used to assess changes in conductive solution species during the MICP process. Although commonly used to assess changes in ureolytic activity due to increases in solution conductivity from the production of polar ammonium and carbonate species from non-polar urea, the measurement may also hold some promise for monitoring solution changes during the precipitation process. The ability of solution electrical conductivity to resolve important differences in solution chemistry of this indirect measurement is dependent on the urea to calcium ratios used and the pH of solutions. This is due to the consumption of calcium and carbonate ions during $CaCO_3$ precipitation (expected to reduce EC) and the simultaneous release of ammonium and carbonate species due to urea hydrolysis during the MICP process (expected to increase EC). As a result, solution conductivity changes are pH-dependent and will also depend on the balance between the concentrations

of ions being consumed and generated. While such measurements can provide insights regarding urea hydrolysis activity in the absence of added Ca^{2+} and mineral precipitation, caution should be taken when attempting to use such measurements to obtain meaningful insights during cementation treatments.

4.2.5 *Solution pH*

Solution pH measurements provide only a fraction of the geochemical information needed to understand a solution's saturation state, though solution pH has commonly been used to infer the potential for precipitation. This is because while urea hydrolysis in isolation can increase pH values by virtue of ammonia generation and speciation, calcium consumption during $CaCO_3$ precipitation results in proton production and pH decreases when occurring in the absence of continued urea hydrolysis. During MICP treatments, both processes often occur simultaneously, and solution pH can appear to remain constant despite the presence of active $CaCO_3$ precipitation. In fact, when urea is provided in excess, it may not be until near the end of reactions when calcium is finally fully consumed that any pH rise is observed during cementation at all. Modeling and measurements of urea and solution pH changes during stimulation and cementation are presented in Figure 36 and further illustrate this point. As shown for cementation solutions containing 350 mM urea and 250 mM calcium, solution pH increases rapidly once 250 mM calcium is consumed (~250 mM urea degradation) and the remaining 100 mM urea is hydrolyzed with minimal $CaCO_3$ precipitation occurring. From this context, the increase in pH is not indicating a potential for precipitation, but rather is indicative of the end of precipitation due to a lack of calcium. While the authors would not contend that solution pH is entirely useless, as the speciation of carbonate/bicarbonate/carbonic acid and ammonia/ammonium are pH-dependent and pH may have important effects on microbial enrichment, it is suggested that the possibility or inability for $CaCO_3$ to precipitate cannot be inferred from solution pH measurements alone. Instead, such tendencies are governed by saturation state and the activities of calcium and carbonate species. From this perspective, solution pH may provide an indicator of when $CaCO_3$ precipitation is either finished or unlikely, but conversely pH may convey very little information about when precipitation should be expected.

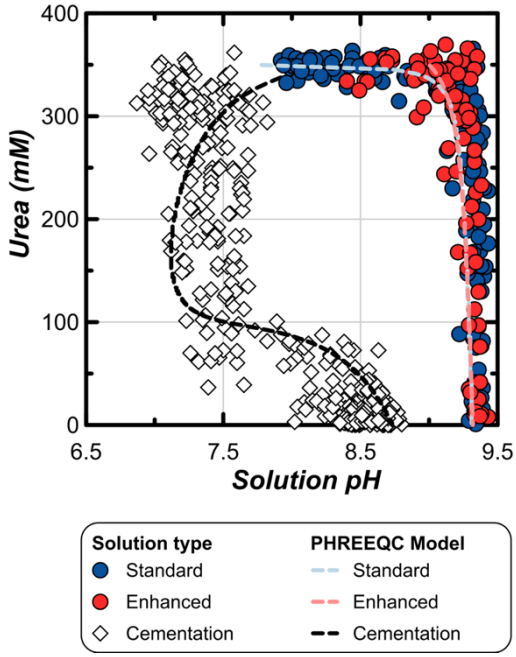

Figure 36. Corresponding urea concentration and solution pH measurements for standard stimulation (i.e., 350 mM urea, no calcium), enhanced stimulation (i.e., 350 mM urea, no calcium), and cementation treatments (i.e., 350 mM urea, 250 mM calcium chloride) with PHREEQC reaction modeling results. Trends show that solution pH remains relatively stable during cementation until supplied calcium is depleted (~250 mM urea degradation) suggesting that solution pH differences alone may provide very little insight about the status of an MICP system, but may be useful towards assessing reaction completion (adapted from Gomez et al. 2018b).

4.3 *Byproduct process monitoring*

Following the MICP treatment process, the quantification and removal of generated ammonium byproducts may be of high priority (Section 3.4). Such concentrations may be removed through post-treatment rinse injections and/or other remediation strategies, however, monitoring and characterization of ammonium concentrations both during and after removal will likely remain needed. A brief summary of several approaches that can be used to monitor ammonium byproducts during MICP treatments and removal processes is provided below.

4.3.1 *Aqueous total ammonium measurements*

Aqueous total ammonium concentrations can be measured using a variety of methods including colorimetric assays and titrations. One of the most common methods employed is a colorimetric assay that utilizes reactions between ammonium and salicylate (Krom 1980), wherein variations in aqueous ammonium manifest in differences in blue colorations that develop between aqueous samples once colorimetric reagents are supplied. Lee et al. (2019a, b) used a method similar to Krom (1980) for measurement of aqueous ammonium concentrations during post-treatment rinsing of bio-cemented soils wherein two reagents (Reagent A & B) were added to dilute sample volumes, samples were allowed to sit for a consistent time period to develop colorimetric differences, and sample absorbance were then measured at 650 nm. Reagent A consisted of 1.9 mM sodium nitroprusside, 811 mM sodium salicylate, 387 mM sodium citrate, and 515 mM sodium tartrate in water. Reagent B consisted of 1.32 mM sodium hypochlorite and 1.5 M sodium hydroxide in water. The working concentration range for the assay can be modified by changing supplied ratios of colorimetric reagents to aqueous samples and/or sample dilution factors depending on the magnitude of ammonium concentrations. While the method quantifies total ammonium (NH_4^+ & NH_3), the specific concentrations of ammonium (NH_4^+) and ammonia (NH_3) may also be determined from such measurements using the pKa of the ammonium/ammonia system when solution pH is known. An example of aqueous total ammonium concentrations measured during post-treatment rinsing was shown earlier in Section 3.4 (Figure 27a).

4.3.2 *Adsorbed ammonium measurements*

Quantification of adsorbed ammonium masses may be of interest in addition to pore fluid ammonium concentrations in many cases. Adsorbed ammonium represents the fraction of positively charged ammonium molecules that are bound to negatively-charged soil surfaces as a result of surface association. Such concentrations although perhaps bound temporarily, merit post-treatment characterization due to the potential for subsequent leaching in time and related impacts on pore fluid concentrations. While a more complete method is described in Lee et al. (2019a), a brief summary of the method is provided here. When quantification of adsorbed ammonium masses are desired, moist soil samples can be destructively sampled, frozen, and stored at -20°C until subsequent chemical analyses can be completed.

Once samples are ready for measurements, soils should be first thawed, and an extraction process should be used to extract and quantify NH_4^+ masses present in soils and pore fluids. First, thawed soil samples are centrifuged to extract free soil solutions. A small sample of the extracted free pore fluid is collected, frozen, and stored at -20° C until NH_4^+ concentrations are measured. Next, a second soil sample of known water content is extracted using a KCl extraction process similar to Keeney & Nelson (1983). In this process, moist soil samples are mixed with a known volume of 2 M KCl solution, allowed to equilibrate for at least 4 hours, and resulting mixtures are centrifuged to remove KCl extracted soil solutions. A small sample of this KCl extracted pore fluid is then collected, frozen, and stored at -20° C until NH_4^+ concentrations are measured. Finally, absorbed ammonium masses can be determined by accounting for NH_4^+ present within free soil solutions as well as adsorbed NH_4^+ masses obtained from the KCl extraction. Adsorbed NH_4^+ masses can then be estimated by subtracting NH_4^+ masses expected from free solution from NH_4^+ measurements obtained following KCl extractions and adsorbed masses can be normalized per gram of dry soil. While other approaches may be used, the key objective of such measurements is to quantify the presence of adsorbed ammonium masses rather than simply aqueous concentrations. As a soil's cation exchange capacity (CEC) increases, larger masses of adsorbed ammonium are possible and therefore adsorbed ammonium quantification may be increasingly critical for sites containing soils with high fines contents. An example of sorbed ammonium masses measured in soil samples following post-treatment rinsing was shown earlier in Section 3.4 (Figure 27b).

4.3.3 *Aqueous calcium measurements*

Monitoring of cementation integrity during the ammonium removal process may be desired when the potential for cementation degradation is identified. Solution calcium concentrations may provide an opportunity to detect $CaCO_3$ dissolution directly, which would elevate solution calcium concentrations. Although calcium ions may be supplied in rinse solutions themselves, when other rinse solution chemistries are used (e.g., KCl additions), calcium concentrations may be monitored during the rinsing process with integration of calcium concentrations over injected volumes allowing for determination of $CaCO_3$ mass losses. When completing such measurements, it may be important to determine baseline calcium concentrations expected in injected solutions and groundwater prior to biocementation treatments and rinse injections in order to resolve dissolution induced changes.

4.3.4 *Shear wave velocity measurements*

Shear wave velocity measurements can also be used to assess cementation degradation during byproduct removal in addition to during cementation treatment (see Section 3.4). Although previous studies have shown that when alkaline, cation-rich rinse injections are supplied to biocemented soils only minimal changes in V_s values are observed (Lee et al. 2019a), differences in groundwater and soil chemistry may merit further monitoring particularly when rinse injections are completed over prolonged time periods and injected volumes are large. Furthermore, when potential oxidation of residual ammonium is of concern, long-term monitoring of shear wave velocity may be used to assess potential impacts on cementation integrity following treatments. Although such measurements do not provide more specific insights regarding solution geochemical changes, such measurements can provide important feedback during implementation of ammonium removal strategies, which can be used to further guide and modify field management efforts to minimize detrimental impacts on cementation integrity.

4.4 *Precipitate characterization*

The impact of MICP precipitation on the improvement of soil engineering behaviors is determined by the: (1) magnitude of precipitation, (2) mineralogy and morphology of the mineral solids generated, and (3) location of the precipitation including its association with particle surfaces and contacts.

4.4.1 *Magnitude of $CaCO_3$*

The magnitude of $CaCO_3$ precipitation achieved in a given soil at the end of treatment can be evaluated by a number of different methods, including pressure chamber reactions (ASTM D4373-21, Gomez et al. 2014, Choi et al. 2016), gravimetric acid washing (Rebata-Landa 2007, Mortensen et al. 2011, Burbank et al. 2013, Zhao et al. 2014, Li 2015), thermogravimetric analysis (TGA) (van Tittelboom et al. 2010, Park et al. 2014a), x-ray diffraction analysis (XRD) (Park et al. 2014b), and others (Chu et el. 2012, Li 2015, Lin et al. 2016a). None of these methods measure soil $CaCO_3$ contents. Rather, they induce some measurable change (e.g., pressure chamber increase, mass reduction, diffraction of x-rays at specified peaks and intensities) as a result of the procedure applied.

Pressure chamber reactions provide a reliable, straightforward, and low-cost method for analyzing relatively large soil samples (dry masses of 5 to 20 g). In this process, an oven-dried soil sample is placed in a sealed vessel of constant volume that is equipped with the capability to measure changes in pressure when $CaCO_3$ is reacted with a relatively concentrated strong acid (e.g., 1-5 M hydrochloric acid) (ASTM D4374-21). In this reaction, $CaCO_3$ is dissolved, producing carbon dioxide gas and a corresponding increase in the pressure inside the vessel. Prior to testing, known reagent-grade calcium carbonate masses are reacted in the same chamber to create a calibration curve. This relationship between $CaCO_3$ masses and pressures generated in the vessel can then be used to interpret the unknown $CaCO_3$ content of some soil sample. The method is non-specific, thus other carbonate and gas-generating minerals can also react with the provided acid and may confound results when more complex soil mineral mixtures are present.

TGA is similarly a relatively straight forward method. In this process, a small dry soil sample of about 30 to 50 mg, is placed in a TGA analyzer and the sample is heated at a constant rate while monitoring mass loss. In process, mineral solids can experience various decomposition reactions dependent on their mineralogy. When calcium carbonate solids are heated to between 600 and 850°C, the mineral is decomposed, releasing CO_2 with only calcium oxide remaining. Ratios between the molecular masses of calcium carbonate and carbon dioxide can be used in combination with the measured mass loss to estimate the soil sample's $CaCO_3$ content. Due to the small sample size used in this process, obtaining a representative subsample is one particular challenge.

XRD is primarily used as a qualitative tool to detect different crystalline mineral phases and the relative ratio of these minerals within some sample. The measurement exposes samples to x-rays at varying inclinations and a detector is used to measure the intensity of the diffraction x-rays as a function of diffraction angles, commonly described by 2θ. From this process, crystalline phases can be identified by comparing observed peaks from some unknown sample to known diffraction angles for specific minerals. This is an inverse problem and requires that the considered mineral phases have at least a few distinct peaks that do not appear in all samples. Calcite mineral has expected diffraction peaks at 23 and 65° and its highest intensity peak at approximately 30°. XRD measurements can be further analyzed using other software packages such as TOPAS, JADE, or EVA, to semi-quantitatively determine relative quantities of minerals

within a sample. Key to this measurement is the preparation of a finely ground sample powder and the addition of some control compound by which the semi-quantitative analysis can be further refined.

ICP-AES, otherwise known as inductively coupled plasma optical emission spectrometry (ICP-OES), can be used to detect particular elements in a given sample. In this process, plasma is used to excite atoms in some sample of interest, and elements can be detected by the characteristic wavelengths that they emit following excitation. For $CaCO_3$ content measurements, a 2 to 15 g oven-dried sample is allowed to react with some acidic solution to dissolve $CaCO_3$ in the sample releasing Ca^{2+}. The resulting fluid can then be analyzed for total Ca^{2+}. From the known added fluid volume and the dry sample mass, the $CaCO_3$ content of the sample can be determined, assuming a 1:1 stochiometric ratio between $Ca^{2+}$and $CaCO_3$ and complete dissolution of all carbonate minerals.

Gravimetric acid washing is a rather crude method that has been used by many researchers presumably due to its low cost, minimal equipment requirements, ability to run many samples, and need for minimal operator experience. In this process, an oven-dried soil sample is weighed and subjected to repeated washing with some strong acid to dissolve and remove carbonate minerals. After, samples are fully reacted, soil solids can be separated from solutions using a fine sieve (e.g., No. 200) to remove all dissolved $CaCO_3$ reaction byproducts. The retained sample is then drained, oven dried, and a final dry mass is obtained. The difference between the initial and final dry mass is then assumed to be the result of $CaCO_3$ masses lost in the specimen. In theory, this approach could account for all carbonate minerals in a sample and thus could be used with success for some soils. However, this method is also susceptible to erroneous mass losses resulting from the rinsing out of fines from a given sample. Thus, the method can frequently result in overestimation of precipitated $CaCO_3$ in natural and more well-graded soils, and would not be recommended for measurements in these materials.

Choi et al. (2017) performed a study comparing the different methodologies described above, where 20 gram dry soil samples were taken at the center of a specimen after an unconfined compression testing. Results from their study are reanalyzed in Figure 37 against the ASTM standard pressure chamber reaction method. XRD, TGA, and the pressure chamber reaction method achieved similar values close to the average of all the methods tested. In the authors' collective experience, the pressure chamber reaction method is recommended due to its efficiency, increased sensitivity at low $CaCO_3$ contents, and ease of use. While many of the other methods can be similarly used with success, acid washing and ICP methods appear to be more susceptible to error and are therefore not recommended.

For all measurement methods it is critical that a baseline $CaCO_3$ content measurement for an untreated soil be obtained and subtracted from post-treatment measurements to more accurately account for potential carbonate contributions from the parent soil material and the loss of fines, among other effects. Further care should be taken to rinse soils prior to measurements to remove other soluble salts that may have resulted from the drying process. For example, deionized water or ethanol can be equilibrated with samples, and subsequently removed before drying and performing measurements. Additional controls are also needed when significant carbonate minerals are present in the parent soil material themselves such as the case for MICP treatment of biogenic carbonate sands.

4.4.2 *$CaCO_3$ mineralogy, composition, & structure*

The mineralogy and composition of achieved precipitate can be evaluated through a variety of different microscale techniques,

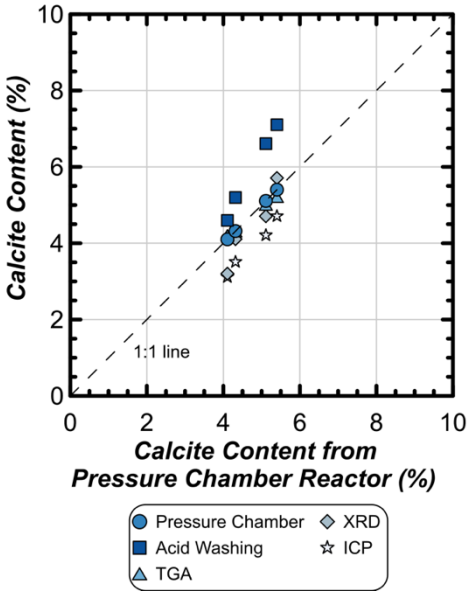

Figure 37. Comparison of different calcite content methods against the calcite content measured from the pressure chamber reactor (data from Choi et al. 2017).

including scanning electron microscopy (SEM), energy-dispersive spectroscopy (EDS), XRD, x-ray computed tomography (CT), and TGA, as discussed earlier in Sections 2 and 3. These methods require and analyze a small soil subsample and therefore evaluation of multiple samples may be needed to ensure representativeness of observations. Application of these techniques is important for a variety of more fundamental reasons but can also be important for pilot studies when ensuring MICP treatment feasibility on sample soils confirming the end state condition achieved in the field, and assessing material permanence

Combined SEM/EDS scans (e.g., Figure 13) provide visual SEM images of the precipitate microstructure enabling identification of mineral morphologies and qualitative evaluation of the spatial distribution of the precipitate while the EDS spatial elemental mapping can be used to confirm the elemental composition of the imaged minerals. EDS line and planar scans from can be used to spatially map expected elements such as calcium present in $CaCO_3$ and silicon present in quartz and other common parent soil minerals. The achieved elemental and visual information can be used to qualitatively assess mineral presence but cannot be used to necessarily confirm mineralogy.

As discussed earlier, XRD analyses can be used to assess the mineralogy of soil samples identifying both the parent soil minerals (e.g., quartz, feldspar) and precipitated cementation (e.g., calcite, vaterite, aragonite). The measurement requires that the sample be ground into a fine powder (< ~100μm) and that the minerals to be identified be crystalline with some definitive material structure and thus distinct diffraction planes. Therefore, for cases such as amorphous $CaCO_3$, which lacks a definitive structure, this method is indeterminant. For such samples, other processes such as Fourier Transform Infrared Spectroscopy (FTIR) may prove more useful. An example of XRD data obtained from biocemented Ottawa F-65 sand samples treated using augmented *S. pasteurii* at 3.4 x 10^8 cells/mL and a solution of 250 mM urea and calcium is presented in Figure 38 (Burdalski & Gomez 2020). As shown, measured XRD diffraction patterns can be used to semiquantitatively fit known diffraction peaks for different $CaCO_3$ mineral polymorphs using various software packages and diffraction databases thereby allowing for mineral quantities by mass to be estimated. In this particular sample, it

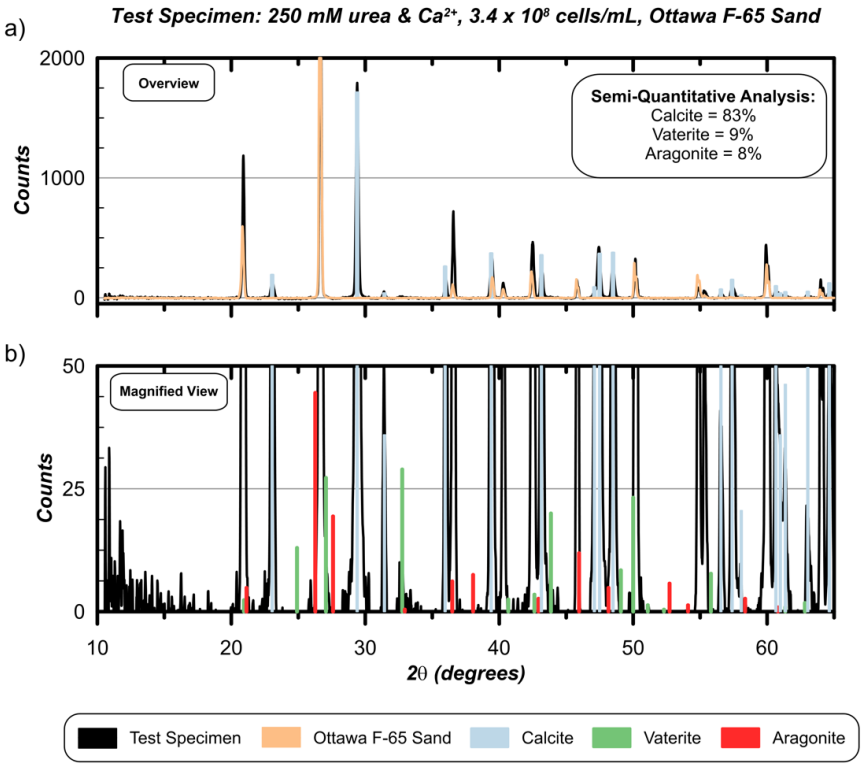

Figure 38. X-ray diffraction measurements from a biocemented Ottawa F-65 test specimen and untreated Ottawa F-65 sand are compared to known reference patterns for calcite, vaterite, and aragonite, with (a) patterns from measurements and calcite shown in an overview and (b) patterns for other mineral polymorphs shown in a magnitude view. From such measurements, semiquantitative analyses can be used to determine compositional differences with the test specimen shown containing ~83% calcite, ~9% vaterite, and ~8% aragonite (adapted from Burdalski & Gomez 2020).

was determined that the material had ~83% calcite, ~9% vaterite, and ~8% aragonite. The observed diffraction patterns are shown in Figure 38a for the biocemented test specimen and the untreated sand along with known values for calcite with smaller known peaks for vaterite and aragonite compared to the biocemented test specimen in a magnitude view shown in Figure 38b. As provided, such mineralogical compositional values may only be accurate to about ±3 to 5%, however, such trends can still provide important insights regarding mineralogical differences, especially between similar test specimens wherein isolated factors are varied (Burdalski et al. 2022a). Lastly, when more precise mineralogical compositional changes are desired, the authors recommend supplementing samples with some standard material at known masses to act as a reference.

Three-dimensional x-ray CT scans (Figure 16) can provide some of the greatest insights regarding the spatial distribution of $CaCO_3$ precipitation within a soil particle structure. With this technology, scanning quality is governed by the maximum achievable image resolution, which is typically about 0.01% of the specimen dimension through which rays are penetrated. Hence, the detection of a $CaCO_3$ coating with a thickness of 5 µm on a soil particle surface, would require a specimen size no larger than 5 mm. Recent work by Roy (2021) has used CT data to analyze the spatial distribution of $CaCO_3$ as well as the effect of this precipitation on soil pore space geometries and overall connectivity. Although infrequently examined, such characterizations can also allow for changes in soil particle microstructure and/or fabric to be quantified. This can include the use of CT reconstructions to evaluate changes in soil particle and bond orientations as has been done by Terzis & Laloui (2018) and others. Observations from CT scans have been instrumental in conceptually understanding how MICP treatment can change the mesoscale soil properties and be used to guide particle-scale based investigations of biocemented soil engineering properties using discrete element codes (PFC3D) as discussed further in Section 6.

While not yet demonstrated extensively, emerging methods including low-field nuclear magnetic resonance (NMR) may provide yet another method to examine soil microstructural changes during the MICP process. For example, Kirkland et al. (2017) found that this method was sensitive to both physical and chemical changes caused by MICP including but not limited to changes in soil pore size distributions, porosities, and permeabilities.

4.5 *Non-destructive monitoring*

Non-destructive monitoring methods can be particularly useful towards evaluating real-time improvements in engineering properties during the biocementation process with no detrimental effects on further experimentation. Such measurements provide the opportunity to assess the current state of some material, thereby allowing for the number of cementation treatments necessary to achieve target criterion to be adapted. Geophysical methods ,such as shear wave velocity (V_s), compression wave velocity (V_p), and resistivity measurements are commonly used to monitor the mechanical improvement that can be realized with MICP. Shear wave velocity and compression wave velocity measurements induce essentially negligible strains (~10^{-6}) within a soil (Santamarina et al. 2001), while resistivity induces no strains. In addition to these other methods, recently, spectrally-induced polarization (SIP) (Saneiyan et al. 2018) has been investigated and shown to be sensitive to the presence of microbial cells (Ntarlagiannis et al. 2005), biofilm formation (Davis et al. 2006), and other biogeochemical processes (Flores Orozco et al. 2011).

4.5.1 *Shear wave velocity measurements*

Shear wave velocity (V_s) measurements have been extensively used to monitor MICP progression due to their sensitivity to changes in soil particle contact stiffnesses, their direct relation to soil small-strain shear modulii ($G_{max} = \rho V_s^2$), and general insensitivity to pore fluid saturation conditions. In the laboratory, V_s measurements can be obtained by measuring the time required for a shear wave to propagate a known distance between a pair of bender elements, which are typically constructed from piezoceramic materials (Stokoe et al. 1985, Lee & Santamarina 2005a). When completed appropriately, bender element measurements yield V_s values that are consistent with resonant column measurements (Brignoli et al. 1996, Lee et al. 2005).

V_s measurements have been widely used as an effective tool to monitor the progressive improvement realized with each MICP treatment and relationships between soil $CaCO_3$ contents. Figure 39 presents results from a range of studies wherein soil type, confining stresses, testing length scales, and biological and cementation treatment schemes (open symbols are bioaugmentation, closed symbols are biostimulation) were all varied. As shown, laboratory experiments include results from studies involving simple shear, triaxial, and 1D rigid column specimens. Upscaling experiments include 1g models with length scales ranging from 0.5 to 3.7 m. System level experiments include results from models tested on 1-m and 9-m radius centrifuges. As evident, there is clear proportionality between soil $CaCO_3$ contents and shear wave velocities invariant of testing length scales, confining stresses, soil types, and treatment schemes. However, the amount of V_s increase per percent soil $CaCO_3$ by mass can vary considerably between studies. The source of this variability is difficult to isolate due to the many inconsistencies between these studies, however, important differences affecting these relationships likely include differences in soil composition (classification, mineralogy, grain size distribution, grain shape), prepared initial state (density, coordination number), preparation method (moist tamped, air pluviation), treatment scheme (formulations, stimulated versus augmented), and confining stress conditions during cementation (confining stress, isotropic versus one-dimensional).

This same data set can be presented as a change in shear wave velocity (ΔV_s) versus soil $CaCO_3$ by mass, as shown in Figure 40, which removes some dependence of these measurements on the initial specimen conditions prior to treatment. Additional analysis of a data subset controlling for soil and experimental design showed that the ΔV_s per percent calcite is not dependent on whether stimulation or augmentation was used.

Figure 41 presents the same data set binned on the basis of fines content and D_{10} values. Clean soils, defined as having less than 3% fines, have a larger V_s increase per $CaCO_3$ content than sands with greater fines contents. This is reasonable as higher fines content can reduce precipitation efficiency due to sorption of calcium ions to clay mineral surfaces (Gomez & DeJong 2017) and the overall soil skeleton stiffness. The same trend is observed by separation according to the D_{10} values. As shown, the rate of V_s increase per $CaCO_3$ content increases as the D_{10} increases. This apparent trend may result from the correlation between D_{10} values and fines contents, however, it may also reflect other physical mechanisms including but not limited to differences in soil particle coordination numbers and cementation magnitudes at each particle contact.

4.5.2 *Compression wave velocity measurements*

Compression wave velocities are a function of the constrained modulus ($M = \rho V_p^2$) with sensitivity to the degree of pore fluid saturation, soil Poisson's ratio, and Young's modulus (Weil et al. 2011). Consequently, the utility in V_p for monitoring MICP improvement can be obscured by saturation conditions.

Weil et al. (2011) observed that V_p only began to increase significantly once the bulk modulus of the soil skeleton became comparable to that of the pore fluid (i.e., governed by the stiffness of water wherein V_p = ~1480 m/s, Lee and Santamarina 2005b). At low cementation, the compression waves primarily travel through the pore fluid causing the V_p to be close to 1500 m/s under fully saturated conditions and insensitive to changes in cementation. At higher cementation levels, the stiffening of the soil skeleton can then be detected by V_p as compression wave velocities become increasingly influenced by the cemented particle matrix. This phenomenon was further explored by cycling the saturation conditions of a cemented soil while measuring V_s and V_p concurrently. Figure 42a shows observed V_s and V_p seismic wave velocities during dry and saturated conditions (Weil et ail. 2011). While the V_s measurements remain relatively constant, there is a noticeable difference in V_p, with the V_p of the dry specimen clearly increasing from about 280 to 1400 m/s with increases in $CaCO_3$ contents while the V_p under saturated conditions begins at 1500 m/s and gradually increases to about 1900 m/s.

The evolution of Poisson's ratio (ν) with increasing cementation, determined through measurements of V_s and V_p using Equation 18, can also be determined for both dry and saturation conditions. Figure 42b shows the effect of saturation on Poisson's ratio, with the Poisson's ratio being higher for the saturated condition than the dry condition for all cases, but with values decreasing with cementation level increases. Specifically, as $CaCO_3$ content increased, the Poisson's ratio for the saturated condition decreased from 0.50 to 0.43. For the dry condition, the Poisson's ratio appeared to initially increase from 0.3 to 0.38 with cementation, but then decreased to 0.33. A reduction in Poisson's ratio with increasing cementation is consistent with measurements by Gercek (2007) where the Poisson's ratio for calcite was 0.31 but for intact sandstone, which can be thought of as an analog for biocemented sands, the ratio ranged from 0.05 to 0.4.

$$\upsilon = \frac{0.5\left(\frac{V_p}{V_s}\right)^2 - 1}{\left(\frac{V_p}{V_s}\right)^2 - 1} \tag{18}$$

The ratio of V_p/V_s for both saturated and dry conditions versus V_s is plotted in Figure 42c. As evident in the broader literature (Kramer 1996), this ratio increases as the Poisson's ratio increases. As shown, data by Weil et al. (2011) for soils of varying cementation agreed well with these expected trends under both saturated and dry conditions. Such trends also further confirmed that the observed Poisson's ratio differences with higher cementation contents were also largely reasonable given the related changes in V_p/V_s ratios.

4.5.3 *Resistivity measurements*

Direct and indirect resistivity measures are directly dependent on how strongly a soil resists electric current, which in turn is dependent on numerous factors including soil porosity, mineral composition, pore fluid composition, interactions at the soil particle surface, pore fluid saturation, and soil fabric. The biogeochemical and mechanical changes that occur during a single MICP treatment cycle and over a treatment program can make it difficult for resistivity measurements to reliably discern specific changes (e.g., chemical reaction progression versus amount of $CaCO_3$ precipitated). Nonetheless, its potential for tracking specific parameters has been demonstrated.

Direct resistivity measurements can be readily implemented by measuring the induced voltage between an electrode array (Rinaldi et al. 2006) and can be effective in monitoring isolated soil changes when other conditions (including pore fluid

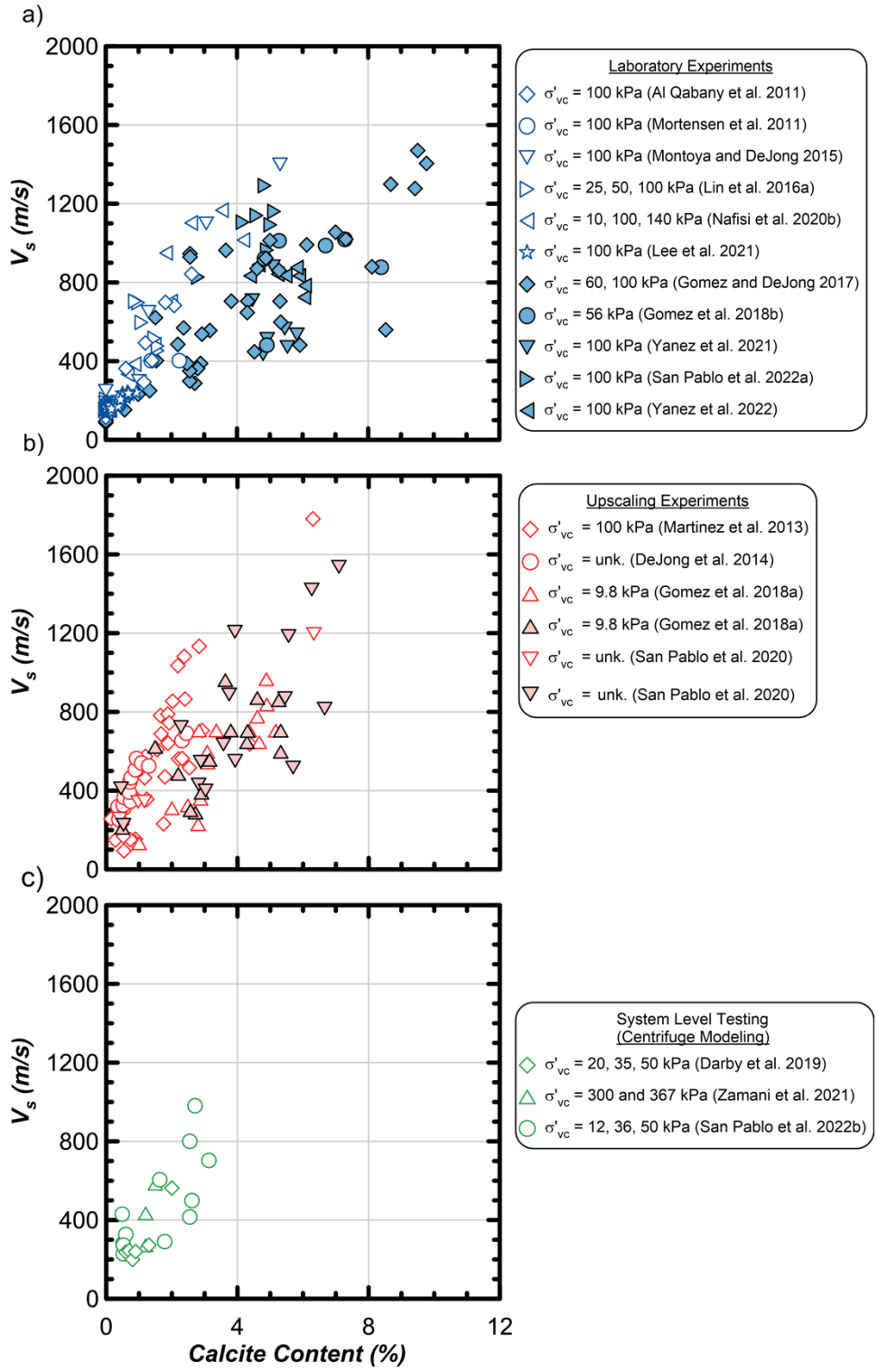

Figure 39. Shear wave velocity versus calcite content measurements from (a) laboratory experiments, (b) upscaling experiments, and (c) system level testing in the centrifuge (closed symbol = stimulated, open symbol = augmented).

chemistry) remain constant. For MICP treatments, it can be difficult to monitor soil improvement since the chemical composition of the pore fluid is continuously changing in a complex manner (DeJong et al. 2009). Weil et al. (2011) was unable to detect significant and reliable changes that correlated with $CaCO_3$ precipitation during MICP treatments. However, changes that occur during the treatment enrichment stage, such as during stimulation, may offer some possibility for improved monitoring. During stimulation, the conductivity (inverse of resistivity) of a given treatment solution gradually increases as ureolysis progresses due changes in the presence of charged species (ammonium and carbonate). As an example, Whiffin (2004) used measured pore fluid conductivity rates to estimate urea hydrolysis rates. During cementation, however, monitoring with direct conductivity can be complicated by the continuous precipitation of $CaCO_3$ which can accordingly decrease conductivity. This is shown in Gomez (2017) wherein the ionic strength of a cementation solution was essentially constant

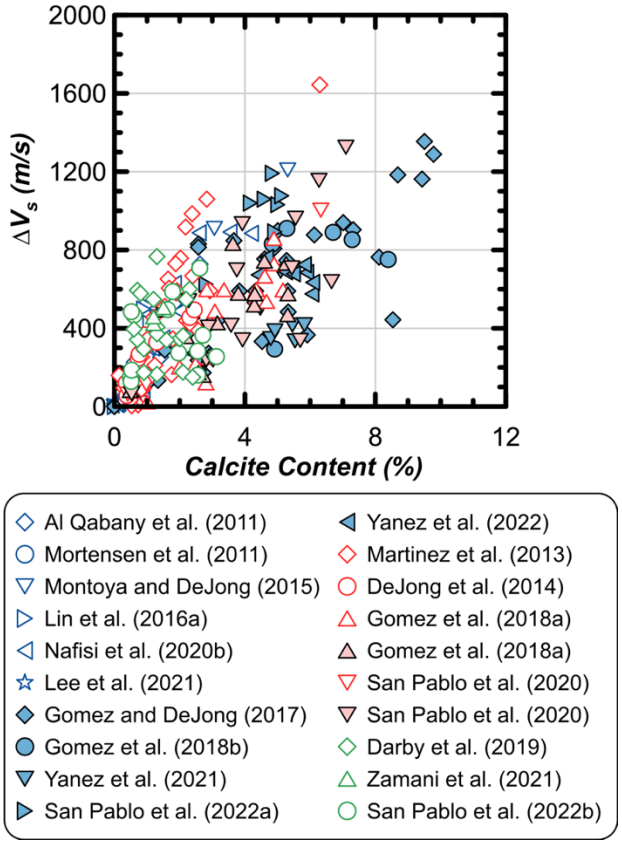

Figure 40. Increase in shear wave velocity versus calcite content for the same set of experiments shown in Figure 39 differentiated by testing length scales and reported enrichment method (closed symbol = stimulated, open symbol = augmented).

during the cementation process due to the production of ammonium and carbonate species and simultaneous consumption of calcium and carbonate ions. However, if employed urea to calcium concentration ratios significantly exceed 1:1, it may be possible to detect when the calcium concentration has been depleted and excess urea is being consumed, thus generating excess ammonium ions in solution.

Indirect resistivity measurements can be obtained using spectrally-induced polarization (SIP), which has been used in the past for mineral exploration (Moon et al. 2006) and most recently in near surface environmental applications (Williams et al. 2009, Flores Orozco et al. 2012, Ntarlagiannis et al. 2016). In SIP, the conductivity magnitude and phase are measured and analyzed to determine the real and imaginary components of complex conductivity, wherein the real component represents energy loss while the imaginary component provides some insights regarding the energy stored. More specifically, complex conductivity measurements and polarization signals may provide information about precipitation magnitudes and crystal sizes which influence the polarization magnitude and relaxation times, respectively (Wu et al. 2010). Saneiyan et al. (2018) further suggested that SIP can allow for more long-term monitoring due to its sensitivity to both carbonate mineral formation and dissolution. A proof-of-concept experiment was conducted by Saneiyan et al. (2019) where an aquifer was stimulated in a 15-day field-scale MICP project. SIP was shown to have the potential to spatially and temporally track the progression of MICP in the treated zone at this site.

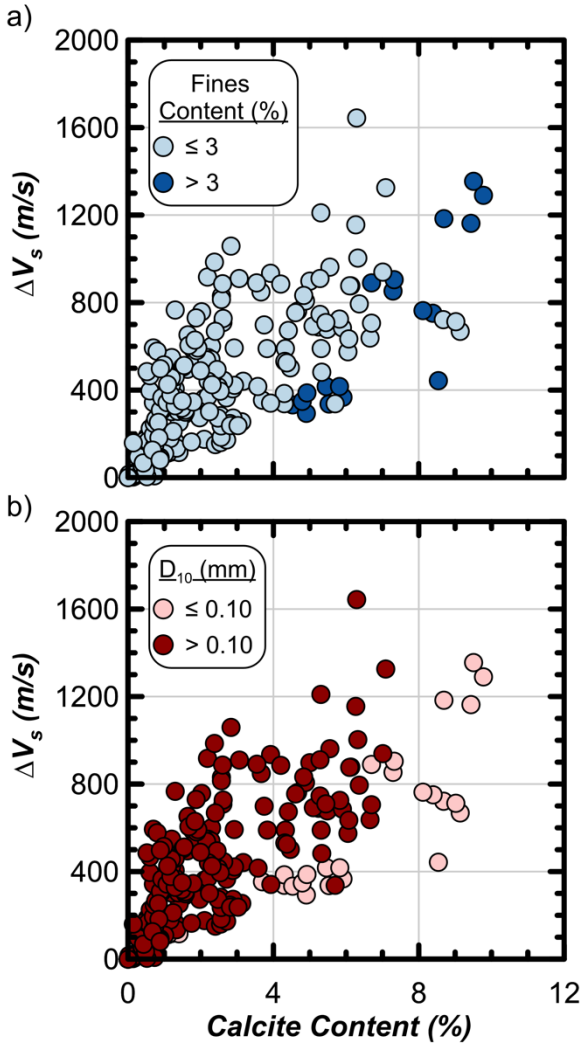

Figure 41. Comparisons of increases in shear wave velocities versus calcite contents grouped by (a) fines contents and (b) D_{10} (mm).

4.5.4 *Hydraulic conductivity measurements*

Calcite precipitation can reduce the hydraulic conductivity (k) of a soil, with the magnitude being dependent on the amount and spatial distribution of the precipitation. Consequently, changes in hydraulic conductivity can be used as an indirect indicator of the magnitude of $CaCO_3$ precipitation but can also indicate when $CaCO_3$ precipitation is occurring non-uniformly, which can lead to localized clogging and/or increased injection pressures during treatments.

Baek et al. (2022) performed a series of tests in rigid columns equipped with differential pore pressure measurements from within the test specimen. Hydraulic conductivity was determined through differential pressure transducer (DPT) measurements obtained during steady state flow and during falling head tests, with the latter expected to be adversely influenced by clogging in the device plumbing and/or near the injection or extraction specimen boundaries. MICP treatments were performed once daily until a total $CaCO_3$ content of about 20% was achieved. Tests were performed on poorly graded soils with D_{50} values of 0.18, 0.51, 1.39, and 2.74 mm (100A, 100B, 100C, 100D), and final conditions at the end of treatment are shown in Figure 16.

Figure 43 presents variations in hydraulic conductivity with respect to the $CaCO_3$ contents, along with results from previous studies on clean sands (e.g., Al Qabany & Soga 2013, Martinez

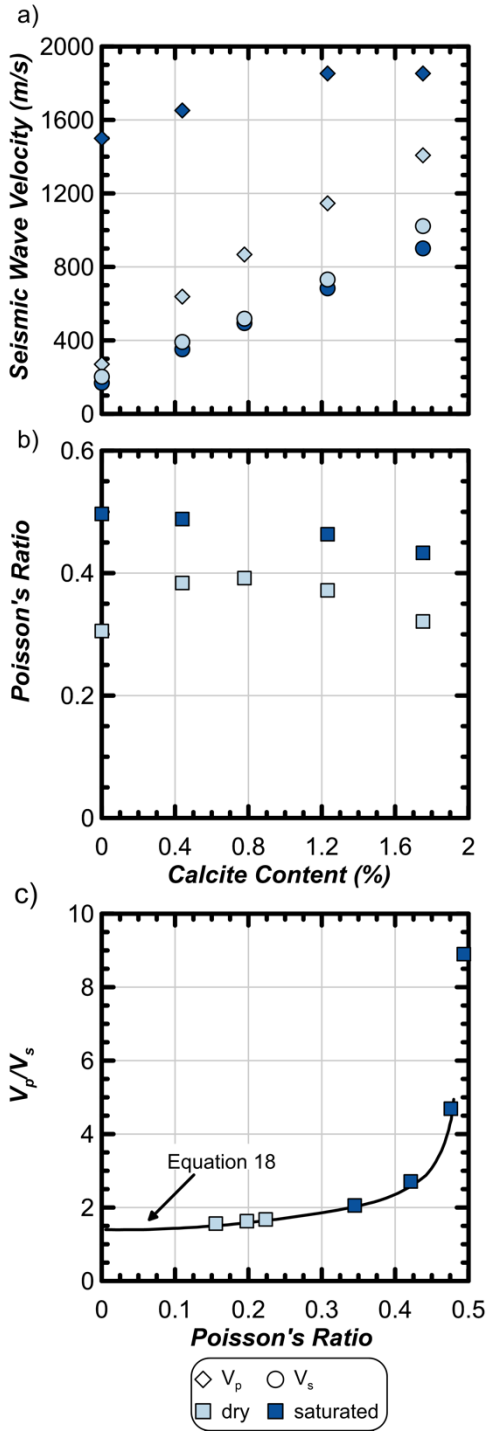

Figure 42. Changes in (a) seismic wave velocity and (b) Poisson's ratio with calcite content and (c) relationship between V_p/V_s ratio and Poisson's ratio (data from Weil et al. 2011.).

et al. 2013, Gomez & DeJong 2017). Continued $CaCO_3$ precipitation causes gradual reductions in k in all sand columns up to a $CaCO_3$ content of ~25% (Figure 43a). Figure 43b presents variations in k normalized by its initial value, k/k_o, with respect to $CaCO_3$ content. $CaCO_3$ precipitation of ~20% only causes a reduction in k of less than one order of magnitude (<70%). The pore-scale imaging of the $CaCO_3$ precipitation achieved also further corroborated this minimal reduction in k. This is consistent with the observed changes at the pore scale, as evident in Figure 16, and in measured $CaCO_3$ content distributions along the length of the columns.

Changes in D_{50} showed an insignificant effect on the normalized reduction rate in *k* for the tested sands that were uniformly graded with C_u values of less than 1.8. Importantly, in fine sands (100A and 100B) the k values measured by the falling head method begin to deviate from the k values obtained by the DPT when $CaCO_3$ contents >10%, indicating local clogging likely occurring near the specimen boundaries and/or in the device plumbing.

Comparison of trends with previous studies (Al Qabany & Soga 2013, Martinez et al. 2013, Gomez & DeJong 2017) show that prior results indicate much more significant k reductions. This significant difference could possibly be attributed to two primary mechanisms. First, the treatment formulation could have triggered initial precipitation in the pore space, which then sedimented by gravity near pore throats forcing accelerated reduction in k. Second, localized precipitation may have

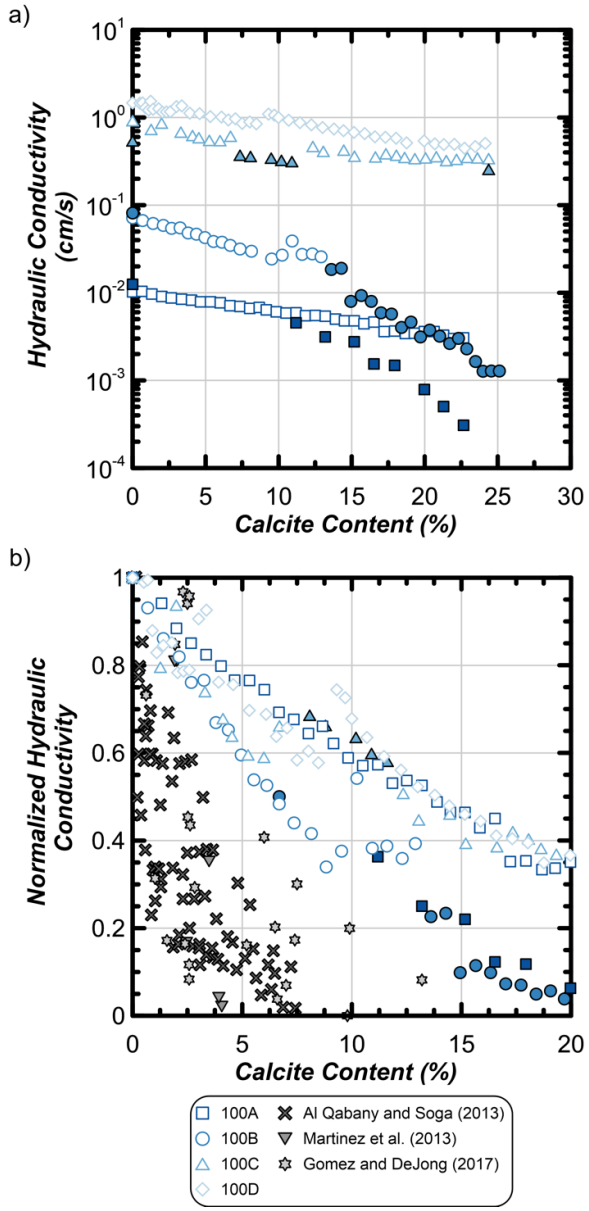

Figure 43. Variations in (a) hydraulic conductivity and (b) normalized hydraulic conductivity with an increase in calcite content for different soils. Note the open symbols are measured by using the differential pressure transducer or the piezometers connected to two ports at the column wall, and the solid symbols are measured by using the falling head method (adapted from Baek et al. 2022).

occurred near the injection and/or extraction boundaries, or within the device plumbing, resulting in a localized regions with reduced k and misinterpretation of the actual global k values.

The observed trends can be reasonably modeled with a family of Kozeny-Carman models. Specifically, the Kozeny grain-coating model can be used which correlates k/k_o with the pore volume fraction of calcite S_{cc}:

$$k/k_O = (1 - S_{cc})^{n+1} \quad (19)$$

where n is the power exponent (Kleinberg et al. 2003, Noh et al. 2016, Baek et al. 2019). This model is simple but robust, and the model with n = 2 is identical to the original Kozeny-Carman model. Figure 44 shows the model predictions while varying the empirical power exponent n, with n = 2 to 6 reasonably capturing the observed k reductions. Previously published data show more significant k reductions, hence an n > 10 is required for agreement with the previously reported data and may be again somewhat confounded by the above testing limitations.

4.6 *Cone penetration test measurements*

Cone penetration (CPT) tip resistance, q_c, is directly dependent on soil stiffness and strength (Lunne et al. 1997), and is therefore effective in estimating a wide spectrum of geotechnical engineering parameters (e.g., relative density, friction angle, stiffness, compressibility) capable of predicting engineering performances, including liquefaction triggering (e.g., Idriss & Boulanger 2008, Boulanger & Idriss 2014). For these reasons, CPT soundings are frequently used to (1) evaluate initial baseline site conditions and design the soil improvement programs, including the treatment zone extent and desired improvement magnitude, by performing soundings prior to an improvement program and (2) verify improvement effectiveness by performing additional soundings after the improvement program has been completed. The efficacy of the CPT in evaluating improvement maps directly to how MICP improves soils, with CPT q_c and V_s being the most effective measures of detecting interparticle cementation and verifying treatment effectiveness.

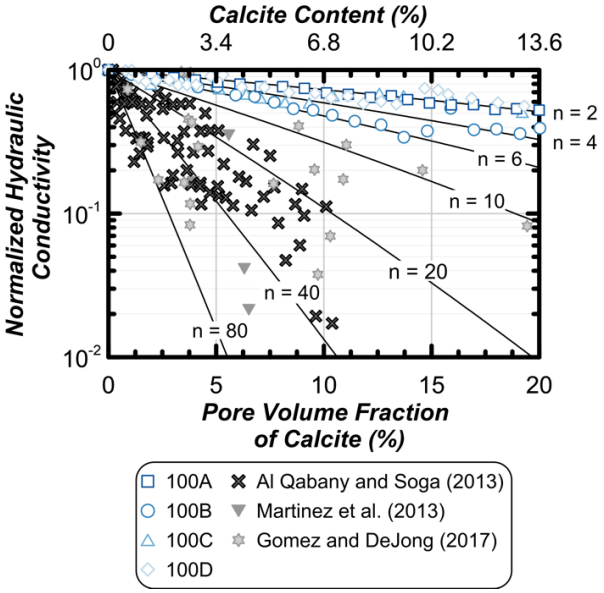

Figure 44. Reduction in hydraulic conductivity (k/k_o) with respect to pore volume fraction of calcite (S_{cc}). The curves are plotted with Kozeny grain model: $k/k_o = (1 - S_{cc})^{n+1}$. *CC* at the upper x-axis is calculated from the S_{cc} assuming *e* of 0.667 and $G_{S\,calcite}$ of 2.71 (adapted from Baek et al. 2-22).

The effectiveness of CPT measurements to evaluate MICP improvement has been primarily performed in large 1-g tank tests and in centrifuge tests. Gomez et al. (2018a) performed MICP treatment on two large 1g tank tests, with CPT soundings performed pre- and post-treatment in the sand layer to determine how q_c relates to $CaCO_3$ content. CPT q_c measurements were obtained across a range of soil $CaCO_3$ contents, from untreated to 5.3%, as the overall test objective was to achieve a cementation gradient across the tested specimens. The average mid-depth CPT q_c measurements respectively increased from a baseline value near 3.6 MPa to a maximum value of 32.1 MPa.

Darby et al. (2019) (described in more detail in Section 7) measured CPT q_c pre-treatment, post-treatment, and following select shaking events in the 1-m radius centrifuge at the Center for Geotechnical Modeling at the University of California, Davis. Three different treatment levels were investigated: including

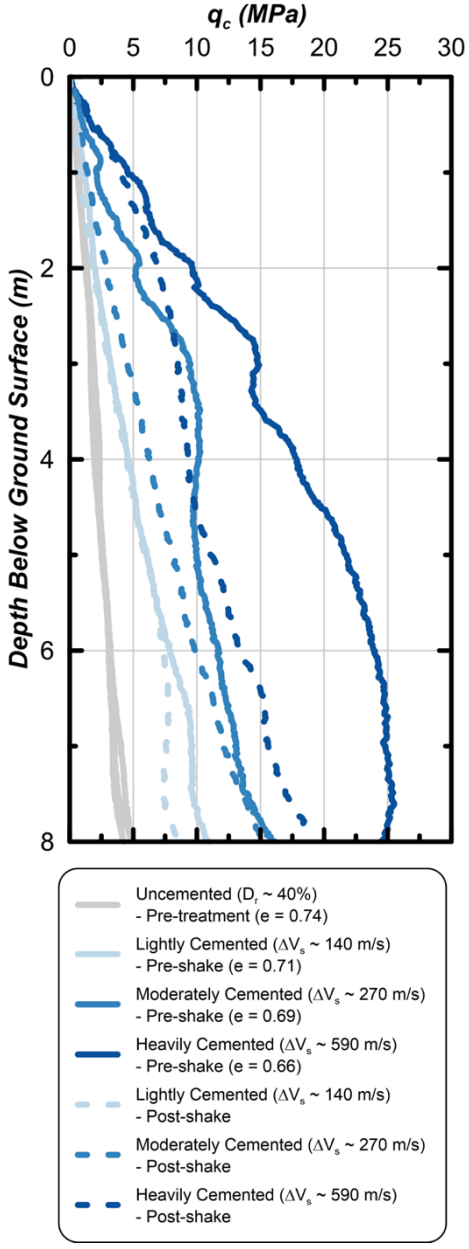

Figure 45. q_c profiles in untreated, lightly cemented, moderately cemented, and heavily cemented centrifuge models for the initial soil conditions as well as prior to shaking and after all shaking was completed (adapted from Darby et al. 2019).

lightly cemented (ΔV_s = 140 m/s), moderately cemented (ΔV_s = 270 m/s), and heavily cemented (ΔV_s = 590 m/s). Figure 45 presents representative CPT q_c profiles for untreated, after MICP treatment to various treatment levels, and following numerous shaking events that triggered liquefaction and degraded the cementation. The CPT q_c increased due to MICP treatments relative to the uncemented condition, and then degraded following severe shaking. For example, at 4 m depth, q_c for the lightly, moderately, and heavily cemented models increased by a factor of 2.2, 4.3, and 9.1, respectively. Following shaking, however, the respective q_c values largely decreased with improvement factors of only 2.1, 2.6, and 4.8, respectively. Despite MICP degradation following numerous shaking events, the q_c at the end of the tests remained higher relative to the initial uncemented condition, indicating that MICP at higher magnitudes could permit more permanent changes to q_c. These results are consistent with that observed more recently by San Pablo et al. (2022b) in similar centrifuge tests.

Given the observed dependence of q_c on cementation level shown in Figure 46, and the dependence of V_s on cementation level shown earlier (Figure 39), it is logical that q_c and V_s are also correlated. Compiled results from 1-g and centrifuge tests where q_c, V_s, and $CaCO_3$ content were measured are shown in Figure 46. As evident, both q_c and V_s are correlated with $CaCO_3$ content, albeit it with some scatter. Nonetheless, trends show V_s to increase more rapidly than q_c with $CaCO_3$ content, particularly at low cementation levels. Direct comparison of q_c versus V_s, shown in Figure 46c, captures the relative rates of improvement. In aggregate, this data indicates that V_s is more sensitive than q_c for cementation levels less than about 3% $CaCO_3$ content by mass, while at higher cementation levels both measures are comparably sensitive to added cementation. The changes in q_c and V_s relative to their respective uncemented baseline values, shown in Figure 47, further clarifies this relationship. Again, V_s is more sensitive at low cementation levels than q_c, while both track added cementation effectively at higher cementation levels.

The influence of increased stiffness and strength for cemented sands can be evaluated together considering the ratio of the small-strain modulus, G_0, to q_c (Eslaamizaad & Robertson 1996, Schnaid et al. 2004). As evident in Figure 48a, the ratio measured in 1-g and centrifuge tests increases to a value of about 30 at 0.5% $CaCO_3$ content and asymptotically approaches a value of about 60 at 5% $CaCO_3$ content. The small strain rigidity index (K_G), adapted from Rix & Stokoe (1991) by Schneider & Moss (2011), explicitly accounts for the impact of both relative density and effective stress on q_c, and is defined as:

$$K_G = \frac{G_O/q_c}{(q_{c1N})^{-0.75}} \quad (20)$$

with the stress normalized penetration resistance, q_{c1N}, defined as $q_{c1N} = (q_c/p_a)/(\sigma'_{vo}/p_a)^{0.5}$ where p_a is atmospheric pressure and σ'_{vo} is the vertical effective stress. For the centrifuge tests conducted by Darby et al. (2019), the corresponding average K_G factors for these soil profiles are 117, 1133, 2048, and 4117 for cementation levels of 0, 0.8, 1.33, and 2.18%. Figure 47b presents results from 1-g and centrifuge tests for K_G versus $CaCO_3$ content. For reference, K_G values between 110-330 are representative of Holocene and uncemented sands, whereas K_G values between 330 and 1100 represent aged, cemented, and calcareous sands (Schneider & Moss 2011). Figure 48b shows uncemented tests to agree well with the range proposed by Schneider & Moss (2011), while most of the MICP cemented values are above a K_G of 1100, indicating a strong microstructure due to cementation and bonding that likely exceeded that considered when developing the original K_G framework.

Figure 49 presents the soil behavior type charts from Robertson et al. (1995) and Robertson (2016) where G_o/q_c is again used to differentiate the presence of cementation. Both charts successfully delineate uncemented soils from cemented soils, and furthermore the normalized parameters systematically track increasing cementation. These results are encouraging and suggest that existing CPT-based methods for identifying and quantifying cementation in sands can be directly applicable to and effective for MICP improved sands.

5 EXPERIMENTAL INVESTIGATIONS OF STRESS-STRAIN BEHAVIOR

Biocementation of sands fundamentally changes conditions at the particle scale, which map directly to distinct and significant

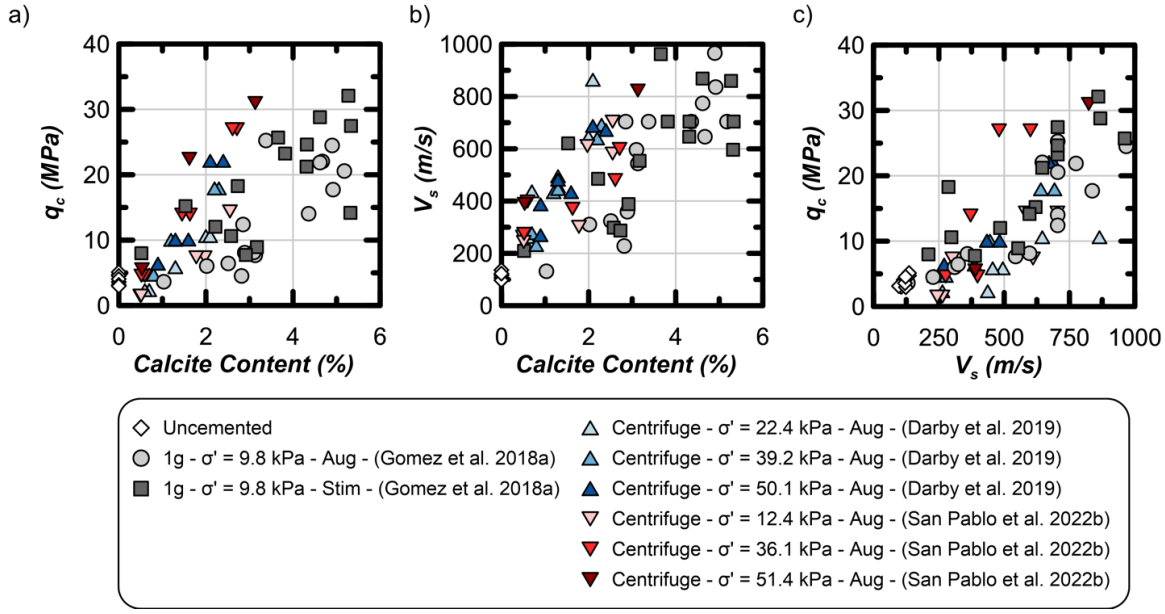

Figure 46. q_c, V_s, and calcite content relationships of data compiled from 1-g tank tests (Gomez et al. 2018a) and 1-m radius centrifuge tests (Darby et al. 2019, San Pablo et al. 2022b).

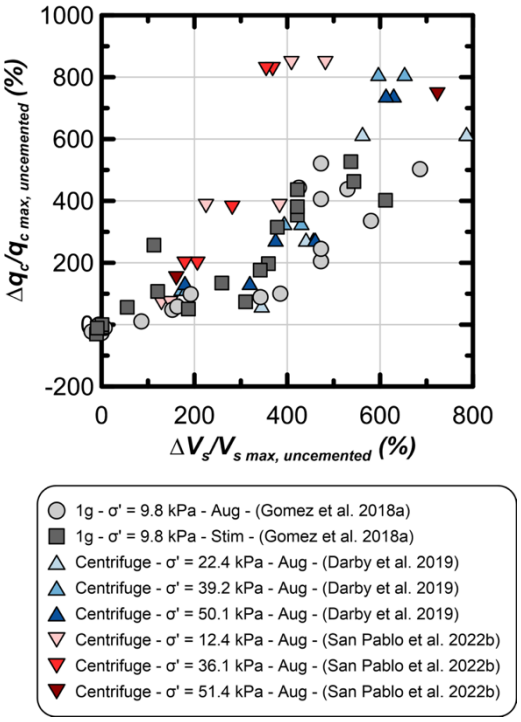

Figure 47. Δq_c and ΔV_s relationships of data compiled from 1-g tank tests (Gomez et al. 2018a) and 1-m radius centrifuge tests (Darby et al. 2019, San Pablo et al. 2021b).

changes in element behavior when subjected to monotonic or cyclic loading. As detailed in Section 2.4, precipitation within the soil matrix on particle contacts and exposed particle surfaces results in a variety of important microstructural changes including: (1) cementation of particle-particle contacts, (2) densification, and (3) increased particle angularity. The following section is not an exhaustive review of past experimentation, but rather provides a summary of the primary mechanical behaviors of biocemented silica sands relative to untreated silica sands.

5.1 *Small-strain dynamic behaviors*

Cementation at particle contacts directly increases the soil matrix shear stiffness as evidenced by the linear increase in the shear wave velocity in proportion to the amount of $CaCO_3$ precipitation (up to ~10% CC) which indicates that non-destructive shear wave velocity measurements are an effective real-time cementation monitoring method (Section 4.4). The presence of cementation also results in significant changes to the strain dependent shear modulus degradation and damping curves. However, the magnitude of these changes depends on cementation levels and confining stresses, among other variables. Although shear wave velocity measurements can effectively measure initial small-strain shear stiffness (G_{max}) changes, resonant column testing can provide more comprehensive insights into how cementation changes dynamic small-strain soil properties relevant to site response changes.

Figure 50 presents results of resonant column tests performed on Ottawa F-65 sand prepared to an initial D_r of 61% and treated to various levels of cementation with confining stresses of 30 and 100 kPa. Varying cementation levels were achieved through consecutive MICP treatment of untreated sand specimens, which resulted in shear wave velocity increases between ~100 and 350 m/s, corresponding to $CaCO_3$ contents between 0.5 to 3.6%, respectively. Tests were performed using 50 mm diameter specimens that were augmented and received

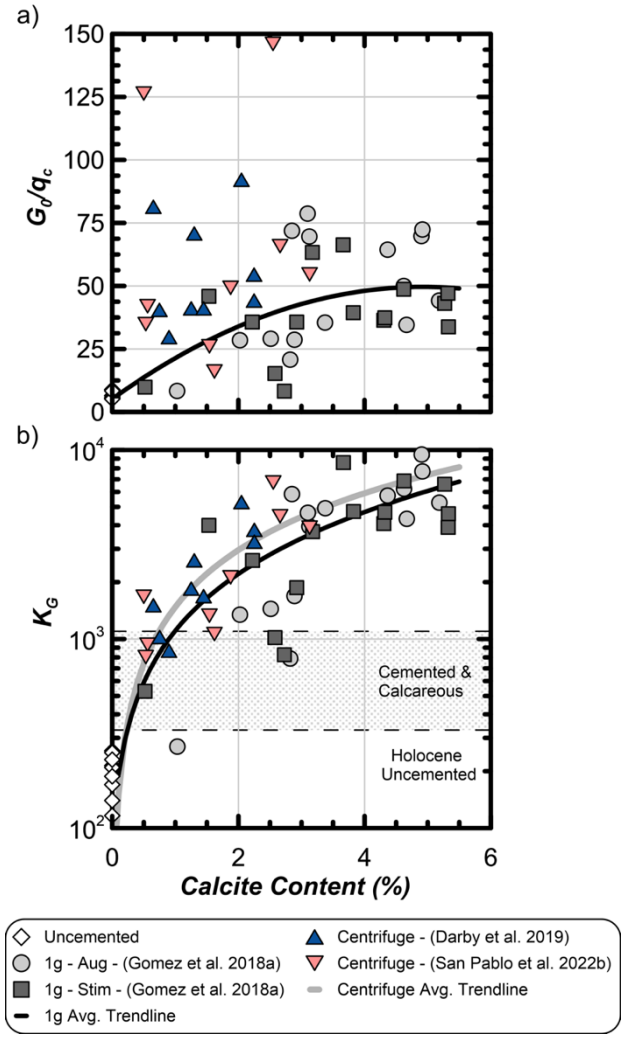

Figure 48. (a) (G_o/q_c) and (b) K_G versus calcite content of data compiled from 1-g tank tests (Gomez et al. 2018a) and 1-m radius centrifuge tests (Darby et al. 2019, San Pablo et al. 2022b).

cementation treatments under a constant confining stress in a resonant column (RC) device (GDS Instruments, further described in Na et al. 2022). It is noted that for specimens with higher cementation-induced initial stiffnesses, the maximum strain levels achievable in the RC device became more limited (i.e., elastic shear strain threshold decreased with increasing cementation).

The effect of cementation on the modulus reduction curves is immediately evident in Figures 50a and 50d, with G_{max} being proportional to the achieved $CaCO_3$ contents, and secant G progressively decreasing with increased strain. The threshold shear strain at which the modulus reduction begins ($G=0.99*G_{max}$) decreases as cementation increases. This is more evident in the normalized G/G_{max} curves in Figures 50b and 50e. The increase in G_{max} follows a systematic trend with the relative magnitude being proportional to the level of cementation similarly to what is seen for the V_s measurements. For example, for the tests performed at 100 kPa confinement, the strain corresponding to $G/G_{max} = 0.5$ decreases from 0.1 to 0.07 to 0.02 to 0.01% as the cementation level is increased from 0 (ΔV_s = 0 m/s) to 0.5 (ΔV_s = 91 m/s) to 2 (ΔV_s = 251 m/s) to 3.6 (ΔV_s = 350 m/s) $CaCO_3$ by mass. The threshold shear strain also decreases systematically from roughly 0.002% for the uncemented case to 0.001, 0.0006 and 0.0002% for cementation levels of 0.5, 2 and 3.6% $CaCO_3$ by mass. This is presumably attributable to the brittleness of the $CaCO_3$ cementing agent. The

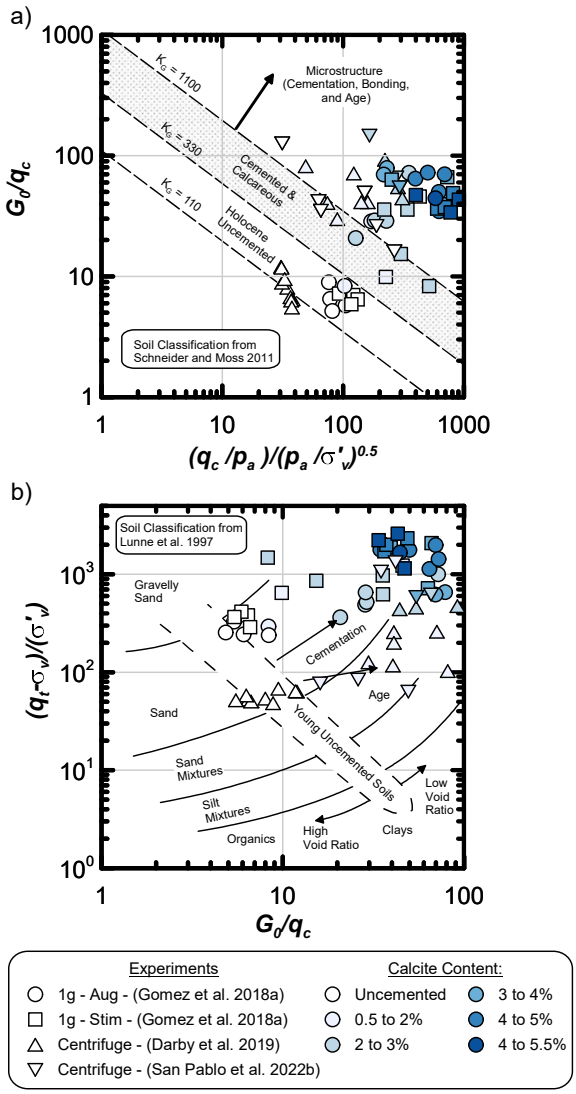

Figure 49. (a) (G_o/q_c) and (b) K_G versus calcite content of data compiled from 1-g tank tests (Gomez et al. 2018a) and 1-m radius centrifuge tests (Darby et al. 2019, San Pablo et al. 2022b).

effect of confining stress leads to an increase in G_{max} and a shift in G degradation to the higher strain levels, as shown in Figure 51a. The increase in confinement also extends the range the shear strains that remain elastic, as shown by the threshold shear strain increasing from about 0.0002% for a confinement of 30 kPa to 0.0008% to a confinement of 200 kPa (Figure 51b).

The corresponding effect of cementation on soil damping is shown in Figures 50c and 50f. At very small strains, the minimum damping increases with cementation when compared to the uncemented soil. At strains greater than the threshold shear strain, damping begins to increase at lower strains in the most highly cemented specimen followed by lower cementation levels and the uncemented case. For example, for specimens at 100 kPa confinement, the shear strain corresponding to 2% damping occurs at shear strains of 0.035, 0.01, 0.006, and 0.00025%, for the 0 (ΔV_s = 0 m/s), 0.5 (ΔV_s = 91 m/s), (ΔV_s = 250 m/s), and 3.6% (ΔV_s = 350m/s) $CaCO_3$ specimens, respectively. Additionally, as confinement increases the degradation of cementation is suppressed until larger shear strains are achieved. This is reflected by an increase in the threshold shear strain, as shown in Figure 51b. However, above the respective threshold shear strain the rate of modulus degradation appears to increase with $CaCO_3$ content. These trends are largely consistent with a broader understanding of dynamic soils properties for cemented soils from past studies (e.g., Acar & El-Tahir 1986, Delfosse-Ribay et al. 2004, Dupas & Pecker 1979, Haeri et al. 2005, Saxena & Reddy 1987, Saxena et al. 1988, Simatupang et al. 2018, Tsai & Ni 2012).

The dependence of the small-strain shear modulus on confining stress decreases with increasing cementation; at low cementation levels, the shear modulus closely follows the stress dependence documented for uncemented soils (Hardin & Black 1968, Stokoe et al. 1985), but becomes essentially independent of confining stress for cementation levels above about 7% $CaCO_3$ (or a ΔV_s of about 650 m/s). Figure 52 presents results from bender element measurements obtained in both triaxial and centrifuge model experiments for a range of cementation levels subjected to multiple confining stress unloading and reloading cycles between about 1 and 80 kPa. As the cementation level decreases, two observations are evident. First, stress cycling gradually degrades the initial stiffness and integrity of the cemented soils, resulting in G decreasing. Second, the dependence on confining stress increases as the cementation level decreases, as evidenced by the increasing slope of G with confining stress.

These results show that, with increasing cementation, initial shear moduli increase and threshold shear strains decrease, collectively resulting in the G/G_{max} and damping curves shifting to lower strain levels. Further, the effect of confinement on cementation integrity as well as modulus reduction and damping curves is diminished as cementation levels increase and the material approaches a stress-independent condition.

5.2 *Monotonic stress-strain behaviors*

5.2.1 *Response to drained monotonic triaxial shearing*

The effect of cementation on monotonic shearing behaviors, and its dependence on the induced microstructural changes, are evident in drained triaxial tests on miniature 1 cm diameter specimens. Figure 53 presents shearing results for uncemented and moderately cemented (CC ~5%) specimens. The details of the first set of tests are detailed in Tagliaferri et al. (2011), with a follow-up study across a range of cementation levels presented in DeJong et al. (2017).

The triaxial tests were performed on Ottawa 50-70 sand (D_{50} = 0.21 mm, C_u= 1.0) under an isotropic confining stress of 100 kPa applied via vacuum. The specimen was sheared at a rate of 0.021 mm/min and paused at select global axial strain levels, at which point a 3D X-ray computed tomography (CT) scan of the specimen was obtained with a voxel resolution of about 15 mm by gradually rotating the specimen 360º while scanning intermittently. Decreases in deviator stress shown in Figure 53a correspond to the stress relaxation that occurred while the shearing process was paused for scanning.

The stress strain response shown in Figure 53a for the cemented specimen exhibits the expected differences relative to the uncemented clean sand condition. Consistent with the macroscopic observations described earlier and shown in Figures 50 – 53, added cementation induces a stiffer response at small strains. Additionally, a higher peak strength is attained at a lower strain level, followed by softening to a residual strength that approaches a critical state condition comparable to that observed in the uncemented sand. This trend indicates that, as shearing progresses, the cementation bonds gradually break and therefore, the effects of the cementation on the small strain behavior diminishes. At the tested cementation level (~3% $CaCO_3$), this moderate cementation magnitude does not appear to have a significant effect on larger-strain behaviors after cohesive bonds have been largely degraded.

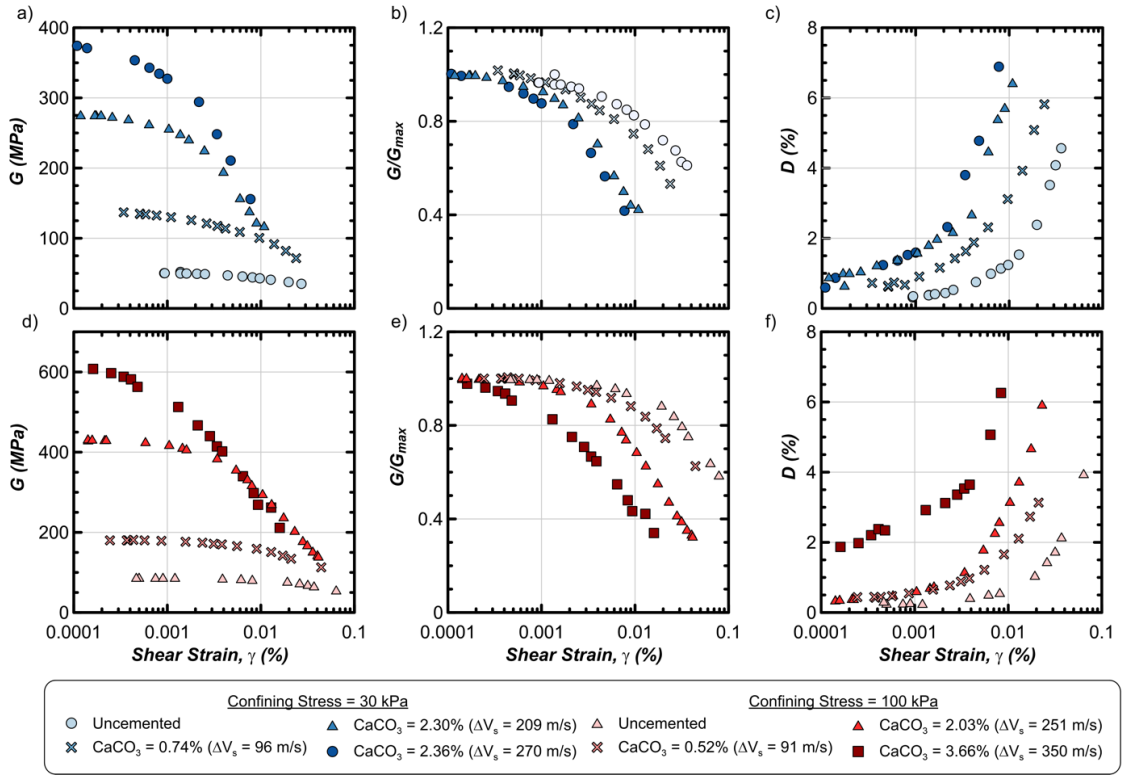

Figure 50. Modulus reductions and damping curves obtained from resonant column tests performed on Ottawa F-65 sand (D_r = 61%) at confining stresses of 30 and 100 kPa at varying levels cementation (ΔV_s = 0 to 350 m/s) (adapted from Na et al. 2022).

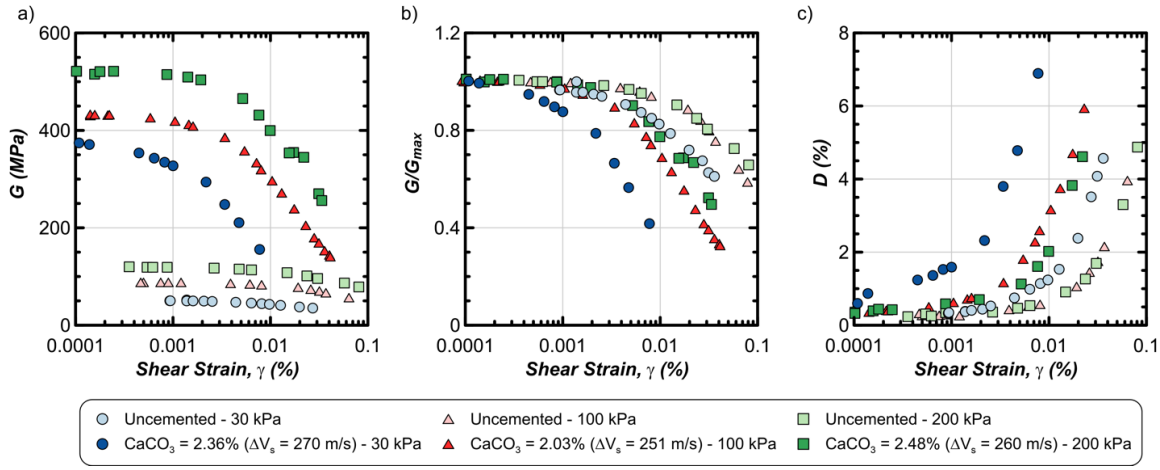

Figure 51. Modulus reductions and damping curves obtained from resonant column tests at increasing confining stresses of 30, 100, and 200 kPa (adapted from Na et al. 2022).

The presence of cementation forces the formation of shear banding within the specimen where shearing and cementation degradation is localized, and critical state conditions may be achieved. In contrast, cemented regions outside of the shear band remain largely intact with minimal deformations. This is evident in Figure 53b, where the mapped local porosity and shear strain changes between select stages (beginning, middle, and end of the test) are shown. Blue boxes indicate the progression in the biocemented sand and the red boxes indicate the response of the uncemented sand. There was no observed evidence of localization in the biocemented sand sample prior to the peak strength, while in the uncemented specimen, significant dilation is observed in a localized zone prior to peak.

Further analyses of additional tests performed across a range of cementation levels (DeJong et al. 2017) identified how the progressive formation and thickness of the shear band depend on the cementation level. Specifically, the local shear strains within the shear band corresponding to mobilization of the peak strength was near 10% for the uncemented specimen, averaged about 4% for a specimen with a $CaCO_3$ content of about 3.5%, and decreased to about 1% for a specimen with a $CaCO_3$ content of 4.8%. The shear band for the uncemented case was rather diffuse and developed gradually, eventually reaching a thickness in excess of ~30 particle diameters after an axial global strain of about 5%. In contrast, the shear band became more localized with increasing cementation level. The 3.5% $CaCO_3$ specimen began to localize after 3% shear strain and reached a shear band thickness of about 8 particle diameters at a shear strain of 5.8%, while the 4.5% $CaCO_3$ specimen further localized within a shear band of about 6 particle diameters. Evidently, cementation

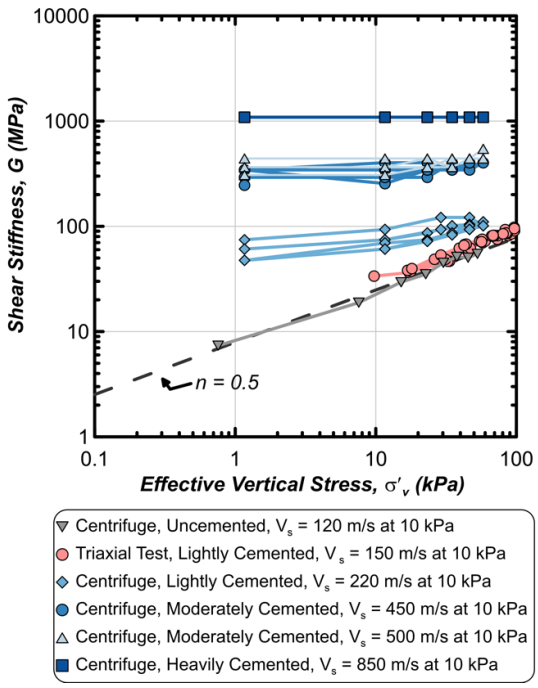

Figure 52. Shear stiffness results from triaxial and centrifuge model experiments at various cementation levels subjected to multiple stress level cycles between 1 and 80 kPa (adapted from Montoya et al. 2013).

stabilizes the soil matrix, resulting in a more localized failure mechanism within a shear band, with the shear band thickness decreasing with increasing cementation.

5.2.2 *Response to undrained monotonic triaxial shearing*

The increased stiffness, increased peak strength, and strong dilatancy observed at larger strains for biocemented sands under drained conditions map directly to undrained conditions resulting in the generation of significant negative excess pore pressures during the shearing process. Results from a series of 70 mm diameter undrained triaxial tests performed on Ottawa 50-70 sand prepared at a D_r of 40% under an isotropic confining stress of 100 kPa following cementation treatments that increased the shear wave velocity from the untreated baseline of V_s = 190 m/s (0% $CaCO_3$) to values of 300 m/s (1.0% $CaCO_3$), 650 m/s (1.3% $CaCO_3$), 1100 m/s (3.1% $CaCO_3$), and 1400 m/s (5.3% $CaCO_3$) are shown in Figure 54.

The mean stress normalized deviatoric stress (q/p') versus shear strain measurements shown in Figure 54a, highlight a progressive increase in initial stiffness and peak strength with cementation, followed by proportional softening towards a constant residual normalized strength. Normalization of the deviatoric stress with the initial isotropic consolidation stress (q/p'_c), shown in Figure 54b, captures the substantial absolute increase in deviatoric stress with cementation, owing to the significant increase in negative excess pore pressure generation (Figure 54c).

The resulting q-p' stress paths for the tests, shown in Figure 54e, reveal several notable changes in behavior as the cementation increases. Firstly, the initial stress path from the isotropic consolidation state for the uncemented specimen follows the expected vertical path consistent with initially perfectly elastic behavior. This is immediately followed with a reduction in p' due to positive pore pressure generation and leftward curvature of the stress path indicative of contractive volumetric tendencies. Once the CSL is reached, the specimen follows the failure envelop typical of a clean sand with a cohesive intercept of 0 kPa and a friction angle of 33º. In contrast, as cementation increases, the increased dilatancy of the cemented soil matrix affects the initial stress path at small strains, resulting in the deviatoric load inducing an increase in the effective stress as negative excess pore pressures are generated. The initial path slope is 3.6:1 for the specimen treated to a V_s = 1400 m/s. It then follows that strain softening of q is not observed as strains progress in this particular test. Projecting the failure envelopes of the treated specimens to the origin of the axes results in a cohesion intercept and a friction angle which tend to increase with the level of cementation. This increase in strength parameters (cohesion and friction angle) is more significant for the cohesion but can also be observed, to a lesser degree, for the friction angle.

Bender element measurements obtained throughout this testing enabled the tracking of how the normalized shear

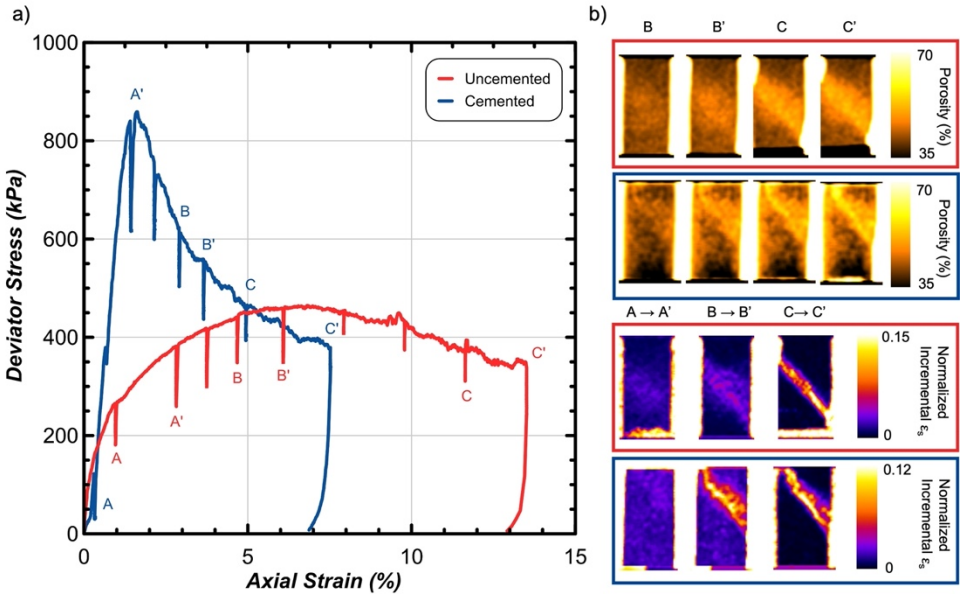

Figure 53. Small-scale x-ray CT scanned triaxial test results including (a) stress-strain for cemented and uncemented specimen and (b) strains and porosity values from image analysis of 3D CT scans with the upper red image series being for the uncemented specimen and the lower value image series being for the cemented specimen (adapted from Tagliaferri et al. 2011).

modulus degraded during the shearing process, defined as $G/(p/p_a)^{0.5}$, to account for the changing effective stress conditions due to excess pore pressure generation (Figure 54d). Due to the placement of the bender elements in the top and bottom cap of the apparatus, the shear wave velocity measurements can be interpreted as being average values across the sheared sample, meaning that the transmitted waves from the bender elements traveled within an intact region (away from the shear band) as well as an increasingly narrow sheared region (within the shear zone) of the sample as the level of cementation increased. Consequently, the magnitude of the reduction in the normalized shear modulus (Figure 54d) is less than the actual decrease expected within the shear band, which at high strains leads to residual values that do not converge between conditions.

The breadth of monotonic drained and undrained triaxial tests in the literature is extensive and has reaffirmed and expanded the trends summarized here. Systematic, secondary dependencies have been mapped for the effect of MICP cementation on clean sand specimen behavior in triaxial tests across variations including relative density (e.g., Tsukamoto et al. 2013, Xiao et al. 2019), confining stress (e.g., Feng & Montoya 2015, Lin et al. 2016a, Nafisi et al. 2020b), stress paths (e.g., Montoya & DeJong 2015, Nafisi et al. 2021), and treatment solutions (e.g., Terzis et al. 2016, Xiao et al. 2021a). The observations have also been extended to variations in soil classification (size and gradation) and mineral composition (e.g., Simatupang et al. 2018, Nafisi et al. 2018, Nafisi et al. 2020b).

Aggregated data from the literature contains variability given the (sometimes significant) differences in the soil characteristics, MICP treatment procedure implemented, test device type and compliance, and testing protocols and procedures. Nonetheless, trends of properties dependent on $CaCO_3$ content can be clearly defined. For example, as detailed in a comprehensive synthesis by El Kortbawi et al. (2022a) and presented in Figure 55, the apparent cohesion increases with cementation at a proportion of about 100 kPa increase in the cohesive intercept per 5 to 6% increase in $CaCO_3$ content and the peak friction angle on average increases by about 5º per 5% increase in $CaCO_3$ content (observations consistent with those observed by Choi et al. 2020).

Degraded MICP can be readily re-established through re-treatment as the open pore structure maintained after initial MICP treatments allow for additional treatment injections as desired. The effectiveness of retreatment following damage from monotonic loading has been investigated using laboratory triaxial tests, while the impacts of earthquake-induced damage on cementation effectiveness have been investigated using centrifuge model tests (Montoya & DeJong 2013). Figure 56 from (Montoya & DeJong 2013) shows the engineering behavior to 10% axial strain in undrained triaxial testing following initial treatment to a V_s = 650 m/s (1.3% $CaCO_3$), and the subsequent behavior following retreatment to an additional 10% axial strain (strain redefined as 0% strain after retreatment). As evident, the monotonic engineering behavior can be fully recovered through retreatment.

5.2.3 *Response to drained monotonic simple shearing*

The previously described behaviors observed in drained and undrained monotonic triaxial tests have been similarly observed in direct simple shear tests on biocemented and uncemented sands. A series of drained monotonic direct simple shear tests were performed on loose (D_r = 30%) biocemented specimens of varying cementation magnitudes (ΔV_s ~ 0 to 500 m/s) under a vertical effective stress of 100 kPa (Lee et al. 2021, Lee & Gomez 2022). Figure 57 provides representative drained monotonic responses for specimens of varying cementation including (a) shear stress versus shear strain, (b) shear stress versus vertical

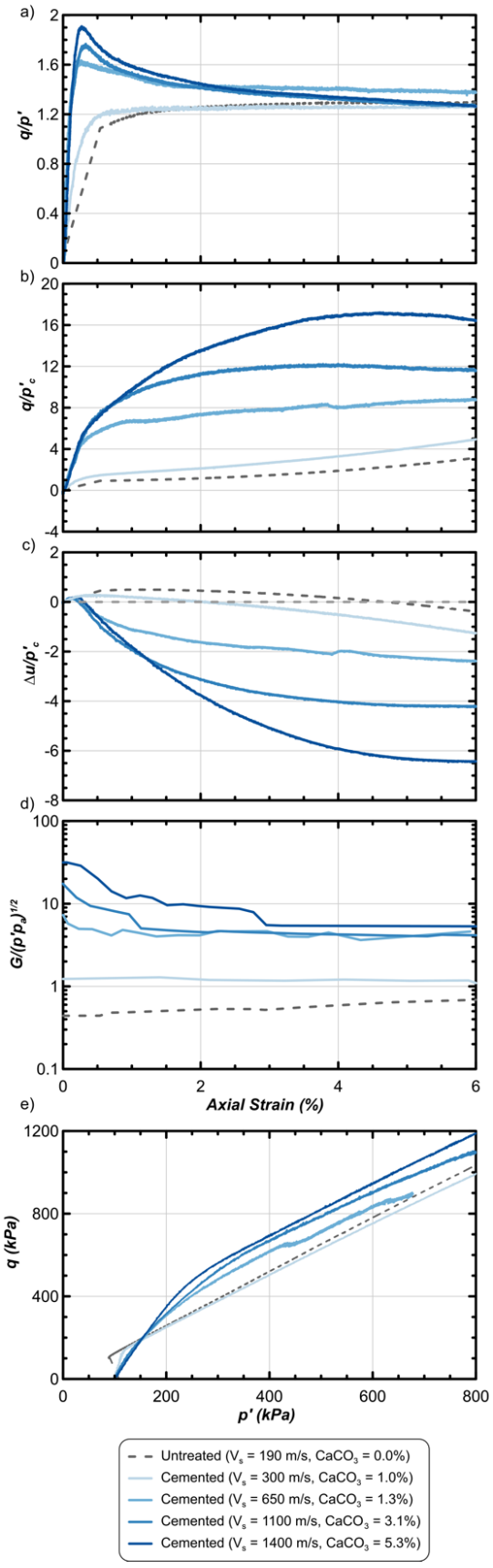

Figure 54. (a) q/p' versus strain, (b) q/p'$_c$ versus strain, (c) Δu/p'$_c$ versus strain, (d) q versus p', and (e) $G/(p'p_a)^{1/2}$ versus strain for uncemented (ΔV_s = 190 m/s) and cemented samples (ΔV_s = 300, 650, 1100, 1400 m/s) (adapted from Montoya & DeJong 2015).

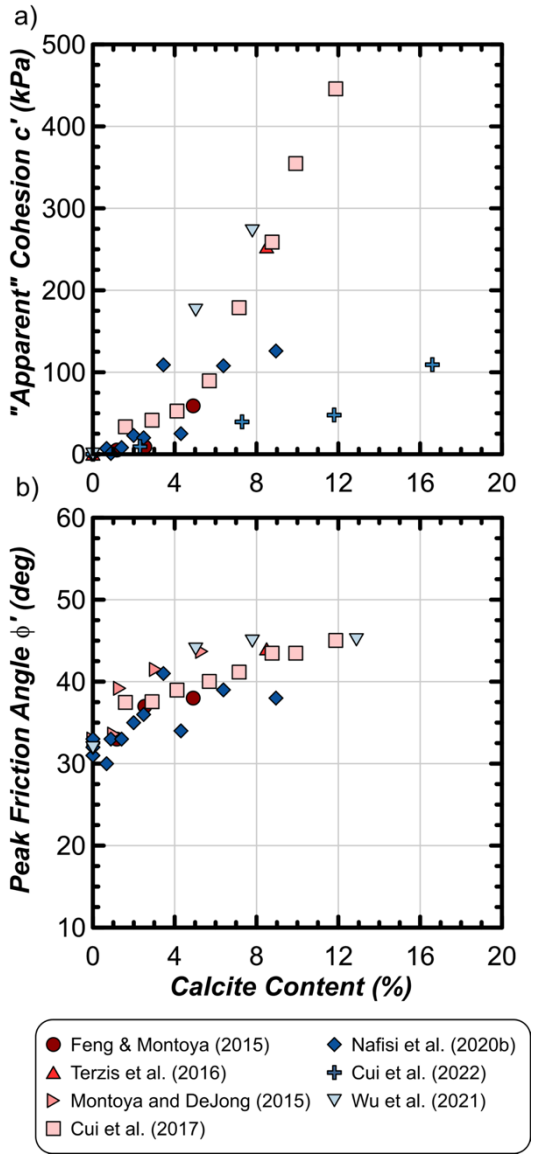

Figure 55. (a) cohesion vs $CaCO_3$ content and (b) peak friction angle versus $CaCO_3$ content trends summarized from multiple research studies (adapted from El Kortbawi et al. 2022a).

effective stress, (c) shear stress versus log-scale shear strain, and (d) axial strain versus shear strain responses. Similar to drained triaxial tests, progressive increases in shear stiffnesses and peak shear strengths can be observed with increases in cementation. While an untreated specimen exhibited a peak shear strength near 75 kPa, the most highly cemented specimen (ΔV_s ~ 485 m/s) achieved a peak shear strength near twice as large near 140 kPa (Figure 57a**)**. Furthermore, stress-strain responses show a progressive shift from strain-hardening to strain-softening behaviors with increases in cementation. Significant enhancements in initial shear stiffnesses can also be distinguished from these responses when plotted versus shear strains in log-scale (Figure 57c**)**. When considering differences in volumetric behaviors shown in Figure 57b and 57d, the uncemented and very lightly cemented samples were largely contractive as expected, while almost no volumetric changes were observed for the specimen treated to a light level of cementation near a ΔV_s of 80 m/s. As cementation magnitudes increased, however, strong dilation during shearing was observed. In more heavily cemented specimens (ΔV_s > 300 m/s) the mobilization of volumetric strains occurred only after the

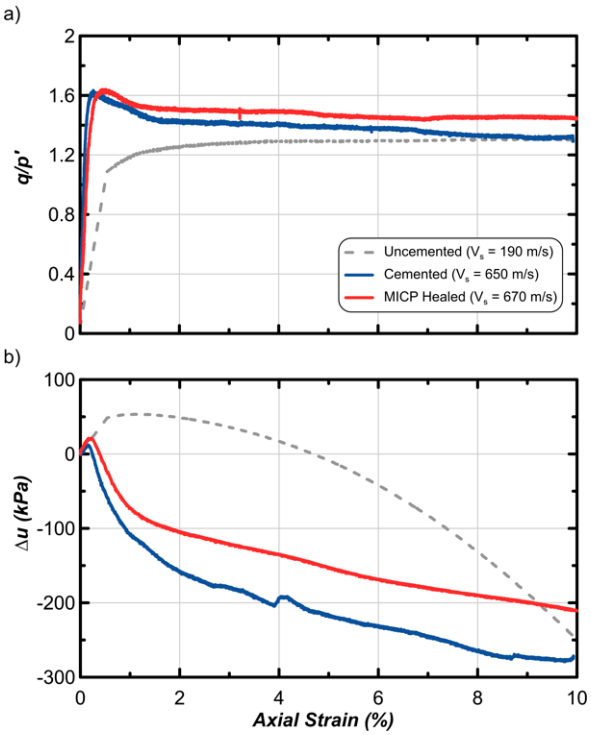

Figure 56. (a) stress ratios and (b) excess pore pressure generation for undrained triaxial compression tests on untreated and biocemented Ottawa 50-70 sand specimens, with the latter sheared after initial MICP treatment and after MICP retreatment following shearing (adapted from Montoya and DeJong 2013).

peak strength was observed. Such behaviors are consistent with other tests from the literature (e.g., Wu et al. 2021, Wang et al. 2021) and reflect the limited contribution of volumetric behaviors to peak shear strengths observed in biocemented soils with cementitious bonds instead providing the majority of the observed peak strength enhancements. Mobilization of dilative behaviors, although significantly impacted by the presence of added cementation, instead occurs post-peak only after interparticle shearing has been more fully mobilized. Progressive increases in large strain shear strengths (strain > 5%) can also be observed once cementation magnitudes exceed ΔV_s values near 80 m/s. These large strain changes may be due to changes in interparticle friction from the coating of soil particles surfaces with $CaCO_3$ crystals, which could increase interparticle frustration and constant volume friction angles.

5.2.4 *Response to undrained monotonic simple shearing*

Undrained monotonic trends from DSS tests show similar shifts in shear strength, stiffness, and volumetric behaviors as undrained triaxial tests with increases in cementation magnitudes. A similar series of undrained monotonic direct simple shear tests were performed on loose (D_r = 30%) bio-cemented specimens of varying cementation magnitudes (ΔV_s ~ 0 to 500 m/s) subjected to an initial vertical effective stress of 100 kPa (Lee et al. 2021, Lee & Gomez 2022). Figure 58 provides representative undrained monotonic responses for specimens of varying cementation including (a) shear stress versus shear strain, (b) shear stress versus vertical effective stress, and (c) excess pore pressure versus shear strain responses. As shown in Figure 58b and Figure 58c, large differences in volumetric tendencies were observed with even small magnitudes of cementation. Although all samples exhibited initially contractive behaviors at shear strains of less than 0.5%, as expected, at larger shear strains, significant differences in

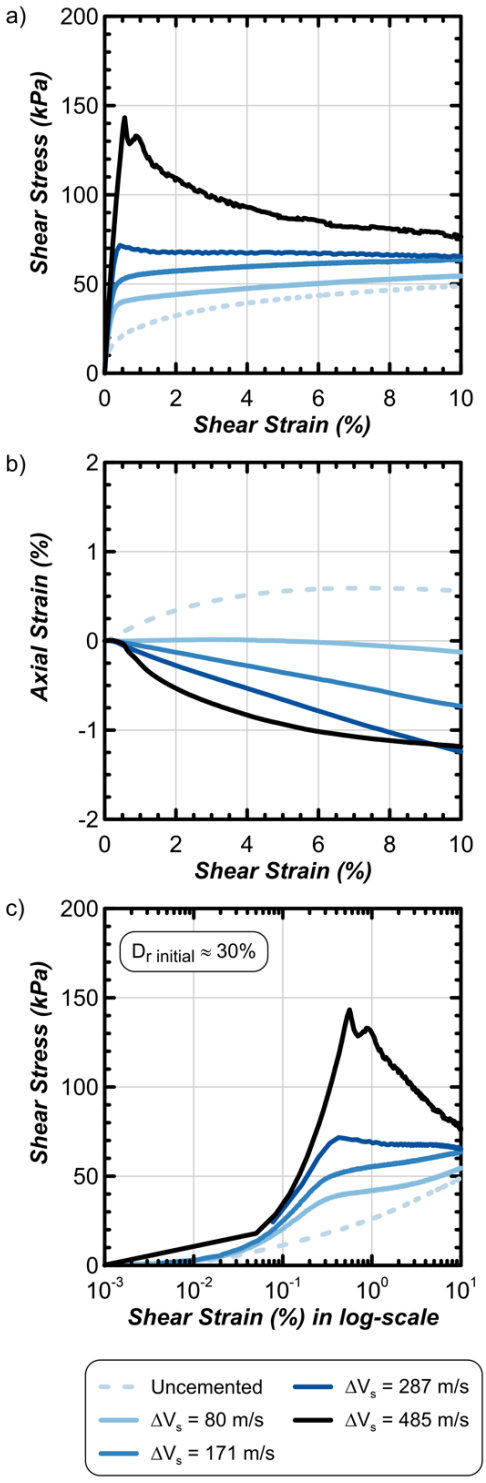

Figure 57. Summary of monotonic drained direct simple shear tests performed on specimens of varying biocementation (ΔV_s ~ 0 to 500 m/s) including (a) shear stress versus shear strain, (b) axial strain versus shear strain, and (c) shear stress versus shear strain (in log-scale) (adapted from Lee & Gomez 2022b).

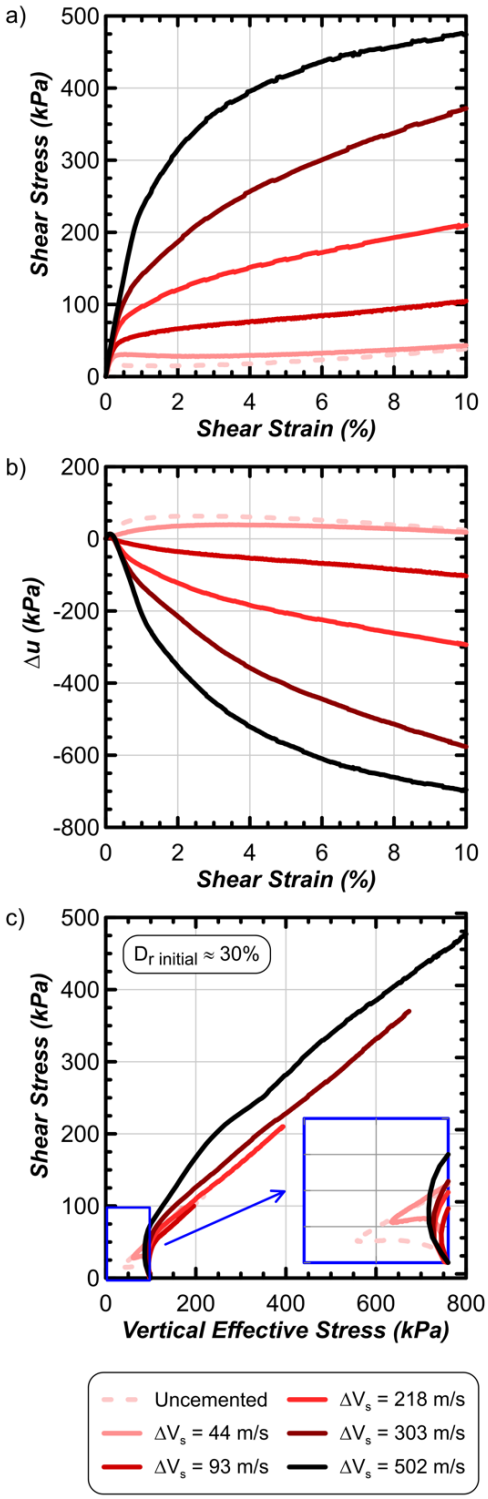

Figure 58. Summary of monotonic undrained direct simple shear tests performed on specimens of varying biocementation (ΔV_s~0 to 500 m/s) including (a) shear stress versus shear strain, (b) excess pore pressure versus shear strain, and (c) shear stress versus vertical effective stress (adapted from Lee & Gomez 2022b).

excess pore pressure generation were observed. Uncemented specimens exhibited contractive excess pore pressure responses expected for loose of critical specimens. As cementation magnitudes increased, however, more limited volumetric behaviors were again observed at very light cementation (ΔV_s of ~ 44 m/s). Within increasing cementation, increasingly dilative behaviors were observed particularly once ΔV_s values exceeded ~ 100 m/s. Large negative excess pore pressures in more highly cemented samples resulted in greater effective stresses during shearing and higher undrained shear strengths as expected. For the most highly cemented specimen (ΔV_s ~ 500 m/s), negative excess pore pressures exceeded 600 kPa at shear strains near 6% and continued to increase with added strain. While such pore pressure values may be unrealistic for shallower soils relevant to

liquefaction mitigation applications, due to the cavitation of pore fluids under suction pressures, the observed responses do provide insights regarding the progressive shift in undrained mechanical behaviors with added cementation. Responses plotted in shear stress versus vertical effective stress space (Figure 58b) further suggest that while more lightly cemented specimens (ΔV_s < ~ 200 m/s) may follow a similar failure surface as uncemented sands, this surface may shift with added cementation with greater differences observed once ΔV_s values exceed ~300 m/s.

5.2.5 *Summary of monotonic behaviors*

Collective observations from the above studies and broader literature, in combination with fundamental understandings of the MICP precipitation process, including the interparticle distribution, morphology, mineralogy, and strength of the achieved precipitates (Section 2 and 3), enables synthesis and summary of how soil properties and monotonic behaviors are expected to change with the addition of cementation. Table 3 details how a range of properties and behaviors change as cementation increases for uncemented loose (D_r ~ 30%) poorly-graded silica sands when subjected to undrained and drained monotonic shearing.

5.3 *Cyclic stress-strain behaviors*

The undrained cyclic behavior of biocemented soils has been characterized at the element-scale using triaxial (Hayashi et al. 2010, Burbank et al. 2013, Feng 2015, Sasaki & Kuwano 2016, Simatupang & Okamura 2017, Simatupang et al. 2018, Xiao et al. 2018, 2019) and direct simple shear (DSS) testing (Montoya et al. 2013, Zamani & Montoya 2018, 2019, Riveros & Sadrekarimi 2020, Lee et al. 2020, 2021). Such tests have demonstrated the ability of biocementation to alter liquefaction

Table 3. Summary of the effect of biocementation on monotonic soil behaviors.

Property/Behavior	Effect as Cementation Increases on Uncemented Loose Poorly Graded Silica Sand Subjected to Monotonic Undrained/Drained Shearing
Small-strain Shear Modulus (Shear Wave Velocity)	Shear wave velocity increases at about 50-125 m/s per 1% $CaCO_3$ content. Modulus computed with $G = \rho V_s^2$. Density changes can be determined via $CaCO_3$ while assuming specific gravity of calcite comparable to silica (Gs ~ 2.71). When G_{max} > ~400 MPa ($CaCO_3$ > ≈ 3%) modulus of biocemented soils is largely independent of confining stress.
Threshold Shear Strain	Threshold shear strains decrease with cementation due to increased brittleness of cementitious bonds. Threshold strains decrease from about 0.002% for uncemented sands to 0.0002% at ~3.5% $CaCO_3$ at 100 kPa confinement.
Shear Modulus Degradation	Shear modulus degradation occurs at lower strains with added cementation due to increasing brittleness. Strain to reach G_{50} at 100 kPa decreases by 10x relative to untreated condition when $CaCO_3$ is ~3.5%.
Damping	Damping initiates at smaller strains due to lower threshold shear strain.
Shear Localization	Shearing becomes increasingly localized with higher cementation due to increased dilatancy. Effects are most pronounced at low confining stresses. Shearing zone decreases down to about 8 particle diameters thick when $CaCO_3$ is ~3.5%.
Dilation Rate	Dilation rate increases rapidly as $CaCO_3$ increases due to cementation and densification. The strain level at which the maximum dilation rate occurs shifts increasingly beyond the strain level corresponding to peak strength as the $CaCO_3$ increases.
Peak Shear Strength	Peak shear strength increases regardless of drainage conditions or shearing mode, with characteristics similar to soft rock as $CaCO_3$ increases (i.e., stress-invariant). Tensile strength increases as $CaCO_3$ increases.
Strain at Peak Strength	Strain at which peak strength is mobilized decreases with $CaCO_3$ due to increased initial stiffness and failure localization. Strains at peak decrease from ~3.5% on average for the uncemented condition, down to ~0.5% or less at 10% $CaCO_3$.
MC Cohesive Intercept	Apparent MC cohesive intercept increases due to cementation bonds, from 0 kPa for untreated sand up to about 350 kPa for 10% $CaCO_3$. Failure envelope shifts with the accumulation of shear strain due to progressive damage.
Peak Friction Angle	Peak friction angle increases due to cementation bonds and increased interparticle friction, from typical uncemented sand values of 30-34º to about ~43º for 10% $CaCO_3$.
Volumetric Tendencies	Volumetric tendencies transition from contractive towards dilative due to added cementation, increased soil density, and increased interparticle friction. Magnitude of change depends primarily on cementation level and confining stress.
Critical State Friction Angle	Critical state friction angle appears to change insignificantly at $CaCO_3$ less than ≈3-5%. At higher $CaCO_3$, the angle begins to increase slightly, however no significant changes are evident at less than ~10% $CaCO_3$.

behaviors as well as considered a suite of other variables including the presence of soil fines (Sasaki & Kuwano 2016, Zamani & Montoya 2018, 2019), calcareous soils (Xiao et al. 2018, 2019), and differences in specimen saturation during treatments (Simatupang & Okamura 2017). Collectively, these studies have clearly shown that biocementation can increase soil liquefaction resistances, however, understanding of the effects of factors including confining stress changes, relative density differences, static shear stresses, cementation contents, and applied loading magnitudes as well as the post-triggering consequences of such loading events have remained less understood. Ongoing studies will continue to improve understanding of the behaviors, particularly for biocemented clean sands, however, the current understandings and more recent findings are summarized herein.

5.3.1 *Response to undrained cyclic simple shearing*

Recent DSS testing has examined the undrained cyclic behavior of loose ($D_{r\ initial}$ = 30%) biocemented Ottawa F-65 Sand treated to varying cementation magnitudes (ΔV_s ~ 0 to 500 m/s) under an initial vertical effective stress of 100 kPa and subjected to varying cyclic loading demands (Lee et al. 2021, Lee & Gomez 2022b). All specimens were sheared under equivalent undrained conditions to achieve a double amplitude shear strain (DASS) of 24%, after which specimens were reconsolidated back to the initial effective stress of 100 kPa.

Representative responses for biocemented specimens treated to ΔV_s values between 0 m/s (uncemented) and ~500 m/s, subjected to Cyclic Stress Ratio (CSR = $\tau/\Delta\sigma'_{v\ initial}$) values of either 0.2 ($\Delta V_s$ = 0 m/s, 95 m/s), 0.75 (ΔV_s = 194 m/s, 294 m/s), or 1.5 (ΔV_s = 476 m/s) are presented in Figure 59. Provided responses include measurements of shear stress versus effective vertical stress (column i), shear stress versus shear strain (column ii), and excess pore pressure ratio ($r_u = \Delta u/\Delta\sigma'_{v\ initial}$) versus cycle number (column iii). Modest increases in biocementation magnitudes can substantially decrease excess pore pressure generation and shear strain development early on during undrained cyclic loading for a given applied loading magnitude (i.e., CSR value). For example, for tests subjected to a CSR of 0.2, a small amount of cementation corresponding to ΔV_s = 95 m/s resulted in an increase in the number of cycles to r_u =0.95 from approximately 0.5 cycles to nearly 650 cycles when compared to the untreated condition. Similar improvements were observed at higher CSR values with the number of cycles to r_u =0.95 increasing from approximately 2.5 cycles to 575 cycles as ΔV_s increased from 194 to 294 m/s. When considering shear stress versus vertical effective stress responses (column i), shifts in behaviors can occur, with significant increases in vertical effective stresses and negative r_u values observed early during cyclic loading with an abrupt transition to increased contraction at some threshold cycle number after which cemented bonds are degraded and the volumetric tendencies of the specimen become increasingly mobilized. At larger shear strains following liquefaction triggering, higher magnitudes of cementation resulted in an increased number of cycles required to accumulate similar post-triggering shear strains, however, such improvements were less pronounced than triggering improvements. Failure envelopes observed during tests exhibited minimal changes in apparent cohesion with increased cementation, however, clear shifts in such envelopes were evident during the loading process and were likely reflective of changes in interparticle friction and cohesive bonding as bonds degraded and interparticle shearing became increasingly mobilized.

Although liquefaction triggering can be defined using either shear strain (single amplitude shear strain [SASS] = 3%) or excess pore pressure ($r_u = \Delta u/\Delta\sigma'_{v\ initial}$ = 0.95) criteria, recent tests have suggested that differences between criteria are likely relatively minor for biocemented sands results (Lee et al. 2021), therefore liquefaction triggering resistances are discussed herein on the basis of shear strain development. Results from undrained cyclic tests on loose biocemented Ottawa F-65 sand similar to those shown earlier in Figure 59 can be further analyzed to assess changes in liquefaction triggering resistance with changes in cementation magnitudes and applied loading demands. Figure 60 presents (a) the number of cycles to 3% SASS for bio-cemented loose sand specimens versus ΔV_s values reflective of cementation-induced initial shear stiffness enhancements and (b) the number of cycles to 3% SASS for bio-cemented loose sand specimens of varying cementation and uncemented specimens with varying initial relative densities (D_r = 30% to 85%) versus specimen dry densities as reflected by both dry density and porosity values. Although all bio-cemented specimens were prepared initially loose (D_r = 30%) and cemented to varying degrees, uncemented specimens were prepared to varying initial densities (D_r = 30% to 85%) to compare the effects of biocementation to that of solely densification. As shown in Figure 60a, near log-linear improvements in liquefaction triggering resistances can be observed with increases in ΔV_s values even at relatively low magnitudes of cementation (ΔV_s < 100 m/s, $CaCO_3$ content < 0.9%). At higher cementation levels (indicated by greater ΔV_s increases), increases in applied CSR were necessary in order to trigger liquefaction over numbers of loading cycles more representative of earthquake applications (< 1,000 cycles). Such investigations preliminarily suggest that as applied loading magnitudes increase (i.e., CSR values increase) the effect of ΔV_s or cementation increases may become less pronounced, as indicated by trendlines with increasingly flatter slopes. At higher CSR values, a threshold amount of cementation may also be required for specimens not to achieve 3% SASS monotonically.

Figure 60b presents the number of cycles to 3% SASS for biocemented and uncemented specimens versus dry density and porosity values. As shown, cemented samples exhibited large increases in triggering resistances with minimal changes in dry densities (~ 0.43 to 0.93 %) under conditions where applied CSR values were less than 0.3. When higher CSR magnitudes were applied, however, higher cementation magnitudes were needed to achieve similar numbers of cycles to 3% SASS and more significant cementation-induced increases in specimen dry densities were observed (~1.60 to 4.76%). Triggering resistance enhancements for biocemented specimens, however, can be seen to exceed those achievable through dry density increases alone as shown by comparing biocemented specimens to uncemented specimens at similar dry densities and loading magnitudes.

The relationships between applied CSRs versus number of cycles to liquefaction triggering (3% SASS) for specimens of varying cementation are presented in Figure 61. For the same CSR value, the number of cycles to liquefaction triggering increased by 2 to 3 orders of magnitude even for lightly cemented specimens (ΔV_s < 100 m/s, $CaCO_3$ < 0.9%). While extrapolated trends are provided for higher cementation levels, ongoing investigations will provide a more comprehensive assessment of how such curves may vary with increasing cementation. These liquefaction triggering curves can be described using the power-law function CSR = a × N_{cyc}^{b}, where N_{cyc} is number of cycles to 3% SASS, and a and b values are parameters that capture the vertical position and slope of these curves, respectively. In past studies, the slope of liquefaction triggering curves (b values) have been shown to decrease (Hernandez 2018, Xiao et al. 2018, 2019), remain constant, and even increase (Riveros & Sadrekarimi 2020) with increasing cementation. This functional

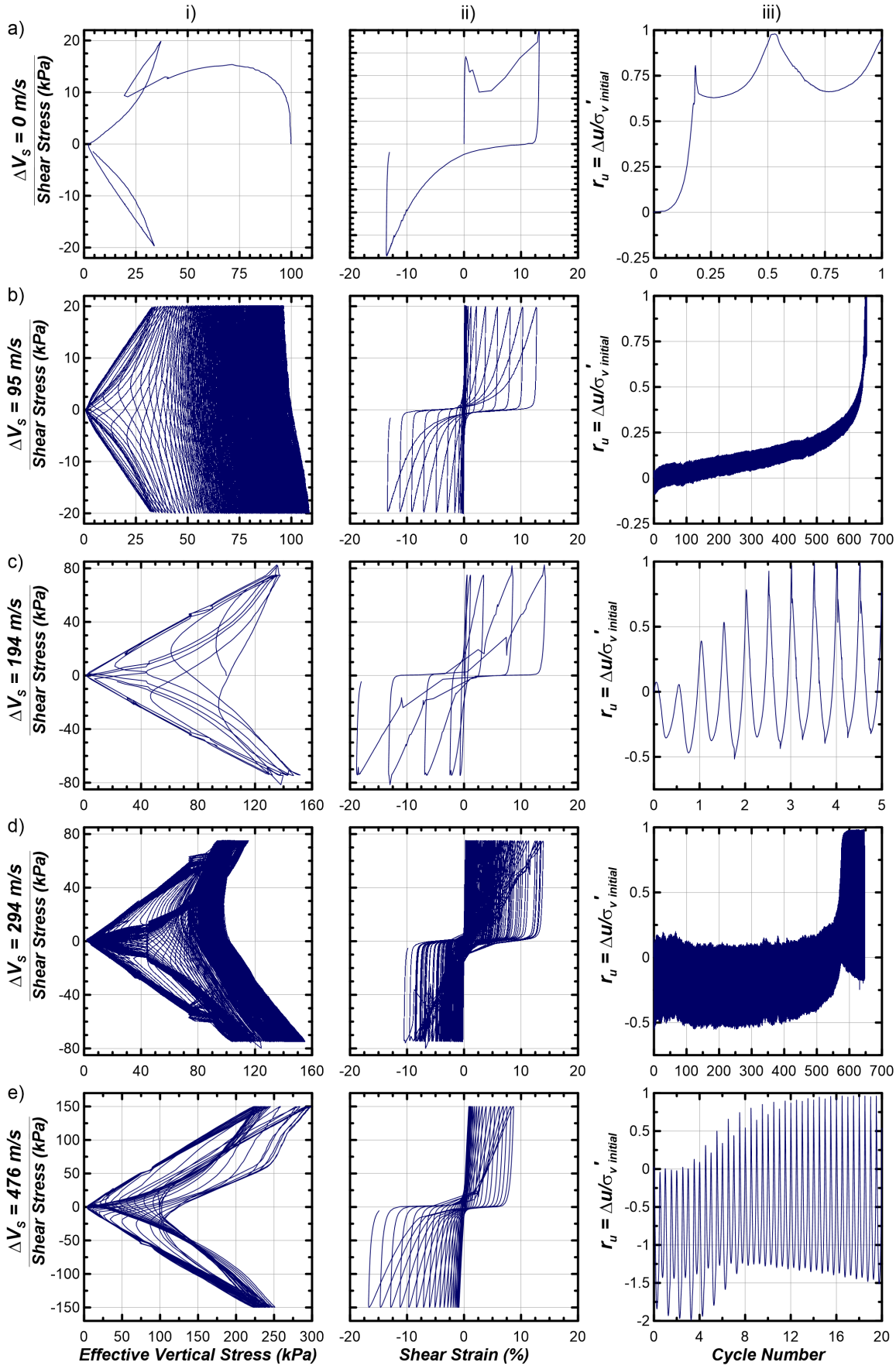

Figure 59. Responses of loose (D_r = 30%) biocemented sand specimens of varying cementation magnitudes (ΔV_s = 0 to ~500 m/s) subjected to differing applied loading magnitudes including plots of (i) shear stress versus vertical effective stress, (ii) shear stress versus shear strain, and (iii) excess pore pressure ratio versus cycle number (adapted from Lee & Gomez 2022b).

form did not appear to reasonably capture the trends observed for bio-cemented specimens in Lee et al. (2021) and given the discrepancies in the literature further investigation is necessary to assess the adequacy of power law trends to fit the data.

Figure 62 presents number of cycles from 3% to 24% SASS versus ΔV_s for loose specimens of varying cementation (Figure 62a) as well as dry density and porosity differences for loose biocemented specimens and uncemented specimens of varying initial relative densities (Figure 62b). More modest improvements in post-triggering strain accumulation can be observed, in contrast with earlier liquefaction triggering resistances that observed orders of magnitude increases with added cementation. Although for the tests presented in Figure 62 both applied CSR values and cementation levels were varied, the achieved trends collectively suggest that post-triggering strain accumulation may be only minimally impacted by added cementation until ΔV_s values exceed ~250 m/s, after which more significant improvements may be observed with increases in cycles required to obtain the same shear strain increases approaching values near one order greater (Figure 62a). When comparing trends instead on the basis of dry densities (Figure 62b), minimal differences in post-triggering strain accumulation can be observed between uncemented and cemented specimens. Although further investigations are needed, such trends suggest that cementation-induced density changes may be the primary contributor towards influencing post-triggering strain accumulation with the effects of cementitious bonding becoming diminished at larger-strains once bonds become largely sheared and cemented soil matrices become destructured.

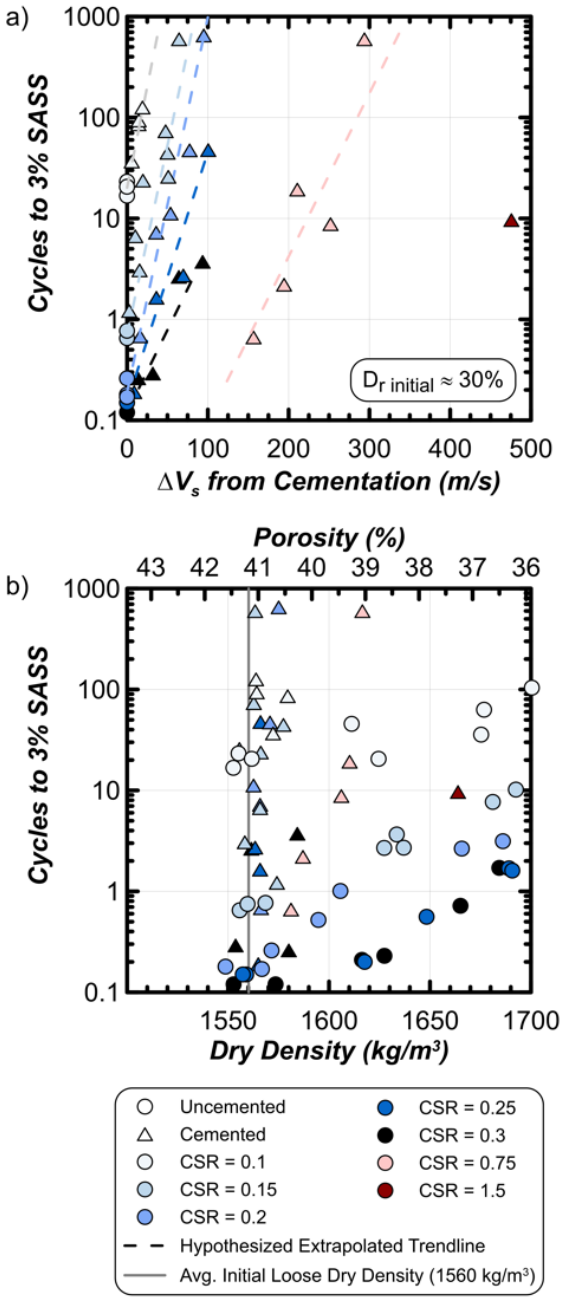

Figure 60. Number of cycles to liquefaction triggering (as expressed by number of cycles to 3% SASS) versus (a) ΔV_s from cementation, and (b) soil dry densities and porosities (adapted from Lee & Gomez 2022b).

The reconsolidation strains versus ΔV_s for loose specimens of varying cementation and dry density and porosity differences for loose biocemented specimens and uncemented specimens of varying relative densities are presented in Figures 63a and 63b, respectively. Reconsolidation strains can be similar for all loose specimens up to cementation levels near ΔV_s values of ~200 m/s, above which more considerable reductions in reconsolidation strains were observed. At V_s values exceeding ~ 300 m/s reconsolidation strains of less than 0.5% were observed in comparison to baseline values near 2.5% observed for loose uncemented specimens (Figure 63a). When considering reconsolidation strains as a function of dry density and porosity values (Figure 63b), trends for cemented specimens appeared to follow trends for uncemented denser specimens up to ΔV_s values of ~ 200 m/s, after which significantly lower reconsolidation strains were observed for cemented specimens. These trends were similar to those observed for post-triggering strain accumulation and suggest that while higher cementation levels may alter post-triggering reconsolidation at larger cementation magnitudes, such enhancements were not as significant as pre-triggering enhancements. That said, reconsolidation strains may be altered at higher cementation levels than the post-triggering strain accumulation behaviors discussed earlier, which may reflect increased shear localization with added cementation and the presence of largely intact cemented regions in more highly

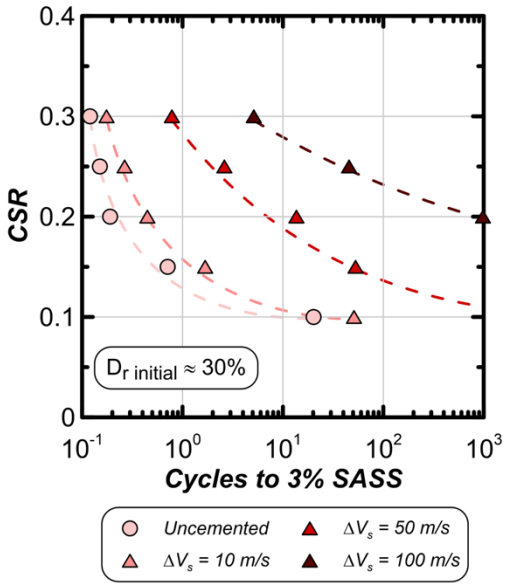

Figure 61. Liquefaction triggering curves for biocemented specimens at constant cementation levels (as expressed by ΔV_s values) including applied cyclic stress ratio (CSR) values versus number of cycles to liquefaction triggering (as expressed by number of cycles to 3% SASS) (adapted from Lee et al. 2021).

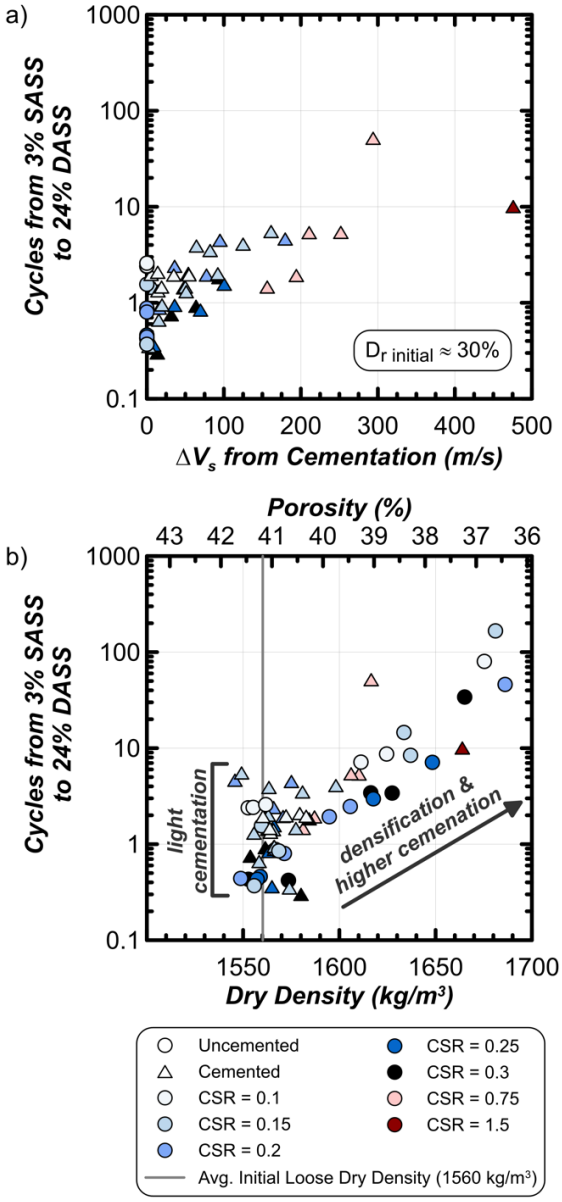

Figure 62. Number of cycles from 3% to 24% SASS versus (a) ΔV_s from cementation for loose (D_r ~ 30%) specimens of varying bio-cementation and (b) D_r for all bio-cemented specimens and uncemented specimens prepared at varying D_r (adapted from Lee & Gomez 2022b).

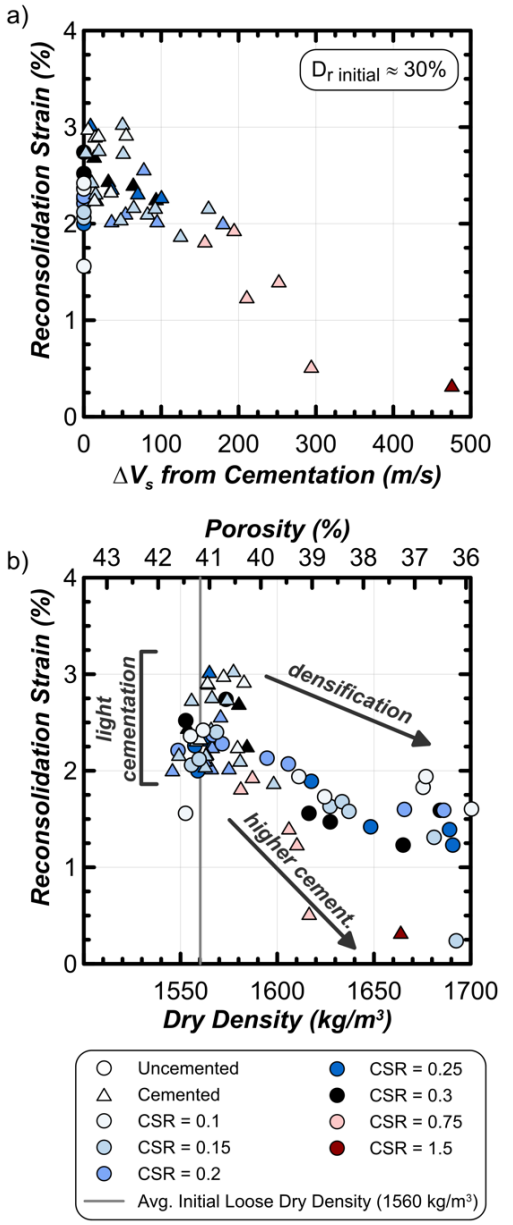

Figure 63. Reconsolidation strains versus (a) ΔV_s from cementation for loose (D_r ~ 30%) specimens of varying bio-cementation levels and (b) total D_r for all bio-cemented loose specimens and uncemented specimens prepared at varying initial D_r (adapted from Lee & Gomez 2022b).

cemented specimens following the cyclic loading and reconsolidation process.

5.3.2 *Summary of cyclic behaviors*

Recent cyclic triaxial and direct simple shear testing has provided new insights regarding the liquefaction behavior of loose biocemented sands. These results suggest that even small magnitudes of cementation can dramatically alter soil liquefaction triggering resistances, however, improvement of larger strain post-triggering behaviors including strain accumulation and reconsolidation strains may require higher magnitudes of cementation. The liquefaction behaviors of loose clean sand specimens treated to lower cementation levels (ΔV_s < 100 m/s) has been more extensively investigated recently at the element scale, however, the impacts of higher cementation levels for clean sands are still being explored through element- and systems-level testing (i.e., centrifuge testing). Such testing will likely shed further light on potential improvements in post-triggering behaviors due to cementation-induced densification and particle surface roughness changes. Current understanding nonetheless allow for broader trends in undrained cyclic behaviors with added cementation to be summarized. Table 4 details how behaviors shift as cementation levels increase for uncemented loose (D_r ~30%) poorly-graded silica sands when subjected to undrained cyclic shearing.

6 NUMERICAL INVESTIGATIONS OF STRESS-STRAIN BEHAVIOR

Changes induced to the mechanical behavior of sands through MICP treatment evident in the experimental element test results (Section 5) have been studied numerically as well. Discrete element modeling, wherein particle-scale properties and mechanical contact laws are defined to provide insights into micro- and element-scale behaviors, and constitutive models, wherein the element response are cast within a continuum scale

Table 4. Summary of the effect of biocementation on cyclic soil behaviors.

Property/Behavior	Effect as Cementation Increases on Uncemented Poorly Graded Silica Sand Subjected to Cyclic Undrained Shearing
Triggering Resistance (3% SASS Criteria)	Number of cycles required to reach 3% SASS increases rapidly with cementation primarily due to cementation induced initial shear stiffness improvements and to a lesser degree increased dilative tendencies. At CSR = 0.2, N increases from <1 cycle for uncemented sand to ~200 cycles for ΔV_s = 100 m/s (@ 100kPa, Dr = 30%). Increase in cycles primarily occurs at very small shear strains. Once ~0.5-1% strain is exceeded, the rate of strain accumulation is more similar to uncemented sands but depends on cementation level.
Excess Pore Pressure Generation	Pore pressure generation up to r_u = 0.95 largely maps with 3% single amplitude shear strain accumulation for ΔV_s < 100 m/s. Minimal excess pore pressure is generated per cycle in cemented sands initially, followed by an abrupt increase at some threshold r_u and shear strain whereas pore pressure in an uncemented sand is more gradual for all cycles.
CSR vs. N Fitting ($CSR = a\ N^{-b}$)	"a" value increases with cementation. Reported changes in "b" values are not consistent between past studies but have been shown to primarily decrease with added cementation for similar conditions. Functional form may require modification for cemented sands.
Post-triggering Strain Accumulation	Number of cycles required to achieve an increase from 3% to 9% SASS increases with cementation level. Magnitude of decrease negligible at ΔV_s < 100 m/s , but become significant at ΔV_s > 250 m/s.
Post-triggering Reconsolidation Strains	Post-liquefaction reconsolidation strains decrease with cementation level. Strain reductions are insignificant at ΔV_s < 100 m/s due to limited cementation-induced densification, but become significant at ΔV_s > 200 m/s.

constitutive model for upscaled system modeling, have both been successfully implemented. This section reviews and highlights these current capabilities for simulating the behaviors of biocemented sands.

6.1 *Discrete element models & simulations*

Discrete element modeling (DEM) provides a platform to interrogate at the particle-scale the hypotheses outlined in Section 2 and 3 regarding how the cementation at particle-contacts and on particle surfaces, the increased particle angularity, and the increased density drive the observed element engineering behaviors detailed in Section 5, including altered stiffness, strength, dilative tendency, failure localization, and residual strength.

6.1.1 *MICP representation in DEM*

The effect of MICP on the interparticle contact properties, the increase in particle angularity, and the increase in total density have been studied to varying degrees. The inclusion of cementation to the contact law can be incorporated in a straightforward manner through parallel bonds, which follow a Mohr-Coulomb failure criterion with a tension cut-off. The inclusion of a bond model with a tensile capacity has been the primary modification in a majority of studies, both for MICP studies (Feng et al. 2017, Dong & Fatahi 2020) as well as for sands cemented by other means (Wang & Leung 2008, Obermayr et al. 2013, Jiang et al. 2015, Shen et al. 2016).

The cementation strength (i.e., tension cut-off) has been typically defined as a constant value for all particle-particle contacts throughout a simulated specimen. However, this often leads to the simulated responses being more brittle than MICP experimental data. More recent studies have defined the precipitation at particle contacts to have a variable distribution throughout the simulated specimens, often modelled through defining the cementation level (tensile capacity) to have a Weibull (or some other) distribution (Evans et al. 2015, de Bono et al. 2015, Shen et al. 2016). This has allowed for more progressive failure of the cementation at contacts with loading, resulting in a more gradual global specimen strain softening response.

Inclusion of a physical representation of the $CaCO_3$ precipitate as a solid mass to investigate how its presence alters particle angularity and the total density (as well as the cementation) has been limited to one study (Evans et al. 2015). In this more realistic, but computationally expensive, implementation of the $CaCO_3$ precipitate binding two sand particles together has been realized with a ring of miniature particles that are bound to the two sand particles. This approach has the potential to produce greater insights into load transfer, failure progression, bond breakage, and coordination number evolutions with continued shearing.

6.1.2 *Monotonic stress-strain behavior – triaxial loading*

The DEM investigation by Feng et al. (2017) of the drained triaxial behavior of MICP-cemented Ottawa 50-70 sand at varying levels of cementation is representative of the agreement achievable and the insights produced when modeling the cementation bond strength as being uniform with a parallel contact law. Their observations are generally consistent with studies by Yang et al. (2017, 2019) and Abbas et al. (2020).

Feng et al. (2017) performed a baseline calibration of the particle properties using the measured experimental response of loose, medium, and dense untreated Ottawa sand when subjected to drained triaxial loading under 100 kPa confining stress. Additional tests of loose sand MICP treated to light, moderate, and heavy $CaCO_3$ contents of 1, 3, and 4.3%, respectively, were used for evaluation of the simulations. Calibration of the parallel bond contact model was performed calibrating the properties to

obtain agreement with the specimen response of the heavily cemented specimen, and the bond radii was subsequently reduced proportionally to the cementation level to simulate the lightly and moderately cemented specimens.

Figure 64 presents the DEM and experimental results for the lightly, moderately, and heavily cemented specimens in terms of stress-strain response and volumetric change. As evident, and expected with direct calibration, good agreement was achieved in the initial stiffness and peak strength. The rate of strain softening post-peak is more rapid in the DEM simulation, which is attributed to the parallel bond contact model and the assignment of uniform cementation properties to all bonds in the specimen. The residual strength decreases below the experimental results at large strains, which is attributed to the cementation model not capturing the increase in density associated with the presence of cementation. The volumetric response in the DEM simulations is initially more gradual than the experimental data, but then continues to increase at large strains throughout the shearing process due to the simulated triaxial walls being more rigid than a latex membrane and thereby amplifying the specimen volumetric change (see Yang et al. 2019 for implementation of a flexible membrane boundary).

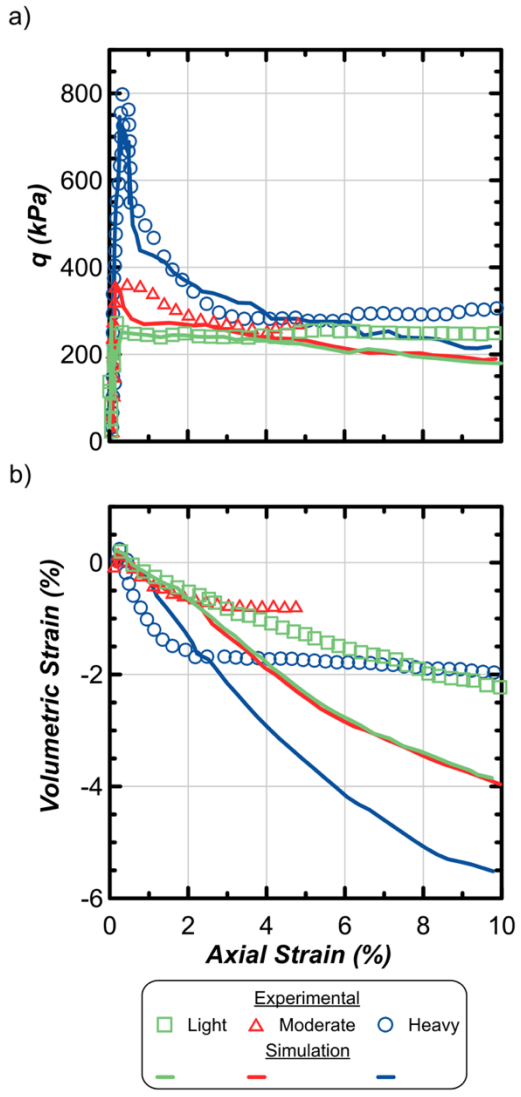

Figure 64. DEM numerical simulations and experimental specimen data of (a) stress-strain and (b) volumetric behavior for varying cementation levels (adapted from Feng et al. 2017).

The insights regarding how the cementation bonds break and the coordination number changes with added strain are exemplified in Figure 65 using data from the heavily cemented specimen. Coordination number refers to the average number of contacts per particle and is thus used to measure the interconnectivity of an assembly of particles. During loading up to peak strength, which occurs at 0.3% axial strain, more than 98% of bonds remain intact, which is consistent with the stiffness remaining nearly linear up to the peak strength. As the peak strength is reached, the bond breakage increases and 20% of the bonds have been broken between 0.3% and 0.5% strain. By 3% axial strain, about 50% of the bonds have been broken, which is sufficient to generate a shear band across the specimen. Additional bond breakage with continued shearing to 10% axial strain is relatively minimal. The coordination number evolves with strain in a consistent manner. The initial average coordination number of about 6 remains constant until the peak strength, after which it degrades rapidly to a value of about 5 by 0.5% axial strain and then remains at this value to 10% strain. The average coordination number of the entire specimen reported does obscure the coordination number present within the shear band that would be expectedly lower.

Improvements in DEM modeling of MICP treated soils with incorporation of the MICP precipitated mass, have captured the more gradual strain softening, residual strength values, and

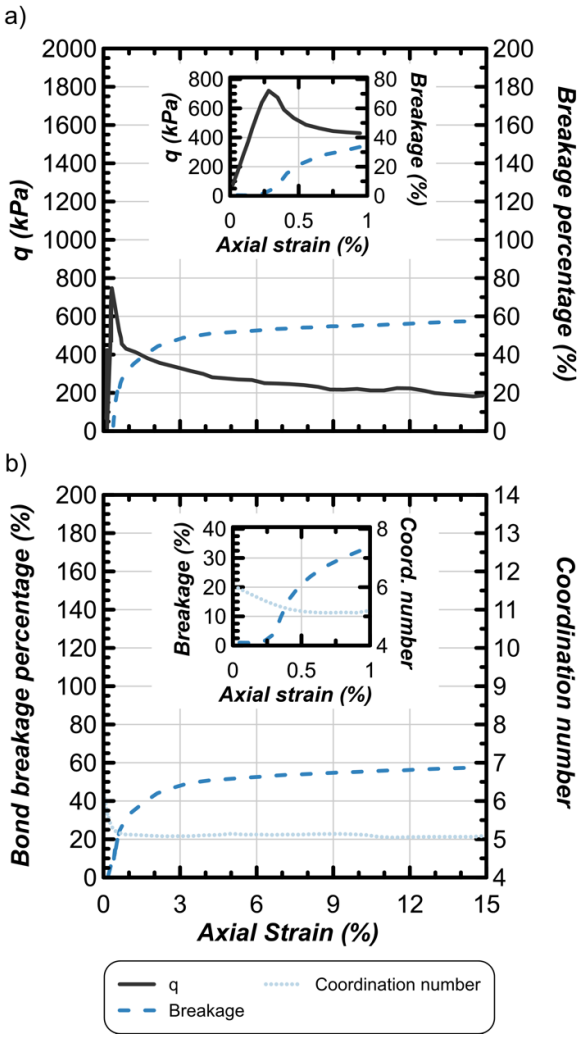

Figure 65. DEM numerical simulations for a heavily cemented specimen exemplifying (a) bond breakage percentage and (b) coordination number changes with axial strain level (adapted from Feng et al. 2017).

provided greater insights into behavior of the contacts (Evans et al. 2015, Khoubani et al. 2016, Khoubani 2018, Dong and Fatahi 2020). Khoubani (2018) implemented the $CaCO_3$ precipitate binding two sand particles using a ring of small $CaCO_3$ particles that are bound to the two sand particles and to each other (Figure 66). In this implementation, contact laws and associated properties are defined at sand-sand contacts, sand-calcite contacts, and calcite-calcite contacts. Calibration of the parameters generally followed Feng et al. (2017), with additional details required given the greater number of parameters. The parametric studies performed by Khoubani (2018) on two sand particles bound together showed more realistic behaviors with respect to how a cementation bond degrades when subjected to compression and tension, shear, bending, and twisting. The cemented fragments that resulted from breakage occupy the pore space and affect the system response as well.

Figure 67 presents the DEM and experimental results for $CaCO_3$ contents of 1.2, 2.4, and 5.3%, corresponding to lightly, moderately, and heavily cemented specimens, in terms of stress-strain response and volumetric change for undrained drained triaxial loading at a confining stress of 200 kPa. As evident, good agreement is achieved throughout the stress-strain curve, including the initial stiffness, peak strength, rate of strain softening, and residual strength. In particular, the more gradual progression of cementation bond breakage this contact model provides produces a more gradual softening of the stiffness as the peak strength is approached as well as the subsequent non-linear post-peak softening. The volumetric tendency at small strains is also well captured, though the more rigid boundaries still magnify the dilative response at higher strain levels.

Interrogation into particle scale trends provided in the DEM simulation of the 5.3% $CaCO_3$ specimen are shown in Figure 68. Bond degradation with strain, separately for calcite-sand and calcite-calcite bonds as well as in aggregate, are presented as a percentage of respective total bonds in Figure 68a. The total bond breakage percentage is generally consistent with Feng et al. (2017), however the rate of change is more gradual at small strain levels both before and after peak strength. About 50% of the calcite-calcite bond failures occur by 0.5% axial strain, which coincides with the peak strength. More than 80% have failed by 1% strain, and more than 90% fail by 10% strain. The percent of sand-calcite failures are substantially less and occur more gradually with further strain, with about 13, 30, and 60% reached at strains of 0.5, 1.0, and 10%, respectively. This suggests that the internal strength of $CaCO_3$ is weaker than the calcite-sand bond strength, an outcome which is also consistent with experimental tests on two particles bonded together (Section 2.4).

Figure 68b shows the coordination number of the sand particle contacts with sand and $CaCO_3$ particles, of sand particles with other sand particles, and of $CaCO_3$ particles with sand and other calcite particles. For all metrics, the coordination numbers are highest initially and the calcite particle contacts degrade most rapidly, which is consistent with cementation bond breakage occurring primarily within 1.0% axial strain. The sand-sand coordination numbers degrade to a value of about 5 during strain softening and continue to decrease as straining continues. The sand contacts with both sand and calcite particles decreases to about 3.5 at 3% strain, and then remains fairly constant.

Finally, Figure 68c reveals how the global boundary stress is distributed through the contact forces in the simulated specimens. Prior to shearing, the isotopic global stress of 200 kPa is carried solely through both the vertical and radial sand-sand contact forces. The calcite-calcite and calcite-sand contact forces are zero as the calcite bonds were formed after the specimen was subjected to the confining stress, consistent with experimental processes. However, after only 0.5% axial strain, about 80% of

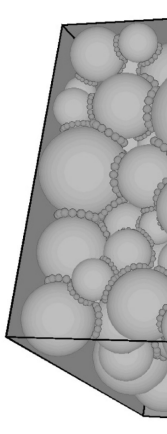

Figure 66. Image of spherical sand particles bound together with rings of small calcite particles binding sand particles together (adapted from Evans et al. 2015).

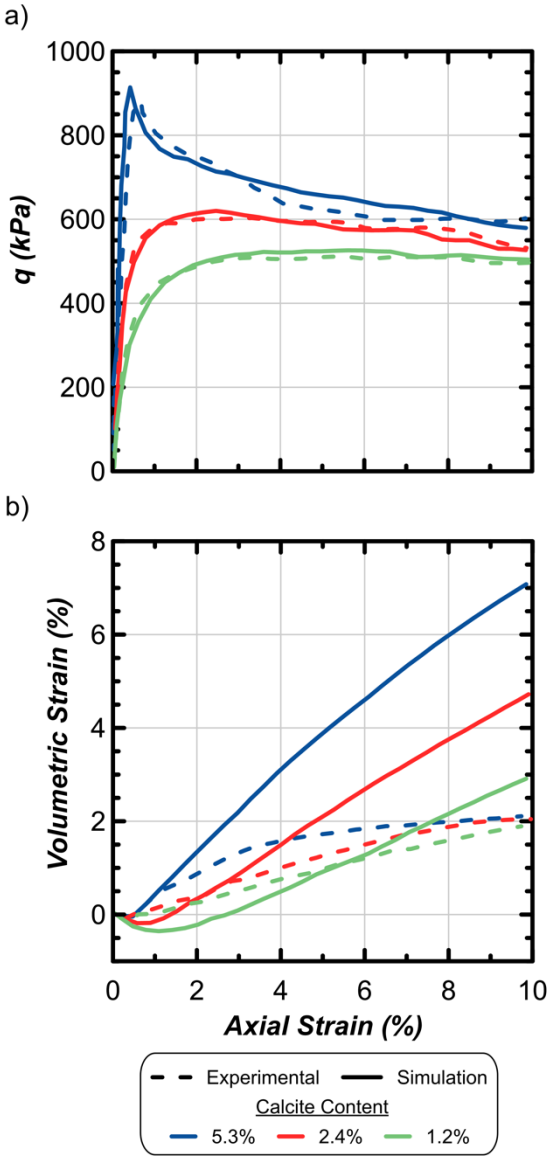

Figure 67. DEM numerical simulations and experimental specimen data of (a) q and (b) volumetric strain versus axial strain for varying cementation levels (adapted from Khoubani 2018).

the contact forces are transferred to calcite contacts. This occurs since the calcite-sand and calcite-calcite contacts have a tensile capacity, while the sand-sand contacts do not. By 1.0% strain, which corresponds to post-peak strain softening conditions, the force distribution begins to rebalance, with sand-sand contacts starting to carry a larger percentage of the forces. This trend continues, with the forces being approximately equally distributed at 3.8% strain, and after 10% strain, the sand-sand contacts carry about 67% of the forces due to the breakage of the calcite bonds.

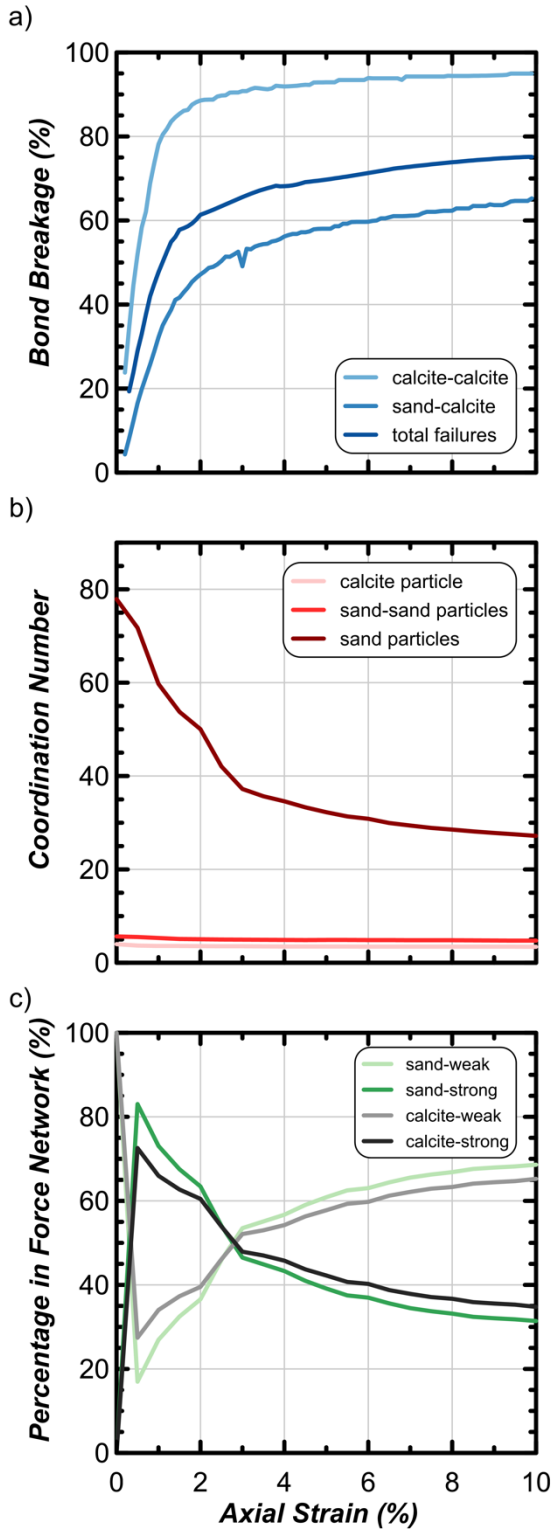

Figure 68. Evolution of (a) bond breakage, (b) coordination number, and (c) percentage of bonds active in force network from DEM numerical simulations of a heavily cemented sand ($CaCO_3$ = 5.3%) (adapted from Khoubani 2018).

6.1.3 *Cyclic stress-strain behavior – simple shear loading*

Very few DEM studies have been performed on the cyclic behavior of biocemented sands with Yang (2018) simulating cyclic simple shear loading and Zhang et al. (2022a) simulating cyclic triaxial loading. Yang (2018) performed undrained cyclic simple shear simulations of untreated and MICP treated sands. Calibration of sand and cementation parameters was performed using the consolidated undrained triaxial test simulation approach detailed in Yang et al. (2019) and corresponding experimental triaxial data of untreated and treated poorly graded Ottawa 20-30 sand (O'Donnell et al. 2017a). The simple shear device implemented was a square box where the leading and trailing walls induced a uniform shear strain across the specimen height during stress-controlled cycles at a frequency of 1 Hz. Figure 69 shows images of a confined specimen within the rigid walls and the boundary conditions applied, and the contact force distribution with the specimen prior to cyclic shearing.

Figure 70 presents the DEM simulation results for untreated and cemented specimens when subjected to a CSR = 0.30 under a vertical confining stress of 100 kPa. As evident and consistent with the experimental data shown in Section 5, cementation results in a significantly stiffer initial response, which is largely maintained through the first 10 cycles and will require 100s of additional cycles before the liquefaction threshold criteria (defined as 3.75% single amplitude shear strain). In contrast, the uncemented specimen reaches the criteria after only 3 cycles.

Aggregated results from simulations of the untreated and treated specimens in terms of cyclic strength and number of cycles to trigger liquefaction (CSR versus N) curves are shown in Figure 71. As evident, agreement between the numerical simulations and the experimental data can be achieved, and the presence of cementation significantly improves the cyclic strength.

6.2 *Continuum constitutive models & simulations*

Constitutive models are stress-strain laws that describe the element-level response of a target material under loading paths of interest. Such laws for geomaterials have ranged from relatively simple elastic or elastoplastic to more advanced

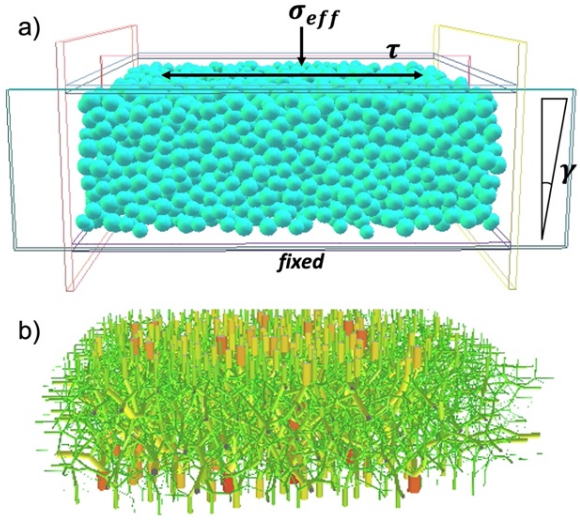

Figure 69. Images from DEM simulations performed by Yang (2018) of the (a) initial confined specimen within the rigid walls and the boundary conditions applied and (b) the contact force distribution within the specimen prior to cyclic shearing.

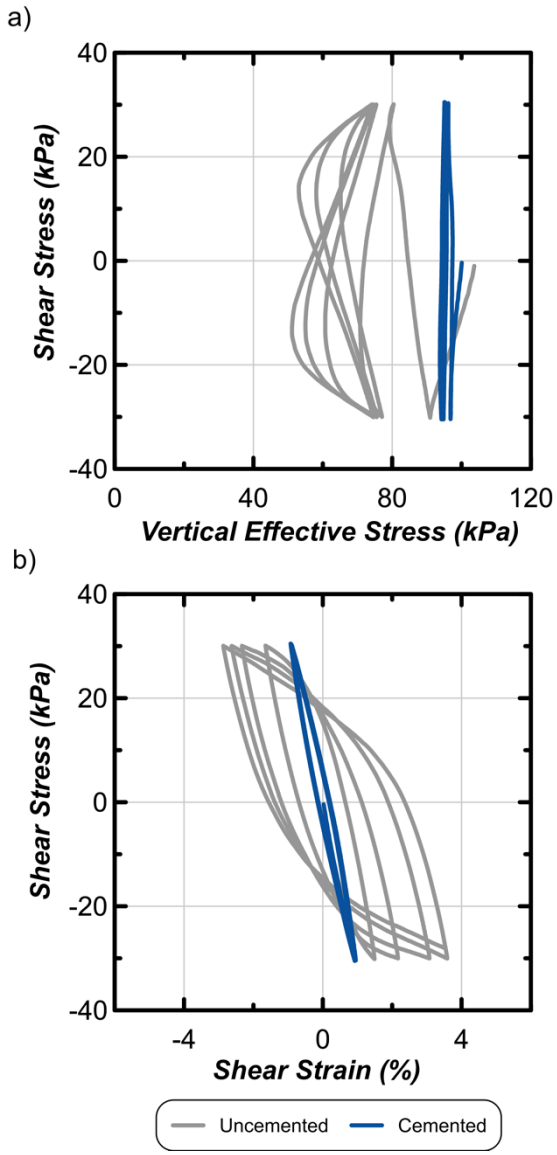

Figure 70. DEM cyclic simple shear simulations performed by Yang (2018) on untreated and biocemented specimens.

multisurface or bounding surface plasticity models. The formulation of a constitutive model typically depends on the targeted behaviors as well as the availability of a validation basis upon which comparisons can be performed, and conclusions can be drawn regarding the model's capabilities and limitations. Constitutive models for cemented soils in a variety of applications must be able to approximate the broad mix of states of cementation and conditions in the field. Furthermore, the calibration of constitutive models in research and, even more importantly, in practice must be feasible within the amount and extent of information available from characterizing and testing these materials at various scales. The engineering effort is greatly reduced if the constitutive model can already reasonably approximate the predicted stress-strain behaviors under a broad range of conditions. This can be realized only if enough knowledge has been compiled from laboratory data that the mechanical response of the material can be well established within a framework.

6.2.1 *Continuum modeling of cemented soils*

The development of several continuum models commenced in the late 1980s following the recognition and characterization of

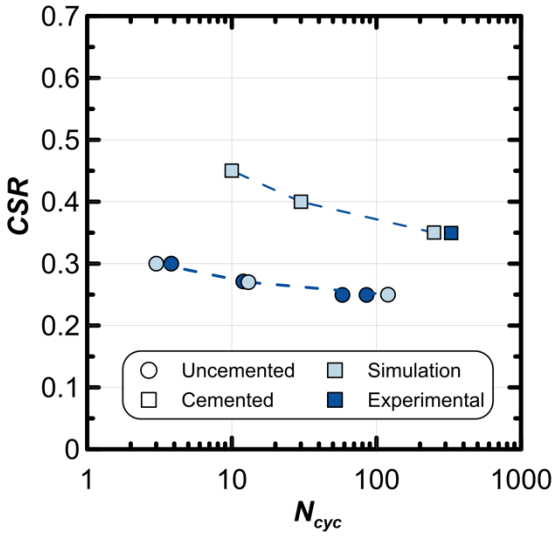

Figure 71. Compiled CSR versus N_{cyc} results from DEM cyclic simple shearing simulations and experimental results for untreated and biocemented sands (adapted from Yang 2018).

naturally cemented sands in the field and the establishment of artificial bio-cementation as a feasible and sustainable soil improvement method. Some models were developed specifically for naturally cemented soils and later for artificially cemented soils. Other models targeted soft rocks, structured, and unsaturated soils recognizing that they all demonstrate comparable macroscopic behaviors. For example, constitutively, an increased tensile strength can be either due to matric suction of an unsaturated soil or due to cementation bonds in an artificially cemented soil. Developed models differ with respect to their parent formulation, the constitutive components added or modified to capture select mechanisms, their target material and application (e.g., monotonic, cyclic, isotropic compression loading), and the data used for their validation. Earlier models by Hirai et al. (1989) and Reddy & Saxena (1992), and later by Vatsala et al. (2001), Nova et al. (2003), Lee et al. (2004), Yu et al. (2007), Arroyo et al. (2012), Gao & Zhao (2012), Gajo et al. (2015, 2019), Rahimi et al. (2016, 2018), Rios et al. (2014), Panico et al. (2018), Chong (2019), Zhang et al. (2021), and Fu et al. (2022) have targeted bonded or cemented sands and clays with a variety of artificial non-MICP treatment methods (tough-lock, Portland cement, and lime). Select models have targeted soft rocks (e.g., Rumpelt 1990, Gens & Nova 1993, Vaunat & Gens 2003, Ciantia & di Prisco 2016), structured soils (e.g., Kavvadas & Amorosi 2000, Yang et al. 2008), and unsaturated soils (e.g., Yang et al. 2008, Nguyen et al. 2014, 2017, Bruno et al. 2020) recognizing that at certain high levels of cementations, the response of a treated soil macroscopically resembles that of a soft rock or structured or unsaturated soil. Models specifically developed on the basis of bio-cementation have been those by Fauriel (2012) based on Laloui & François (2009), Nweke & Pestana (2017) on the basis of NorSand (Jefferies 1993), Gai & Sanchez (2018) on the basis of the Modified Cam Clay model, and Xiao et al. (2021b). Out of all the mentioned models, few can capture cyclic loading and specifically those of Xiao et al. (2021b) and Zhang et al. (2021) (developed on the basis of Portland-cemented sands), the latter being a descendant of the SANISAND family of constitutive models and essentially of the Dafalias & Manzari (2004) simple plasticity model accounting for fabric in the cyclic loading of sands.

Despite the progress made in the field of constitutive modeling for cemented soils, the developments have been challenged by the lack of: (1) broader frameworks that describe the mechanical response of these materials, (2) extensive

experimental datasets for a broad range of loading and boundary conditions, and loading paths, and (3) most importantly large- or field-scale testing of treated soils such that the validity of a constitutive model could be examined more holistically towards field upscaling and usage. Recognizing the need for usability and calibration of a model with parameters commonly available in practice, the range and discrepancy of descriptors used to quantify cementation (e.g., $CaCO_3$ content, increase in shear wave velocity, increase in cone penetration resistance) in the lab and in the field further challenges the extensive adoption of a constitutive model for (bio-)cemented soils.

6.2.2 *PM4SandC constitutive model*

The PM4SandC constitutive model (El Kortbawi et al. 2022b) for biocemented sands is a plasticity model aimed at capturing the mechanical response of a treated biocemented sand specimen. As such, it does not simulate the process of MICP treatment itself. The model inherits the formulation and input parameters of PM4Sand (Boulanger & Ziotopoulou 2017) and extends it to bio-cemented sands through a targeted reformulation to incorporate the initial contribution of the cementation bonds to the response and its subsequent degradation with damage accumulation. Herein the baseline model PM4Sand is presented followed by the modifications implemented to incorporate the effects of cementation.

6.2.2.1 *PM4Sand model formulation*

The PM4Sand (version 3.1, Boulanger & Ziotopoulou 2017) plasticity model for geotechnical earthquake engineering applications follows the basic framework of the stress-ratio controlled, critical state compatible, bounding surface plasticity model for sand initially presented by Manzari & Dafalias (1997) and later extended by Dafalias & Manzari (2004). Modifications to the Dafalias-Manzari model were developed and implemented to improve its ability to approximate engineering design relationships that are used to estimate the stress-strain behaviors that are important to predicting liquefaction-induced ground deformations during earthquakes. The model was calibrated at the equation level to provide for better approximation of the trends observed across a set of experimentally- and case history-based design correlations.

In PM4Sand, the mechanical response is dependent on the functions controlling the bounding M^b and dilatancy M^d surfaces, both depending on the state of the sand and on the shear stiffness, among other parameters. PM4Sand uses the relative state parameter index ξ_R presented in Boulanger (2003) which in turn uses Bolton's (1986) dilatancy relationship to define the critical state line. The relative state parameter index, ξ_R, is defined as (all stress terms are effective, and the prime symbol is dropped):

$$\xi_R = D_{R,cs} - D_R \tag{21}$$

$$D_{R,cs} = \frac{R}{Q - ln\left(100\frac{p}{p_A}\right)} \tag{22}$$

where $D_{R,cs}$ is the relative density at critical state for the current mean effective stress, p, D_R is the apparent relative density, and parameters Q and R are 10 and 1.5, respectively, for quartzitic sands (Bolton 1986). The latter two parameters are secondary input parameters to the model and can be calibrated when data are available. Together, the bounding, dilation, and critical state surfaces are shown in Figure 72, visualized as lines in q – p space (for a constant ξ_R) where the relative location of the dilatancy and bounding lines are shown for a dense-of-critical state condition. The model is simplified and restrained in plane strain conditions by removing the Lode angle θ dependency and the bounding and dilatancy surfaces are scaled from the critical surface with exponential functions of the relative state parameter. The yield surface follows the Dafalias & Manzari (2004) model, the back-stress ratio α defines its center and thus tracks its location, and the parameter m defines the radius of the elastic cone in terms of stress ratio. The constitutive equations for the PM4Sand model are presented in Ziotopoulou & Boulanger (2016) and Boulanger & Ziotopoulou (2017).

The elastic shear stiffness in PM4Sand is dependent on the mean effective stress according to:

$$G = G_0 p_A \left(\frac{p}{p_A}\right)^n \tag{23}$$

Where G_0 is the shear modulus coefficient, chosen to match estimated or measured V_s, p_A is the atmospheric pressure, p is the mean effective stress, and n is the exponent relating the dependency of G on stress and is 0.5 for clean sands (Andrus & Stokoe 2000). Accounting for the damage induced during cyclic loading by degrading G and subsequently the plastic modulus, has advanced the model's ability to better approximate the stress-strain response of a liquefying sand.

Other constitutive modifications relative to the Dafalias and Manzari (2004) have included: (1) revising the fabric formation/destruction to depend on plastic shear rather than plastic volumetric strains, (2) adding fabric history and cumulative fabric formation terms, (3) modifying the plastic modulus relationship and making it dependent on fabric, (4) modifying the dilatancy relationships to include dependence on fabric and fabric history, and to provide more distinct control of volumetric contraction versus expansion behavior, (5) providing a constraint on the dilatancy during volumetric expansion so that it is consistent with Bolton's (1986) dilatancy relationship, (6) modifying the elastic modulus relationship to include dependence on stress ratio and fabric history, (7) modifying the logic for tracking previous initial back-stress ratios (i.e., loading history effect), (8) incorporating a methodology for improved modeling of post-liquefaction reconsolidation strains, and (9) providing default values for all but three primary input parameters. The model is coded as a dynamic link library (DLL) for use with the commercial program FLAC 8.1 (Itasca 2019).

6.2.2.2 *Modifications in PM4SandC model formulation*

PM4SandC incorporates select extensions or reformulations of the PM4Sand equations in order to better approximate behaviors observed in biocemented sands.

An equivalent tensile strength due to the cementation bonds, $p_{cem,initial}$, is added to the effective mean stress p as shown in Figure 73. This approach has been used in a number of other constitutive models for cemented soils (e.g., Nova et al. 2003, Gao & Zhao 2012, Gai & Sanchez 2018, Rahimi et al. 2018). The addition of $p_{cem,initial}$ represents an increase in the size of the bounding and dilatancy surfaces (M^b and M^d, respectively) related to the effective mean stress p through the relative state parameter index ξ_R. This modification is key to the behavior of biocemented sands since the bounding and dilatancy surfaces relate to the peak strength and the cyclic resistance. $p_{cem,initial}$ is estimated internally as a function of the degree of cementation. As the magnitude of the cementation increases, the occurrence of cementation bonds at particle contacts increases, the cohesion between particles increases and while assuming a slight increase in the peak friction angle, $p_{cem,initial}$ increases accordingly. This is mathematically described by a failure envelope with an intercept similar to the one in the Mohr-Coulomb constitutive model for cohesive soils:

$$p_{cem,initial} = \frac{c}{\tan \varphi_{peak}} \tag{24}$$

The elastic shear stiffness is increased with a larger G_0, now called G_{cem}, an enhanced p with the additional $p_{cem,initial}$ and a smaller n exponent (Equation 25), the latter being informed by the broader range of data collected on these materials.

$$G_{cem} = G_{0,cem} p_A \left(\frac{p_{initial}+p_{cem,initial}}{p_A}\right)^n \quad (25)$$

G_o can also be expressed as a function of in-situ data and specifically of the shear wave velocity after cementation, $V_{S,cem}$, with both G_o and n being a function of the degree of cementation. As cementation increases, G_o also increases to reflect a stiffer response and n decreases indicating that the stiffness becomes less depth (or effective stress) dependent, with values of n ranging from 0 for heavily cemented sands (equivalent to rock) to 0.5 for clean sands.

Upon shearing, the initial contribution of the cementation bonds to the stiffness and the strength ($p_{cem,initial}$) degrades as a function of damage tracked here through the accumulation of strains. This approach of degrading cementation is consistent with the approaches used in other constitutive models for degrading cementation with strain accumulation or some damage index (e.g., Kavvadas & Amorosi 2000, Nova et al. 2003, Fauriel & Laloui 2012, Gao & Zhao 2012, Gai & Sanchez 2018). The accumulation of strains is initiated when the total accumulated plastic deviatoric strain ($\Sigma d\varepsilon^{pl}_{q,tot}$) reaches an elastic threshold strain (γ_{deg}) and is fully contributing to the damage by the time it reaches a "residual" strain (γ_{res}). These parameters have default values through the model's generalized calibration targeted towards capturing the broader set of data available (Section 5) but can also be assigned other values for a lab-specific calibration. Therefore, the incremental plastic deviatoric strains $d\varepsilon^{pl}_q$ are factored using a multiplier F_s which increases from 0 to 1 and are accumulated into $\Sigma d\varepsilon^{pl}_{q,degrad}$ (Equation 26). The functional form for F_s (Equation 27) follows a zero plateau before γ_{deg}, picks up as the plastic deviatoric strains reach γ_{deg}, and reaches a value of 1 as the plastic deviatoric strains reach or exceed γ_{res}:

$$\sum d\varepsilon^{pl}_{q,degrad} = F_S \cdot d\varepsilon^{pl}_q \quad (26)$$

$$F_S = 1 - \frac{1}{1+\left(\frac{\sum d\varepsilon^{pl}_{q,tot}}{\gamma_{deg}+\frac{1}{8}(\gamma_{res}-\gamma_{deg})}\right)^{rate}} \quad (27)$$

The accumulated plastic deviatoric strain $\Sigma d\varepsilon^{pl}_{q,degrad}$ constitutes the damage tracked by the model to initiate the degradation of the cementation $p_{cem,initial}$ to a "secant" or degraded p_{cem} using a similar factor F_{deg}. The factor F_{deg} follows a reverse trend compared to F_s, it starts and remains at a value of 1 until the elastic threshold strain (γ_{deg}) is reached and then it decays at a degradation rate (rate) and goes to 0 as the "residual" strain (γ_{res}) is attained. The degradation rate (rate) can be a user input parameter or can default to a function of the range between γ_{deg} and γ_{res}. The rate is increased to have the

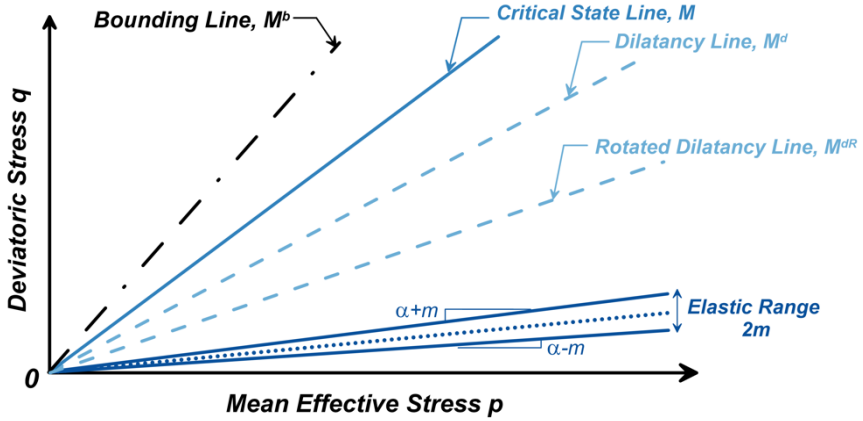

Figure 72. Schematic of the PM4Sand yield, critical, dilatancy, and bounding lines in q-p space (Boulanger and Ziotopoulou 2017) shown for a constant value of relative state parameter.

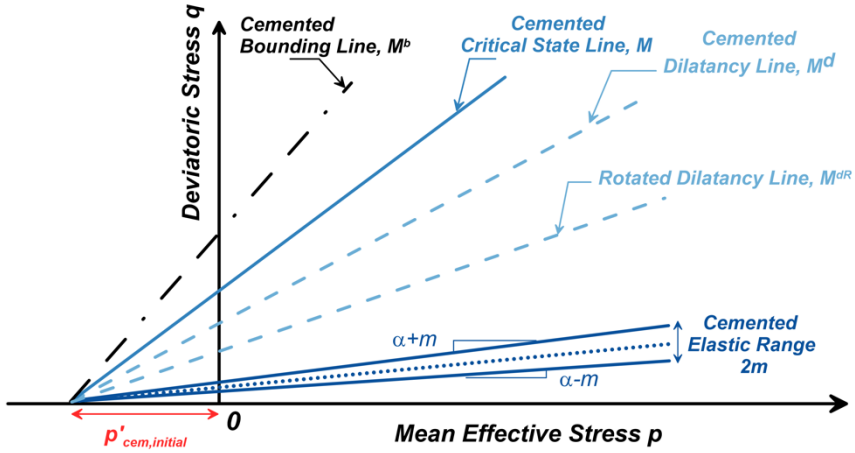

Figure 73. Schematic of PM4SandC model in q-p space at initialization shown for a constant value of relative state parameter. Following degradation, it reverts to the PM4Sand space of Figure 72.

cementation degrade over a smaller γ_{res} - γ_{deg} range and vice versa.

$$p_{cem} = F_{deg} \cdot p_{cem,initial} \quad (28)$$

$$F_{deg} = \frac{1}{1+\left(\frac{\Sigma d\varepsilon_{q,degrad}^{pl}}{\gamma_{deg}+\frac{1}{2}(\gamma_{res}-\gamma_{deg})}\right)^{rate}} \quad (29)$$

The equations from Equations 26 to 29 are essentially slowing down the accumulation of plastic deviatoric strains at the onset of degradation and then releasing it to progressively accumulate damage and subsequently decay the cementation. This is found to improve the slope of the relationship between the cyclic resistance ratio (CRR) and the number of cycles required to trigger liquefaction (N_{cyc}). From the evolution of the degradation parameters and the progressive degradation of p_{cem} the outcomes include: (1) the shrinking of the bounding and dilatancy surfaces to their original PM4Sand configuration (Figure 73) and (2) the degradation of the stiffness and the value of n exponent from its initial cemented value to 0.5, such that the model can default back to a clean sand as is the case of a sheared and damaged treated sand.

The initial contribution of cementation and its subsequent degradation are controlled by five new secondary parameters. The cohesion and peak friction angle enable the determination of $p_{cem,initial}$, while the strain at onset of degradation (γ_{deg}), the "residual" strain (γ_{res}) and the degradation rate (rate) control the degradation of the initial cementation. All these parameters have a physical meaning and a straightforward interpretation and can be calibrated based on laboratory test data which was is one of the key goals of PM4SandC. Despite the common origin of their proposed constitutive models, biocemented sands and clean sands are different geomaterials with different mechanical responses. As a result, the calibration of PM4SandC for a biocemented sand should be independent from any prior calibration of PM4Sand for its clean sand counterpart.

6.2.3. *Monotonic stress-strain behavior – simple shear loading*

Figure 74 illustrates PM4SandC simulation results for two undrained monotonic DSS tests on loose Ottawa F-65 sand treated at two different levels of cementation with D_R = 28% and initial shear wave velocity ($V_{s,o}$) 140 m/s, σ'_{vc} = 1 atm, and ΔV_s ~44 m/s and ΔV_s ~218 m/s respectively, corresponding to VsR (= $V_{s,cem}$ / $V_{s,o}$) ratios of 1.31 and 2.49 respectively. Figure 74 shows comparisons between experimental data and single element monotonic undrained DSS numerical simulation results in terms of shear stress versus shear strain deformations, stress paths, and excess pore pressure build up as a function of deformations. With the exception of some discrepancies, all comparative results show a reasonable agreement after minimal calibration, indicating that PM4SandC can capture such responses of interest.

6.2.4. *Cyclic stress-strain behavior – simple shear loading*

Figure 75 illustrates PM4SandC simulation results for an undrained cyclic DSS test on a MICP-treated Ottawa F-65 sand with D_R = 42%, σ'_{vc} = 1 atm, $V_{s,o}$ ~146 m/s, $V_{s,cem}$ ~182 m/s, and thus a V_{SR} of 1.25, subjected to a uniform CSR = 0.2. The cemented specimen triggered at 8.5 cycles based on the two triggering criteria: a single-amplitude strain of γ = 3% and an excess pore water pressure ratio r_u > 98%. While the experiment triggered at 8.5 cycles, the simulation was continued to illustrate the post-triggering strain accumulation and the damage to the cementation bonds. The simulation results are consistent with the experimental results with minimal calibration effort. The general response was prioritized in this example calibration to illustrate the behaviors of the biocemented sands instead of a test-specific calibration.

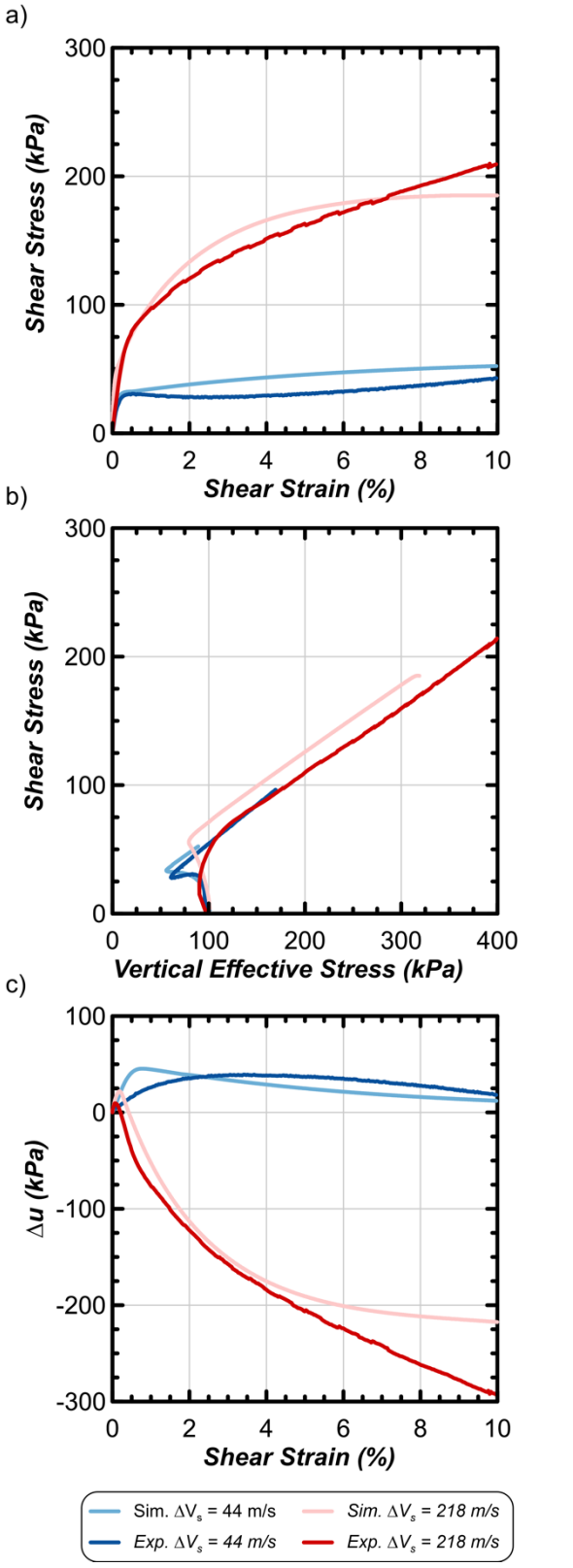

Figure 74. Comparison between experimental and simulations results for monotonic undrained DSS testing on MICP-treated sands using PM4SandC (experimental data from Lee & Gomez et al. 2022b).

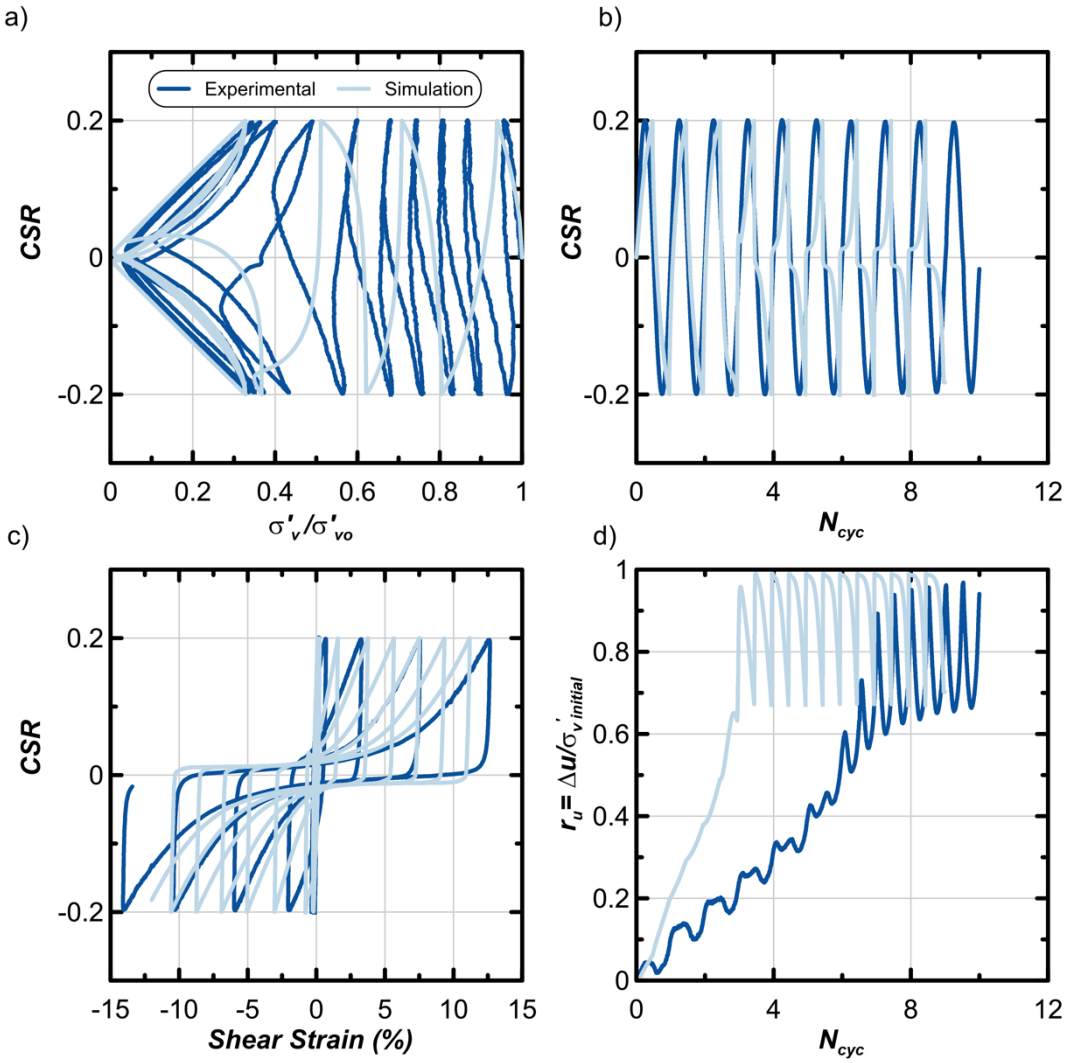

Figure 75. Comparisons between experimental and simulation results for an undrained cyclic DSS test on an MICP-treated sand using PM4SandC (experimental data from Lee et al. 2021).

Extending this calibration exercise to different CSRs defines the cyclic resistance ratio CRR versus number of cycles (N_{cyc}) curves for bio-cemented sands, where CRR is the CSR required to reach liquefaction using some triggering criterion in a certain number of cycles (N_{cyc}). In earthquake engineering, this relationship is often approximated with a power function $CSR = aN_{cyc}^{-b}$, where the parameters a and b represent the CSR at one cycle and the slope of the curve, respectively. For clean sands, the value of these parameters is a function of p and D_R, with parameter b generally ranging from 0.25 to 0.37. For biocemented sands, the same dependencies are expected to hold with an additional dependency on the level of cementation, however the applicability of the power law for treated sands is not fully established yet (Lee et al. 2021). While the value of parameter a should presumably be larger than sands due to the presence of the cementation, the value of parameter b is hypothesized to be smaller due to the larger number of cycles needed to trigger liquefaction at low CSRs. Accordingly, PM4SandC yields CRR curves that are visibly higher for biocemented sands than the curves for clean sands which, as shown in Figure 75. This is in agreement with the experimental data by Lee et al. (2021) on lightly cemented MICP-treated Ottawa F-65 sands under comparable conditions.

7 UPSCALING TO THE FIELD

Realization of the MICP technology at field scale as well as widescale acceptance as a viable and sustainable soil improvement technique requires: (1) demonstration that the technology can be reliably implemented at a cost, performance, and feasibility level that is either competitive with or superior to existing business-as-usual soil improvement techniques and (2) that engineering design guidance and numerical tools be available such that treatment magnitudes and dimensions can be designed to mitigate site-specific liquefaction hazards, including those related to both liquefaction triggering resistance and the consequences when triggering does occur.

Upscaling of the MICP technology from the research setting to the more practical field implementation setting will require that challenges similar to those encountered by existing soil improvement technologies (e.g., chemical grouting) and geoenvironmental remediation techniques (e.g., dechlorination, contaminant immobilization) be overcome. Such challenges include those related to treatment extent and uniformity, environmental controls, material use, specialty equipment, and monitoring and QA/QC evaluation. Consequently, the similarities between MICP and some existing technologies will enable use of equipment and materials processing methods that are already established industry practices and readily available from specialty contractors. Similarly, prior research on the effect

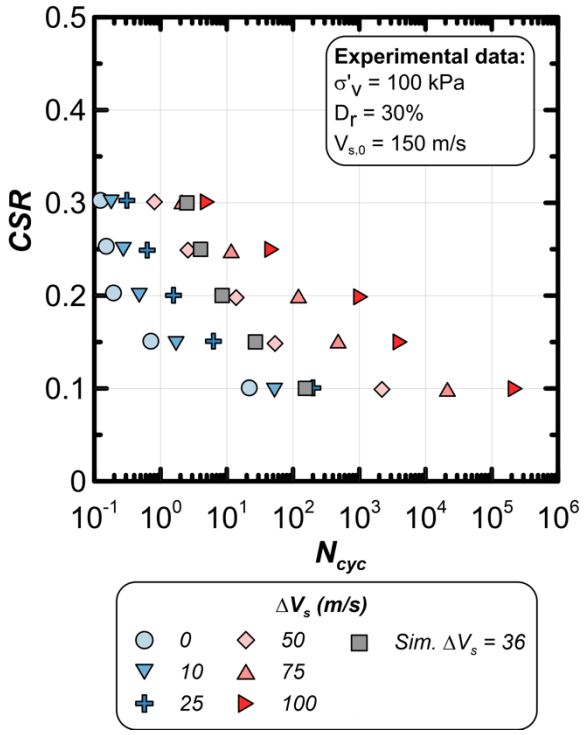

Figure 76. Comparison between the experimental CSR versus N_{cyc} curves from Lee et al. (2021) and the one from the calibration using PM4SandC for undrained cyclic DSS tests on MICP-treated sands (adapted from Lee & Gomez et al. 2022b).

of natural and artificial cementation on the liquefaction susceptibility of sands (e.g., Saxena et al. 1988. Clough et al. 1989) and the treatment extent required to provide structural stability (Dashti et al. 2010a,b) provide a basis from which MICP-specific guidelines can be further developed. Other aspects, including process monitoring and QA/QC evaluation, will leverage both existing technologies and implementation methods including the CPT q_c and V_s assessment approaches described (Section 4), and new methods that may, in return, also provide benefits for existing soil improvement technologies.

MICP's unique attributes relative to other existing soil improvement technologies make it a promising alternative technology specifically for liquefaction hazard mitigation. These attributes as detailed in the prior sections include the ability to: (1) reliably control reaction rates by using well understood biological catalysts (effectively controlling the "set time"), (2) potentially achieve greater uniformity and increased treatment extent relative to existing grouting methods (thereby allowing for reduced implementation costs), (3) treat soils with minimal site disruption requiring only fluid injections between installed wells, (4) maintain an open pore structure allowing for subsequent treatments and minimizing the impact on ambient groundwater flow conditions, (5) re-treat and heal MICP treated soils during the service life in the event of increased loading demands or damage following earthquakes, and (6) verify and monitor improvement integrity using non-invasive and other more conventional methods following application and throughout the improvement's service life.

It is envisioned that these attributes will make MICP particularly competitive and advantageous for liquefaction mitigation applications near existing infrastructure, an application for which arguably no satisfactory solution currently exists. Furthermore, MICP may also afford unique advantages with respect to the treatment of sands with high fines content (e.g., silty sands) and a variety of other anthropogenically-generated waste materials (e.g., dredge materials, hydraulic fill, fly ash, mine tailings). Similar to current soil improvement technologies, MICP will have a niche of effective applications and will not be the most economical nor practical method for every site. For instance, MICP will not likely be competitive when addressing improvement of unoccupied project sites with shallow liquefiable materials for which energy densification methods (e.g., deep dynamic compaction, vibro-densification) will remain most time, material, and cost efficient.

Significant effort has been placed on both upscaling of the MICP treatment technology for field implementation and determining the cementation magnitudes and extent required for acceptable performance of supported geosystems, specifically for instances when liquefaction susceptibility under seismic loading is of concern. A generalized design process for MICP treatment at the field scale is outlined first, followed by a section focused on upscaling of the MICP treatment method to the field and finally a section highlighting how MICP treatment can be effective towards mitigating liquefaction hazards.

7.1 *MICP design process for field implementation*

The envisioned design process for MICP field implementation is presented in Figure 77. The six stages, preliminary suitability evaluation, technology compatibility with site conditions, site characterization, design requirements, implementation plan, and monitoring and QA/QC, each require that specific activities be performed to achieve stage objectives. This process is expected to be non-linear during process implementations, with several iterations likely required in the latter stages (as indicated by the feedback arrows in Figure 77). The process is also likely applicable to other emerging biomediated technologies, including microbially induced desaturation and precipitation (MIDP) and enzymatically induced $CaCO_3$ precipitation (EICP), and is broadly consistent with the design processes used for existing soil improvement technologies as detailed by Mitchell et al. (1981, 2008), USACE (1999), NHI (2017a, 2017b) and (Nicholson 2015). The following sections further detail each stage of this design process.

7.1.1 *Preliminary suitability evaluation*

The initial screening stage evaluates the suitability of MICP for some project by considering the anticipated site conditions, earthquake loading, and performance requirements. Site conditions of specific interest to MICP implementations include information about groundwater chemistry, soil mineralogy, classification, and state, obtained from prior site specific, regional, or geologic model information, which can be used to further evaluate biogeochemical treatment compatibility and expected success of MICP towards improving soil engineering properties at the level needed for project requirements. The knowledge base regarding treatment feasibility, exemplified in Figures 28 and 29, may be sufficient when initial screening evaluations reflect advantageous conditions.

The estimated earthquake loading, obtainable from regional hazard maps or more site-specific studies, and the performance requirements of the infrastructure system being stabilized/supported, such as deformation tolerances or system stability, may be used to estimate the magnitude and spatial extent of improvement required. The magnitude of cementation required can be approximated from laboratory derived cyclic resistance curves (e.g., Figure 60), and given that MICP treatment can increase the CRR by an order of magnitude or more for a given loading demand when sufficient cementation is present (Figure 61), it is likely that the required improvement for some system could be realized. The treatment dimensions required would be estimated at this stage primarily from

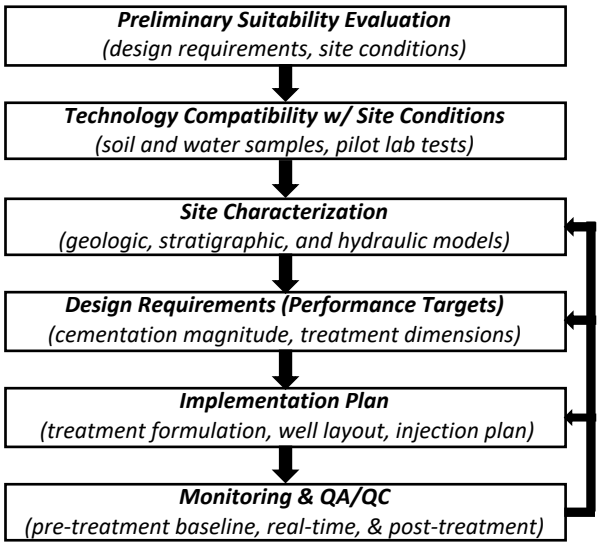

Figure 77. Overview of design process for MICP field implementation.

information obtained regarding stratigraphic conditions and site footprints.

7.1.2 *Technology compatibility with site conditions*

Once identified as a potentially viable improvement alternative, site-specific evaluations can commence to further verify specific applicability to and effectiveness for some targeted treatment zone. The realization of and ability to control the MICP biogeochemical reaction network is primarily dependent on site-specific environmental and geologic conditions, with an understanding of groundwater chemistry and soil mineralogy being particularly important. Soil and groundwater samples may be aseptically obtained during an investigation program and can be further analyzed to establish baseline in situ conditions, and subsequently used to perform site-specific soil column laboratory tests to evaluate the efficacy of the MICP process, including the success of stimulation, cementation, and by-product removal stages. A suite of columns tested in parallel may be desirable to parametrically evaluate treatment process variables and identify the preferred treatment formulation. Monitoring of pressures and flow rates during column tests can further constrain hydraulic conditions which may be desirable for field implementation as well as provide some understanding of the potential for soil hydraulic conductivity reductions during the treatment process. Monitoring of shear wave velocity during such tests will further indicate the rate of shear modulus improvement per treatment cycle, and when paired with post-treatment soil $CaCO_3$ content measurements can provide a measure of treatment efficiency that can be evaluated upon comparison with the existing knowledge base for similar materials (e.g., Figure 40 & 41) and further used to constrain expected treatment solution concentrations and required numbers of treatment cycles.

Evaluation of the improvement in soil undrained cyclic behaviors can either be estimated by comparing achieved metrics from columns tests, including shear wave velocities, $CaCO_3$ contents, and other soil strength parameters, to existing studies for similar levels of improvement (Figures 39-41 & 60) or can be evaluated rigorously at a site-specific level through treatment and testing of simple shear or triaxial specimens using the preferred treatment formulation identified in the first portion of this stage. Due to the small levels of cementation necessary to produce a significant improvement in cyclic resistance (e.g., Figure 61), specimens obtained from rigid column tests should not be extruded and subsequently tested to obtain estimates of cyclic resistances, as material integrity will almost certainly be compromised (see Section 3.8.2). Thus, for sandy soils, dedicated testing on reconstituted moist tamped samples where treatments are applied to specimens under effective stress conditions representative of in situ conditions and subsequently subjected to cyclic loading events are likely most appropriate.

7.1.3 *Site characterization*

A 3D subsurface model that is informed by geologic depositional sequences and processes and contains comprehensive details regarding the soil stratigraphy and layer connectivity, mechanical properties, and hydraulic conditions is necessary to characterize the site at a level that enables design requirements, implementation plans, and monitoring and QA/QC methods to be specified. This stage begins with the development of a depositional process informed geologic model and follows with in situ testing and laboratory characterization of the soil stratigraphy and engineering properties of soil units, as is typical for all geotechnical projects, with more detailed evaluation of site hydraulic conditions that will likely strongly influence the implementation plan.

Identifying the treatment zone will require both simplified 1D analyses on individual soundings/borings and generation of 2D/3D spatial realizations that are conditioned on the soundings/borings. Initial evaluation of the engineering properties and the target treatment zone for liquefaction mitigation will include analysis of CPT/SPT profiles using 1D liquefaction methods to estimate susceptibility to triggering (Boulanger & Idriss 2015) and potential volumetric and shear strains (Iwasaki et al. 1978, Zhang et al. 2002, 2004, van Ballegooy et al. 2014). Further insights may be obtained by generating conditioned 2D/3D realizations of the subsurface, particularly for the identified liquefiable layers. Intra-spatial modeling of the depositional variation within the potentially liquefiable layers can provide insights into density variations across the target treatment zone, while interspatial modeling of the liquefiable and surrounding layers can better define the bounds of treatment necessary. Stochastic conditional modeling (e.g., Fenton & Vanmarcke 1990, Griffiths et al. 2002, Jaksa et al. 2005, Montgomery & Boulanger 2017) and categorical conditional modeling (e.g., Carle & Fogg 1996, DeJong et al. 2021, Bassal et al. 2021, 2022) approaches have been shown to be effective methods for generating realistic geostatistical subsurface realizations that are conditioned on obtained in situ data. Obtained realizations of the subsurface conditions, including the engineering properties of each layer, can then be directly incorporated into continuum models (e.g., FLAC) for subsequent design purposes including non-linear dynamic analyses.

Evaluation of site hydraulic conditions, with particular focus on the potentially liquefiable layers, can begin using hydraulic properties estimated from in situ tests (e.g., CPT) and lab data, but may also include the use of additional dedicated in situ tests to better resolve hydraulic properties with depth (e.g., hydraulic profiling tool). Such characterization will also likely include the installation of a test well(s) through which both staged pumping (lugeon) tests and long-term monitoring of ambient conditions can be performed. The hydraulic model developed can be used to assign hydraulic properties to the units in the conditioned stratigraphic model generated for liquefaction evaluation and should resolve the locally defined values with the staged hydraulic pumping test results, which provide a global spatially averaged hydraulic system response. Reconciliation of the fine stratigraphically linked hydraulic conditions against the global pumping response can be achieved using a variety of hydraulic modeling software programs (e.g., ModFlow, PhT3D, etc.). Once resolved, these 2D/3D hydraulic models afford subsequent

investigation and development of specific treatment implementation plans.

7.1.4 *Design requirements & performance targets*

The MICP treatment program design requires specification of the targeted improvement magnitudes and spatial extent. The improvement magnitude can be estimated based upon the expected seismic demand throughout the soil profile as calculated by 1D liquefaction triggering evaluation methods and the level of cementation required to increase the CRR in the susceptible soil layers such that a factor of safety of one or higher exists throughout the soil profile. The cementation level required, as identified by either a soil $CaCO_3$ content or shear wave velocity increase (Figure 40), can be estimated from general relationships such as those shown in Figure 61. However, it may be preferrable if a site-specific CSR versus N_{cyc} curve is developed using simple shear or triaxial test results performed on soil specimens sampled from the liquefiable layer and reconstituted to conditions similar to that in situ. The improvement magnitude estimated with this approach is the improvement required for free field conditions only and ignores three dimensional aspects of treatment non-uniformity, subsurface non-uniformity, infrastructure load distributions and other specifics, as well as site-specific dynamic wave propagation, among other factors. Consequently, it is likely that the improvement level specified during this phase will underestimate the improvement level required for some acceptable performance.

MICP improvements as realized in the subsurface will inevitably have some degree of inherent non-uniformity despite the design measures taken to minimize such variations. Therefore, it is likely that some zones will be improved below the target improvement level with others being at or above the desired improvements. From this perspective, the improved soil and related system will likely behave as a composite of both weaker zones, which would trigger at a lower cyclic demand if considered in isolation, and stronger, stiffer, and more dilative zones, which may act to dampen excess pore pressure generation and limit shear strains in surrounding weaker soil regions. Such systems-level behaviors have yet to be fully explored and understood, however, it is clear that treatment uniformity and its post-treatment characterization will play an important role in this response and thus continues to be a focus of ongoing research.

The treatment extent and spatial distribution required depends directly on whether or not the site supports a structure, and if so, what structural characteristics are critically important. When infrastructure is already present at some site to be improved, the desired treatment zone can be estimated following related earthquake engineering and soil improvement studies which have characterized the effect of discrete treatment zone volumes (i.e., depths and widths) and normalized such dimensions in accordance with the surrounding infrastructure dimensions and knowledge of stratigraphic layers with simplified geometries in order to enable more general use (e.g., Hausler 2002, Dashti et al. 2010a, b). MICP specific guidelines for treatment zone extents and distributions, however, have not yet been developed to a level where these guidelines can be detailed.

Furthermore, non-linear dynamic analyses using FLAC or other numerical platforms provide the opportunity to develop site-specific treatment magnitude and extent designs that incorporate the three-dimensional aspects of subsurface non-uniformity, infrastructural load distributions, and dynamic wave propagation. Implementation of this complexity requires accurate calibration of appropriate constitutive models for cemented soils (such as PM4SandC described earlier in Section 6.2) and verification and validation of such models against detailed case histories (e.g., centrifuge model data). At this time, geomechanical numerical modeling of a project site with an MICP improved zone has not yet been performed. Instead, only the initial study shown subsequently in Section 7.3 has been performed using a simplified 2D analysis.

7.1.5 *Implementation plan*

The implementation plan to deploy MICP at some project site requires details regarding the achieved microbial and related precipitation reaction rates, solution transport rates and distributions during applied treatment injections, specific dimensions regarding well spacings, layouts, and their relation to the intended treatment zone, as well as injection details such as treatment volumes and the associated required infrastructure needed for preparation, mixing, and application of MICP treatment solutions.

Treatment spatial distribution and uniformity is governed largely by the advective-dispersive injection regime as well as the reactive transport during injections which is directly dependent on the achieved ureolytic reaction rates relative to applied solution transport rates. Ideally, every treatment solution would be injected with minimal reactions occurring during injections, thereby achieving a near uniform distribution of reactants after injections that is governed only by the advective-dispersive flow characteristics of the application system and surrounding soil. In this case, a stop flow retention period could be provided and near uniform improvement could be achieved. Instead for actual field applications, some fraction of reactants will be consumed during injections thereby precipitating more $CaCO_3$ closer to injection sources, with dispersion generating further gradients in transported concentrations, and surrounding groundwater gradients perhaps altering the distribution of generated $CaCO_3$ during the stop-flow retention and reaction period. The practical objective to achieve greater cementation uniformity is to ensure that reactions occurring during injections are minimized. This is accomplished when the microbial reaction rates are much slower than transport rates, resulting in only a small percentage of reactants being consumed during the injection of solutions. Non-uniformity is inevitable, however, practical tolerances for desired reaction rates and flow rates can be determined from passive tracer simulations and more refined reactive transport simulations.

Microbial reaction rates and thus $CaCO_3$ precipitation rates can be controlled by varying the applied treatment solution formulation during both the stimulation (Section 3.2) and cementation phases (see Section 3.3). As shown previously, variations in reaction rates can be largely accomplished by varying supplied growth factors and nutrients as shown by varying yeast extract in the authors' experiments (Figure 20). The transport rate is primarily controlled by the hydraulic conductivity, hydrostatic pressure, and hydraulic fracturing pressure and the distribution of flow is primary controlled by soil porosity, dispersive properties, and fluid density gradients, when present. Conceptually, when low ureolytic and precipitation rates are achieved, reaction completion for a single treatment could occur over 50 to 100 hours providing the opportunity for longer injection durations (10 to 20 hours) to still achieve significant treatment uniformity and a large extent of improvement. The authors' experiments, while not exhaustive, have shown that ureolytic activities can be slowed to achieve reaction completion over at least 48 hours (Lee et al. 2022). Maximizing treatment extent is key towards enabling larger spacings between treatment wells, thereby reducing implementation costs. In reasonably permeable sands with low dispersivities, well spacings near 5 to 10 m may be achievable and practical.

The well layout pattern at the project site is driven by the: (1) geometry of the desired treatment zone, (2) level of uniformity

required, (3) flow rate and dispersion constraints, and (4) need for post-treatment byproduct removal. Pilot field trials may involve simplistic injection layouts such as well dipoles or larger well networks consisting of some center injection/extraction well surrounded by a set of injection/extraction wells (Sorenson 2021) and can be used to evaluate soil advective-dispersive flow characteristics, potential treatment distributions, as well as guide optimization of well patterns, treatment control, and uniformity. When upscaled it is expected that some variation of a repeating triangular or square well pattern with both injection and extraction wells can form a near-closed loop treatment system that can be implemented. It may be advantageous to extract solutions at higher volumes than those injected to better control treatment extent and contain byproducts. It may also be advantageous to reverse flow directions on occasion in order to improve treatment uniformity. This strategy is consistent with that used for some chemical grouting and bioremediation technologies; hence, the application system infrastructure required and associated operations are already known in industry. To ensure ease of monitoring, monitoring wells and or other sampling devices should be installed prior to treatments, with locations determined by non-reactive and reactive transport simulations as discussed later.

Design of the desired biomediated reaction rate, injection and extraction rates and volumes, and well spacings, layouts, and other geometries, have interdependencies that are best optimized by performing numerical advective-dispersive flow simulations that are anchored to site characteristics determined during in prior stages and calibrated to achieved field data. Although bulk and or localized permeabilities can be crudely determined using a single injection well test (with packers used to potentially isolate some treatment zone), calibration of soil advective-dispersive properties requires at least two well tests wherein a conservative tracer is injected at some known concentration and observed at surrounding outlet wells. This process, referred to as a breakthrough curve or passive tracer testing, will yield data similar to that shown in Figure 26 from a simple 1D soil column test receiving injected bromide ions, however, similar processes and other conservative tracers, such as chloride ions, can and have been used with equal success in the field. Such data can allow for refinement of the hydrogeological model in order to account for bulk properties of the porous media in the treatment zone including soil porosities, dispersion coefficients, and other physical flow non-uniformities resulting from containment loss and or inherent soil hydraulic heterogeneity, among other features. Hydrogeological modeling software capable of 3D non-reactive transport modeling include FEFFLOW, MODFLOW, and Hydrus, among others.

To account for reactive transport during simulations, however, more complicated means are necessary. Reaction rates can be designed initially leveraging soil column pilot test data, however, ultimately, monitoring of reaction rates as observed in the field condition will be necessary. Soil column data, therefore, can be used to guide initial implementation plans with collected real-time site data allowing for modifications in applied treatments and updating of reactive transport simulations, as necessary. While a variety of software packages can be used for simple 1D reactive transport simulations including PHREEQC, TOUGHREACT, and others, field scale modeling will require more complicated 3D reactive transport platforms such as PHT3D, OPENFOAM, COMSOL, and TOUGHREACT V3.3-OMP, among others. Ultimately, such models require a non-trivial effort, thus, considerations should be made regarding the value of such reactive transport simulations over the use of more simplified non-reactive simulations. The need for refinement may be largely determined by considering the effect of uncertainty on such simulations and the related impacts anticipated for predicted improvement distributions.

7.1.6 *Monitoring & QA/QC*

Monitoring during the treatment implementation period is necessary to ensure that the project is being realized as predicted and designed, while post-treatment QA/QC is necessary to verify that the desired design was realized in situ. It may also be desirable to continue to monitor the integrity of the cementation over the service life of some project to assess the potential for long-term chemical damage and or mechanical degradation after some extreme loading event (e.g., earthquake loading). The array of monitoring tools available, as described in Section 4, are extensive and are capable of discerning specific biogeochemical and geotechnical changes that occur throughout all treatment stages (i.e., stimulation, cementation, byproduct removal). However, only a subset of such measures are well suited for real-time monitoring of the process in situ during treatments.

Prior to injections, solutions should be subsampled and chemical analyses should be performed to verify that intended solution chemical compositions were achieved. Similar subsamples can be retained from production well locations during injections to examine changes in effluent solution chemistry in time during solution replacement. During stop-flow residence periods, aqueous samples can be periodically obtained from monitoring wells and embedded non-destructive probes and/or sampling devices should be present to capture reaction dynamics. While in-situ chemical specific probes can be suspended within injection, production, and monitoring wells at some treatment depth, it may be more practical to use simple probes capable of continuous fluid conductivity and pH measurements, if solution chemistry allows for some indirect measure of reaction progression in time. For example, as shown in Figure 3 and 36, solution pH can provide a useful method for indirect monitoring of cementation completion, as a large pH increase can be observed once calcium is fully consumed, provided that urea is provided in excess of calcium (urea to calcium ratio > 1.0).

Shear wave velocity is the preferred practical approach for tracking mechanical improvements in soils during treatments given its direct proportionality to soil $CaCO_3$ content (Figure 40), the breadth of established methods for measuring such velocities in situ (e.g., SCPT, cross-hole), and its non-destructive nature. With a sufficiently dense sensor array tomographic images of the spatial changes in shear wave velocity could be tracked during the treatment phase (e.g., Lee et al. 2005, Kim & Kim 2010). Other measures, such as compression wave velocity, are either less sensitive to such mechanical enhancements, and/or may only be practically useful at existing well/borehole locations.

Preferred post-treatment QA/QC processes include many of the same methods used to determine the initial site baseline conditions. Such methods may include drilling and destructive sampling (e.g., split spoon, sonic coring), seismic CPT soundings, and other geophysical measurements for biogeochemical and mechanical engineering analysis. Data obtained during assessment of the final improved state can be compared against the targeted designed improvement levels (e.g., soil $CaCO_3$ content, V_s increases) and against existing broader databases of such values (e.g., Figure 46) to ensure that the intended treatment program was realized and that the process followed conventional expectations for improvement progression. Collection of such data provides an opportunity to contribute to refinement of such relationships and our broader understanding of these behaviors.

Finally, continued monitoring over the service life of the improvement may be necessary, particularly when MICP improved zones are subject to somewhat undersaturated

groundwater and extreme loading events that might compromise cementation integrity. For these instances, depending on the mechanisms (i.e., mechanical versus chemical degradation), both soil $CaCO_3$ content and shear wave velocity measurements may be useful towards characterizing degradation (e.g., Figure 19 & 54). Furthermore, additional evaluation could be performed by SCPT or cross-hole seismic methods (particularly if cased holes remain accessible), and in some cases surface wave methods (e.g., SASW) when the treatment zone is relatively shallow.

7.1.7 *Summary*

The design process recommended and outlined above has been informed by past upscaling and liquefaction mitigation experiments performed using MICP to date as well as by established practices developed by others performing conventional soil improvement and geoenvironmental remediation methods. This envisioned process articulates the authors' vision regarding how MICP can be successfully and systematically designed and implemented in the field. It is important to reiterate that this design process is not a linear series of events and stages. Instead, this process may be frequently revisited during the implementation of MICP at some site to incorporate new information and understandings that will guide final application strategies. It should also be mentioned that field applications of MICP for liquefaction mitigation purposes have not yet been realized to the authors' knowledge. With this in mind, the following sections focus on specific studies performed in a research context wherein understanding of how MICP can be upscaled to the field and effectively mitigate liquefaction hazards in sandy soils has been both demonstrated and expanded.

7.2 *Upscaling of MICP treatment methods*

Following its initial conception, research efforts regarding MICP have been largely divided between exploring the more fundamental science governing the biogeochemical process and developing the engineering capacity needed to implement the technology at field scale and achieve practical industry acceptance and adoption. This dual approach has proven very useful, with improved scientific understandings guiding upscaling efforts, and upscaling efforts in turn allowing for the identification of critical development challenges and knowledge gaps requiring improved fundamental understandings.

Table 5 presents a summary of the upscaling projects to date that have been performed at length scales exceeding ~0.5 m, with target applications including slope stabilization, fractured rock sealing, strontium immobilization, and grouted piles, among other uses. Projects are listed in Table 5 in order of publication year, with information regarding the length scales, flow and geometric conditions, treatment methods, targeted applications, and primary reference(s) also provided. As shown, numerous upscaling studies have been performed by the broader MICP research community, each of which have provided new insights and address aspects of practical upscaling challenges. San Pablo et al. (2020) presents the most recent upscaling experiment by the authors and is described in greater detail as it addressed aspects of all six stages of the proposed design process presented in Figure 77. Although each of the above studies in Table 5 merit an extended discussion, this particular study is the focus of the next section as it highlights current state of the art processes for technology upscaling as recommended by the authors.

7.2.1 *MICP upscaling in ~4 m long 1D columns*

San Pablo et al. (2020), with particular aspects detailed further in Lee et al. (2019b), performed MICP treatments in five 3.7-m long horizontal columns (0.15 m^3 total soil volume) containing one of three different natural sands. The upscaling study was performed specifically to address outstanding field upscaling issues including the: (1) success of pure augmentation approaches versus different stimulation strategies, (2) improvement of treatment spatial uniformity, (3) optimization of stimulation and cementation treatment formulations, (4) evaluation of practical treatment extents, and (5) removal of generated treatment byproducts. A subset of these test results from three columns containing the same alluvial poorly graded silica sand (Concrete Sand) is presented herein to highlight the study's findings with respect to the above objectives, highlight the interdependencies between different aspects of the treatment process, and exemplify how different stages of the treatment design and implementation process can be addressed.

7.2.2 *Test design*

The test design leveraged insights from small-scale laboratory soil column tests involving the same alluvial sand which demonstrated advances regarding: (1) the ability of modified stimulation techniques to reliably control achieved bulk ureolytic rates and related cementation rates thereby minimizing reactions during solution transport (Lee et al. 2022), (2) the optimization of the treatment solution compositions used during stimulation and cementation which afforded reduced material usage and environmental impacts (San Pablo et al. 2022a), (3) monitoring of biogeochemical and geomechanical aspects of the MICP treatment process in near-real time (Gomez et al. 2019), and (4) techniques for effective removal of ammonium byproducts following cementation (Lee et al. 2019a).

Prior to treatments, reactive transport pre-modeling was performed involving similar 3.7 m long 1D columns in PHREEQC. In order to ensure representative transport, modelled column advective-dispersive properties and porosities were calibrated to observed passive tracer test data obtained from the physical column experiments immediately prior to treatments (Lee et al. 2019a, b). Leveraging measured bulk ureolytic reaction rates from the earlier laboratory experiments, a Michaelis-Menten ureolytic kinetic model similar to that described in Section 4.1.2 was calibrated to the experimental data. Column reactive transport models then assumed these similar rates applied at all locations along columns and reaction rates were varied to explore the sensitivity of predicted cementation distributions in columns to these factors while assuming a constant injection flow rate that would be used for all columns. From these results, it was determined that one column would receive modified stimulation and cementation treatments intended to achieve "slow" ureolytic reaction rates which were expected to minimize cementation non-uniformity and increase cementation extent. These "slow" reaction rate treatments targeted ~90% degradation of the supplied 250 mM urea over a 48 hour period, with the injection period (3.1 hrs.) consisting of only ~6% of this primary reaction time. A second column received unmodified stimulation and cementation treatments used frequently in past stimulation experiments performed on cm-scale laboratory columns and achieved a relatively "fast" bulk ureolytic rate. In this case, "fast" reaction rate treatments targeted ~90% degradation of the supplied 250 mM urea over an 8 hour period, with the injection period now consisting of ~40% of the primary reaction time. While these two columns provided the opportunity to contrast differences in reactive transport conditions afforded by differences ureolytic rates, a third column was augmented with *S. pasteurii* to compare the success of stimulation approaches to that afforded by augmentation. This augmentation approach did not provide additional nutrients (yeast extract) following introduction of non-native cells, thus the potential for unintended stimulation was minimized. The provided cell densities in the augmented column were intended to enable a similar bulk ureolytic rate as the "high" rate

Table 5. Summary of MICP upscaling projects performed.

Year	*Model vs. In situ*	*Flow geometry (1D, 2D, 3D), Shape*	*Dimensions[1] (m)*	*Soil Type*	*Treatment Method*	*Application(s)*	*References*
2007	In situ	1D, column	5.0 long x 0.06 diameter	SP (Itterbeck Sand)	Augmentation	Soil improvement	Whiffin et al. 2007
2009	Model	3D, box	0.9 x 1.1 x 1.0	SP (Maas River Sand)	Augmentation	Soil improvement	van Paassen et al. 2009
2009	Model	3D, box	8.0 x 5.6 x 2.5	SP (Itterbeck Sand)	Augmentation	Soil stabilization for horizontal drilling, QA/QC methods	van Paassen et al. 2009, 2010
2011	In situ	3D, zone	1.25 deep x 0.9 diameter	SP (alluvial sand)	Stimulation	Stimulation, soil improvement, QA/QC methods	Burbank et al. 2011
2011	In situ	3D, zone	1000 m^3 (limits unknown)	GP	Augmentation	Soil stabilization for horizontal drilling, QA/QC methods	van Paassen 2011
2012	Model	3D, box	6.0 x 4.5 x 1.5	SP (Itterbeck Sand)	Augmentation	Soil improvement	Esnault Filet et al. 2012
2012	In situ	3D, zone	4.7 x 4.3 x 1.5	GP (river alluvium)	Stimulation	Strontium immobilization	Smith et al. 2012
2013	In situ	2D, planar	25 m deep x 4 m^2 area	dacite volcanic rock formation	Augmentation	Fracture sealing	Cuthbert et al. 2013
2014	Model	2D, 1/4 well pattern	0.5 x 0.5 x 0.15	SP (Ottawa 50-70)	Augmentation	Soil improvement	DeJong et al. 2014
2015	In situ	3D, test plots	4.9 x 2.4 x 0.3	SP	Augmentation	Surface erosion	Gomez et al. 2015
2016	Model	2D, rock slabs	1.75 x 1.75	granite	Augmentation	Fracture sealing	Minto et al. 2016
2016	In situ	3D, zone	341 m deep injection	fractured sandstone	Augmentation	Fracture sealing	Phillips et al. 2016
2017	Model	2D, circular tanks	1.7 diameter x 0.5 long	SP w/ fines (Concrete Sand)	Augmentation & Stimulation	Augmentation vs. stimulation, treatment monitoring	Gomez et al. 2016, 2018, Graddy et al. 2018
2018	In situ	3D, zone	310 m deep injection	wellbore cement	Augmentation	Wellbore sealing	Phillips et al. 2018
2019	Model	3D, box	2.0 x 2.0 x 2.5 m	various sands	Augmentation	Erosion control	Beguin et al. 2019, Esnault Filet et al. 2020
2019	Model	1D, square column	3.7 x 0.2 x 0.2	SP w/ fines (Concrete, Delta, & Covelo Sands)	Augmentation & Stimulation	Augmentation vs. stimulation, treatment monitoring, QA/QC methods, byproduct removal	Lee et al. 2019, San Pablo et al. 2020
2019	In situ	3D, zone	4.7 x 4.3 x 1.5	GP (river alluvium)	Stimulation	Biogeochemical processes, geophysical measurements	Saneiyan et al. 2019, Ohan et al. 2020
2020	Model	3D, box	0.91 x 0.91 x 0.91	SP (silica sand)	Augmentation	Scour mitigation around piles	Do et al. 2020, Montoya et al. 2021
2020	In situ	3D, test plot	1.0 x 8.0 x 0.2	SP	Augmentation	Slope stability	Ghasemi and Montoya 2020, 2022
2020	In situ	3D, zone	698 m deep injection	wellbore cement	Augmentation	Wellbore sealing	Kirkland et al. 2020
2020	In situ	3D, slope	100 x 10 x 4.5	silty clay	Augmentation	Slope stability	Terzis et al. 2020
2020	Model	3D, box	1.0 x 0.6 x 0.6	SP calcareous sand	Augmentation	Pile capacity	Xiao et al. 2020
2021	In situ	3D, zone	310 m deep injection	wellbore cement annulus	Augmentation	Wellbore sealing	Kirkland et al. 2021a
2021	In situ	3D, zone	697 m deep injection	sandstone	Augmentation	Wellbore sealing	Kirkland et al. 2021b
2021	Model	3D, zone	1.0 x 1.0 x 1.6	SP (Bar Sand)	Augmentation	Pile capacity	Lin et al. 2021
2021	Model	3D, zone	15 x 1.2 x 0.5	SP	Augmentation	Erosion control	Montoya et al. 2021
2021	Model	3D, box	1.1 x 1.0 x 0.9	SP (Ottawa sand)	Augmentation	Soil improvement	Wu et al. 2021
2021	In situ	3D, zone	5.0 deep x 5.0 diameter	fine grained soils	Augmentation	Soil improvement	Zeng et al. 2021
2022	Model	3D, box	1.0 x 0.4 x 0.3	SP (silica, calcareous)	Augmentation	Road base improvement	Xiao et al. 2022

[1] *Dimensions specified are of the treated zone when possible, otherwise dimensions specified based on container dimensions.*

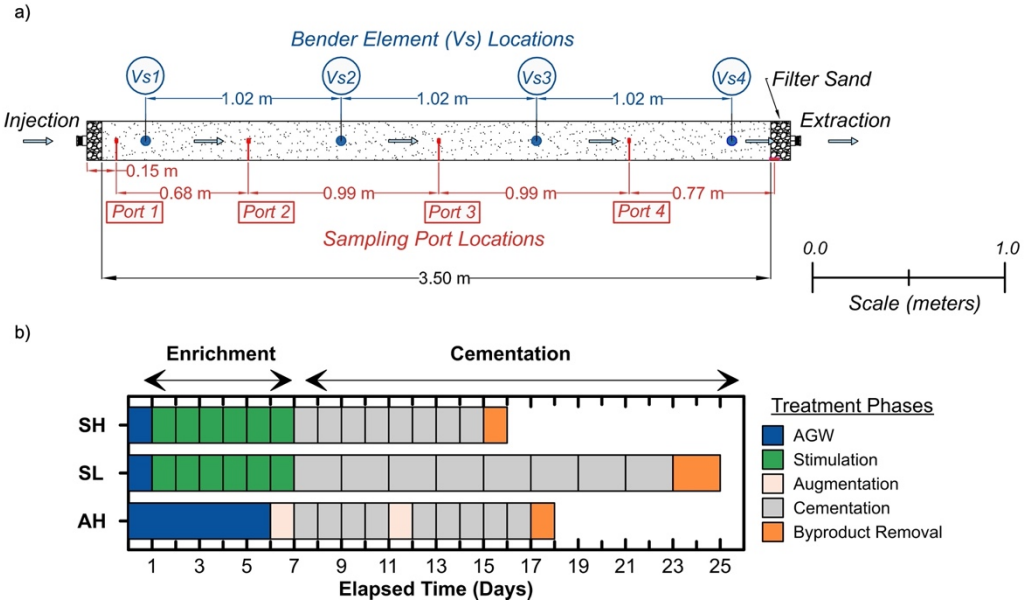

Figure 78. Overview of (a) 3.7 m column set-up and (b) treatment program (adapted from San Pablo et al. 2020).

stimulated column (at the time of the first cementation treatment) across the entire column length. Herein these three treatment approaches are referred to as SL for "stim low", SH for "stim high", and AH for "aug high".

The test configuration, designed to simulate a single stream tube within a well-to-well half space, is shown in Figure 78a. Each setup consisted of a horizontal 3.7-m long steel column with a square cross-section (0.2 x 0.2 m) that contained 0.15 m^3 of soil. The natural soil was moist tamped in place to a relative density of about 62% (and a corresponding porosity of about 0.35), resulting in the total pore volume (PV) being about 50 L. Pairs of bender element sensors were placed at equally spaced intervals along the column to measure soil shear wave velocities at various times during treatments. Aqueous sampling ports enabled direct sampling from the middle of column cross-sections and were placed at five offset locations along the column lengths. Solutions injections during all treatment stages except for the byproduct removal stage was performed at a constant rate of about 0.6 L/min and involved a treatment volume of near 1.5 PV (76 L). Injection durations were ~3.1 hours for all treatments. The pumping system involved a closed circulation system at the influent location in order to control injection flow rates and pressures and a static tailwater head was used to maintain full saturation. Pressure sensors were used to measure fluid pressures during injections in order to track soil hydraulic conductivity changes in time.

The 26 day treatment program implemented, as summarized in Figure 78b, consisted of the following steps. First, columns were saturated with artificial groundwater and passive tracer testing was performed by injecting 1.5 PV of a 15 mM NaBr solution followed by 1.5 PV of deionized water in all columns while monitoring effluent concentrations in time to establish passive tracer breakthrough curves. Soil columns were then subjected to varying biological treatments (either stimulation or augmentation), followed by cementation and ammonium byproduct removal phases, with the treatment timeline and injection frequency of each phase indicated in Figure 78b. Importantly, the number of stimulation treatments were identical between the two stimulation columns (SL and SH) and the number of cementation solution injections were identical between all three columns. As shown, augmentation treatment injections were performed twice due to the poor performance observed during the initial cementation treatments following the first augmentation. Particular treatment formulations used are detailed in San Pablo et al. (2020) as well as provided in Table 2 in Section 3.3. Prior to and at select times following each treatment injection, aqueous samples were collected for chemical and biological measurements, bender element measurements were performed to examine shear wave velocity progression, and flow rate and fluid pressure measurements were obtained during injections for hydraulic conductivity determination. Following test completion, all columns were destructively sampled along their length for further evaluation, including measurements of soil $CaCO_3$ contents and residual sorbed ammonium masses as well as SEM imaging of select soil subsamples.

7.2.3 *Bacterial distributions and progression*

Aqueous total cell densities along column lengths were measured using total direct counts of aqueous subsamples at various times including after initial saturation and after the 1st, 4th, and 9th cementation treatments are presented in Figure 79a. While aqueous counts do not account for cell densities attached to soil particles, it is reasonable to assume that there is some equilibrium between suspended and attached cells and therefore the relative abundance of suspended cells may be proportional to total cell densities. It should also be mentioned that total aqueous cells in stimulated columns do not solely reflect ureolytic cells and cannot distinguish between cell densities facilitating ureolysis and those that may not be active in this process. Nevertheless, such measurements can be useful towards verifying that microbial growth is occurring during stimulation and/or the distribution of augmented cells. As shown in Figure 79a, such measurements demonstrate total cell growth within the treatment zone during the stimulation phase with aqueous cell densities largely maintained throughout subsequent cementation treatments. Initial suspended total cell densities were initially uniform along column lengths with values near 1 x 10^6 cells/mL. Measurements after the 1st cementation treatment, which followed all stimulation and augmentation treatments, however, showed a near 350% increase in the suspended cell populations for the SL column and a greater than 600% increase in the SH and AH columns. Increased cell densities in SH in comparison to SL were consistent with the rate altering stimulation processes employed and the similarity between the SH and AH values

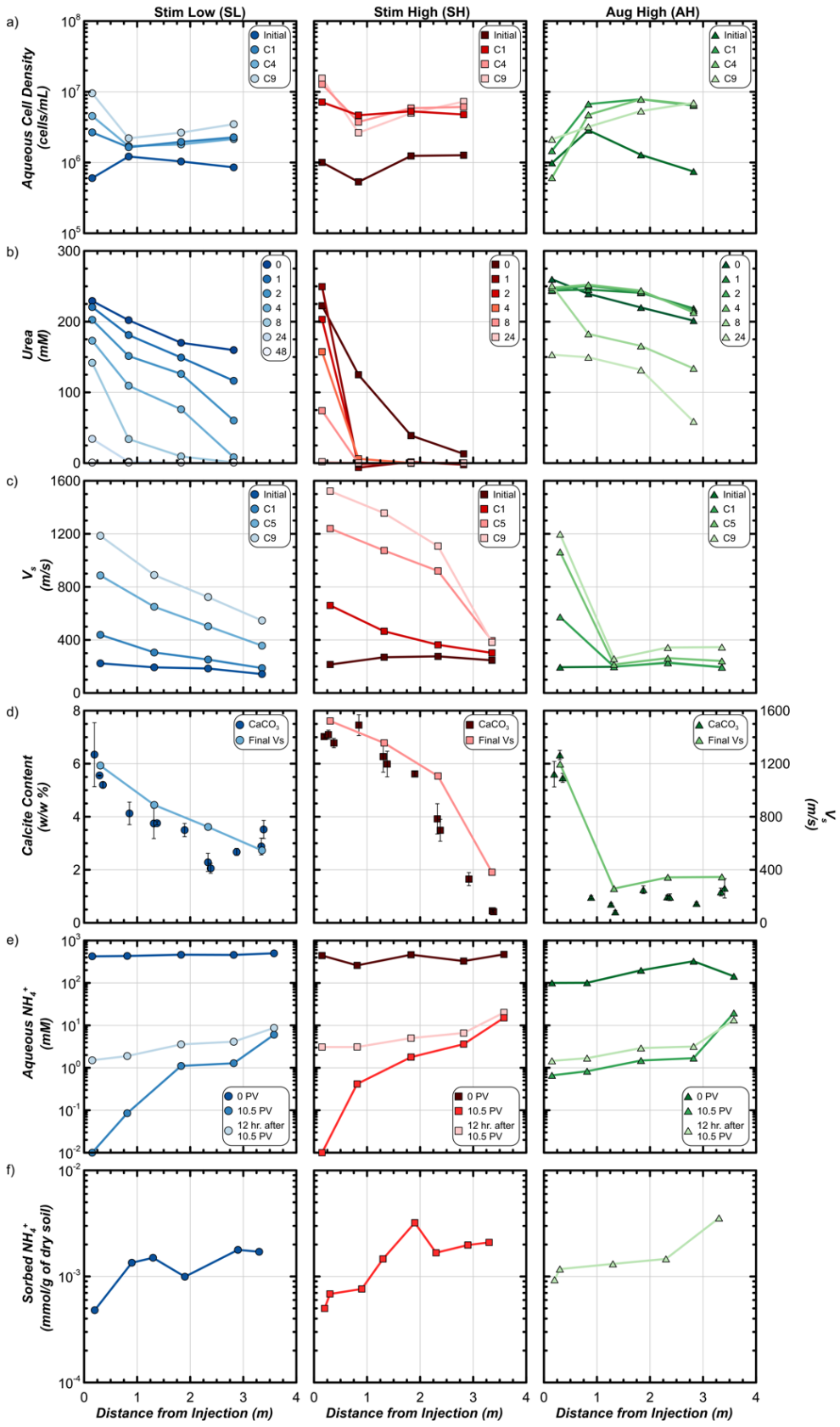

Figure 79. Comparison of SL, SH, and AH columns for (a) aqueous cell densities obtained initially, during the 1st (C1), 4th (C4), and 9th (C9) cementation treatment, (b) urea concentrations in time during the 9th cementation treatment sampled at 0, 1, 2, 4, 8, 24, and 48 hours after injection, (c) V_s measured initially, during the 1st (C1), 5th (C5), and 9th (C9) cementation treatment, (d) end condition improvement through calcite content and V_s, (e) aqueous NH_4^+ concentrations during by-product rinsing with initial (0 PV), after the full injection (10.5 PV), and 12 hours after injection (12.5 hr after 10.5 PV), and (f) sorbed NH_4^+ concentrations from soil samples (adapted from San Pablo et al. 2020).

indicated that comparable cell densities that were targeted were indeed realized. Further measurements after the 4th and 9th cementation treatments demonstrated that aqueous cell populations remained relatively constant along column lengths in all columns, with the largest changes occurring closer to injection sources. This can be at least partially attributed to the region closer to the injection location receiving higher concentrations of treatment solution constituents (including organics) as well as dissolved oxygen concentrations during the treatment injection process, which likely yielded higher bacterial cell growth in stimulated columns. In contrast, trends in the augmented column, which received no nutrients, suggested that cells may have been eluted near the injection source during repeated treatments.

7.2.4 *Urea degradation rates*

Urea degradation was further monitored in all columns to characterize bulk reaction rates during injections. Measured urea concentrations along column lengths are shown in Figure 79b for various times after the 9th cementation treatment in all three columns. Such measurements confirmed that urea degradation and related $CaCO_3$ precipitation reactions occurred along the column length as designed for different treatment variations. The distribution of urea concentrations across the column lengths measured immediately following injections, indicated as 0 hrs. after injection in Figure 79b, reveal the concentrations of urea that were delivered versus consumed during the injection period. For the SL column, the urea concentration near the injection source was near 230 mM, only a slight decrease from the injected concentration of 250 mM, while the urea concentration at the most distant sampling location (> 3 m) was near 160 mM (reflective of both dispersion and reactions during transport). In SL, the urea concentrations measured from all ports right after injection were 190 mM on average, about 76% of the injected concentration of 250 mM suggesting that more minimal urea degradation had occurred during injection. In contrast, urea concentrations in the SH column immediately after injections decreased rapidly with increases in column length such that the concentration at the most distant sampling location (> 3 meters) was near 13 mM which was only 6% of the 220 mM urea concentration measured near the injection source. Consequently, this more rapid urea degradation during the injection in SH resulted in a minimal amount of cementation occurring near the end of the column. Interestingly, urea concentrations in the AH column immediately after the treatment injection indicated that a minimal amount of urea was consumed during treatments. This was unexpected, and indicated that the augmented bacteria population present in AH was not distributed in a manner that achieved bulk rates that were similar and spatially comparable to SH.

Examination of the additional trends of urea concentrations along column lengths over the retention time, which was ~24 hours for SH and AH and ~48 hours for SL, provide further details regarding the spatiotemporal reduction of urea. In the SL column, the rate of urea reduction was slowest near the injection source, with a 90% reduction of the initial urea concentration requiring more than 30 hrs., and was most rapid at the largest injection distance, where a similar 90% reduction required only about 4 hours. Nevertheless, the ability to control the treatment process such that the majority of urea degradation and associated $CaCO_3$ precipitation occurred during the retention period instead of during the injection period resulted in more uniform $CaCO_3$ precipitation along the column length. In contrast, the urea trends in time for the SH column show that urea is consumed along almost the entire column length within about 1 hour (near injection source). This high reaction rate was expected to produce non-uniformity in delivered reagents and more localized $CaCO_3$ precipitation at relatively short distances from the injection source, leaving much of the column length with more minimal cementation. Urea degradation trends in the AH column indicated that less than 50% of the injected urea concentrations were consumed along the column length, resulting in a much lower precipitation yield.

7.2.5 *Shear wave velocities*

Shear wave velocity measurements provide the most direct indication of $CaCO_3$ precipitation occurring along the column lengths due to the direct and robust correlation between biocementation magnitudes and soil shear stiffnesses (Figure 41). Figure 79c presents shear wave velocity profiles measured along column lengths after initial saturation and at the end of the retention period for the 1st, 5th, and 9th cementation treatments. As shown, differences in the magnitude and uniformity of improvement between columns is clearly evident. In the SL column, V_s trends are relatively flat along the column length, indicating a relatively uniform improvement that was consistent with the treatment objective for this column. After the 9th and final cementation treatment, the shear wave velocity ratio between the furthest (V_s = 546 m/s) and closest (V_s = 1186 m/s) bender element measurement locations from the injection source was ~0.46. The rate of V_s increase per cementation treatment was also relatively constant with treatment number, such that projections to higher treatment levels could be made. The increase in shear wave velocity closest to the injection source was near 1000 m/s and exceeded many of the improvement levels discussed earlier in Section 5. It is also evident that an increase in V_s would have been realized in SL at distances further than the 3.7 m column length if the test set up was different, indicating (based on extrapolation and conservation of added reagent masses) that measurable improvements at distances greater than 5 m likely could have been realized.

In contrast with trends observed in the SL column, SH column shear wave velocity trends are higher near the injection source but decrease significantly with injection distance and particularly after a distance of 2.3 m. This results in a lower V_s ratio between the furthest and closest measurement locations of only ~0.25. These V_s trends are consistent with the earlier urea degradation trends shown in Figure 79b and suggest that a majority of the reactions and precipitation observed in this column occurred during the treatment injection period. However, surprisingly the magnitude of V_s near the middle of the column is higher than what the urea trends might have suggested. In this column, the rate of V_s increase per treatment was more rapid initially, but began to decrease with additional treatments, particularly at further treatment distances, indicating that additional treatment injections (if applied) would have likely only magnified the treatment non-uniformity observed. The AH column only showed detectable V_s increases close to the injection source at the first measurement location, with negligible V_s increases further along the column length. This further confirms the ineffectiveness of the employed non-nutritive augmentation strategy used, particularly for applications where achieving improvement over large treatment distances is of high priority. However, other augmentation protocols could have been designed and employed to likely improve performance. Such strategies could have included additional/more frequent augmentation treatments and a mixture of augmentation and stimulation through the inclusion of organics in treatments, such as yeast extract.

7.2.6 *Soil $CaCO_3$ contents*

Final soil $CaCO_3$ contents, measurable through destructive testing after completion of the entire treatment program (including the byproduct removal phase discussed subsequently),

provide the first direct measure of treatment success and directly map to the targeted changes in engineering properties (Sections 4 & 5). Soil $CaCO_3$ content measurements in samples obtained from the middle of column cross-sections with column length (including between bender elements) are plotted in Figure 79d. The increase in V_s at the end of the cementation treatment is also plotted for comparison. The final measured soil $CaCO_3$ contents were about 5 to 8% immediately adjacent to the injection source in all columns, but the differences in uniformity and magnitude of improvement are apparent at injection distances of 1 m and beyond. A comparison of the theoretical soil $CaCO_3$ contents that could have been precipitated (considering treatment concentrations and volumes) against the measured soil $CaCO_3$ contents showed that in the SL column appreciable aqueous calcium and urea concentrations exited the column and remained available for improvements at a distances beyond the 3.7 m column length. In the SH column, the amount of precipitation near the injection source was larger, but reduced significantly with distance due to reactions during injections, which reduced transported reagent concentrations.

Soil $CaCO_3$ content trends agreed very well with observations made on the basis of V_s; the final trends of SL were the most uniform and indicated that improvement could have been realized at even further injection distances, the SH trends indicated that improvement was concentrated within 2.3 m of the injection source, and the AH trends indicated that improvement was only realized within about 0.5 m of the injection source. The robust correlation between V_s and soil $CaCO_3$ contents allows for treatment progression and uniformity to be assessed in real time, is critical to ensuring that targeted improvements in engineering properties can be realized, and affords the opportunity to adjust the treatment program during implementation, if/as necessary.

7.2.7 *Byproduct removal*

Following the completion of all cementation treatments, ammonium byproduct concentrations residing within columns were targeted for removal by pumping ~10.5 PV of an alkaline calcium rich rinse solution over continuously over 700 min in a single injection. Following this injection, rinse solutions resided within columns under stop flow conditions for 12 hours, which small scale laboratory test results showed was effective in displacing sorbed NH_4^+ ions from particle surfaces (Lee et al. 2019b). Figure 79e presents aqueous ammonium concentrations along soil column lengths at various times during rinsing. As shown, gradients in aqueous ammonium were observed within columns during rinsing with greater ammonium removed closer to the injection source (distance of 0 m) and continued reductions in concentrations at all locations with increases in injected volumes. Initial ammonium concentrations near 500 mM were observed, which was expected given the applied urea concentrations of 250 mM, and were reduced to values between 0.01 and 10 mM after rinsing. Final aqueous ammonium concentrations were less than 10 mM throughout the SL column and within the first 3 meters of the SH and AH columns, with all columns achieving near 99.7% aqueous ammonium removal. Although not shown, the rate of aqueous ammonium removal was much more rapid during the first few pore volumes of pumping, with outlet well ammonium concentrations decreasing from 500 mM to about 10 mM after 3 PVs of continuous rinse injections and further reductions occurring more gradually.

In addition to aqueous ammonium concentrations, sorbed ammonium masses were also quantified after rinsing. Figure 79f presents sorbed ammonium masses for all columns with length. These results suggested that not insignificant sorbed ammonium may persist after rinse injections and may require characterization following field-scale applications (Lee et al. 2019b). Such results also demonstrated that an equilibrium may exist between sorbed and aqueous ammonium concentrations with a near linear relationship observed between both at low ammonium concentrations (< 10 mM). While these results conclusively demonstrated the feasibility of removing generated ammonium byproducts, subsequent studies (Lee & Gomez 2022a) (Section 3.3) have shown that even more effective removal of the remaining low concentrations can occur through staged injections and the use of alternative cation formulations (i.e., K^+ ions).

7.2.8 *Summary*

The 3.7 meter long soil column experiments performed in San Pablo et al. (2020) (as well as the complimentary works summarized in Table 5) represents the integrated depth of understanding and control of the enabling biogeochemical processes and associated monitoring methods that can be used throughout the treatment process and shows that the technology has matured to a point where deployment at field sites may be performed reliably in a controlled manner.

7.3 *MICP mitigation of liquefaction hazards*

Significant research effort has focused on understanding the relationships between engineering behaviors afforded by MICP in parallel with the previously described upscaling efforts considering that the magnitude and extent of MICP improvement required at a given site will be application specific. This has been done more extensively at the laboratory element scale, as detailed in Sections 5 and 6, than at the systems level, however, such efforts have significantly advanced understandings of the technology for liquefaction hazard mitigation applications.

Table 6 presents a summary of the system level studies that have been performed which have evaluated the effect of MICP improvement on liquefaction triggering susceptibility and the consequences of liquefaction once triggered. As evident, the majority of these systems level evaluations have been investigated using geotechnical centrifuge modeling.

One of these more recent studies, Darby et al. (2019), used centrifuge modeling to examine how MICP treatment could increase soil liquefaction triggering resistance and alter the consequences of liquefaction once triggered using models consisting of a uniform free-field liquefiable loose sand deposit. This study is highlighted in the following section to describe the primary insights gained, and is further supplemented by recent 1D numerical simulations, which demonstrate the agreement that can be realized between the physical experiments and responses predicted using the recently developed PM4SandC model described in Section 6.2.

7.3.1 *Centrifuge modeling of MICP soil liquefaction behaviors*

Darby et al. (2019) prepared saturated Ottawa F-65 sand models, treated to varying degrees of MICP improvement, and subjected models to repeated shaking events using the 1m radius centrifuge at the UC Davis Center for Geotechnical Modeling in order to evaluate how (1) MICP improvement changes the free-field system response as indicated by measured accelerations, induced shear strains, and pore pressure generation during shaking, (2) cementation degrades spatially and temporally with increases in the applied loading magnitudes, (3) cone penetration resistances increase following treatments and degrade with progressive loading events, (4) existing liquefaction triggering curves may shift as a function of MICP cementation, and (5) resulting displacements following triggering events can be reduced by MICP improvement.

Table 6. Summary of MICP upscaling projects performed focused on liquefaction hazard mitigation.

Year	Model & [Prototype] Dimensions (m)	Container	Shake Table (1g) vs. Centrifuge (radius @ Ng)	Soil Type	Application(s)	References
2013	0.50 x 0.24 x 0.11 [25 x 12 x 6]	Flexible Shear Beam	Centrifuge (1m @ 50g)	SP (Ottawa 50-70)	Triggering, system reponse, Vs monitoring, settlement	Montoya et al. 2013
2019	0.50 x 0.24 x 0.11 [40 x 19 x 9]	Flexible Shear Beam	Centrifuge (1m @ 80g)	SP (Ottawa F-65)	Triggering relationships, Vs & qc monitoring, settlement	Darby et al. 2019
2020	0.7 x 0.7 x 0.5	Laminar Shear	Shake Table (1g)	SP (Calcareous Sand)	Triggering, spectral response, settlement	Zhang et al. 2020
2021	1.65 x 0.80 x 0.53 [99 x 48 x 32]	Flexible Shear Beam	Centrifuge (9m @ 60g)	SP (Ottawa F-65)	Triggering, foundation interactions, settlement, teatment zone, stratigraphic effects	Zamani et al. 2021
2022	0.50 x 0.24 x 0.11 [40 x 19 x 9]	Flexible Shear Beam	Centrifuge (1m @ 80g)	SP (Ottawa F-65)	Triggering, settlement, treatment zone	San Pablo et al. 2022b

7.3.1.1 *Test design*

Darby et al. (2019) leveraged previous advances and findings from an earlier centrifuge study by Montoya et al. (2013) which showed how MICP treatment can alter systems level responses, a previous upscaling study by Gomez et al. (2018a) that indicated how CPT q_c can progressively track increases in MICP cementation, and laboratory studies (Section 5) that characterized how the monotonic and cyclic behaviors of sandy soils can be modified as a function of MICP treatment magnitudes and other factors. The resulting test design sought to build upon these earlier findings and extend them to realistic field stress conditions to examine achieved performances at a more global systems level.

A set of centrifuge models comprised of a uniform saturated sand profile representing a simple free-field condition were treated to varying levels of MICP cementation and were subjected to repeated shaking events, which progressively increased the applied loading magnitudes. Separate models with an initial relative density (D_r) of 38% were treated to "light", "moderate", and "heavy" cementation levels, and two additional untreated models prepared to 38% and 53% relative density were performed and allowed for characterization of baseline reference conditions. For simplicity, only the untreated and "moderately" treated specimens are discussed herein, with details regarding all other tests available in Darby et al. (2019).

The models consisted of Ottawa F-65 sand placed at an initial relative density (D_r) of 38% by dry pluviation into a flexible shear beam container, thereby producing a level ground free-field profile. The constructed model dimensions as well as the instrumentation and cone penetration sounding locations are shown in Figure 80. Instrumentation included: (1) matching arrays of accelerometers and pore pressure transducers which allowed for monitoring of the system's dynamic response during shaking, (2) two arrays of bender elements that enabled shear wave monitoring of cementation formation during MICP treatments as well as the gradual mechanical degradation of cementation during progressive shaking events, and (3) a displacement sensor that allowed for measurement of ground surface settlements. Furthermore, cone penetration tests were performed using a 6 mm penetrometer at four locations across the model, at various times including: (1) after model saturation (and before MICP treatment), (2) after all MICP treatments (when performed), (3) after the first shaking event triggering soil liquefaction, and (4) following the completion of all shaking events.

Following model construction, the moderately cemented specimen was treated using three cementation injections to achieve an average shear wave velocity of about 400 m/s, which corresponded to a soil $CaCO_3$ content near 1.4% by mass. In order to establish ureolytic activity, augmentation with *S. pasteurii* was used to minimize the potential for injection related model disturbances and to maximize time efficiency. As shown earlier in Section 4.5, regardless of biological approach (stimulation versus augmentation), comparable improvements in engineering properties can be observed on the basis of similar soil $CaCO_3$ contents and thus comparable results would have been expected if stimulation had been used instead. Augmentation treatments applied to the model were also nutritive and may also have allowed for unintended stimulation as described in Section 2.3. Following augmentation, models received a flush injection to remove generated carbonate species and cementation injections proceeded. Specific solution formulations for each treatment stage are detailed in Darby et al. (2019). After preparation, both the cemented and uncemented models were saturated under vacuum with a solution of

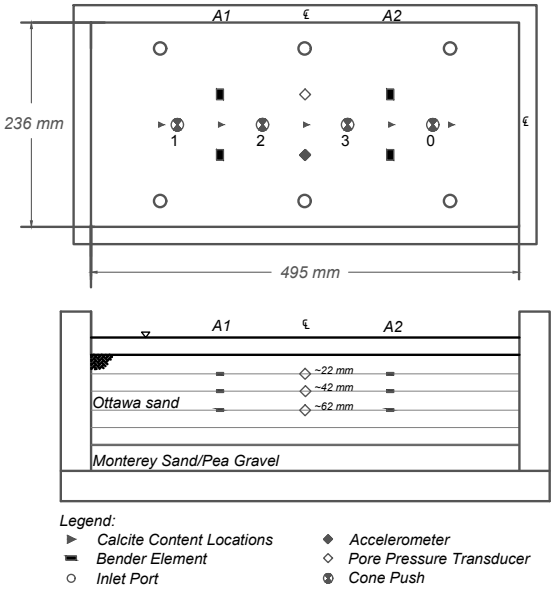

Figure 80. Design of centrifuge test model (adapted from Darby et al. 2019).

methylcellulose and DI water prepared to a viscosity of approximately $5x10^{-5}$ m^2/s, near 50 times the viscosity of water, to improve scaling of dynamic pore pressure generation and related dissipation during shaking events.

After saturation, models were mounted on the centrifuge and subjected to an 80g acceleration field for testing, with spin-up/spin-down cycles occurring as necessary to mount/unmount the cone penetrometer between particular shaking events. The applied shaking event consisted of 15 cycles of a uniform amplitude 1.25-Hz frequency sine wave, with the acceleration magnitude varying from 0.02 g to 0.2 g, as required to trigger liquefaction in the model. In total, the uncemented model was subjected to 11 shaking events that progressed from 0.02 g to 0.25 g while the moderately cemented model was subjected to 9 shaking events that progressed from 0.02 g to 0.20 g.

7.3.1.2 *Dynamic responses*

Shaking sequences for the loose and moderately cemented models are shown in Figure 81, with the progression of peak base accelerations (PBA) and mid-depth cone tip resistances (q_c), shear wave velocities (V_s), maximum shear strains (γ_{max}), and excess pore pressure ratios (r_u) plotted versus shaking event number. As shown, the shaking magnitude gradually intensified until the model liquefied at mid-depth, which was defined to have occurred when excess pore pressure ratios ($r_u = \Delta u/\sigma'_v$) exceeded 0.95. Model responses were evaluated immediately after each shaking event. Initial triggering of liquefaction in the uncemented model occurred at a PBA of 0.06 g during shaking event 2 and occurred in the moderately cemented model at 0.17 g during shaking event 5. Shear strains, computed following the procedure by Brandenberg et al. (2010), remained relatively small throughout all shaking events, an outcome which was primarily attributed to the boundary conditions induced by the flexible shear beam container. V_s measurements obtained between every shaking event increased slightly with progressive shaking in the uncemented model due to gradual soil densification; however, V_s remained nearly constant and then decreased rapidly upon liquefaction triggering in the moderately cemented model due to cementation degradation. CPT q_c values measured at mid-depth correspondingly increased slightly with progressive densification in the uncemented model, while such values decreased dramatically in the moderately cemented model following liquefaction triggering, with more minor increases than observed during subsequent shaking events, which gradually densified the model.

The substantial increase in liquefaction triggering resistances provided by the moderate level of MICP treatment is particularly evident in Figure 82, which presents time histories for the 0.06 g shaking event 2 applied to the uncemented sand and the 0.17 g shaking event 5 applied to the moderately cemented sand. Provided are excess pore pressures measured at mid-depth, surface accelerations (approximately 2.0 m from the surface), CSR values at mid-depth (determined following Kamai & Boulanger 2010), shear strains at mid-depth, and base accelerations in time. As evident, the CSR sustained throughout the shaking time history reached a maximum value of about 0.8 and remained above about 0.3 in the moderately cemented specimen until the end of shaking, whereas the uncemented soil had an initial CSR at mid-depth of 0.15 and then attenuated to insignificant values after the onset of liquefaction. Correspondingly, the measured excess pore pressure and surface acceleration time histories track well with the applied shaking frequency. The cemented model demonstrated clear amplification of the input motion, with the input base acceleration of 0.17 g amplifying to 0.49 g near the ground surface, whereas the uncemented model exhibited deamplification of the input motion. Shear strains were higher in the moderately cemented model than in the uncemented model, which is attributed to the deformations required to degrade the cementation to level at which liquefaction could be induced.

7.3.1.3 *Cone penetration resistances*

The cone penetration resistance profiles obtained in the loose uncemented and moderately cemented models are shown in Figure 83. Profiles from the uncemented model show a steady increase in tip resistances with continued shaking throughout the sounding depth, which can be attributed to gradual densification. The profiles obtained in the moderately cemented model indicated that pre-treatment penetration resistances were similar to the untreated model, but then increased by more than 100% following MICP cementation. For example, the q_c at mid-depth

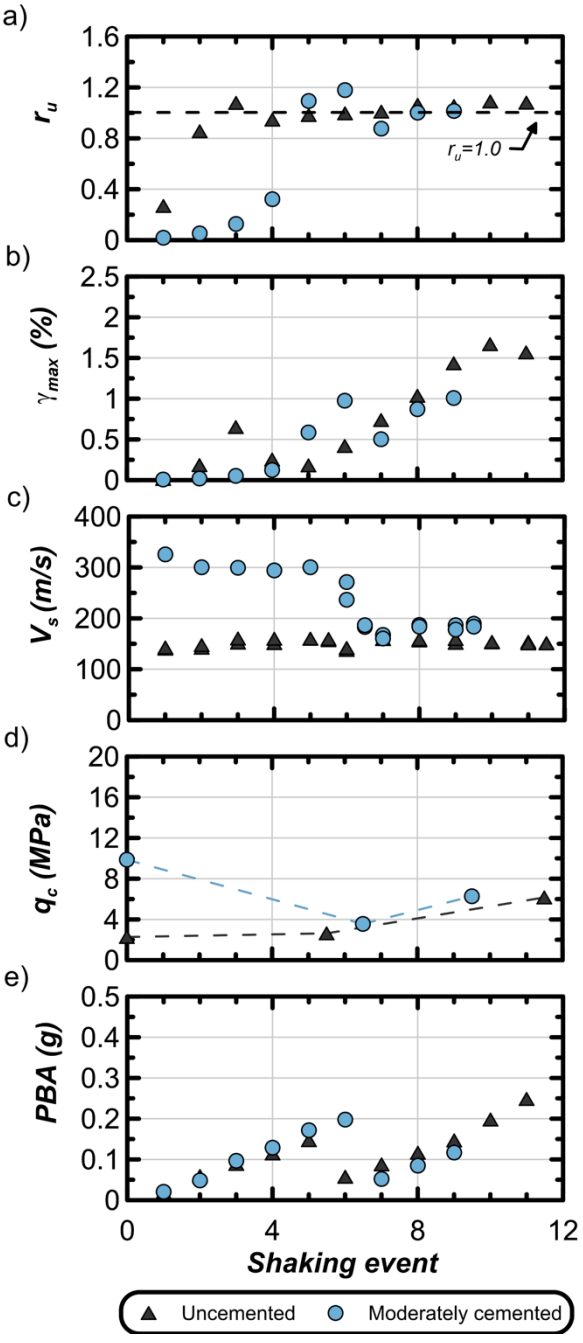

Figure 81. Summary of dynamic response at mid-depth in the uncemented and moderately cemented models (adapted from Darby et al. 2019).

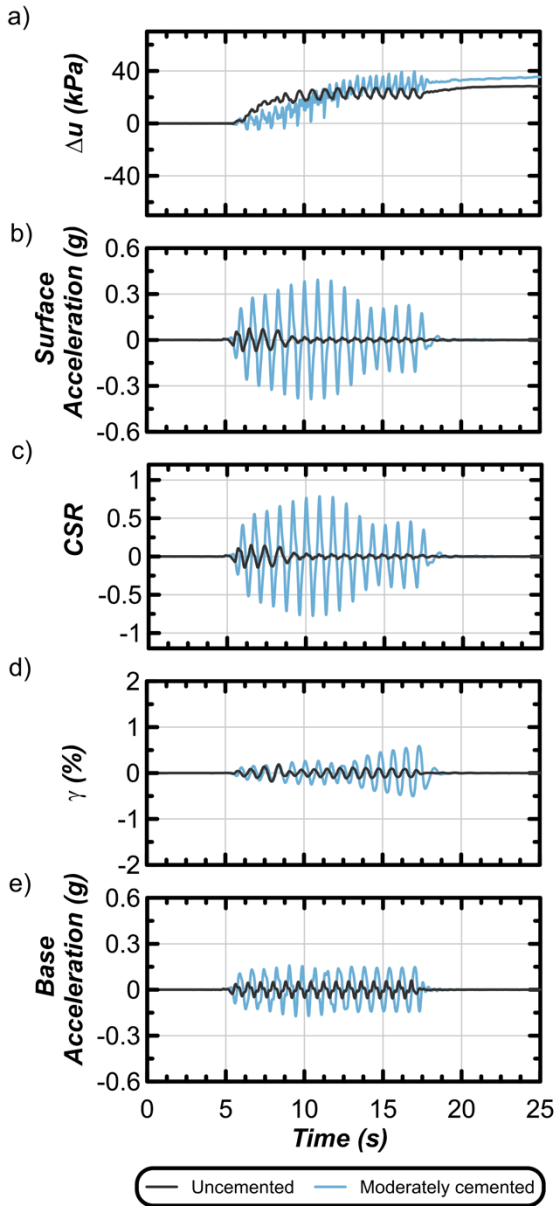

Figure 82. Dynamic response comparison of uncemented and moderately cemented of (a) Δu at mid-depth, (b) surface acceleration, (c) CSR at mid-depth, (d) shear strain at mid depth, and (e) base acceleration versus time (adapted from Darby et al. 2019).

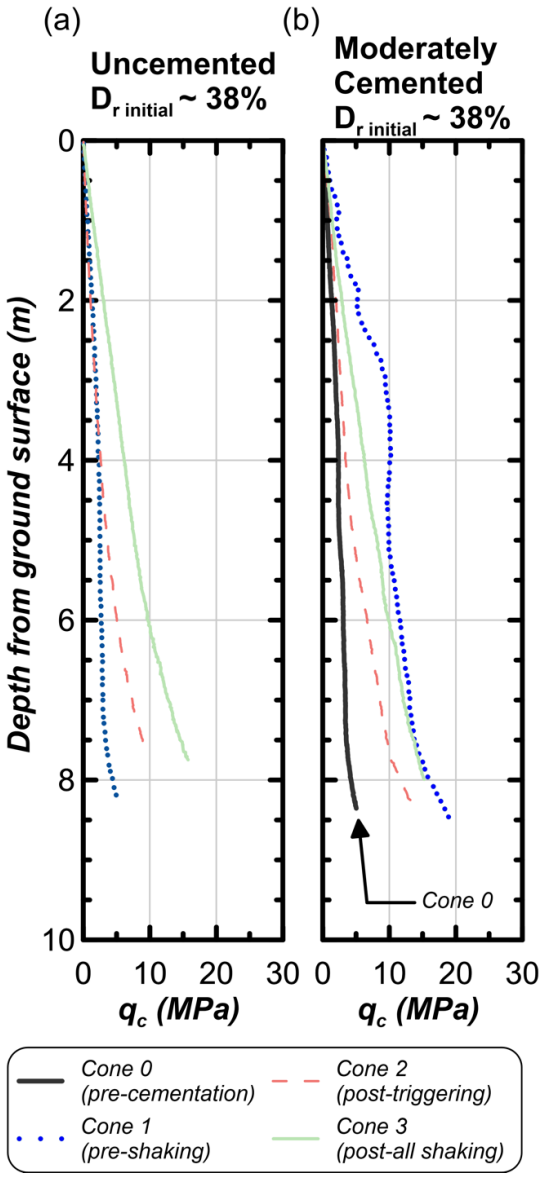

Figure 83. Progression of cone penetration resistances for (a) uncemented and (b) moderately cemented model (where both models initially were prepared at a relative density of 38%) (adapted from Darby et al. 2019).

was 2.3 MPa prior to treatment (similar to the uncemented model) and increased to 9.9 MPa following MICP. Following the 0.17 g shaking event 5 in the cemented model, the q_c at mid-depth decreased to 4.5 MPa, and then gradually increased to a final value near 6.3 MPa after all shaking events were completed. This degradation after initial liquefaction triggering followed by progressive densification was consistent with V_s trends. Furthermore, this moderate cementation level appeared to be unique in the sense that the treated soil degraded towards similar conditions as observed in the uncemented model, albeit with some clear residual benefits resulting from cementation. This outcome can be attributed to the interaction of three hypothesized mechanisms: (1) densification of the soil skeleton, (2) damage to generated cemented bonds, and (3) the reduction of initial void ratios by the addition of precipitate solids. It is noted that the additional cementation levels tested did confirm these processes and indicated that the moderately cemented model existed at a unique cementation threshold at which all three mechanisms were present and compensated for one another (Darby et al. 2019).

7.3.1.4 *Liquefaction triggering*

Cone penetration measurements in combination with the embedded instrumentation provided an opportunity to investigate how MICP improvement may affect the CPT case history-based liquefaction triggering curves for clean sands used routinely in practice (i.e., Boulanger and Idriss 2015). Further processing of the obtained centrifuge data was necessary for such comparisons to be made. First, equivalent uniform time series were produced from the irregular CSR time series induced in the centrifuge models following the procedure by Seed et al. (1975) as detailed in (Idriss & Boulanger 2008), with an assumed b-value of 0.20, which was deemed reasonable following review of cyclic laboratory data. Measured cone tip resistances and developed CSRs at mid-depth in all models were subjected to a vertical effective stress of 35 kPa. Typically, measured q_c values

would be normalized to 1 atm overburden stress using a C_N relationship, however, similar stress-normalization relationships for measurements in cemented soils do not currently exist. Therefore, the CPT based liquefaction triggering curve for clean sands by Boulanger & Idriss (2015), typically presented for 1 atm (100 kPa) stress normalized conditions, was instead shifted to an overburden effective stress of 35 kPa to allow for comparisons to be made.

The results from all shaking events applied to all models is shown in Figure 84, along with the liquefaction triggering curve for uncemented sands. All model shaking events that did not trigger liquefaction are shown with open symbols, while all model shaking events that did trigger liquefaction, regardless of prior shaking history, are shown as closed symbols. Provided arrows indicate the progression of shaking events for the moderately cemented specimen only. From this comparison, several insights can be made. First, the progression of the moderately cemented model data points clearly illustrates the increased resistance that MICP can provide with respect to liquefaction triggering relative to an uncemented soil as well as how gradual cementation degradation over multiple shaking events eventually decreases q_c and then further decreases the CRR. For the moderately cemented soil, liquefaction triggering occurs at an equivalent CRR of 0.56, which is significantly higher than the expected value for uncemented soil of about 0.13. In addition, the initial normalized cone tip resistance of 88 decreases to 60 due to the liquefaction triggering event, and further decreases to a value of about 37 before it then increases due to densification, ultimately reaching a final value near 55. Even near the end of the applied shaking sequence it is evident that the degraded cementation still increases the CRR by 100% or more relative to the uncemented triggering curve. When considering data from all three cemented models, it is clear that MICP treatments provides significant benefits with respect to liquefaction triggering resistances. The Boulanger & Idriss (2015) triggering curve for uncemented sands is based upon the strong correlation between CPT, $q_{cN,}$ and D_r; with higher stress-normalized q_{cN} values corresponding to denser (higher D_r) sands. However, all of the centrifuge models were prepared to the same initial density, and therefore increases in q_{cN} are solely the result of cementation increases instead. If a trendline were drawn between the initial triggering points for each of the three models, this new triggering curve would indicate that MICP treatment can increase the resistance to initial triggering by up to 400% when compared to uncemented soils at similar q_{cN} values. Furthermore, a trendline drawn between points observed during the final shaking event in all models would indicate a residual benefit across all cementation levels of 100% or more.

7.3.1.5 *Liquefaction consequences*

The consequences of liquefaction for the described free-field level ground models can be captured by evaluating how estimated maximum shear strains induced in the model at mid-depth and measures of incremental surface settlements varied with the applied equivalent CSR magnitudes in the presence and absence of triggering. Figure 85 presents this data for the uncemented and moderately cemented models for triggering and non-triggering events. As shown, a distinct separation between trends exists for events where liquefaction was and was not triggered. The maximum shear strain induced during non-triggering events remained below 0.05% for the uncemented model and below 0.5% for the moderately cemented model. However, such strains increased to 1.7% for the uncemented model at the maximum applied CSR of about 0.11, and maximum strains in the moderately cemented model were near 1% when subjected to a CSR of 0.56. Incremental settlements were negligible for the uncemented soils for non-triggering events, however, settlements increased between 35 and 75 mm for all liquefaction events, regardless of the CSR loading magnitude or shaking sequence. The moderately cemented model similarly did not have any significant settlements during non-triggering shaking events prior to the initial liquefaction event. However, the liquefaction event and subsequent strong shaking events resulted in incremental settlements between 40 and 80 mm. Some additional settlement also was observed in this model near the end of the shaking sequence even though the liquefaction triggering criteria of $r_u > 0.95$ was not formally met.

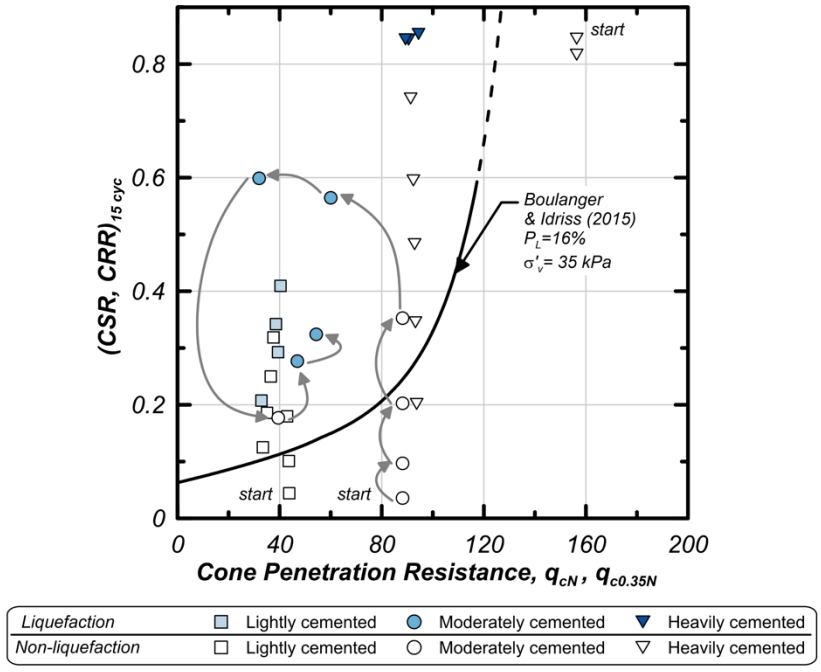

Figure 84. Comparison to existing liquefaction triggering correlation showing progression of shaking events for moderately cemented model (adapted from Darby et al. 2019).

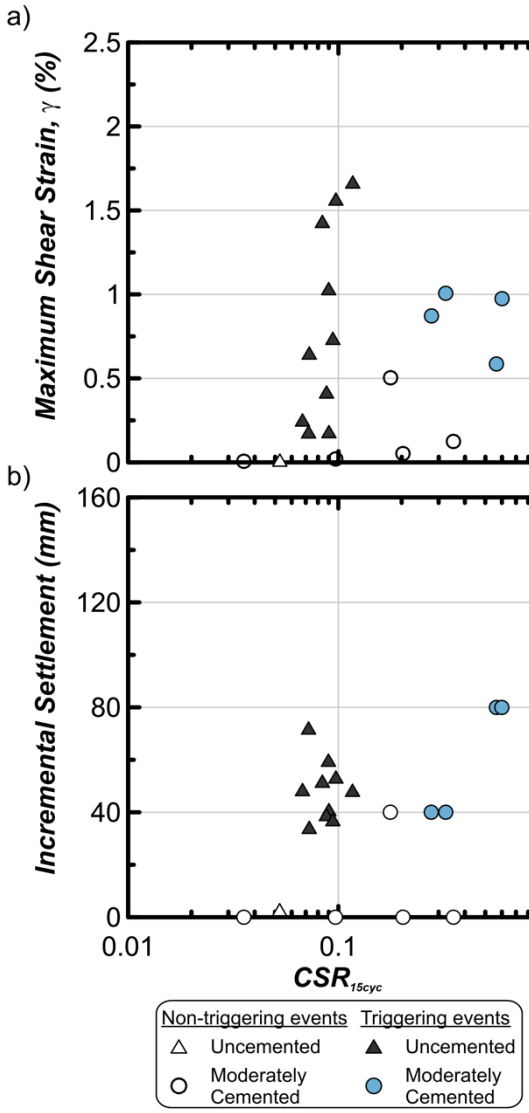

Figure 85. (a) Maximum shear strain and CSR_{15cyc} and (b) incremental settlement and CSR_{15cyc} for non-triggering events (open symbol) and triggering events (closed symbol) (adapted from Darby et al. 2019).

7.3.2 *Numerical modeling of centrifuge tests*

Nonlinear effective stress 1D and 2D site response analyses with an appropriately calibrated constitutive model are routinely performed to predict the response of uniform and layered soils during shaking and in turn capture the generation of excess pore pressures along with stress strain responses. While these analyses have been performed for uniform and nonuniform soils with stochastic V_s layering (e.g., Montgomery and Boulanger 2017) or conditioned upon site investigation data (e.g., Pretell et al. 2022) and sloping ground (e.g., Montgomery and Ziotopoulou 2020), no site response analyses have been performed for deposits that have been either partially or fully treated using biocementation. The following subsection presents a numerical simulation of the Darby et al. (2019) centrifuge test described in the previous Section 7.3.1. This analysis serves as a validation of the constitutive model for biocemented sands PM4SandC (Section 6.2) at the system level as well as under free-field conditions.

7.3.2.1 *Model design*

The centrifuge model considered involved an instrumented level-ground free-field centrifuge test on uncemented and moderately cemented Ottawa F-65 sand as described earlier. A 1D site response analysis was performed using the explicit finite difference program FLAC (Fast Lagrangian Analysis of Continua, Itasca 2016) and the user-defined plasticity model for bio-cemented sands PM4SandC (Section 6.2) was used to predict the response of biocemented sands when subjected to cyclic loading. The two analyses presented here represent a 1D soil column model in FLAC where model boundary conditions, constraints, and soil properties were prescribed to best approximate the conditions of the reference centrifuge model tests. Initially, a grid of 11.4 m prototype-scale is defined with two soil layers: (1) the liquefiable Ottawa sand and (2) a mix of Monterey sand and fine gravel that was beneath the Ottawa F-65 sand and used for drainage. The base layer was 2.4 m thick and was discretized into 0.6 m elements, and the liquefiable sand was 9 m thick and was discretized into 0.5 m elements (Figure 86). The liquefiable Ottawa sand was further divided into three sublayers: (1) bottom, (2) middle, and (3) top, which was based upon the location of the included instrumentation and specifically the bender element sensors. This was performed to account for the modest nonuniformity observed in MICP treatments within the centrifuge models as discerned by bender element V_s measurements. As such, the liquefiable Ottawa sand is assigned three different sets of parameters to better approximate the realized soil conditions which were present in the centrifuge model. The soil column was fixed at the base in both the x- and y- directions prior to initializing stresses. Stresses were then initialized in the model due to gravity and the model was run to establish static equilibrium with no water present. After static equilibrium was confirmed, pore pressures were initialized by fully saturating the model. Pore pressures increased from zero at the top of the model to hydrostatic pressures at the 11.4 m depth. The cyclic loadings applied at the base of the models were comparable to the shaking events which initially triggered liquefaction in these models were prescribed at the base of the models. As described earlier, for the uncemented model, liquefaction was initially triggered during shaking event 2 which applied a PBA of 0.06 g, whereas for the moderately cemented model liquefaction was initially triggered during shaking event 5

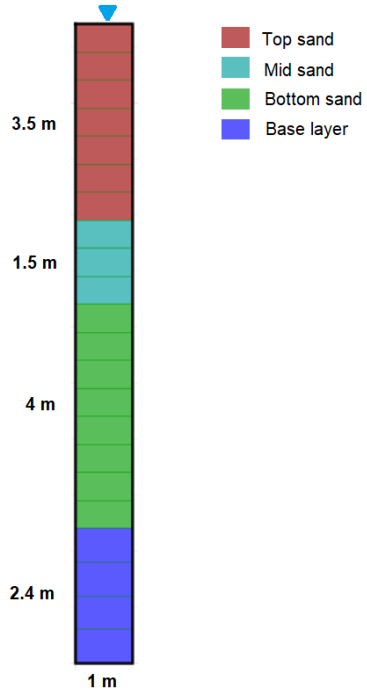

Figure 86. 1D site responses analysis in FLAC represented by a 1D soil column with different soil layers in prototype scale.

which applied a PBA of 0.16 g. Due to the use of a flexible shear beam container in the centrifuge, the lateral nodes of the column at each elevation are connected to each other and, as such, forced to move together as would be the case in the free field.

7.3.2.2 *Model parameters*

Soil properties for each layer were assigned using values determined during the experimental centrifuge tests as well as from other values available in the literature. The minimum and maximum void ratios and specific gravity of Ottawa F-65 sand were assumed using reported values from previous tests (Carey et al. 2020a). The relative density (D_r) of the base drainage layer was estimated from previous experiments (D_r ~70 %) as direct D_r measurements were not available. The relative density of the Ottawa F-65 sand layer was adjusted from the reported 38% based on the measured cone penetration resistances at 2 m depth (Carey et al. 2020b). The permeability of the base layer (Monterey sand and fine gravel) and the Ottawa F-65 sand were set to 2 $x10^{-3}$ and 1.3 x 10^{-5} m/s, respectively, to better approximate pore pressure generation. Table 7 summarizes the soil properties for both the uncemented and cemented models.

Soil shear wave velocities were determined from bender element measurements obtained near the bottom, middle, and top of the model as reported in Darby et al. (2019). The observed V_s nonuniformity warranted further sublayering of the untreated and treated Ottawa F-65 sand layers in the model. While V_s values in the uncemented Ottawa sand model were more uniform than in the moderately cemented sand model, both were subdivided into three layers for consistency between analyses. Since the base layer was not instrumented during the experiment, the V_s of this layer was estimated to be 204 m/s using available relationships between V_s, D_r, and effective vertical stresses and the assumption that this compacted base layer was stiffer than the liquefiable layer (e.g., Andrus & Stokoe 2000, Biryaltseva et al. 2016).

The parameters requiring calibration in the PM4SandC constitutive model were determined through a variety of means. Table 8 summarizes these calibrated parameters for both the uncemented and cemented models. In both models, mass-based D_r values were adjusted to be consistent with the measured cone penetration resistances and stresses. Small-strain shear moduli (G_o) were computed using both the measured Ottawa F-65 sand dry densities and the square of the measured shear wave velocity at each layer, which were first stress-normalized using atmospheric pressure and an assumed coefficient of lateral earth pressure at-rest (K_o) value (Allmond & Kutter 2012, CGM Report 12-01). The contraction rate parameter (h_{po}) was iteratively estimated using single element direct simple shear (DSS) calibrations where a target CRR, initial h_{po}, D_r, and G_o were specified until the single element driver triggered liquefaction at 15 cycles. For this analysis, a liquefaction criterion of an r_u larger than 95% was selected in agreement with the centrifuge test. The ratios between the cemented and uncemented shear wave velocities (V_{sR}) were further specified. For the uncemented model, V_{sR} was prescribed to be 1.0 and the constitutive model therefore reverts to PM4Sand. For the cemented model, V_{sR} was assigned as reported in Table 8, following the measured V_s from the experiment. For the base layer, the dynamic behavior was represented using the hysteretic model (sig3 model) with selected parameters of a = 1.014, b = -0.4792 and x_o= -1.249 as recommended by Seed & Idriss (1970).

Table 7. Initial soil properties selected for uncemented and moderately cemented models.

Soil	Base layer	Bottom Ottawa sand layer	Mid Ottawa sand layer	Top Ottawa sand layer
Uncemented Model				
e_{min}	0.536	0.51	0.51	0.51
e_{max}	0.843	0.78	0.78	0.78
G_s	2.64	2.67	2.67	2.67
D_r (%)	70	41	41	41
V_s (m/s)	300	155	150	150
Moderately Cemented Model				
V_s (m/s)	300	155	150	150
$V_{s\ cem}$ (m/s)	300	217	230	200

7.3.2.3 *Dynamic responses*

Validation of numerical results against the centrifuge measurements necessitates the selection of recording points on the soil column, which closely approximate the location of the actual instrumentation used in the centrifuge tests. At about 2 m (i.e., TOP), 4 m (i.e., MID), and 5.5 m (i.e., BOT) from the soil surface, numerical time histories were extracted. Figure 87 presents a comparison of the 1D site response simulation and centrifuge experimental results obtained at mid-depth in the Ottawa F-65 sand layer. For the uncemented sand, the dynamic response from the simulation agrees well with the centrifuge test. As shown, simulated shear strain, CSR, surface acceleration, and pore pressure generation time histories are comparable to the experimental recordings. The simulated maximum strain (Figure 87d) and CSR (Figure 87c) are 0.11% and 0.26, respectively, for the uncemented model. These values are only slightly different from those measured in the centrifuge experiment (1.7% shear strain; 0.15 CSR) and were therefore deemed acceptable.

In addition, measured and simulated surface accelerations (Figure 87b) confirm that the applied base accelerations were de-amplified for the uncemented case (from PBA of 0.06 g to a peak surface acceleration of about 0.03 g). Good agreement between the centrifuge measurements and the simulation results are also observed for the moderately cemented sand model. The maximum strain achieved in the simulation (Figure 87d) was 0.37% and was consistent with the experimentally observed behavior from the standpoint that it increased when compared to the uncemented sand. However, the experimental centrifuge results for both the uncemented and moderately cemented cases show a higher maximum shear strain than simulations, which may be attributable to the reconsolidation processes that occur

Table 8. Soil properties and constitutive models selected for the uncemented and moderately cemented model simulations.

Soil	Base layer	Bottom Ottawa sand layer	Mid Ottawa sand layer	Top Ottawa sand layer
Uncemented Model				
dynamic model	hysteretic	PM4SandC	PM4SandC	PM4SandC
h_{po}	-	0.2	0.44	0.44
G_o	-	547.8	513	513
V_{sR} (V_s ratio)	-	1.0	1.0	1.0
Moderately Cemented Model				
dynamic model	hysteretic	PM4SandC	PM4SandC	PM4SandC
h_{po}	-	5	2	4
G_o	-	1074	1206	912
V_{sR} (V_s ratio)	-	1.40	1.53	1.33
e_{deg}	-	0.002	0.002	0.002
e_{res}	-	0.01	0.01	0.01

simultaneously during shaking in the experiments that are not considered in the simulations. The maximum achieved CSR in the simulation (Figure 87c) is 0.81, which is identical to the CSR observed from the centrifuge experiment. The measured surface acceleration (Figure 87b) shows a similar amplification of the base acceleration as the shaking propagates to the ground surface with a maximum achieved surface acceleration of 0.4 g (compared to a PBA of 0.16 g). The pore pressure generation simulated and measured at mid-depth in the Ottawa F-65 sand layer (Figure 87a) shows similar pore pressure generation behaviors for both uncemented and moderately cemented cases.

Figure 88 presents the response spectra computed at various locations within the liquefiable Ottawa F-65 sand layer consistent with the experimental accelerometer locations. These locations include: (1) the base of the Monterey sand and fine gravel mix (11.4 m from the ground surface; Figure 88a), (2) a location within the Ottawa F-65 sand layer towards the bottom of the layer (5.5 m from the ground surface; Figure 88b), (3) a location at the middle of the Ottawa F-65 sand layer (4 m from ground surface; Figure 88c), and (4) a location within the Ottawa F-65 sand layer towards the top of the layer (2 m from ground surface; Figure 88d). It can be observed in the spectral accelerations shown that the uncemented sand deamplified the acceleration achieved near the ground surface from a peak ground acceleration (PGA) of 0.06 g to ~0.03 g at period of 0 seconds, whereas the moderately cemented sand tended to amplify the acceleration near the ground surface from a PGA of 0.16 g to 0.4 g at a period of 0 seconds. This behavior is seen in both the centrifuge measurements and simulation results. The predominant period (~0.75 seconds) experimentally observed for both the uncemented and cemented models are largely consistent, however, the spectral accelerations observed at this predominant

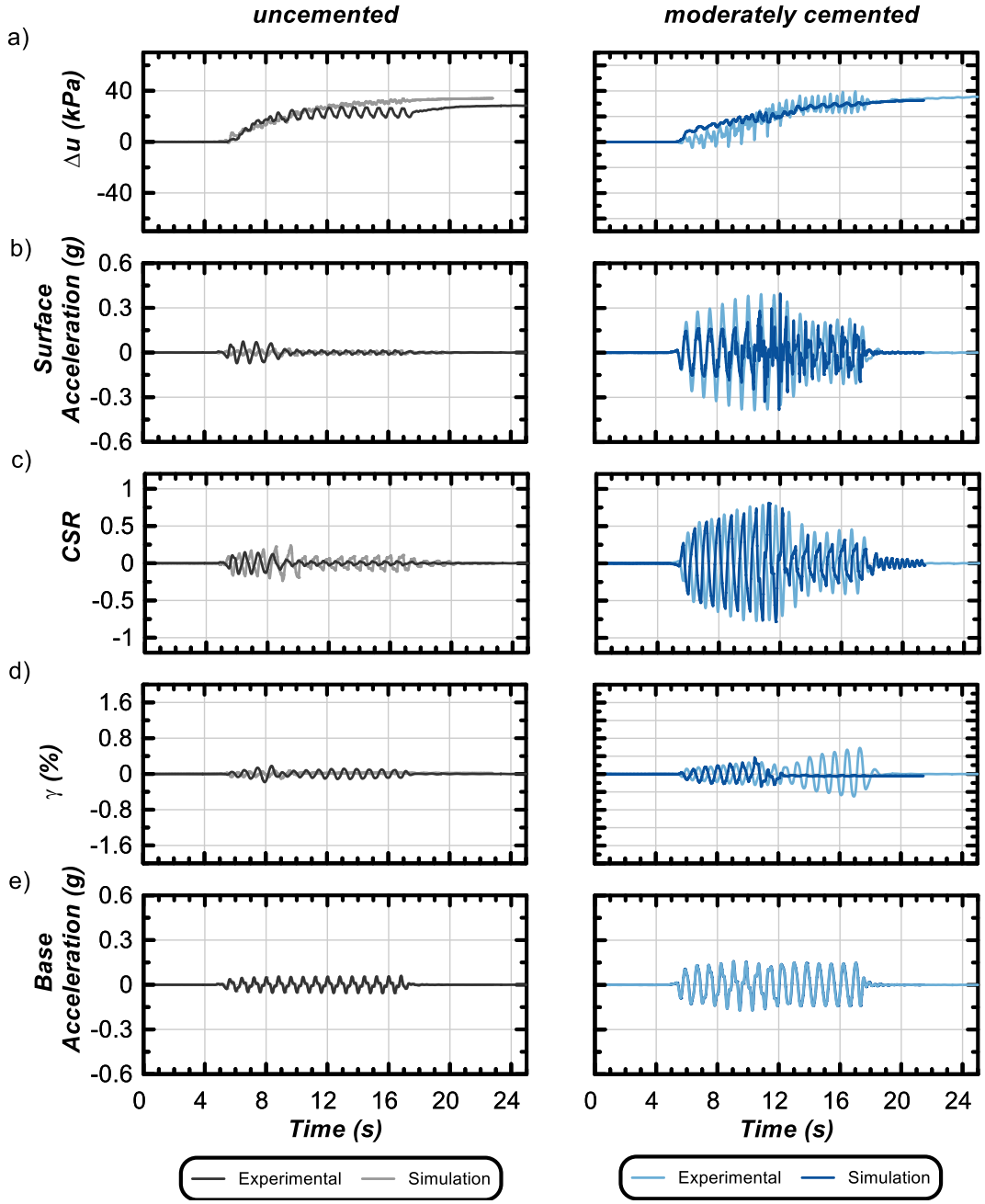

Figure 87. Dynamic responses from centrifuge experiments and simulations compared for the uncemented and moderately cemented cases at the middle of Ottawa F-65 sand layer (centrifuge data from Darby et al. 2019).

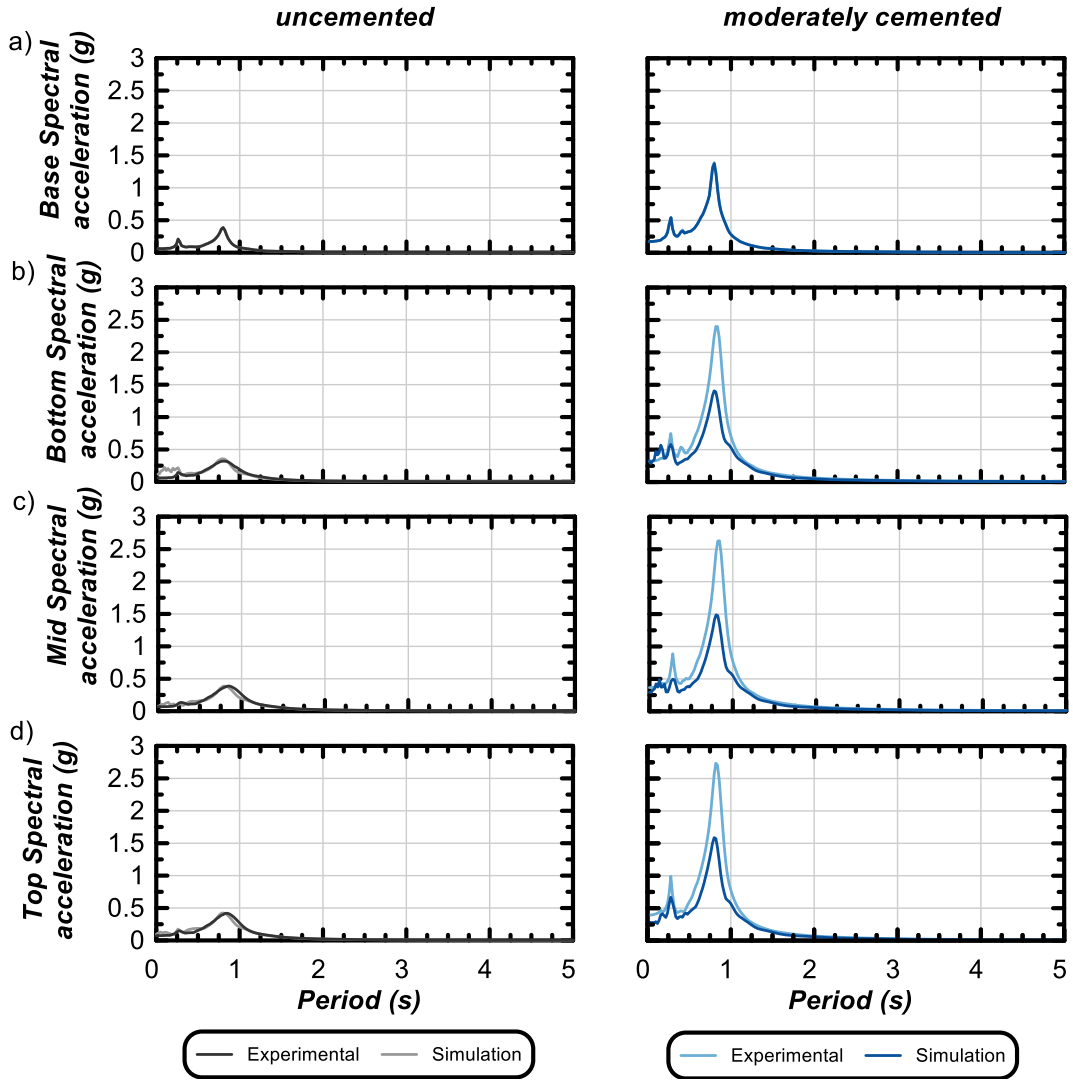

Figure 88. Response spectra obtained for the (a) uncemented and (b) moderately cemented centrifuge experiments and simulations at various depths within the Ottawa F-65 sand layer (centrifuge data from Darby et al. 2019).

period for the moderately cemented sand case are significantly amplified when compared to the uncemented case. While this amplification behavior is generally also captured by the simulation, simulated results do not perfectly match those from the centrifuge experiments because pore pressure generation was prioritized during this calibration, as prediction of liquefaction triggering was of primary interest ($r_u > 95\%$).

7.3.3 *Summary*

Geotechnical centrifuge experiments have and will continue to improve understanding of the liquefaction behaviors of biocemented sands at the systems level. Recent centrifuge tests have demonstrated that biocementation can afford clear changes in dynamic wave propagation behaviors, excess pore pressure generation, cone penetration responses, and related shear strains, with large improvements in liquefaction triggering resistances. Following triggering, such tests suggest that the consequences of liquefaction can also be reduced using MICP, although to a lesser extent than triggering behaviors, consistent with earlier results described in Section 5. Leveraging these results, the PM4SandC constitutive model (Section 6) was used to model both the uncemented and moderately cemented centrifuge experiments and showed good agreement between experimental responses and 1D site response simulations following initial model calibration. While future analyses will continue to expand understanding of the utility of this model for MICP treated soils, the presented results are an encouraging validation of the formulation and implementation of the model and highlight its ability to capture the undrained monotonic and cyclic behaviors of biocemented sands at both the element and system levels. Furthermore, it is important to note that the presented simulated responses were obtained through minimal calibration effort (i.e., by prioritizing only primary input variables). This modeling decision was intentional to demonstrate the utility of the model for future practical field-scale implementations of MICP and potentially other similar cementitious technologies.

8 CONCLUSIONS

This paper presents current state of the art understandings regarding MICP soil improvement and its applicability to liquefaction mitigation. The emerging field of biogeotechnics presents a breadth of opportunities to develop bioinspired and biomediated technologies. Of these solutions, biomediated soil improvement processes have advanced rapidly over the past 25 years and been shown to be capable of modifying the soil engineering behaviors through unconventional mechanisms including the generation of inorganic minerals, gas phases, and biopolymers within the soil matrix. Such technologies have the potential to realize transformative engineering performance and

sustainability gains relative to current soil improvement technologies, and will benefit from continued evaluation during their development using frameworks such as life cycle sustainability assessment to maximize their environmental, financial, and societal benefits. Of the biomediated soil improvement technologies, MICP is the most mature, with envisioned applications spanning across civil engineering subdisciplines and its application to liquefaction mitigation arguably at the forefront of geotechnical development efforts.

The MICP process wherein carbonate generation occurs via microbial ureolysis enables production rates that are nearly 100 times greater than any known alternative microbial pathway. Augmentation with non-native *Sporosarcina pasteurii*, a ureolytic bacterium, has been used to complete the MICP process, but has associated practical challenges and clear disadvantages related to cell injection processes and treatment uniformity. Stimulation is the alternative and preferred biological approach for MICP and involves the enrichment of indigenous ureolytic bacteria through the application of solutions containing nutrients and environmental factors that effectively select for ureolytic microorganisms. Use of the stimulation process provides important practical implementation and performance benefits, including improved treatment control and uniformity, reduced soil ecological and environmental impacts, and reductions in implementation costs and field requirements. The stimulation process is robust and soils incapable of stimulation efforts have yet to be encountered. Although the presented treatment formulations have been shown to select for the genus *Sporosarcina* effectively, there is also a significant amount of diversity between the microbial species identified in stimulated soils, suggesting that ureolytic bacteria may be ubiquitous in geotechnically-relevant soils and the success of stimulated MICP is not dependent on the presence of a small subset of bacterial strains.

Differences in the treatment processes employed in combination with surrounding environmental conditions have been shown to impact the mineralogy of the precipitation generated during MICP, which may have important implications with respect to the realized engineering benefits. Furthermore, microstructural changes resulting from MICP have been captured through a diverse range of direct imaging approaches and have yielded new understandings regarding interparticle precipitation distributions and their effects on engineering behaviors. Recent studies have further advanced understandings regarding the long-term geochemical permanence of MICP by characterizing the abundance of $CaCO_3$ polymorphs present in precipitates as well as their dissolution kinetics. Existing dissolution kinetic models have been incorporated in reactive transport models and calibrated to physical experiments, thus providing a path for assessment of in situ material longevity and lifespan prior to and following treatment implementation.

Preferred treatment techniques and associated influencing factors have been identified through the practical application of this realized fundamental understanding. The preferred treatment process presented uses stimulation of indigenous ureolytic bacteria and represents a culmination of understandings with respect to process geochemistry, microbiological phenomena, and engineering property enhancements, all within the context of optimizing sustainability metrics. Specific recommendations for stimulation and cementation treatment phases have been discussed, including the impact of treatment formulations and injection processes on reactive transport conditions and their impact on the realized biocementation spatial distribution. The presented techniques may merit modification for specific applications, with such decisions ultimately requiring that the fundamentals described in the earlier paper sections be understood so that such treatment decisions can be informed and carefully considered. Recent advances with respect to byproduct management including how generated ammonium can be removed and effectively monitored after treatments are also outlined. The range of soils and environmental conditions that are physically and practically amendable to biocementation include an extensive range of quartz-based soils, carbonate sands, silty materials, and anthropogenically-produced waste materials. The capability of stimulated MICP to improve soils using solely the transport of soluble reactants may extend the range of treatable soils into smaller particle size ranges relative to that which has already been established.

An extensive range of monitoring processes exist to track microbiological, geochemical, and mechanical changes during MICP implementation. Microbiological methods provide the ability to quantify microbial growth, activities, strain purity, and soil community changes, and can provide the fundamental basis for reactive transport models needed for upscaling. Geochemical measurements can be used to interrogate the status of precipitation processes, quantify byproducts produced and their removal, as well as indirectly assess microbially-mediated reaction rates. Cementation magnitudes can be effectively quantified using many different methods and metrics, with soil calcite contents and shear wave velocity changes being the authors' preferred metrics through which expected behavioral improvements can be inferred. Advanced material analyses and non-destructive imaging techniques can further characterize other important aspects regarding the generated cementation, including its mineralogy, morphology, and interparticle spatial distribution. Monitoring and assessment methods also include more traditional geotechnical testing techniques including hydraulic conductivity and cone penetration testing. Existing frameworks that leverage information at both large (CPT) and small (V_s) strains are effective in identifying cemented materials in the presence of other complicating factors expected at field-scale including soil and confining stress variations.

The mechanical behaviors of MICP treated soils have been comprehensively characterized for a variety for different strain levels, loading types, and drainage conditions. Low-strain dynamic behaviors shift with added cementation and include increases in initial shear stiffnesses, decreases in the threshold shear strains at which shear stiffness degradation occurs, and increases in damping ratios at lower strain levels. Monotonic undrained and drained shearing behaviors are established for biocemented sands, with significant improvements in strengths, stiffnesses, and volumetric behaviors possible. Undrained cyclic testing has shown that biocementation can produce orders of magnitude improvements in liquefaction triggering resistances even at low cementation levels (ΔVs <100 m/s), though significant improvements in post-triggering strain accumulation and reconsolidation behaviors require greater cementation magnitudes to achieve more significant precipitation-induced densification.

Numerical models of the mechanical behaviors of biocemented soils have leveraged the wealth of experimental data on MICP treated soils and provide the opportunity to advance understandings regarding how treated soils will behave when subjected to conditions that have not yet been experimentally assessed. Discrete element models are able to appropriately account for experimental behaviors for both monotonic and cyclic loading cases. Such models can also yield insights that cannot be achieved in physical experiments, such as the effect of global shearing conditions on microscale calcite bond integrity. At the continuum scale a number of constitutive models have attempted to capture the impact of cementation on soil mechanical behaviors. The fundamental basis of the recently developed PM4SandC constitutive model was presented, with simulations providing validation that the model can accurately

capture both monotonic and cyclic behaviors for biocemented sands.

An envisioned design process was presented for future MICP field-scale applications and encompasses six stages including: (1) preliminary suitability evaluation, (2) technology compatibility with site conditions, (3) site characterization, (4) design requirements, (5) implementation plan, and (6) monitoring and QA/QC. Considerations and activities specific to each design stage were presented and discussed in detail. Current understandings regarding process upscaling were evident through a review of nearly 30 meter-scale experiments, with detailed review of one project clearly demonstrating the advances that have been realized with respect to process efficiency, cementation spatial uniformity and control, and byproduct management, among other aspects.

The effect of MICP on liquefaction behaviors at the systems level are highlighted through review of a recent centrifuge experimental program which improved understandings of both liquefaction triggering and post-triggering behaviors for biocemented sands as well as reexamined how well-established liquefaction susceptibility assessment frameworks may need to be modified to incorporate the benefits of biocementation. The PM4SandC constitutive model has been further shown to accurately simulate the responses of past centrifuge experiments, including those related to liquefaction triggering, post-triggering, and dynamic wave propagation behaviors. These simulations provide an important validation of the model's formulation, and clearly demonstrate how behaviors key to liquefaction mitigation applications can be effectively captured.

The path forward for MICP is exciting. The collective advancements to date have matured the technology to a level where it is ready for more comprehensive field-scale trials, which will hopefully lead to widespread practical adoption and implementation in time for liquefaction mitigation as well as a host of other broader applications. Continued advancements will present both new challenges and opportunities as MICP transitions to practical field implementation, and the state of the art understandings presented herein may provide a knowledge base from which these challenges can be addressed and overcome.

9 ACKNOWLEDGEMENTS

The work of Kyunguk (Thomas) Na in generating the resonant column data and of Seung-Hun (Phillip) Baek in generating the X-ray CT images and the hydraulic conductivity data is greatly appreciated. The contributions of the following individuals in providing data, references, and/or reviewing the manuscript is also appreciated: Dellen Behrend, Ben Blair, Liam Bradshaw, Scott Braswell, Bob Burdalski, Susan Burns, Jian Chu, Grainne El Mountassir, Annette Esnault Filet, Matthew Evans, David Frost, Soo-Min Ham, Hai Lin, Nick Gorski, Alejandro Martinez, Ashly Cabas Mijares, James Minto, Narayanan Neithalath, Adrienne Phillips, Bruna G.O. Ribeiro, Michael Tsesarsky, Leon van Paassen, Yuze Wang, Matthew Weil, Pu Yang, Xiao Yang, and Samantha Young.

The manuscript development has been supported by the Engineering Research Center Program of the National Science Foundation under NSF Cooperative Agreement No. EEC-1449501 as well as the National Science Foundation grants ECI-1824647 and ECI-1554056. Operation of the centrifuge facility at the University of California, Davis was supported by the NSF as part of the Natural Hazards and Engineering Research Infrastructure (NHERI) network under award CMMI-1520581. Some SEM images presented were made possible by the Molecular Analysis Facility, a National Nanotechnology Coordinated Infrastructure site at the University of Washington, which is supported in part by the NSF Grant NNCI-1542101, the University of Washington, the Molecular Engineering & Science Institute, and the Clean Energy Institute. Any opinions, findings and conclusions or recommendations expressed in this manuscript are those of the authors and do not necessarily reflect the views of the National Science Foundation or other supporting agencies.

10 REFERENCES

Abbas M., Kunhappan D., Dadda A., Geindreau C., Emeriault F., Esnault-Filet A., and Garandet A. 2020. Discrete element modelling for biocemented sand: Effect of calcite distribution at the microscopic scaleCardoso, R., Jommi, C., and Romero, E. (Eds.), *4th European Conference on Unsaturated Soils*. 6. https://doi.org/10.1051/e3sconf/202019505005

Acar Y.B., and El-Tahir E.A. 1986. Low strain dynamic properties of artificially cemented sand. *Journal of Geotechnical Engineering* 112 (11), 15. https://doi.org/10.1061/(ASCE)0733-9410(1986)112:11(1001)

Al Qabany A., Mortensen B., Martinez B., Soga K., and DeJong J. 2011. Microbial Carbonate Precipitation: Correlation of S-Wave Velocity with Calcite Precipitation *Geo-Frontiers 2011*. American Society of Civil Engineers, Dallas, Texas, United States, 3993–4001. https://doi.org/10.1061/41165(397)408

Al Qabany A., and Soga K. 2013. Effect of chemical treatment used in micp on engineering properties of cemented soils. *Geotechnique; London* 63 (4), 331–339. https://doi.org/10.1680/geot.SIP13.P.022

Al Qabany A., Soga K., and Santamarina C. 2012. Factors affecting efficiency of microbially induced calcite precipitation. *J. Geotech. Geoenviron. Eng.* 138 (8), 992–1001. https://doi.org/10.1061/(ASCE)GT.1943-5606.0000666

Allmond J., and Kutter B. 2012. Centrifuge testing of rocking foundations on saturated and submerged sand: centrifuge data report for jda01 (No. UCD/CGM report12/01).

Almajed A., Lateef M.A., Moghal A.A.B., and Lemboye K. 2021. State-of-the-art review of the applicability and challenges of microbial-induced calcite precipitation (MICP) and enzyme-induced calcite precipitation (EICP) techniques for geotechnical and geoenvironmental applications. *Crystals* 11 (4), 370. https://doi.org/10.3390/cryst11040370

Andrus R.D., and Stokoe II K.H. 2000. Liquefaction Resistance of Soils from Shear-Wave Velocity. *Journal of Geotechnical and Geoenvironmental Engineering* 126 (11), 1015–1025. https://doi.org/10.1061/(ASCE)1090-0241(2000)126:11(1015)

APHA 2005. Standard methods for the examination of water and wastewater, 21st ed. American Public Health Association/American Water Works Association/Water Environment Federation, Washington DC.

Arroyo M., Ciantia M., Castellanza R., Gens A., and Nova R. 2012. Simulation of cement-improved clay structures with a bonded elasto-plastic model: A practical approach. *Computers and Geotechnics* 45, 140–150. https://doi.org/10.1016/j.compgeo.2012.05.008

Asghari S., Chittoori B.C.S., Burbank M., and Hudyma N. 2021. Studying the relationship between indigenous microbial communities, urease activity, and calcite precipitation in artificial mixes of clay and sand *IFCEE 2021*. American Society of Civil Engineers, Dallas, Texas, 130–138. https://doi.org/10.1061/9780784483428.014

Assadi-Langroudi A., O'Kelly B.C., Barreto D., Cotecchia F., Dicks H., Ekinci A., Garcia F.E., Harbottle M., Tagarelli V., Jefferson I., Maghoul P., Masoero E., El Mountassir G., Muhunthan B., Geng X., Ghadr S., Mirzababaei M., Mitrani H., and van Paassen L. 2022. Recent advances in nature-inspired solutions for ground engineering (NiSE). *Int. J. of Geosynth. and Ground Eng.* 8 (1), 3. https://doi.org/10.1007/s40891-021-00349-9

ASTM International 2021. Standard test method for rapid determination of carbonate content of soils (No. D4373 − 21). ASTM International. https://doi.org/10.1520/D4373-21

ASTM International 2016. Standard test methods for acidity or alkalinity of water (No. D1067 − 16). ASTM International. https://doi.org/10.1520/D1067-16

Bachmeier K.L., Williams A.E., Warmington J.R., and Bang S.S. 2002. Urease activity in microbiologically-induced calcite precipitation. *Journal of Biotechnology* 93 (2), 171–181. https://doi.org/10.1016/S0168-1656(01)00393-5

Baek S.-H., Hong J.-W., Kim K.Y., Yeom S., and Kwon T.-H. 2019. X-ray computed microtomography imaging of abiotic carbonate precipitation in porous media from a supersaturated solution: Insights into effect of CO2 mineral trapping on permeability. *Water Resources Research* 55 (5), 3835–3855. https://doi.org/10.1029/2018WR023578

Baek S.-H., Kwon T.-H., and DeJong J.T. 2022. Impact of microbially induced calcite precipitation (MICP) on hydraulic conductivity of coarse sands *20th International Conference on Soil Mechanics and Geotechnical Engineering*. Sydney, Australia.

Bakken L.R., and Olsen R.A. 1983. Buoyant densities and dry-matter contents of microorganisms: conversion of a measured biovolume into biomass. *Appl Environ Microbiol* 45 (4), 1188–1195. https://doi.org/10.1128/aem.45.4.1188-1195.1983

Bang S.S., Galinat J.K., and Ramakrishnan V. 2001. Calcite precipitation induced by polyurethane-immobilized Bacillus pasteurii. *Enzyme and Microbial Technology* 28 (4), 404–409. https://doi.org/10.1016/S0141-0229(00)00348-3

Barkouki T., Martinez B., Mortensen B., Weathers T., Dejong J., Spycher N., Ginn T., Fujita Y., Smith R., Barkouki T., Martinez B., Mortensen B., Weathers T., Dejong J., Spycher N., Ginn T., Fujita Y., and Smith R. 2011. Forward and inverse bio-geochemical modeling of microbially induced calcite precipitation in half-meter column experiments. *Transp. Porous Media* 23–39. https://doi.org/10.1007/s11242-011-9804-z

Bassal P.C., Boulanger R.W., and DeJong J.T. 2022. System response of an interlayered deposit with spatially distributed ground deformations in the Chi-Chi earthquake.*To Be Submitted.*

Bassal P.C., Boulanger R.W., and DeJong J.T. 2021. Dynamic analyses of liquefaction and lateral spreading for an interlayered deposit in the Chi-Chi earthquake 426–441. https://doi.org/10.1061/9780784483695.042

Baum M.J., Kovalev A.E., Michels J., and Gorb S.N. 2014. Anisotropic friction of the ventral scales in the snake lampropeltis getula californiae. *Tribol Lett* 54 (2), 139–150. https://doi.org/10.1007/s11249-014-0319-y

Baveye P.C., Otten W., Kravchenko A., Balseiro-Romero M., Beckers É., Chalhoub M., Darnault C., Eickhorst T., Garnier P., Hapca S., Kiranyaz S., Monga O., Mueller C.W., Nunan N., Pot V., Schlüter S., Schmidt H., and Vogel H.-J. 2018. Emergent properties of microbial activity in heterogeneous soil microenvironments: Different research approaches are slowly converging, yet major challenges remain. *Front. Microbiol.* 9, 1929. https://doi.org/10.3389/fmicb.2018.01929

Beal S.L. 1982. On the solution to the Michaelis-Menten equation. *Journal of Pharmacokinetics and Biopharmaceutics* 10 (1), 109–119. https://doi.org/10.1007/BF01059186

Béguin R., Oxarango L., Sapin L., Garandet A., Viglino A., François E., Mora H., Martins F., Duchesne L., Albrecht D., Esnault-Filet A., Gutjahr I., and Lépine L. 2019. Experimental tests of soil reinforcement against erosion and liquefaction by microbially induced carbonate precipitation *Internal Erosion in Earthdams, Dikes and Levees*, Lecture Notes in Civil Engineering. Springer International Publishing, Cham, 16–24. https://doi.org/10.1007/978-3-319-99423-9_2

Benini S., Rypniewski W.R., Wilson K.S., Miletti S., Ciurli S., and Mangani S. 1999. A new proposal for urease mechanism based on the crystal structures of the native and inhibited enzyme from Bacillus pasteurii: why urea hydrolysis costs two nickels. *Structure* 7 (2), 205–216. https://doi.org/10.1016/S0969-2126(99)80026-4

Bhutange S.P., and Latkar M.V. 2020. Microbially induced calcium carbonate precipitation in construction materials. *J. Mater. Civ. Eng.* 32 (5), 03120001. https://doi.org/10.1061/(ASCE)MT.1943-5533.0003141

Biryaltseva T., Lunne T., Kreiter S., and al et 2016. Relative density prediction based on in-situ and laboratory measurements of shear wave velocity *5th International Conference on Geotechnical and Geophysical Site Characterisation, ISC 2016. Proceedings. Vol.1*. Australian Geomechanics Society, Australia, 389–394.

Blackwell P.G., Rennolls K., and Coutts M.P. 1990. A root anchorage model for shallowly rooted Sitka spruce. *Forestry* 63 (1), 73–91. https://doi.org/10.1093/forestry/63.1.73

Bladh K.W., Bideaux R.A., Anthony-Morton E., and Nichols B.G. 2001. Handbook of mineralogy. Mineralogical Society of America, Berkeley.

Bolton M.D. 1986. The strength and dilatancy of sands. *Géotechnique* 36 (1), 65–78. https://doi.org/10.1680/geot.1986.36.1.65

Borela R., Frost J.D., Viggiani G., and Anselmucci F. 2021. Earthworm-inspired robotic locomotion in sand: An experimental study using x-ray tomography. *Géotechnique Letters* 11 (1), 1–22. https://doi.org/10.1680/jgele.20.00085

Boulanger R.W. 2003. High overburden stress effects in liquefaction analyses. *Journal of Geotechnical and Geoenvironmental Engineering* 129 (12), 1071–1082. https://doi.org/10.1061/(ASCE)1090-0241(2003)129:12(1071)

Boulanger R.W., and Idriss I.M. 2015. CPT-based liquefaction triggering procedure. *J. Geotech. Geoenviron. Eng.* 142 (2), 04015065. https://doi.org/10.1061/(ASCE)GT.1943-5606.0001388

Boulanger R.W., and Idriss I.M. 2014. CPT and SPT based liquefaction triggering procedures (UCD/CGM-14/01).

Boulanger R.W., and Ziotopoulou K. 2017. PM4Sand (Version 3.1): A sand plasticity model for earthquake engineering applications (Center for Geotechnical Modeling, Department of Civil and Environmental Engineering No. UCD/CGM-17/01). University of California, Davis, Davis, CA.

Bradford M.M. 1976. A rapid and sensitive method for the quantitation of microgram quantities of protein utilizing the principle of protein-dye binding. *Analytical Biochemistry* 78, 248–254. https://doi.org/10.1016/0003-2697(76)90527-3

Brandenberg S.J., Wilson D.W., and Rashid M.M. 2010. Weighted Residual Numerical Differentiation Algorithm Applied to Experimental Bending Moment Data. *Journal of Geotechnical and Geoenvironmental Engineering* 136 (6), 854–863. https://doi.org/10.1061/(ASCE)GT.1943-5606.0000277

Brignoli E.G., Gotti M., and Stokoe K.H. 1996. Measurement of shear waves in laboratory specimens by means of piezoelectric transducers. *Geotech. Test. J.* 19 (4), 384. https://doi.org/10.1520/GTJ10716J

British Columbia Contaminated Sites Regulation 2020. British columbia environmental management act contaminated sites regulation [WWW Document]. *Contaminated Sites Regulation*.

Bruno A.W., Gallipoli D., Rouainia M., and Lloret-Cabot M. 2020. A bounding surface mechanical model for unsaturated cemented soils under isotropic stresses. *Computers and Geotechnics* 125, 103673. https://doi.org/10.1016/j.compgeo.2020.103673

Burbank M., Weaver T., Lewis R., Williams T., Williams B., and Crawford R. 2013. Geotechnical tests of sands following bioinduced calcite precipitation catalyzed by indigenous bacteria. *J. Geotech. Geoenviron. Eng.* 139 (6), 928–936. https://doi.org/10.1061/(ASCE)GT.1943-5606.0000781

Burbank M.B., Weaver T.J., Green T.L., Williams B.C., and Crawford R.L. 2011. Precipitation of calcite by indigenous microorganisms to strengthen liquefiable soils. *Geomicrobiology Journal* 28 (4), 301–312. https://doi.org/10.1080/01490451.2010.499929

Burbank M.B., Weaver T.J., Williams B.C., and Crawford R.L. 2012. Urease activity of ureolytic bacteria isolated from six soils in which calcite was precipitated by indigenous bacteria. *Geomicrobiology Journal* 29 (4), 389–395. https://doi.org/10.1080/01490451.2011.575913

Burdalski R.J. 2020. Investigating the effect of biological and chemical factors on the reaction kinetics and mineralogy of ureolytic bio-cementation (Master of Science in Civil & Environmental Engineering). University of Washington, Seattle, Washington.

Burdalski R.J., and Gomez M.G. 2020. Investigating the effect of microbial activity and chemical concentrations on the mineralogy and morphology of ureolytic bio-cementation *Geo-Congress 2020*, Proceedings. American Society of Civil Engineers, Minneapolis, Minnesota, 83–95. https://doi.org/10.1061/9780784482834.010

Burdalski R.J., Gomez M.G., and Gorman-Lewis D. 2022a. Effect of environmental factors on the mineralogy and morphology of ureolytic bio-cementation.*To Be Submitted.*

Burdalski R.J., Ribeiro B.G.O., Gomez M.G., and Gorman-Lewis D. 2022b. Effect of ureolytic rates and treatment additions on the mineralogy and morphology of ureolytic bio-cementation.*To Be Submitted.*

Burdalski R.J., Ribeiro B.G.O., Gomez M.G., and Gorman-Lewis D. 2022c. Effect of biological factors on the mineralogy and morphology of ureolytic bio-cementation.*To Be Submitted.*

Burrall M., DeJong J.T., Martinez A., and Wilson D.W. 2020. Vertical pullout tests of orchard trees for bio-inspired engineering of anchorage and foundation systems. *Bioinspir. Biomim.* 16 (1), 016009. https://doi.org/10.1088/1748-3190/abb414

Carey T.J., Gavras A., and Kutter B.L. 2020a. Grain size analysis and maximum and minimum dry density testing of ottawa f-65 sand for

leap-ucd-2017Kutter, B.L., Manzari, M.T., and Zeghal, M. (Eds.), *Model Tests and Numerical Simulations of Liquefaction and Lateral Spreading*. Springer International Publishing, Cham.

Carey T.J., Stone N., and Kutter B.L. 2020b. Comparison of leap-ucd-2017 cpt resultsKutter, B.L., Manzari, M.T., and Zeghal, M. (Eds.), *Model Tests and Numerical Simulations of Liquefaction and Lateral Spreading*. Springer International Publishing, Cham, 117–129. https://doi.org/10.1007/978-3-030-22818-7_6

Carle S., and Fogg G. 1996. Transition probability-based indicator geostatistics. *Mathematical Geology* 28, 453–476. https://doi.org/10.1007/BF02083656

Castanier S., Le Métayer-Levrel G., and Perthuisot J.-P. 1999. Ca-carbonates precipitation and limestone genesis — the microbiogeologist point of view. *Sedimentary Geology* 126 (1–4), 9–23. https://doi.org/10.1016/S0037-0738(99)00028-7

Chen X., and Achal V. 2020. Effect of simulated acid rain on the stability of calcium carbonate immobilized by microbial carbonate precipitation. *Journal of Environmental Management* 264, 110419. https://doi.org/10.1016/j.jenvman.2020.110419

Chen Y., Khosravi A., Martinez A., DeJong J., and Wilson D. 2020. Analysis of the self-penetration process of a bio-inspired in situ testing probe *Geo-Congress 2020*. American Society of Civil Engineers, Minneapolis, Minnesota, 224–232. https://doi.org/10.1061/9780784482834.025

Cheng L., and Cord-Ruwisch R. 2014. Upscaling effects of soil improvement by microbially induced calcite precipitation by surface percolation. *Geomicrobiology Journal* 31 (5), 396–406. https://doi.org/10.1080/01490451.2013.836579

Cheng L., and Cord-Ruwisch R. 2012. In situ soil cementation with ureolytic bacteria by surface percolation. *Ecological Engineering* 42, 64–72. https://doi.org/10.1016/j.ecoleng.2012.01.013

Cheng L., Cord-Ruwisch R., and Shahin M.A. 2013. Cementation of sand soil by microbially induced calcite precipitation at various degrees of saturation. *Can. Geotech. J.* 50 (1), 81–90. https://doi.org/10.1139/cgj-2012-0023

Cheng L., Shahin M., Cord-Ruwisch R., Addis M., Hartanto T., and Elms C. 2014. Soil stabilisation by microbial-induced calcite precipitation (MICP): Investigation into some physical and environmental aspects.*Soil stabilisation by microbial-induced calcite precipitation (micp)*

Cheng L., and Shahin M.A. 2015. Assessment of different treatment methods by microbial-induced calcite precipitation for clayey soil improvement 7.

Cheng L., Shahin M.A., and Cord-Ruwisch R. 2017a. Surface percolation for soil improvement by biocementation utilizing in situ enriched indigenous aerobic and anaerobic ureolytic soil microorganisms. *Geomicrobiology Journal* 34 (6), 546–556. https://doi.org/10.1080/01490451.2016.1232766

Cheng L., Shahin M.A., and Mujah D. 2017b. Influence of key environmental conditions on microbially induced cementation for soil stabilization. *Journal of Geotechnical and Geoenvironmental Engineering* 143 (1), 04016083. https://doi.org/10.1061/(ASCE)GT.1943-5606.0001586

Cheshomi A., and Mansouri S. 2019. Study the grain size and infiltration method effects for sand soil improvement using the microbial method. *Geomicrobiology Journal* 37 (4), 355–365. https://doi.org/10.1080/01490451.2019.1705437

Choi S.-G., Chang I., Lee M., Lee J.-H., Han J.-T., and Kwon T.-H. 2020. Review on geotechnical engineering properties of sands treated by microbially induced calcium carbonate precipitation (MICP) and biopolymers. *Construction and Building Materials* 246, 118415. https://doi.org/10.1016/j.conbuildmat.2020.118415

Choi S.-G., Park S.-S., Wu S., and Chu J. 2017. Methods for calcium carbonate content measurement of biocemented soils. *J. Mater. Civ. Eng.* 29 (11), 06017015. https://doi.org/10.1061/(ASCE)MT.1943-5533.0002064

Choi S.-G., Wu S., and Chu J. 2016. Biocementation for sand using an eggshell as calcium source. *J. Geotech. Geoenviron. Eng.* 142 (10), 06016010. https://doi.org/10.1061/(ASCE)GT.1943-5606.0001534

Chong S.-H. 2019. Development of constitutive model for simulation of cemented soil. *Geotech Geol Eng* 37 (5), 4635–4641. https://doi.org/10.1007/s10706-019-00903-3

Chu J., Ivanov V., He J., Naeimi M., Li B., and Stabnikov V. 2011. Development of microbial geotechnology in singapore *Geo-Frontiers 2011*. American Society of Civil Engineers, Dallas, Texas, United States, 4070–4078. https://doi.org/10.1061/41165(397)416

Chu J., Stabnikov V., and Ivanov V. 2012. Microbially induced calcium carbonate precipitation on surface or in the bulk of soil. *Geomicrobiology Journal* 29 (6), 544–549. https://doi.org/10.1080/01490451.2011.592929

Ciantia M.O., and di Prisco C. 2016. Extension of plasticity theory to debonding, grain dissolution, and chemical damage of calcarenites. *Int. J. Numer. Anal. Meth. Geomech.* 40 (3), 315–343. https://doi.org/10.1002/nag.2397

Ciurli S., Benini S., Rypniewski W.R., Wilson K.S., Miletti S., and Mangani S. 1999. Structural properties of the nickel ions in urease: novel insights into the catalytic and inhibition mechanisms. *Coordination Chemistry Reviews* 190–192, 331–355. https://doi.org/10.1016/S0010-8545(99)00093-4

Clarke M.A. 2003. SyrupsCaballero, B. (Ed.), *Encyclopedia of Food Sciences and Nutrition (Second Edition)*. Academic Press, Oxford, 5711–5717. https://doi.org/10.1016/B0-12-227055-X/01175-5

Clough G.W., Iwabuchi J., Rad N.S., and Kuppusamy T. 1989. Influence of cementation on liquefaction of sands. *Journal of Geotechnical Engineering* 115 (8), 1102–1117. https://doi.org/10.1061/(ASCE)0733-9410(1989)115:8(1102)

Cohen D., Schwarz M., and Or D. 2011. An analytical fiber bundle model for pullout mechanics of root bundles. *J. Geophys. Res.* 116 (F3), F03010. https://doi.org/10.1029/2010JF001886

Collingridge D. 1980. The social control of technology. Frances Pinter, London, UK.

Colombani J. 2016. The alkaline dissolution rate of calcite. *J. Phys. Chem. Lett.* 7 (13), 2376–2380. https://doi.org/10.1021/acs.jpclett.6b01055

Cortes D.D., and John S. 2018. Earthworm-inspired soil penetration *Proceedings of Biomediated and Bioinspired Geotechnics (B2G) Conference*. Atlanta, GA, 7.

Cubillas P., Köhler S., Prieto M., Chaïrat C., and Oelkers E.H. 2005. Experimental determination of the dissolution rates of calcite, aragonite, and bivalves. *Chemical Geology* 216 (1–2), 59–77. https://doi.org/10.1016/j.chemgeo.2004.11.009

Cui M.-J., Teng A., Chu J., and Cao B. 2022. A quantitative, high-throughput urease activity assay for comparison and rapid screening of ureolytic bacteria. *Environmental Research* 208, 112738. https://doi.org/10.1016/j.envres.2022.112738

Cunningham A.B., Characklis W.G., Abedeen F., and Crawford D. 1991. Influence of biofilm accumulation on porous media hydrodynamics. *Environ. Sci. Technol.* 25 (7), 1305–1311. https://doi.org/10.1021/es00019a013

Cuthbert M.O., McMillan L.A., Handley-Sidhu S., Riley Michael.S., Tobler D.J., and Phoenix Vernon.R. 2013. A field and modeling study of fractured rock permeability reduction using microbially induced calcite precipitation. *Environ. Sci. Technol.* 47 (23), 13637–13643. https://doi.org/10.1021/es402601g

Cycoń M., Mrozik A., and Piotrowska-Seget Z. 2017. Bioaugmentation as a strategy for the remediation of pesticide-polluted soil: A review. *Chemosphere* 172, 52–71. https://doi.org/10.1016/j.chemosphere.2016.12.129

Dadda A., Geindreau C., Emeriault F., du Roscoat S.R., Garandet A., Sapin L., and Filet A.E. 2017. Characterization of microstructural and physical properties changes in biocemented sand using 3D x-ray microtomography. *Acta Geotech.* 12 (5), 955–970. https://doi.org/10.1007/s11440-017-0578-5

Dafalias Y.F., and Manzari M.T. 2004. Simple plasticity sand model accounting for fabric change effects. *Journal of Engineering Mechanics* 130 (6), 622–634. https://doi.org/10.1061/(ASCE)0733-9399(2004)130:6(622)

Darby K.M., Hernandez G.L., DeJong J.T., Boulanger R.W., Gomez M.G., and Wilson D.W. 2019. Centrifuge model testing of liquefaction mitigation via microbially induced calcite precipitation. *J. Geotech. Geoenviron. Eng.* 145 (10), 04019084. https://doi.org/10.1061/(ASCE)GT.1943-5606.0002122

Dashti S., Bray J.D., Pestana J.M., Riemer M., and Wilson D. 2010a. Mechanisms of seismically induced settlement of buildings with shallow foundations on liquefiable soil. *Journal of Geotechnical and Geoenvironmental Engineering* 136 (1), 151–164. https://doi.org/10.1061/(ASCE)GT.1943-5606.0000179

Dashti S., Bray J.D., Pestana J.M., Riemer M., and Wilson D. 2010b. Centrifuge testing to evaluate and mitigate liquefaction-induced building settlement mechanisms. *J. Geotech. Geoenviron. Eng.* 136 (7), 918–929. https://doi.org/10.1061/(ASCE)GT.1943-5606.0000306

Davis C.A., Atekwana Estella, Atekwana Eliot, Slater L.D., Rossbach S., and Mormile M.R. 2006. Microbial growth and biofilm formation in geologic media is detected with complex conductivity measurements: microbial growth and geophysics. *Geophys. Res. Lett.* 33 (18), n/a-n/a. https://doi.org/10.1029/2006GL027312

de Bono J., McDowell G., and Wanatowski D. 2015. Investigating the micro mechanics of cemented sand using DEM. *Int. J. Numer. Anal. Meth. Geomech.* 39 (6), 655–675. https://doi.org/10.1002/nag.2340

De Muynck W., Verbeken K., De Belie N., and Verstraete W. 2013. Influence of temperature on the effectiveness of a biogenic carbonate surface treatment for limestone conservation. *Appl Microbiol Biotechnol* 97 (3), 1335–1347. https://doi.org/10.1007/s00253-012-3997-0

DeJong J.T. 2020. Biogeotechnics: Bio-mediated processes and bio-inspired ideas for geotechnical engineering innovation.

DeJong J.T., Burrall M., Wilson D.W., and Frost J.D. 2017. A bio-inspired perspective for geotechnical engineering innovation *Geotechnical Frontiers 2017*. American Society of Civil Engineers, Orlando, Florida, 862–870. https://doi.org/10.1061/9780784480472.092

DeJong J.T., Fritzges M.B., and Nüsslein K. 2006. Microbially induced cementation to control sand response to undrained shear. *J. Geotech. Geoenviron. Eng.* 132 (11), 1381–1392. https://doi.org/10.1061/(ASCE)1090-0241(2006)132:11(1381)

DeJong J.T., and Kavazanjian E. 2019. Bio-mediated and bio-inspired geotechnicsLu, N., and Mitchell, J.K. (Eds.), *Geotechnical Fundamentals for Addressing New World Challenges*, Springer Series in Geomechanics and Geoengineering. Springer International Publishing, Cham, 193–207. https://doi.org/10.1007/978-3-030-06249-1_7

DeJong J.T., Krage C.P., Boulanger R.W., and DeGroot D.J. 2021. Optimization of CPT soundings to reduce uncertainty in interpretation of subsurface stratigraphy *6th International Conference on Geotechnical and Geophysical Site Characterization*. Budapest, Hungary, 20.

DeJong J.T., Martinez B.C., Ginn T.R., Hunt C., Major D., and Tanyu B. 2014. Development of a scaled repeated five-spot treatment model for examining microbial induced calcite precipitation feasibility in field applications. *Geotech. Test. J.* 37 (3), 20130089. https://doi.org/10.1520/GTJ20130089

DeJong J.T., Martinez B.C., Mortensen B.M., Nelson D.C., Waller J.T., Weil M.H., Ginn T.R., Weathers T., Barkouki T., Fujita Y., Redden G., Hunt C., Major D., and Tanyu B. 2009. Upscaling of bio-mediated soil improvement. *Proceedings of the 17th International Conference on Soil Mechanics and Geotechnical Engineering (Volumes 1, 2, 3 and 4)* 2300–2303. https://doi.org/10.3233/978-1-60750-031-5-2300

DeJong J.T., Mortensen B.M., Martinez B.C., and Nelson D.C. 2010. Bio-mediated soil improvement. *Ecological Engineering* 36 (2), 197–210. https://doi.org/10.1016/j.ecoleng.2008.12.029

DeJong J.T., Soga K., Kavazanjian E., Burns S., Van Paassen L.A., Al Qabany A., Aydilek A., Bang S.S., Burbank M., Caslake L.F., Chen C.Y., Cheng X., Chu J., Ciurli S., Esnault-Filet A., Fauriel S., Hamdan N., Hata T., Inagaki Y., Jefferis S., Kuo M., Laloui L., Larrahondo J., Manning D.A.C., Martinez B., Montoya B.M., Nelson D.C., Palomino A., Renforth P., Santamarina J.C., Seagren E.A., Tanyu B., Tsesarsky M., and Weaver T. 2013. Biogeochemical processes and geotechnical applications: progress, opportunities and challenges. *Géotechnique* 63 (4), 287–301. https://doi.org/10.1680/geot.SIP13.P.017

Delfosse-Ribay E., Djeran-Maigre I., Cabrillac R., and Gouvenot D. 2004. Shear modulus and damping ratio of grouted sand. *Soil Dynamics and Earthquake Engineering* 24 (6), 461–471. https://doi.org/10.1016/j.soildyn.2004.02.004

Dhami N.K., Alsubhi W.R., Watkin E., and Mukherjee A. 2017. Bacterial community dynamics and biocement formation during stimulation and augmentation: implications for soil consolidation. *Front. Microbiol.* 8, 1267. https://doi.org/10.3389/fmicb.2017.01267

Dickson A.G., and Goyet C. 1994. Handbook of methods for the analysis of the various parameters of the carbon dioxide system in sea water. version 2 (No. ORNL/CDIAC-74). Oak Ridge National Lab., TN (United States). https://doi.org/10.2172/10107773

Dikshit R., Jain A., Dey A., and Kumar A. 2020. Microbially induced calcite precipitation using Bacillus velezensis with guar gum. *PLoS ONE* 15 (8), e0236745. https://doi.org/10.1371/journal.pone.0236745

Do J., Montoya B.M., and Gabr M.A. 2021. Scour mitigation and erodibility improvement using microbially induced carbonate precipitation. *Geotech. Test. J.* 44 (5), 20190478. https://doi.org/10.1520/GTJ20190478

Dong Y., and Fatahi B. 2020. Discrete element simulation of cavity expansion in lightly cemented sands considering cementation degradation. *Computers and Geotechnics* 124, 103628. https://doi.org/10.1016/j.compgeo.2020.103628

Duggan A.R., Goggins J., Clifford E., and McCabe B.A. 2017. The use of carbonation depth techniques on stabilized peat. *Geotech. Test. J.* 40 (6), 20160223. https://doi.org/10.1520/GTJ20160223

Dupas J.-M., and Pecker A. 1979. Static and dynamic properties of sand-cement. *Journal of the Geotechnical Engineering Division* 105 (GT3), 18. https://doi.org/10.1061/AJGEB6.0000778

Dupuy L.X., Fourcaud T., Lac P., and Stokes A. 2007. A generic 3D finite element model of tree anchorage integrating soil mechanics and real root system architecture. *American Journal of Botany* 94 (9), 1506–1514. https://doi.org/10.3732/ajb.94.9.1506

Dyson A.S., and Rognon P.G. 2014. Pull-out capacity of tree root inspired anchors in shallow granular soils. *Géotechnique Letters* 4 (4), 301–305. https://doi.org/10.1680/geolett.14.00061

El Kortbawi M., Ziotopoulou K., Gomez M.G., and Lee M. 2022a. Mechanical behavior of bio-cemented sands: State review of experimental and numerical developments.*To Be Submitted.*

El Kortbawi M., Ziotopoulou K., and Boulanger R.W. 2022b. A constitutive model for bio-cemented sands for plane-strain earthquake engineering applications.*To Be Submitted.*

El Mountassir G., Minto J.M., van Paassen L.A., Salifu E., and Lunn R.J. 2018. Applications of microbial processes in geotechnical engineering *Advances in Applied Microbiology*. Elsevier, 39–91. https://doi.org/10.1016/bs.aambs.2018.05.001

Ellis D.E., Lutz E.J., Odom J.M., Buchanan R.J., Bartlett C.L., Lee M.D., Harkness M.R., and DeWeerd K.A. 2000. Bioaugmentation for accelerated in situ anaerobic bioremediation. *Environ. Sci. Technol.* 34 (11), 2254–2260. https://doi.org/10.1021/es990638e

Eslaamizaad S., and Robertson P. 1996. Seismic cone penetration test to identify cemented sands *In Proceedings of the 49th Canadian Geotechnical Conference*. St. John's, NL, 23–25.

Esnault Filet A., Gadret J.-P., Loygue M., and Borel S. 2012. Biocalcis and its applications for the consolidation of sands 1767–1780. https://doi.org/10.1061/9780784412350.0152

Esnault Filet A., Gutjahr I., Garandet A., Viglino A., Béguin R., Monier J.-M., Oxarango L., Emeriault F., and Perthuisot S.C. 2020. BOREAL, Bio-reinforcement of embankments by biocalcification. *E3S Web Conf.* 195, 05001. https://doi.org/10.1051/e3sconf/202019505001

European Union 2020. Directive (EU) 2020/2184 of the European parliament and of the Council of 16 December 2020 On the quality of water intended for human consumption (No. 435). Off. J. Eur. Union.

Evans T., Khoubani A., and Montoya B. 2015. Simulating mechanical response in bio-cemented sandsOka, F., Murakami, A., Uzuoka, R., and Kimoto, S. (Eds.), *Computer Methods and Recent Advances in Geomechanics*. CRC Press, 1569–1574. https://doi.org/10.1201/b17435-277

Ezzat S.M., and Ewida A.Y.I. 2021. Smart soil grouting using innovative urease-producing bacteria and low cost materials. *J Appl Microbiol* 131 (5), 2294–2307. https://doi.org/10.1111/jam.15117

Fauriel S., and Laloui L. 2012. A bio-chemo-hydro-mechanical model for microbially induced calcite precipitation in soils. *Computers and Geotechnics* 46, 104–120. https://doi.org/10.1016/j.compgeo.2012.05.017

Feng K. 2015. Constitutive response of microbial induced calcite precipitation cemented sands (PhD Dissertation). North Carolina State University, Raleigh, NC.

Feng K., and Montoya B.M. 2015. Drained shear strength of MICP sand at varying cementation levels *IFCEE 2015*. American Society of Civil Engineers, San Antonio, Texas, 2242–2251. https://doi.org/10.1061/9780784479087.208

Feng K., Montoya B.M., and Evans T.M. 2017. Discrete element method simulations of bio-cemented sands. *Computers and Geotechnics* 85, 139–150. https://doi.org/10.1016/j.compgeo.2016.12.028

Fenton G.A., and Vanmarcke E.H. 1990. Simulation of random fields via local average subdivision. *Journal of Engineering Mechanics* 116 (8), 1733–1749. https://doi.org/10.1061/(ASCE)0733-9399(1990)116:8(1733)

Ferris F.G., Phoenix V., Fujita Y., and Smith R.W. 2004. Kinetics of calcite precipitation induced by ureolytic bacteria at 10 to 20°C in artificial groundwater. *Geochimica et Cosmochimica Acta* 68 (8), 1701–1710. https://doi.org/10.1016/S0016-7037(03)00503-9

Ferris F.G., Stehmeier L.G., Kantzas A., and Mourits F.M. 1997. Bacteriogenic mineral plugging. *Journal of Canadian Petroleum Technology* 36 (09). https://doi.org/10.2118/97-09-07

Fidaleo M., and Lavecchia R. 2003. Kinetic study of enzymatic urea hydrolysis in the ph range 4–9. *Chem. Biochem. Eng. Q.* 8.

Finnerty W.R., and Singer M.E. 1983. Microbial enhancement of oil recovery. *Nat Biotechnol* 1 (1), 47–54. https://doi.org/10.1038/nbt0383-47

Flores Orozco A., Kemna A., Oberdörster C., Zschornack L., Leven C., Dietrich P., and Weiss H. 2012. Delineation of subsurface hydrocarbon contamination at a former hydrogenation plant using spectral induced polarization imaging. *Journal of Contaminant Hydrology* 136–137, 131–144. https://doi.org/10.1016/j.jconhyd.2012.06.001

Flores Orozco A., Williams K.H., Long P.E., Hubbard S.S., and Kemna A. 2011. Using complex resistivity imaging to infer biogeochemical processes associated with bioremediation of an uranium-contaminated aquifer. *J. Geophys. Res.* 116 (G3), G03001. https://doi.org/10.1029/2010JG001591

Fu Z., Chen S., Zhong Q., and Ji E. 2022. A damage hypoplasticity constitutive model for cemented sand and gravel materials. *Acta Geotechnica* 17. https://doi.org/10.1007/s11440-021-01206-9

Fujita Y., Ferris F.G., Lawson R.D., Colwell F.S., and Smith R.W. 2000. Subscribed content calcium carbonate precipitation by ureolytic subsurface bacteria. *Geomicrobiology Journal* 17 (4), 305–318. https://doi.org/10.1080/782198884

Fujita Y., Taylor J.L., Gresham T.L.T., Delwiche M.E., Colwell F.S., McLing T.L., Petzke L.M., and Smith R.W. 2008. Stimulation of microbial urea hydrolysis in groundwater to enhance calcite precipitation. *Environ. Sci. Technol.* 42 (8), 3025–3032. https://doi.org/10.1021/es702643g

Gai X., and Sánchez M. 2018. An elastoplastic mechanical constitutive model for microbially mediated cemented soils. *Acta Geotech.* 14 (3), 709–726. https://doi.org/10.1007/s11440-018-0721-y

Gajo A., Cecinato F., and Hueckel T. 2019. Chemo-mechanical modeling of artificially and naturally bonded soils. *Geomechanics for Energy and the Environment* 18, 13–29. https://doi.org/10.1016/j.gete.2018.11.005

Gajo A., Cecinato F., and Hueckel T. 2015. A micro-scale inspired chemo-mechanical model of bonded geomaterials. *International Journal of Rock Mechanics and Mining Sciences* 80, 425–438. https://doi.org/10.1016/j.ijrmms.2015.10.001

Gal J.Y., Bollinger J.C., Tolosa H., and Gache N. 1996. Calcium carbonate solubility: a reappraisal of scale formation and inhibition. *Talanta* 43 (9), 1497–1509. https://doi.org/10.1016/0039-9140(96)01925-X

Ganendra G., De Muynck W., Ho A., Arvaniti E.C., Hosseinkhani B., Ramos J.A., Rahier H., and Boon N. 2014. Formate oxidation-driven calcium carbonate precipitation by Methylocystis parvus OBBP. *Appl Environ Microbiol* 80 (15), 4659–4667. https://doi.org/10.1128/AEM.01349-14

Gao Z., and Zhao J. 2012. Constitutive modeling of artificially cemented sand by considering fabric anisotropy. *Computers and Geotechnics* 41, 57–69. https://doi.org/10.1016/j.compgeo.2011.10.007

Gartner 2018. Understanding Gartner's hype cycles [WWW Document]. URL www.gartner.com

Gat D., Ronen Z., and Tsesarsky M. 2017. Long-term sustainability of microbial-induced CaCO3 precipitation in aqueous media. *Chemosphere* 184, 524–531. https://doi.org/10.1016/j.chemosphere.2017.06.015

Gat D., Ronen Z., and Tsesarsky M. 2016. Soil bacteria population dynamics following stimulation for ureolytic microbial-induced CaCO3 precipitation. *Environ. Sci. Technol.* 50 (2), 616–624. https://doi.org/10.1021/acs.est.5b04033

Gat D., Tsesarsky M., and Shamir D. 2011. Ureolytic calcium carbonate precipitation in the presence of non-ureolytic competing bacteria *Geo-Frontiers 2011*. American Society of Civil Engineers, Dallas, Texas, United States, 3966–3974. https://doi.org/10.1061/41165(397)405

Gehlen M., Bassinot F.C., Chou L., and McCorkle D. 2005. Reassessing the dissolution of marine carbonates: II. Reaction kinetics. *Deep Sea Research Part I: Oceanographic Research Papers* 52 (8), 1461–1476. https://doi.org/10.1016/j.dsr.2005.03.011

Gens A., and Nova R. 1993. Conceptual bases for a constitutive model for bonded soils and weak rocks *Proc. of Geotech. Eng. of Hard Soils-Soft Rocks*. Athens, Greece, 485–494.

Gercek H. 2007. Poisson's ratio values for rocks. *International Journal of Rock Mechanics and Mining Sciences* 44 (1), 1–13. https://doi.org/10.1016/j.ijrmms.2006.04.011

Gerhardt P. 1994. Methods for general and molecular bacteriology. American Society for Microbiology, Washington, D.C.

Ghasemi P., and Montoya B.M. 2022. Field implementation of microbially induced calcium carbonate precipitation for surface erosion reduction of a coastal plain sandy slope.*In Review.*

Ghasemi P., and Montoya B.M. 2020. Field application of the microbially induced calcium carbonate precipitation on a coastal sandy slope *Geo-Congress 2020*. American Society of Civil Engineers, Minneapolis, Minnesota, 141–149. https://doi.org/10.1061/9780784482834.016

Giri R.K., and Reddy K.R. 2014. LCA and sustainability assessment for selecting deep foundation system for high-rise buildings. American Society of Civil Engineers, Reston, VA, 621–630. https://doi.org/10.1061/9780784478745.057

Gollapudi U.K., Knutson C.L., and Bang S.S. 1995. A new method for controlling leaching through permeable channels. *Chemosphere* 30 (4), 695–705. https://doi.org/10.1016/0045-6535(94) 00435-W.

Gomez M.G. 2017. Up-scaling of bio-cementation soil improvement using native soil microorganisms (Ph.D.). *ProQuest Dissertations and Theses*. University of California, Davis, Davis, CA.

Gomez M.G., Anderson C.M., DeJong J.T., Nelson D.C., and Lau X.H. 2014. Stimulating in situ soil bacteria for bio-cementation of sands *Geo-Congress 2014 Technical Papers*, Proceedings. American Society of Civil Engineers, Atlanta, Georgia, 1674–1682. https://doi.org/10.1061/9780784413272.164

Gomez M.G., Anderson C.M., Graddy C.M.R., DeJong J.T., Nelson D.C., and Ginn T.R. 2017. Large-scale comparison of bioaugmentation and biostimulation approaches for biocementation of sands. *J. Geotech. Geoenviron. Eng.* 143 (5), 04016124. https://doi.org/10.1061/(ASCE)GT.1943-5606.0001640

Gomez M.G., and DeJong J.T. 2017. Engineering properties of bio-cementation improved sandy soils *Grouting 2017*. American Society of Civil Engineers, Honolulu, Hawaii, 23–33. https://doi.org/10.1061/9780784480793.003

Gomez M.G., DeJong J.T., and Anderson C.M. 2018a. Effect of bio-cementation on geophysical and cone penetration measurements in sands. *Can. Geotech. J.* 55 (11), 1632–1646. https://doi.org/10.1139/cgj-2017-0253

Gomez M.G., DeJong J.T., Anderson C.M., Nelson D.C., and Graddy C.M. 2016. Large-scale bio-cementation improvement of sands *Geotechnical and Structural Engineering Congress 2016*. American Society of Civil Engineers, Phoenix, Arizona, 941–949. https://doi.org/10.1061/9780784479742.079

Gomez M.G., DeJong J.T., Martinez B.C., Hunt C.E., deVlaming L.A., Major D.W., and Dworatzek S.M. 2013. Bio-mediated Soil Improvement Field Study to Stabilize Mine Sands *GeoMontreal 2013*. Montreal, Canada.

Gomez M.G., Graddy C.M.R., DeJong J.T., and Nelson D.C. 2019. Biogeochemical changes during bio-cementation mediated by stimulated and augmented ureolytic microorganisms. *Sci Rep* 9 (1), 11517. https://doi.org/10.1038/s41598-019-47973-0

Gomez M.G., Graddy C.M.R., DeJong J.T., Nelson D.C., and Tsesarsky M. 2018b. Stimulation of native microorganisms for biocementation in samples recovered from field-scale treatment depths. *J. Geotech. Geoenviron. Eng.* 144 (1), 04017098. https://doi.org/10.1061/(ASCE)GT.1943-5606.0001804

Gomez M.G., Martinez B.C., DeJong J.T., Hunt C.E., deVlaming L.A., Major D.W., and Dworatzek S.M. 2015. Field-scale bio-cementation tests to improve sands. *Proceedings of the Institution of Civil Engineers - Ground Improvement* 168 (3), 206–216. https://doi.org/10.1680/grim.13.00052

Gowthaman S., Iki T., Nakashima K., Ebina K., and Kawasaki S. 2019. Feasibility study for slope soil stabilization by microbial induced carbonate precipitation (MICP) using indigenous bacteria isolated from cold subarctic region. *SN Appl. Sci.* 1 (11), 1480. https://doi.org/10.1007/s42452-019-1508-y

Graddy C.M.R., Gomez M.G., DeJong J.T., and Nelson D.C. 2021. Native bacterial community convergence in augmented and stimulated ureolytic MICP biocementation. *Environ. Sci. Technol.* 55 (15), 10784–10793. https://doi.org/10.1021/acs.est.1c01520

Graddy C.M.R., Gomez M.G., Kline L.M., Morrill S.R., DeJong J.T., and Nelson D.C. 2018. Diversity of Sporosarcina-like bacterial strains obtained from meter-scale augmented and stimulated biocementation experiments. *Environ. Sci. Technol.* 52 (7), 3997–4005. https://doi.org/10.1021/acs.est.7b04271

Gray J., and Lissmann H.W. 1950. The kinetics of locomotion of the grass-snake. *J Exp Biol* 26 (4), 24. https://doi.org/10.1242/jeb.26.4.354

Griffiths D.V., Fenton G.A., and Manoharan N. 2002. Bearing capacity of rough rigid strip footing on cohesive soil: Probabilistic study. *Journal of Geotechnical and Geoenvironmental Engineering* 128 (9). https://doi.org/10.1061/(ASCE)1090-0241(2002)128:9(743)

Gui R., Pan Y., Ding D., Liu Y., and Zhang Z. 2018. Experimental study on the fine-grained uranium tailings reinforced by MICP. *Advances in Civil Engineering* 2018, 1–10. https://doi.org/10.1155/2018/2928985

Guinée J. 2016. Life cycle sustainability assessment: what is it and what are its challenges?Clift, R., and Druckman, A. (Eds.), *Taking Stock of Industrial Ecology*. Springer, Cham, 45–68. https://doi.org/10.1007/978-3-319-20571-7_3

Haeri S.M., Hosseini S.M., Toll D.G., and Ȳasrebi S.S. 2005. The behaviour of an artificially cemented sandy gravel. *Geotech Geol Eng* 23 (5), 537–560. https://doi.org/10.1007/s10706-004-5110-7

Hall C.A., Hernandez G., Darby K.M., van Paassen L., Jr. E.K., DeJong J., and Wilson D. 2018. Centrifuge model testing of liquefaction mitigation via denitrification-induced desaturation 117–126. https://doi.org/10.1061/9780784481455.011

Ham S.-Mi., Kwon T.-H., and DeJong J.T. 2022a. Mechanical testing of single particle contacts.*To Be Submitted.*

Ham S.-Mi., Martinez A., Han G., and Kwon T.-H. 2022b. Grain-scale tensile and shear strengths of glass beads cemented by microbially induced calcite precipitation.*In Review.*

Hamdan N., Kavazanjian E., Rittmann B.E., and Karatas I. 2011. Carbonate mineral precipitation for soil improvement through microbial denitrification *Geo-Frontiers 2011: Advances in Geotechnical Engineering*. Dallas, Texas, 10.

Hardin B.O., and Black W.L. 1968. Vibration modulus of normally consolidated clay. *J. Soil Mech. and Found. Div.* 94 (2), 353–369. https://doi.org/10.1061/JSFEAQ.0001100

Harkes M.P., van Paassen L.A., Booster J.L., Whiffin V.S., and van Loosdrecht M.C.M. 2010. Fixation and distribution of bacterial activity in sand to induce carbonate precipitation for ground reinforcement. *Ecological Engineering*, Special Issue: BioGeoCivil Engineering 36 (2), 112–117. https://doi.org/10.1016/j.ecoleng.2009.01.004

Hausler E.A. 2002. Influence of ground improvement on settlement and liquefaction: A study based on field case history evidence and dynamic geotechnical centrifuge tests (PhD Dissertation). *Ph.D. Thesis*. University of California, Berkeley, Berkeley.

Hayashi K., Okamura M., and Yasuhara H. 2010. Identification of liquefaction resistances in sand improved by calcium carbonate precipitated. *Jiban Kogaku Janaru (Japanese Geotechnical Journal)* 5 (2), 391–400. https://doi.org/10.3208/jgs.5.391

He J., and Chu J. 2014. Undrained responses of microbially desaturated sand under monotonic loading. *J. Geotech. Geoenviron. Eng.* 140 (5), 04014003. https://doi.org/10.1061/(ASCE)GT.1943-5606.0001082

Hermansson M. 1999. The DLVO theory in microbial adhesion. *Colloids and Surfaces B: Biointerfaces* 14 (1), 105–119. https://doi.org/10.1016/S0927-7765(99)00029-6

Hernandez G.L. 2018. Centrifuge model testing of liquefaction mitigation via microbially induced calcite precipitation (Master's Thesis). University of California, Davis, Davis, CA.

Hirai H., Takahashi M., and Yamada M. 1989. An elastic-plastic constitutive model for the behavior of improved sandy soils. *Soils and Foundations* 29 (2), 69–84. https://doi.org/10.3208/sandf1972.29.2_69

Hobbie J.E., Daley R.J., and Jasper S. 1977. Use of nuclepore filters for counting bacteria by fluorescence microscopy. *Appl. Environ. Microbiol.* 33 (5), 1225–1228.

Huang S., Tang Y., Bagheri H., Li D., Ardente A., Aukes D., Marvi H., and Tao J. (Julian) 2020. Effects of friction anisotropy on upward burrowing behavior of soft robots in granular materials. *Advanced Intelligent Systems* 2 (6), 1900183. https://doi.org/10.1002/aisy.201900183

Huang S., and Tao J. 2020. Modeling clam-inspired burrowing in dry sand using cavity expansion theory and DEM. *Acta Geotech.* 15 (8), 2305–2326. https://doi.org/10.1007/s11440-020-00918-8

Huang S., and Tao J. 2018. Modeling of the burrowing mechanism by razor clam: Role of penetration kinematics *IFCEE 2018*. American Society of Civil Engineers, Orlando, Florida, 547–556. https://doi.org/10.1061/9780784481585.053

Idriss I.M., and Boulanger R.W. 2008. Soil liquefaction during earthquakes. Earthquake Engineering Research Institute (EERI), Oakland, California, United States.

Ingraham J.L., Maaløe O., Neidhardt F.C., and others 1983. Growth of the bacterial cell. Sinauer Associates.

Islam M.T., Chittoori B.C.S., and Burbank M. 2020. Evaluating the applicability of biostimulated calcium carbonate precipitation to stabilize clayey soils. *J. Mater. Civ. Eng.* 32 (3), 04019369. https://doi.org/10.1061/(ASCE)MT.1943-5533.0003036

Itasca 2019. FLAC (version 8.1) – fast lagrangian analysis of continua. Itasca Consulting Group, Inc, Minneapolis, MN.

Itasca 2016. FLAC – fast lagrangian analysis of continua, version 8.0. Itasca Consulting Group, Inc, Minneapolis, MN.

Iwasaki T., Tatsuoka F., Tokida K., and Yasuda S. 1978. A practical method for assessing soil liquefaction potential based on case studies at various sites in Japan *Proc. Second Int. Conf. Microzonation Safer Construction Research Application, 1978*. Alexandria, VA:, 885–896.

Jahns T. 1996. Ammonium/urea-dependent generation of a proton electrochemical potential and synthesis of ATP in Bacillus pasteurii. *Journal of Bacteriology* 178 (2), 403–409. https://doi.org/10.1128/jb.178.2.403-409.1996

Jain S., and Arnepalli D.N. 2019. Biochemically induced carbonate precipitation in aerobic and anaerobic environments by Sporosarcina pasteurii. *Geomicrobiology Journal* 36 (5), 443–451. https://doi.org/10.1080/01490451.2019.1569180

Jaksa M.B., Goldsworthy J.S., Fenton G.A., Kaggwa W.S., Griffiths D.V., Kuo Y.L., and Poulos H.G. 2005. Towards reliable and effective site investigations 109–121. https://doi.org/10.1680/geot.2005.55.2.109

Jefferies M.G. 1993. Nor-Sand: a simple critical state model for sand. *Géotechnique* 43 (1), 91–103. https://doi.org/10.1680/geot.1993.43.1.91

Jefferis S.A. 2008. Moving towards sustainability in geotechnical engineering. ASCE, New Orleans, LA, 844–851. https://doi.org/10.1061/40971(310)105

Jenneman G.E., Knapp R.M., McInerney M.J., Menzie D.E., and Revus D.E. 1984. Experimental studies of in-situ microbial enhanced oil recovery. *Society of Petroleum Engineers Journal* 24 (01), 33–37. https://doi.org/10.2118/10789-PA

Jiang M., Zhang F., and Thornton C. 2015. A simple three-dimensional distinct element modeling of the mechanical behavior of bonded sands. *Int. J. Numer. Anal. Meth. Geomech.,* 39 (16), 1791–1820.

Jiang N.-J., and Soga K. 2019. Erosional behavior of gravel-sand mixtures stabilized by microbially induced calcite precipitation (MICP). *Soils and Foundations* 59 (3), 699–709. https://doi.org/10.1016/j.sandf.2019.02.003

Jiang N.-J., and Soga K. 2017. The applicability of microbially induced calcite precipitation (MICP) for internal erosion control in gravel–sand mixtures. *Géotechnique* 67 (1), 42–55. https://doi.org/10.1680/jgeot.15.P.182

Jiang N.-J., Soga K., and Kuo M. 2017. Microbially induced carbonate precipitation for seepage-induced internal erosion control in sand–clay mixtures. *J. Geotech. Geoenviron. Eng.* 143 (3), 04016100. https://doi.org/10.1061/(ASCE)GT.1943-5606.0001559

Jiang N.-J., Tang C.-S., Yin L.-Y., Xie Y.-H., and Shi B. 2019. Applicability of microbial calcification method for sandy-slope surface erosion control. *Journal of Materials in Civil Engineering* 31 (11), 04019250. https://doi.org/10.1061/(ASCE)MT.1943-5533.0002897

Kaltwasser H., and Schlegel H.G. 1966. NADH-dependent coupled enzyme assay for urease and other ammonia-producing systems. *Analytical Biochemistry* 16 (1), 132–138. https://doi.org/10.1016/0003-2697(66)90088-1

Kamai R., and Boulanger R. 2010. Characterizing localization processes during liquefaction using inverse analyses of instrumentation arrays 219–238. https://doi.org/10.1201/b10826-23

Kang C.-H., Kwon Y.-J., and So J.-S. 2016. Soil bioconsolidation through microbially induced calcite precipitation by Lysinibacillus

sphaericus WJ-8. *Geomicrobiology Journal* 33 (6), 473–478. https://doi.org/10.1080/01490451.2015.1053581

Kantzas A., Stehmeier L., Marentette D.F., Ferris F.G., Jha K.N., and Maurits F.M. 1992. A novel method of sand consolidation through bacteriogenic mineral plugging *Annual Technical Meeting*. Petroleum Society of Canada, Calgary, Alberta. https://doi.org/10.2118/92-46

Karatas I., Kavazanjian E.Jr., and Rittmann B.E. 2008. Microbially induced precipitation of calcite using Pseudomonas denitrificans. *Proc. 1st Int. Conf. Biogeotech. Engng, Delft*. Delft, Netherlands.

Kavazanjian E., and Hamdan N. 2015. Enzyme induced carbonate precipitation (EICP) columns for ground improvement *IFCEE 2015*. American Society of Civil Engineers, San Antonio, Texas, 2252–2261. https://doi.org/10.1061/9780784479087.209

Kavvadas M., and Amorosi A. 2000. A constitutive model for structured soils. *Géotechnique* 50 (3), 263–273. https://doi.org/10.1680/geot.2000.50.3.263

Keeney D.R., and Nelson D.W. 1983. Nitrogen—Inorganic Forms *Methods of Soil Analysis*. John Wiley & Sons, Ltd, 643–698. https://doi.org/10.2134/agronmonogr9.2.2ed.c33

Kendall A., Raymond A.J., Tipton J., and DeJong J.T. 2018. Review of life-cycle-based environmental assessments of geotechnical systems. *Proceedings of the Institution of Civil Engineers - Engineering Sustainability* 171 (2), 57–67. https://doi.org/10.1680/jensu.16.00073

Khodadadi Tirkolaei H., Javadi N., Krishnan V., Hamdan N., and Kavazanjian E. 2020. Crude urease extract for biocementation. *Journal of Materials in Civil Engineering* 32 (12), 04020374. https://doi.org/10.1061/(ASCE)MT.1943-5533.0003466

Khosravi A., Martinez A., DeJong J., and Wilson D. 2018. Discrete element simulations of bio-inspired self-burrowing probes in sands of varying density *Proceedings of Biomediated and Bioinspired Geotechnics (B2G) Conference*. Atlanta, GA, 6.

Khoubani A. 2018. A new bonding model for the particulate simulation of bio-cemented sand (with a side excursion on percolation in granular mixtures (PhD Dissertation). Oregon State University.

Khoubani A., Evans T.M., and Montoya B.M. 2016. Particulate simulations of triaxial tests on bio-cemented sand using a new cementation model *Geo-Chicago 2016*. American Society of Civil Engineers, Chicago, Illinois, 84–93. https://doi.org/10.1061/9780784480120.010

Kim N.-R., and Kim D.-S. 2010. A shear wave velocity tomography system for geotechnical centrifuge testing. *Geotechnical Testing Journal* 33 (6), 434–444.

Kirkland C.M., Akyel A., Hiebert R., McCloskey J., Kirksey J., Cunningham A.B., Gerlach R., Spangler L., and Phillips A.J. 2021a. Ureolysis-induced calcium carbonate precipitation (UICP) in the presence of CO2-affected brine: A field demonstration. *International Journal of Greenhouse Gas Control* 109, 103391. https://doi.org/10.1016/j.ijggc.2021.103391

Kirkland C.M., Hiebert R., Hyatt R., McCloskey J., Kirksey J., Thane A., Cunningham A.B., Gerlach R., Spangler L., and Phillips A.J. 2021b. Direct injection of biomineralizing agents to restore injectivity and wellbore integrity. *SPE Production & Operations* 36 (01), 216–223. https://doi.org/10.2118/203845-PA

Kirkland C.M., Thane A., Hiebert R., Hyatt R., Kirksey J., Cunningham A.B., Gerlach R., Spangler L., and Phillips A.J. 2020. Addressing wellbore integrity and thief zone permeability using microbially-induced calcium carbonate precipitation (micp): a field demonstration. *Journal of Petroleum Science and Engineering* 190, 107060. https://doi.org/10.1016/j.petrol.2020.107060

Kirkland C.M., Zanetti S., Grunewald E., Walsh D.O., Codd S.L., and Phillips A.J. 2017. Detecting microbially induced calcite precipitation in a model well-bore using downhole low-field NMR. *Environ. Sci. Technol.* 51 (3), 1537–1543. https://doi.org/10.1021/acs.est.6b04833

Kleinberg R.L., Flaum C., Straley C., Brewer P.G., Malby G.E., Peltzer E.T., Friederich G., and Yesinowski J.P. 2003. Seafloor nuclear magnetic resonance assay of methane hydrate in sediment and rock. *J. Geophys. Res.* 108 (B3). https://doi.org/10.1029/2001JB000919

Knorst M.T., Neubert R., and Wohlrab W. 1997. Analytical methods for measuring urea in pharmaceutical formulations. *Journal of Pharmaceutical and Biomedical Analysis* 15 (11), 1627–1632. https://doi.org/10.1016/S0731-7085(96)01978-4

Kramer S.L. 1996. Geotechnical earthquake engineering. Prentice-Hall Inc.

Krom M.D. 1980. Spectrophotometric determination of ammonia: a study of a modified Berthelot reaction using salicylate and dichloroisocyanurate. *Analyst* 105 (1249), 305. https://doi.org/10.1039/an9800500305

Lai H., Wu S., Cui M., and Chu J. 2021. Recent development in biogeotechnology and its engineering applications. *Front. Struct. Civ. Eng.* 15 (5), 1073–1096. https://doi.org/10.1007/s11709-021-0758-0

Laloui L., and François B. 2009. ACMEG-T: Soil thermoplasticity model. *Journal of Engineering Mechanics* 135 (9), 932–944. https://doi.org/10.1061/(ASCE)EM.1943-7889.0000011

Larson A.D., and Kallio R.E. 1954. Purification and properties of bacterial urease. *J Bacteriol* 68 (1), 67–73. https://doi.org/10.1128/jb.68.1.67-73.1954

Lauchnor E.G., Topp D.M., Parker A.E., and Gerlach R. 2015. Whole cell kinetics of ureolysis by Sporosarcina pasteurii. *Journal of Applied Microbiology* 118 (6), 1321–1332. https://doi.org/10.1111/jam.12804

Lawrence A.J. 1971. Conductimetric enzyme assays. *European Journal of Biochemistry* 18 (2), 221–225. https://doi.org/10.1111/j.1432-1033.1971.tb01234.x

Lee J.-S., Fernandez A.L., and Santamarina J.C. 2005. S-wave velocity tomography: Small-scale laboratory application. *Geotech. Test. J.* 28 (4), 12638. https://doi.org/10.1520/GTJ12638

Lee J.-S., and Santamarina J.C. 2005a. P-wave reflection imaging. *Geotechnical Testing Journal* 28 (2).

Lee J.-S., and Santamarina J.C. 2005b. Bender elements: Performance and signal interpretation. *J. Geotech. Geoenviron. Eng.* 131 (9), 1063–1070. https://doi.org/10.1061/(ASCE)1090-0241(2005)131:9(1063)

Lee K., Chan D., and Lam K. 2004. Constitutive model for cement treated clay in a critical state frame work. *Soils and Foundations* 44 (3), 69–77. https://doi.org/10.3208/sandf.44.3_69

Lee M., and Basu D. 2018. An integrated approach for resilience and sustainability in geotechnical engineering. *Indian Geotechnical Journal* 48 (2), 207–234. https://doi.org/10.1007/s40098-018-0297-3

Lee M., and Gomez M.G. 2022a. Examination of ammonium by-product removal following ureolytic bio-cementation using post-treatment rinsing.*To Be Submitted.*

Lee M., and Gomez M.G. 2022b. Effect of field-representative factors on the liquefaction triggering and post-triggering behavior of biocemented sands.*To Be Submitted.*

Lee M., Gomez M.G., El Kortbawi M., and Ziotopoulou K. 2021. Effect of light biocementation on the liquefaction triggering and post-triggering behavior of loose sands. *J. Geotech. Geoenviron. Eng.* 148 (1), 04021170. https://doi.org/10.1061/(ASCE)GT.1943-5606.0002707

Lee M., Gomez M.G., El Kortbawi M., and Ziotopoulou K. 2020. Examining the liquefaction resistance of lightly cemented sands using microbially induced calcite precipitation (MICP) *Geo-Congress 2020*. American Society of Civil Engineers, Minneapolis, Minnesota, 53–64. https://doi.org/10.1061/9780784482834.007

Lee M., Gomez M.G., Graddy C.M.R., San Pablo A.C.M., DeJong J.T., and Nelson D.C. 2022. Improving the spatial control of bio-cementation soil improvement using stimulated indigenous microorganisms.*To Be Submitted.*

Lee M., Kolbus C.M., Yepez A.D., and Gomez M.G. 2019a. Investigating ammonium by-product removal following stimulated ureolytic microbially-induced calcite precipitation. 260–270.

Lee M., Gomez M.G., San Pablo A.C.M., Kolbus C.M., Graddy C.M.R., DeJong J.T., and Nelson D.C. 2019b. Investigating ammonium by-product removal for ureolytic bio-cementation using meter-scale experiments. *Sci Rep* 9 (1), 1–15. https://doi.org/10.1038/s41598-019-54666-1

Lee Y.S., Kim H.J., and Park W. 2017. Non-ureolytic calcium carbonate precipitation by Lysinibacillus sp. YS11 isolated from the rhizosphere of Miscanthus sacchariflorus. *J Microbiol.* 55 (6), 440–447. https://doi.org/10.1007/s12275-017-7086-z

Leejeerajumnean A., Ames J.M., and Owens J.D. 2000. Effect of ammonia on the growth of bacillus species and some other bacteria. *Letters in Applied Microbiology* 30 (5), 385–389. https://doi.org/10.1046/j.1472-765x.2000.00734.x

Li B. 2015. Geotechnical properties of biocement treated sand and clay. Nanyang Technological University, Singapore. https://doi.org/10.32657/10356/62560

Li X., Scheibe T.D., and Johnson W.P. 2004. Apparent decreases in colloid deposition rate coefficients with distance of transport under unfavorable deposition conditions: a general phenomenon. *Environ. Sci. Technol.* 38 (21), 5616–5625. https://doi.org/10.1021/es049154v

Liang J., Guo Z., Deng L., and Liu Y. 2015. Mature fine tailings consolidation through microbial induced calcium carbonate precipitation. *Can. J. Civ. Eng.* 42 (11), 975–978. https://doi.org/10.1139/cjce-2015-0069

Liang J., Guo Z., Deng L., and Liu Y. 2014. Oil sands mature fine tailings consolidation through microbial induced calcite precipitation. *OSRIN* (Report No, TR-66), 39.

Liang T., Bengough A.G., Knappett J.A., MuirWood D., Loades K.W., Hallett P.D., Boldrin D., Leung A.K., and Meijer G.J. 2017. Scaling of the reinforcement of soil slopes by living plants in a geotechnical centrifuge. *Ecological Engineering* 109, 207–227. https://doi.org/10.1016/j.ecoleng.2017.06.067

Lin H., O'Donnell S.T., Suleiman M.T., Kavazanjian E., and Brown D.G. 2021. Effects of enzyme and microbially induced carbonate precipitation treatments on the response of axially loaded pervious concrete piles. *J. Geotech. Geoenviron. Eng.* 147 (8), 04021057. https://doi.org/10.1061/(ASCE)GT.1943-5606.0002565

Lin H., Suleiman M.T., and Brown D.G. 2020. Investigation of pore-scale CaCO3 distributions and their effects on stiffness and permeability of sands treated by microbially induced carbonate precipitation (MICP). *Soils and Foundations* 60 (4), 944–961. https://doi.org/10.1016/j.sandf.2020.07.003

Lin H., Suleiman M.T., Brown D.G., and Kavazanjian E. 2016a. Mechanical behavior of sands treated by microbially induced carbonate precipitation. *J. Geotech. Geoenviron. Eng.* 142 (2), 04015066. https://doi.org/10.1061/(ASCE)GT.1943-5606.0001383

Lin H., Suleiman M.T., Jabbour H.M., Brown D.G., and Kavazanjian E. 2016b. Enhancing the axial compression response of pervious concrete ground improvement piles using biogrouting. *J. Geotech. Geoenviron. Eng.* 142 (10), 04016045. https://doi.org/10.1061/(ASCE)GT.1943-5606.0001515

Lin H. (Thomas), Suleiman M., Jabbour H., and Brown D. 2017. Bio-grouting to enhance axial pull-out response of pervious concrete ground improvement piles. *Canadian Geotechnical Journal* 55, 1–12. https://doi.org/10.1139/cgj-2016-0438

Liu Q. 2021. Experimental investigation of microbially induced carbonate precipitation on fine mineral tailings (Ph.D.). North Carolina State University, United States -- North Carolina.

Liu Q., and Montoya B.M. 2021. Microbial-induced calcium carbonate precipitation to accelerate sedimentation of fine tailings. *J. Geotech. Geoenviron. Eng.* 147 (10), 02821001. https://doi.org/10.1061/(ASCE)GT.1943-5606.0002651

Liu Q., and Montoya B.M. 2020. Experimental study of consolidation behavior of mature fine tailings treated with microbial induced calcium carbonate precipitation *Geo-Congress 2020*. American Society of Civil Engineers, Minneapolis, Minnesota, 196–204. https://doi.org/10.1061/9780784482834.022

Liu S., Wen K., Armwood C., Bu C., Li C., Amini F., and Li L. 2019. Enhancement of MICP-treated sandy soils against environmental deterioration. *Journal of Materials in Civil Engineering* 31 (12), 04019294. https://doi.org/10.1061/(ASCE)MT.1943-5533.0002959

Lunne T., Powell J.J.M., and Robertson P.K. 1997. Cone penetration testing in geotechnical practice, Reprinted. ed. E & FN Spon, London.

Luria S. 1960. The bacterial protoplasm: composition and organizationGunsalus, I.C., and Stanier, R.Y. (Eds.), *The Bacteria*. Academic Press, New York, NY, 1–34.

Mahawish A., Bouazza A., and Gates W.P. 2019a. Factors affecting the bio-cementing process of coarse sand. *Proceedings of the Institution of Civil Engineers - Ground Improvement* 172 (1), 25–36. https://doi.org/10.1680/jgrim.17.00039

Mahawish A., Bouazza A., and Gates W.P. 2019b. Unconfined compressive strength and visualization of the microstructure of coarse sand subjected to different biocementation levels. *Journal of Geotechnical and Geoenvironmental Engineering* 145 (8), 04019033. https://doi.org/10.1061/(ASCE)GT.1943-5606.0002066

Mahawish A., Bouazza A., and Gates W.P. 2018. Effect of particle size distribution on the bio-cementation of coarse aggregates. *Acta Geotech.* 13 (4), 1019–1025. https://doi.org/10.1007/s11440-017-0604-7

Major D.W., McMaster M.L., Cox E.E., Edwards E.A., Dworatzek S.M., Hendrickson E.R., Starr M.G., Payne J.A., and Buonamici L.W. 2002. Field demonstration of successful bioaugmentation to achieve dechlorination of tetrachloroethene to ethene. *Environ. Sci. Technol.* 36 (23), 5106–5116. https://doi.org/10.1021/es0255711

Mallett S.D. 2019. Mechanical behavior of fibrous root-inspired anchorage systems (PhD Dissertation). Georgia Institute of Technology, Atlanta, GA.

Manzari M.T., and Dafalias Y.F. 1997. A critical state two-surface plasticity model for sands. *Géotechnique* 47 (2), 255–272. https://doi.org/10.1680/geot.1997.47.2.255

Martin K.K., Khodadadi T.H., Chester M., and Kavazanjian E. 2020. Hotspot life cycle assessment for environmental impacts of EICP for ground improvement 321–329. https://doi.org/10.1061/9780784482834.035

Martinez A., DeJong J., Akin I., Aleali A., Arson C., Atkinson J., Bandini P., Baser T., Borela R., Boulanger R., Burrall M., Chen Y., Collins C., Cortes D., Dai S., DeJong T., Del Dottore E., Dorgan K., Fragaszy R., Frost J.D., Full R., Ghayoomi M., Goldman D.I., Gravish N., Guzman I.L., Hambleton J., Hawkes E., Helms M., Hu D., Huang L., Huang S., Hunt C., Irschick D., Lin H.T., Lingwall B., Marr A., Mazzolai B., McInroe B., Murthy T., O'Hara K., Porter M., Sadek S., Sanchez M., Santamarina C., Shao L., Sharp J., Stuart H., Stutz H.H., Summers A., Tao J., Tolley M., Treers L., Turnbull K., Valdes R., van Paassen L., Viggiani G., Wilson D., Wu W., Yu X., and Zheng J. 2021. Bio-inspired geotechnical engineering: principles, current work, opportunities and challenges. *Géotechnique* 1–19. https://doi.org/10.1680/jgeot.20.P.170

Martinez A., DeJong J.T., Jaeger R.A., and Khosravi A. 2020. Evaluation of self-penetration potential of a bio-inspired site characterization probe by cavity expansion analysis. *Can. Geotech. J.* 57 (5), 706–716. https://doi.org/10.1139/cgj-2018-0864

Martinez A., and O'Hara K.B. 2021. Skin friction directionality in monotonically- and cyclically-loaded bio-inspired piles in sand. *DFIJ* 15 (1). https://doi.org/10.37308/DFIJnl.20200831.222

Martinez A., Palumbo S., and Todd B.D. 2019. Bioinspiration for anisotropic load transfer at soil–structure interfaces. *Journal of Geotechnical and Geoenvironmental Engineering* 145 (10), 04019074-undefined. https://doi.org/10.1061/(ASCE)GT.1943-5606.0002138

Martinez B.C., DeJong J.T., Ginn T.R., Montoya B.M., Barkouki T.H., Hunt C., Tanyu B., and Major D. 2013. Experimental optimization of microbial-induced carbonate precipitation for soil improvement. *J. Geotech. Geoenviron. Eng.* 139 (4), 587–598. https://doi.org/10.1061/(ASCE)GT.1943-5606.0000787

Marvi H., Bridges J., and Hu D.L. 2013. Snakes mimic earthworms: propulsion using rectilinear travelling waves. *J. R. Soc. Interface.* 10 (84), 20130188. https://doi.org/10.1098/rsif.2013.0188

Mickovski S.B., Bengough A.G., Bransby M.F., Davies M.C.R., Hallett P.D., and Sonnenberg R. 2007. Material stiffness, branching pattern and soil matric potential affect the pullout resistance of model root systems. *Eur J Soil Science* 58 (6), 1471–1481. https://doi.org/10.1111/j.1365-2389.2007.00953.x

Minto J.M., MacLachlan E., El Mountassir G., and Lunn R.J. 2016. Rock fracture grouting with microbially induced carbonate precipitation. *Water Resour. Res.* 52 (11), 8827–8844. https://doi.org/10.1002/2016WR018884

Misra A. 2010. A multicriteria based quantitative framework for assessing sustainability of pile foundations. University of Connecticut, Mansfield, Connecticut.

Mitchell J.K. 2008. Recent developments in ground improvement for mitigation of seismic risk to existing embankment dams 1–20. https://doi.org/10.1061/40975(318)98

Mitchell J.K. 1981. Soil improvement – state of the art report *Proceedings of 10th ICSMFE*. Balkema, Stockholm, Sweden, 509–565.

Mitchell J.K., and Santamarina J.C. 2005. Biological considerations in geotechnical engineering. *J. Geotech. Geoenviron. Eng.* 131 (10), 1222–1233. https://doi.org/10.1061/(ASCE)1090-0241(2005)131:10(1222)

Mobley H.L., and Hausinger R.P. 1989. Microbial ureases: significance, regulation, and molecular characterization. *Microbiol. Rev.* https://doi.org/10.1128/mr.53.1.85-108.1989

Montgomery J., and Boulanger R.W. 2017. Effects of spatial variability on liquefaction-induced settlement and lateral spreading. *Journal of Geotechnical and Geoenvironmental Engineering* 143 (1), 04016086. https://doi.org/10.1061/(ASCE)GT.1943-5606.0001584

Montgomery J., and Ziotopoulou K. 2020. Numerical Simulations of Selected LEAP Centrifuge Experiments with PM4Sand in

FLACKutter, B.L., Manzari, M.T., and Zeghal, M. (Eds.), *Model Tests and Numerical Simulations of Liquefaction and Lateral Spreading*. Springer International Publishing, Cham, 481–497.

Montoya B.M., and DeJong J.T. 2015. Stress-strain behavior of sands cemented by microbially induced calcite precipitation. *Journal of Geotechnical and Geoenvironmental Engineering* 141 (6), 04015019. https://doi.org/10.1061/(ASCE)GT.1943-5606.0001302

Montoya B.M., and Dejong J.T. 2013. Healing of biologically induced cemented sands. *Géotechnique Letters* 3 (3), 147–151. https://doi.org/10.1680/geolett.13.00044

Montoya B.M., Dejong J.T., and Boulanger R.W. 2013. Dynamic response of liquefiable sand improved by microbial-induced calcite precipitation. *Géotechnique* 63 (4), 302–312. https://doi.org/10.1680/geot.SIP13.P.019

Montoya Brina M., Do J., and Gabr M.A. 2021. Distribution and properties of microbially induced carbonate precipitation in underwater sand bed. *J. Geotech. Geoenviron. Eng.* 147 (10), 04021098. https://doi.org/10.1061/(ASCE)GT.1943-5606.0002607

Montoya Brina M, Evans T.M., Wengrove M.E., Bond H., Yazdani E., Dadashiserej A., and Liu Q. 2021. Resisting dune erosion with bio-cementation 11.

Montoya B.M., Safavizadeh S., and Gabr M.A. 2019. Enhancement of coal ash compressibility parameters using microbial-induced carbonate precipitation. *J. Geotech. Geoenviron. Eng.* 145 (5), 04019018. https://doi.org/10.1061/(ASCE)GT.1943-5606.0002036

Moon C.J., Whateley M.E.G., and Evans A.M. 2006. Introduction to mineral exploration. Blackwell Publishing, Sydney.

Mörsdorf G., and Kaltwasser H. 1989. Ammonium assimilation in Proteus vulgaris, Bacillus pasteurii, and Sporosarcina ureae. *Arch. Microbiol.* 152 (2), 125–131. https://doi.org/10.1007/BF00456089

Morse J.W., and Arvidson R.S. 2002. The dissolution kinetics of major sedimentary carbonate minerals. *Earth-Science Reviews* 58 (1–2), 51–84. https://doi.org/10.1016/S0012-8252(01)00083-6

Morse J.W., and Berner R.A. 1972. Dissolution kinetics of calcium carbonate in sea water: II. A kinetic origin for the lysocline. *American Journal of Science* 272, 840–851. https://doi.org/10.2475/ajs.272.9.840

Mortensen B.M., Haber M.J., DeJong J.T., Caslake L.F., and Nelson D.C. 2011. Effects of environmental factors on microbial induced calcium carbonate precipitation: Environmental factors on MICP. *Journal of Applied Microbiology* 111 (2), 338–349. https://doi.org/10.1111/j.1365-2672.2011.05065.x

Mujah D., Shahin M.A., and Cheng L. 2016. State-of-the-art review of biocementation by microbially induced calcite precipitation (MICP) for soil stabilization. *Geomicrobiology Journal* 34 (6), 524–537. https://doi.org/10.1080/01490451.2016.1225866

Mukherjee S., Sahu R.B., and Mukherjee J. 2021. Effect of biologically induced cementation via ureolysis in stabilization of silty soil. *Geomicrobiology Journal* 39 (1), 66–82. https://doi.org/10.1080/01490451.2021.2005188

Multiphysical modelling of soils with a focus on microbially induced calcite precipitation (PhD Dissertation) 2012. . EPFL, Lausanne, Switzerland. https://doi.org/10.5075/epfl-thesis-5413

Na T.K., Cabas A., and Montoya B.M. 2022. Resonant column testing procedure for microbial induced carbonate precipitated sands. *Geotechnical Testing Journal*.

Nafisi A., Khoubani A., Montoya B.M., and Evans T.M. 2018. The effect of grain size and shape on mechanical behavior of MICP sand I: Experimental study 9.

Nafisi A., Liu Q., and Montoya B.M. 2021. Effect of stress path on the shear response of bio-cemented sands. *Acta Geotech.* 16 (10), 3239–3251. https://doi.org/10.1007/s11440-021-01286-7

Nafisi A., Mocelin D., Montoya B.M., and Underwood S. 2020a. Tensile strength of sands treated with microbially induced carbonate precipitation. *Can. Geotech. J.* 57 (10), 1611–1616. https://doi.org/10.1139/cgj-2019-0230

Nafisi A., Montoya B.M., and Evans T.M. 2020b. Shear strength envelopes of biocemented sands with varying particle size and cementation level. *J. Geotech. Geoenviron. Eng.* 146 (3), 04020002. https://doi.org/10.1061/(ASCE)GT.1943-5606.0002201

Nafisi A., Safavizadeh S., and Montoya B.M. 2019. Influence of microbe and enzyme-induced treatments on cemented sand shear response. *J. Geotech. Geoenviron. Eng.* 145 (9), 06019008. https://doi.org/10.1061/(ASCE)GT.1943-5606.0002111

Nassar M.K., Gurung D., Bastani M., Ginn T.R., Shafei B., Gomez M.G., Graddy C.M.R., Nelson D.C., and DeJong J.T. 2018. Large-scale experiments in microbially induced calcite precipitation (micp): reactive transport model development and prediction. *Water Resources Research* 54 (1), 480–500. https://doi.org/10.1002/2017WR021488

Nelson D.C., and Jannasch H.W. 1983. Chemoautotrophic growth of a marine beggiatoa in sulfide-gradient cultures. *Arch. Microbiol.* 136 (4), 262–269. https://doi.org/10.1007/BF00425214

Nguyen L., Fatahi B., and Khabbaz H. 2017. Development of a constitutive model to predict the behavior of cement-treated clay during cementation degradation: C3 model. *International Journal of Geomechanics* 17 (7), 04017010. https://doi.org/10.1061/(ASCE)GM.1943-5622.0000863

Nguyen L.D., Fatahi B., and Khabbaz H. 2014. A constitutive model for cemented clays capturing cementation degradation. *International Journal of Plasticity* 56, 1–18. https://doi.org/10.1016/j.ijplas.2014.01.007

Nicholson P.G. 2015. Soil improvement and ground modification methods. Butterworth-Heinemann.

Nielsen S.D., Koren K., Löbmann K., Hinge M., Scoma A., Kjeldsen K.U., and Røy H. 2020. Constraints on CaCO3 precipitation in superabsorbent polymer by aerobic bacteria. *Appl Microbiol Biotechnol* 104 (1), 365–375. https://doi.org/10.1007/s00253-019-10215-4

Noh D.-H., Ajo-Franklin J.B., Kwon T.-H., and Muhunthan B. 2016. P and S wave responses of bacterial biopolymer formation in unconsolidated porous media. *Journal of Geophysical Research: Biogeosciences* 121 (4), 1158–1177. https://doi.org/10.1002/2015JG003118

Nova R., Castellanza R., and Tamagnini C. 2003. A constitutive model for bonded geomaterials subject to mechanical and/or chemical degradation. *Int. J. Numer. Anal. Meth. Geomech.* 27 (9), 705–732. https://doi.org/10.1002/nag.294

Ntarlagiannis D., Robinson J., Soupios P., and Slater L. 2016. Field-scale electrical geophysics over an olive oil mill waste deposition site: Evaluating the information content of resistivity versus induced polarization (IP) images for delineating the spatial extent of organic contamination. *Journal of Applied Geophysics* 135, 418–426. https://doi.org/10.1016/j.jappgeo.2016.01.017

Ntarlagiannis D., Yee N., and Slater L. 2005. On the low-frequency electrical polarization of bacterial cells in sands. *Geophys. Res. Lett.* 32 (24), L24402. https://doi.org/10.1029/2005GL024751

Nweke C.C., and Pestana J.M. 2017. Modeling bio-cemented sands: Shear strength and stiffness with degradation 34–45. https://doi.org/10.1061/9780784480793.004

Nzila A., Razzak S.A., and Zhu J. 2016. Bioaugmentation: an emerging strategy of industrial wastewater treatment for reuse and discharge. *International Journal of Environmental Research and Public Health* 13 (9), 846. https://doi.org/10.3390/ijerph13090846

Obermayr M., Dressler K., Vrettos C., and Eberhard P. 2013. A bonded-particle model for cemented sand. *Computers and Geotechnics* 49, 299–313. https://doi.org/10.1016/j.compgeo.2012.09.001

O'Donnell S.T., Kavazanjian E., and Rittmann B.E. 2017a. MIDP: Liquefaction mitigation via microbial denitrification as a two-stage process. II: MICP. *J. Geotech. Geoenviron. Eng.* 143 (12), 04017095. https://doi.org/10.1061/(ASCE)GT.1943-5606.0001806

O'Donnell S.T., Rittmann B.E., and Kavazanjian E. 2017b. MIDP: Liquefaction mitigation via microbial denitrification as a two-stage process. i: desaturation. *J. Geotech. Geoenviron. Eng.* 143 (12), 04017094. https://doi.org/10.1061/(ASCE)GT.1943-5606.0001818

Ohan J.A., Saneiyan S., Lee J., Bartlow A.W., Ntarlagiannis D., Burns S.E., and Colwell F.S. 2020. Microbial and geochemical dynamics of an aquifer stimulated for microbial induced calcite precipitation (MICP). *Front. Microbiol.* 11, 1327. https://doi.org/10.3389/fmicb.2020.01327

O'Hara K.B., and Martinez A. 2020. Monotonic and cyclic frictional resistance directionality in snakeskin-inspired surfaces and piles. *Journal of Geotechnical and Geoenvironmental Engineering* 146 (11), 04020116-undefined. https://doi.org/10.1061/(asce)gt.1943-5606.0002368

Ortiz D., Gravish N., and Tolley M.T. 2019. Soft robot actuation strategies for locomotion in granular substrates. *IEEE Robot. Autom. Lett.* 4 (3), 2630–2636. https://doi.org/10.1109/LRA.2019.2911844

O'Toole C.O., Liu Q., Montoya B.M., Kananizadeh N., and Odle W. 2022. The effect of microbial induced carbonate precipitation on fine-grained mine tailings *GeoCongress 2022*. Charlotte, North Carolina.

Pacheco-Torgal F., and Labrincha J.A. 2013. Biotechnologies and bioinspired materials for the construction industry: an overview.

International Journal of Sustainable Engineering 7 (3), 235–244. https://doi.org/10.1080/19397038.2013.844741

Panico F., Fonseca A.V. da, and Vaunat J. 2018. Modelling the small strain behaviour of a cemented silty sand with bounding plasticity *Numerical Methods in Geotechnical Engineering IX*. CRC Press.

Park S.-S., Choi S.-G., Kim W.-J., and Lee J.-C. 2014a. Effect of microbially induced calcite precipitation on the strength of cemented sand *New Frontiers in Geotechnical Engineering*. American Society of Civil Engineers, Shanghai, China, 47–56. https://doi.org/10.1061/9780784413456.006

Park S.-S., Choi S.-G., and Nam I.-H. 2014b. Effect of plant-induced calcite precipitation on the strength of sand. *J. Mater. Civ. Eng.* 26 (8), 06014017. https://doi.org/10.1061/(ASCE)MT.1943-5533.0001029

Peng J., and Liu Z. 2019. Influence of temperature on microbially induced calcium carbonate precipitation for soil treatment. *PLoS ONE* 14 (6), e0218396. https://doi.org/10.1371/journal.pone.0218396

Pham V.P., van Paassen L.A., van der Star W.R.L., and Heimovaara T.J. 2018. Evaluating strategies to improve process efficiency of denitrification-based MICP. *Journal of Geotechnical and Geoenvironmental Engineering* 144 (8), 04018049. https://doi.org/10.1061/(ASCE)GT.1943-5606.0001909

Phang I.R.K., Wong K.S., Chan Y.S., and Lau S.Y. 2019. Effect of surcharge load on microbial-induced calcite precipitation (MICP) treatment of tropical peat. *IOP Conf. Ser.: Mater. Sci. Eng.* 495, 012068. https://doi.org/10.1088/1757-899X/495/1/012068

Phillips A.J., Cunningham A.B., Gerlach R., Hiebert R., Hwang C., Lomans B.P., Westrich J., Mantilla C., Kirksey J., Esposito R., and Spangler L. 2016. Fracture sealing with microbially-induced calcium carbonate precipitation: a field study. *Environ. Sci. Technol.* 50 (7), 4111–4117. https://doi.org/10.1021/acs.est.5b05559

Phillips A.J., Troyer E., Hiebert R., Kirkland C., Gerlach R., Cunningham A.B., Spangler L., Kirksey J., Rowe W., and Esposito R. 2018. Enhancing wellbore cement integrity with microbially induced calcite precipitation (micp): a field scale demonstration. *Journal of Petroleum Science and Engineering* 171, 1141–1148. https://doi.org/10.1016/j.petrol.2018.08.012

Phradichith C. 2020. Control of biofilm permeability reduction in sand columns by varying the treatment delivery system (Master's Thesis). University of California, Davis.

Pinske M.A. 2011. Life cycle assessment of ground improvement methods (Master of Science in Civil & Environmental Engineering). University of California, Davis, Davis, CA.

Plummer L.N., and Busenberg E. 1982. The solubilities of calcite, aragonite and vaterite in CO2-H2O solutions between 0 and 90°C, and an evaluation of the aqueous model for the system CaCO3-CO2-H2O. *Geochim.* 46, 1011–1040. https://doi.org/10.1016/0016-7037(82)90056-4

Porter H., Dhami N.K., and Mukherjee A. 2018. Sustainable road bases with microbial precipitation. *Proceedings of the Institution of Civil Engineers - Construction Materials* 171 (3), 95–108. https://doi.org/10.1680/jcoma.16.00075

Porter K.G., and Feig Y.S. 1980. The use of DAPI for identifying and counting aquatic microflora. *Limnol. Oceanogr.* 25 (5), 943–948. https://doi.org/10.4319/lo.1980.25.5.0943

Pretell R., Ziotopoulou K., and Abrahamson N.A. 2022. Conducting 1D site response analyses to capture 2D VS spatial variability effects. *Earthquake Spectra* 87552930211069400. https://doi.org/10.1177/87552930211069400

Proto C.J., DeJong J.T., and Nelson D.C. 2016. Biomediated permeability reduction of saturated sands. *J. Geotech. Geoenviron. Eng.* 142 (12), 04016073. https://doi.org/10.1061/(ASCE)GT.1943-5606.0001558

Pungrasmi W., Intarasoontron J., Jongvivatsakul P., and Likitlersuang S. 2019. Evaluation of microencapsulation techniques for MICP bacterial spores applied in self-healing concrete. *Sci Rep* 9 (1), 12484. https://doi.org/10.1038/s41598-019-49002-6

Purdy C.M., Raymond A.J., DeJong J.T., Kendall A., and Krage C. 2021. Life cycle sustainability assessment of geotechnical site investigation. *Canadian Geotechnical Journal*.

Qin Y., and Cabral J.M.S. 1994. Kinetic studies of the urease-catalyzed hydrolysis of urea in a buffer-free system. *Appl Biochem Biotechnol* 49 (3), 217–240. https://doi.org/10.1007/BF02783059

Rahimi M., Chan D., and Nouri A. 2018. Constitutive model for monotonic and cyclic responses of loosely cemented sand formations. *Journal of Rock Mechanics and Geotechnical Engineering* 10 (4), 740–752. https://doi.org/10.1016/j.jrmge.2018.01.010

Rahimi M., Chan D., and Nouri A. 2016. Bounding surface constitutive model for cemented sand under monotonic loading. *Int. J. Geomech.* 16 (2), 04015049. https://doi.org/10.1061/(ASCE)GM.1943-5622.0000534

Rahman M.M., Hora R.N., Ahenkorah I., Beecham S., Karim M.R., and Iqbal A. 2020. State-of-the-art review of microbial-induced calcite precipitation and its sustainability in engineering applications. *Sustainability* 12 (15), 6281. https://doi.org/10.3390/su12156281

Ramachandran S.K., Ramakrishnan V., and Bang S.S. 2001. Remediation of concrete using micro-organisms. *ACI Materials Journal* 98 (1), 3–9. https://doi.org/10.14359/10154

Raymond A.J. 2020. Development and implementation of a life cycle sustainability assessment framework for geotechnical systems (PhD Dissertation). University of California, Davis, Davis, CA.

Raymond A.J., DeJong J.T., Kendall A., Blackburn J.T., and Deschamps R. 2021. Life cycle sustainability assessment of geotechnical ground improvement methods. *Journal of Geotechnical and Geoenvironmental Engineering*. https://doi.org/10.1061/(ASCE)GT.1943-5606.0002646

Raymond A.J., Kendall A., and DeJong J.T. 2020a. Life cycle sustainability assessment (LCSA): a research evaluation tool for emerging geotechnologies. American Society of Civil Engineers, Reston, VA, 330–339. https://doi.org/10.1061/9780784482834.036

Raymond A.J., Kendall A., DeJong J.T., Gomez M.G., San Pablo A.C.M., Lee M., Graddy C.M.R., and Nelson D.C. 2022. Life cycle sustainability assessment of microbially induced calcite precipitation (MICP) bio-cementation techniques.*To Be Submitted.*

Raymond A.J., Kendall A., DeJong J.T., Kavazanjian E., Woolley M.A., and Martin K.K. 2020b. Life cycle sustainability assessment of fugitive dust control methods. *J. Constr. Eng. Manage.* 147 (3), 04020181. https://doi.org/10.1061/(ASCE)CO.1943-7862.0001993

Rebata-Landa V. 2007. Microbial activity in sediments: Effects on soil behavior (PhD Dissertation). Georgia Institue of Technology.

Rebata-Landa V., and Santamarina J.C. 2006. Mechanical limits to microbial activity in deep sediments: microbes. *Geochem. Geophys. Geosyst.* 7 (11). https://doi.org/10.1029/2006GC001355

Reddy K.R., and Saxena S.K. 1992. Constitutive modelling of cemented sand. *Mechanics of Materials* 14, 155–178. https://doi.org/10.1016/0167-6636(92)90012-3

Ribeiro B.G.O., and Gomez M.G. 2022a. Investigating the dissolution behavior of calcium carbonate based bio-cemented sands. *GeoCongress 2022 Technical Papers.Accepted.*

Ribeiro B.G.O., and Gomez M.G. 2022b. Dissolution behavior of ureolytic bio-cementation: physical experiments and reactive transport modeling.*To Be Submitted.*

Rinaldi V., Guichon M., Ferrero V., Serrano C., and Ponti N. 2006. Resistivity survey of the subsurface conditions in the estuary of the rio de la plata. *J. Geotech. Geoenviron. Eng.* 132 (1), 72–79. https://doi.org/10.1061/(ASCE)1090-0241(2006)132:1(72)

Rios S., Da Fonseca A., and Baudet B. 2014. On the shearing behaviour of an artificially cemented soil. *Acta Geotechnica* 9. https://doi.org/10.1007/s11440-013-0242-7

Riveros G.A., and Sadrekarimi A. 2020. Liquefaction resistance of Fraser River sand improved by a microbially-induced cementation. *Soil Dynamics and Earthquake Engineering* 131, 106034. https://doi.org/10.1016/j.soildyn.2020.106034

Rix G.J., and Stokoe K.H. 1991. Correlation of initial tangent modulus and cone penetration resistance. *Calibration Chamber Testing* 351–361.

Robertson P., Fear C., Woeller D., and Weemees I. 1995. Estimation of sand compressibility from seismic CPT *Proceedings of the 48th Canadian Geotechnical Conference*. Vancouver, BC, 25–27.

Robertson P.K. 2016. Cone penetration test (CPT)-based soil behaviour type (SBT) classification system — an update. *Can. Geotech. J.* 53 (12), 1910–1927. https://doi.org/10.1139/cgj-2016-0044

Roden E.E., Leonardo M.R., and Ferris F.G. 2002. Immobilization of strontium during iron biomineralization coupled to dissimilatory hydrous ferric oxide reduction. *Geochimica et Cosmochimica Acta* 66 (16), 2823–2839. https://doi.org/10.1016/S0016-7037(02)00878-5

Roy N. 2021. Pore space architecture of particulate materials: Characterization & applications (PhD Dissertation). Georgia Institute of Technology, Atlanta, GA.

Rumpelt T.K. 1990. Constitutive modeling of weak porous rocks (Ph.D.). University of California, Berkeley, United States -- California.

Rütting T., Boeckx P., Müller C., and Klemedtsson L. 2011. Assessment of the importance of dissimilatory nitrate reduction to ammonium for

the terrestrial nitrogen cycle. *Biogeosciences* 8 (7), 1779–1791. https://doi.org/10.5194/bg-8-1779-2011

Safavizadeh S., Montoya B.M., and Gabr M.A. 2019. Microbial induced calcium carbonate precipitation in coal ash. *Géotechnique* 69 (8), 727–740. https://doi.org/10.1680/jgeot.18.P.062

Safdar M.U., Mavroulidou M., Gunn M.J., Purchase D., Gray C., Payne I., and Garelick J. 2021. Towards the development of sustainable ground improvement techniques—biocementation study of an organic soil. *Circ.Econ.Sust.* https://doi.org/10.1007/s43615-021-00071-8

San Pablo A.C.M., Graddy C.M.R., DeJong J.T., Gomez M.G., and Nelson D.C. 2022a. Solution optimization of stimulated microbially induced calcite precipitation (MICP) for up-scaling by reduction of urea inputs.*To Be Submitted.*

San Pablo A.C.M., DeJong J.T., and Carey T.J. 2022b. Effect of MICP treatment zones on mitigating liquefaction investigated via centrifuge modeling.*To Be Submitted.*

San Pablo A.C.M., Lee M., Graddy C.M.R., Kolbus C.M., Khan M., Zamani A., Martin N., Acuff C., DeJong J.T., Gomez M.G., and Nelson D.C. 2020. Meter-scale biocementation experiments to advance process control and reduce impacts: Examining spatial control, ammonium by-product removal, and chemical reductions. *J. Geotech. Geoenviron. Eng.* 146 (11), 04020125. https://doi.org/10.1061/(ASCE)GT.1943-5606.0002377

Saneiyan S., Ntarlagiannis D., Ohan J., Lee J., Colwell F., and Burns S. 2019. Induced polarization as a monitoring tool for in-situ microbial induced carbonate precipitation (MICP) processes. *Ecological Engineering* 127, 36–47. https://doi.org/10.1016/j.ecoleng.2018.11.010

Saneiyan S., Ntarlagiannis D., Werkema D.D., and Ustra A. 2018. Geophysical methods for monitoring soil stabilization processes. *Journal of Applied Geophysics* 148, 234–244. https://doi.org/10.1016/j.jappgeo.2017.12.008

Santamarina J.C., Klein K.A., and Fam M.A. 2001. Soils and waves: particulate materials behavior, characterization and process monitoring. J. Wiley & Sons, Chichester, New York.

Sasaki T., and Kuwano R. 2016. Undrained cyclic triaxial testing on sand with non-plastic fines content cemented with microbially induced CaCO3. *Soils and Foundations* 56 (3), 485–495. https://doi.org/10.1016/j.sandf.2016.04.014

Saxena S.K., and Reddy K.R. 1987. Mechanical behavior of cemented sands (No. IIT-CE-8701), National Science Foundation Under Grant No.CEE 8313935. Illinois Institute of Technology, Chicago, IL.

Saxena S.K., Reddy K.R., and Avramidis A.S. 1988. Liquefaction resistance of artificially cemented sand 19. https://doi.org/10.1061/(ASCE)0733-9410(1988)114:12(1395)

Schnaid F., Lehane B., and Fahey M. 2004. In situ test characterization of unusual geomaterials *In Proceedings of the 2nd International Conference on Site Characterization*. Millpress, Porto, Portugal, 49–74.

Schneider J.A., and Moss R.E.S. 2011. Linking cyclic stress and cyclic strain based methods for assessment of cyclic liquefaction triggering in sands. *Géotechnique Letters* 1 (2), 31–36. https://doi.org/10.1680/geolett.11.00021

Schnell S., and Mendoza C. 1997. Closed form solution for time-dependent enzyme kinetics. *Journal of Theoretical Biology* 187 (2), 207–212. https://doi.org/10.1006/jtbi.1997.0425

Schwarz M., Cohen D., and Or D. 2011. Pullout tests of root analogs and natural root bundles in soil: experiments and modeling: tensile forces and failure of root bundles. *J. Geophys. Res.* 116 (F2). https://doi.org/10.1029/2010JF001753

Seed H.B., and Idriss I.M. 1970. Soil Moduli and Damping Factors for Dynamic Response Analyses. (No. EERC 70-10). California Univ., Berkeley. Earthquake Engineering Research Center.

Seed H.B., Idriss I.M., Makdisi F., and Banerjee N. 1975. Representation of irregular stress time histories by equivalent uniform stress series in liquefaction analyses. College of Engineering, University of California ; For sale by NTIS, Berkeley; Springfield, Va.

Shen Z., Jiang M., and Thornton C. 2016. DEM simulation of bonded granular material. Part I: Contact model and application to cemented sand. *Computers and Geotechnics* 75, 192–209. https://doi.org/10.1016/j.compgeo.2016.02.007

Shillaber C.M., Mitchell J.K., and Dove J.E. 2016. Energy and carbon assessment of ground improvement works. II: Working model and example. *J. Geotech. Geoenviron. Eng.* 142 (3), 04015084. https://doi.org/10.1061/(ASCE)GT.1943-5606.0001411

Simatupang M., and Okamura M. 2017. Liquefaction resistance of sand remediated with carbonate precipitation at different degrees of saturation during curing. *Soils and Foundations* 57 (4), 619–631. https://doi.org/10.1016/j.sandf.2017.04.003

Simatupang M., Okamura M., Hayashi K., and Yasuhara H. 2018. Small-strain shear modulus and liquefaction resistance of sand with carbonate precipitation. *Soil Dynamics and Earthquake Engineering* 115, 710–718. https://doi.org/10.1016/j.soildyn.2018.09.027

Sjöberg E.L. 1978. Kinetics and mechanism of calcite dissolution in aqueous solutions at low temperatures. *Stockholm Contrib. Geol.* 32, 1–96.

Sjöberg E.L., and Rickard D.T. 1984. Temperature dependence of calcite dissolution kinetics between 1 and 62°C at pH 2.7 to 8.4 in aqueous solutions. *Geochimica et Cosmochimica Acta* 48 (3), 485–493. https://doi.org/10.1016/0016-7037(84)90276-X

Smith D.G., Russell W.C., Ingledew W.J., and Thirkell D. 1993. Hydrolysis of urea by Ureaplasma urealyticum generates a transmembrane potential with resultant ATP synthesis. *J Bacteriol* 175 (11), 3253–3258. https://doi.org/10.1128/jb.175.11.3253-3258.1993

Smith P.K., Krohn R.I., Hermanson G.T., Mallia A.K., Gartner F.H., Provenzano M.D., Fujimoto E.K., Goeke N.M., Olson B.J., and Klenk D.C. 1985. Measurement of protein using bicinchoninic acid. *Analytical Biochemistry* 150 (1), 76–85. https://doi.org/10.1016/0003-2697(85)90442-7

Smith R.W., Fujita Y., Ginn T.R., and Hubbard S.S. 2012. Field investigations of microbially facilitated calcite precipitation for immobilization of strontium-90 and other trace metals in the subsurface (No. DOE/ER64404-01). Univ. of Iowa, Iowa City, IA (United States). https://doi.org/10.2172/1052856

Sneath P.H.A. 1962. Longevity of micro-organisms. *Nature* 195 (4842), 643–646. https://doi.org/10.1038/195643a0

Song C., and Liu S. 2020. A novel approach of bulk strength enhancement through microbially-mediated carbonate cementation for mylonitic coal. *Geomicrobiology Journal* 37 (8), 1–12. https://doi.org/10.1080/01490451.2020.1764675

Sorenson K. 2021. Field trials and long-term monitoring of microbially-induced desaturation for the treatment of liquefiable silty soils (PhD Dissertation). Portland State University, Portland.

Spaulding C., Masse F., and LaBrozzi J. 2008. Ground improvement technologies for a sustainable world. ASCE, New Orleans, LA, 891–898. https://doi.org/10.1061/40971(310)111

Stocks-Fischer S., Galinat J.K., and Bang S.S. 1999. Microbiological precipitation of CaCO3. *Soil Biology and Biochemistry* 31 (11), 1563–1571. https://doi.org/10.1016/S0038-0717(99)00082-6

Stokoe K.H., Lee S.H.H., and Knox D.P. 1985. Shear moduli measurements under true triaxial stresses. *Advances in the Art of Testing Soils Under Cyclic Conditions*. Detroit, Michigan, 166–185.

Su F., and Yang Y.Y. 2020. Microbially induced carbonate precipitation via methanogenesis pathway by a microbial consortium enriched from activated anaerobic sludge. *J. Appl. Microbiol.* 131 (1), 236–256. https://doi.org/10.1111/jam.14930

Tagliaferri F., Waller J., Andò E., Hall S.A., Viggiani G., Bésuelle P., and DeJong J.T. 2011. Observing strain localisation processes in bio-cemented sand using x-ray imaging. *Granular Matter* 13 (3), 247–250. https://doi.org/10.1007/s10035-011-0257-4

Tang C.-S., Yin L., Jiang N., Zhu C., Zeng H., Li H., and Shi B. 2020. Factors affecting the performance of microbial-induced carbonate precipitation (MICP) treated soil: a review. *Environ Earth Sci* 79 (5), 94. https://doi.org/10.1007/s12665-020-8840-9

Tao J. "Julian," Huang S., and Tang Y. 2019. Bioinspired self-burrowing-out robot in dry sand. *J. Geotech. Geoenviron. Eng.* 145 (12), 02819002. https://doi.org/10.1061/(ASCE)GT.1943-5606.0002177

Terzis D., Bernier-Latmani R., and Laloui L. 2016. Fabric characteristics and mechanical response of bio-improved sand to various treatment conditions. *Géotechnique Letters* 6 (1), 50–57. https://doi.org/10.1680/jgele.15.00134

Terzis D., and Laloui L. 2019. A decade of progress and turning points in the understanding of bio-improved soils: a review. *Geomechanics for Energy and the Environment* 19, 100116. https://doi.org/10.1016/j.gete.2019.03.001

Terzis D., and Laloui L. 2018. 3-D micro-architecture and mechanical response of soil cemented via microbial-induced calcite precipitation. *Sci Rep* 8 (1), 1416. https://doi.org/10.1038/s41598-018-19895-w

Terzis D., Laloui L., Dornberger S., and Harran R. 2020. A Full-Scale Application of Slope Stabilization via Calcite Bio-Mineralization

Followed by Long-Term GIS Surveillance *Geo-Congress 2020*. American Society of Civil Engineers, Minneapolis, Minnesota, 65–73. https://doi.org/10.1061/9780784482834.008

Tian Z.-F., Tang X., Xiu Z.-L., and Xue Z.-J. 2020. Effect of different biological solutions on microbially induced carbonate precipitation and reinforcement of sand. *Marine Georesources & Geotechnology* 38 (4), 450–460. https://doi.org/10.1080/1064119X.2019.1595229

Tobler D.J., Cuthbert M.O., Greswell R.B., Riley M.S., Renshaw J.C., Handley-Sidhu S., and Phoenix V.R. 2011. Comparison of rates of ureolysis between Sporosarcina pasteurii and an indigenous groundwater community under conditions required to precipitate large volumes of calcite. *Geochimica et Cosmochimica Acta* 75 (11), 3290–3301. https://doi.org/10.1016/j.gca.2011.03.023

Tobler D.J., Minto J.M., El Mountassir G., Lunn R.J., and Phoenix V.R. 2018. Microscale analysis of fractured rock sealed with microbially induced CaCO3 precipitation: Influence on hydraulic and mechanical performance. *Water Resour. Res.* 54 (10), 8295–8308. https://doi.org/10.1029/2018WR023032

Tominaga T., An S.-Y., Oyaizu H., and Yokota A. 2009. Sporosarcina luteola sp. nov. isolated from soy sauce production equipment in Japan. *The Journal of General and Applied Microbiology* 55 (3), 217–223. https://doi.org/10.2323/jgam.55.217

Trujillo M.E., Dedysh S., DeVos P., Hedlund B., Kämpfer P., Rainey F., and Whitman W.B. 2015. Sporosarcina *Bergey's Manual of Systematics of Archaea and Bacteria*. John Wiley & Sons, Ltd, 1–7. https://doi.org/10.1002/9781118960608.gbm00563

Tsai P.-H., and Ni S.-H. 2012. Effects of types of additives on dynamic properties of cement stabilized soils. *IJASE* 10 (2), 131–144.

Tsukamoto M., Inagaki T., Sasaki Y., and Oda K. 2013. Influence of relative density on microbial carbonate precipitation and mechanical properties of sand *Proceedings of the 18th International Conference on Soil Mechanics and Geotechnical Engineering*. Paris, 2613–2616.

United Nations 2019. The sustainable development goals report. New York.

Updegraff D.M. 1983. Plugging and penetration of petroleum reservoir rock by microorganisms *Proceedings of the 1982 International Conference on Microbial Enhancement of Oil Recovery*. Shangri-La, Afton, Oklahoma. B. Linville, Bartlesville Energy Technology …, 85.

U.S. Army Corps of Engineers 1999. Guidelines on ground improvement for structures and facilities (1110-1-185 No. Engineer Technical Letter).

U.S. Department of Agriculture, Agricultural Research Service 2021. USDA food and nutrient database for dietary studies 2017-2018 [WWW Document]. *Food Surveys Research Group Home Page*. URL http://www.ars.usda.gov/nea/bhnrc/fsrg

US EPA 2013. Aquatic life ambient water quality criteria for ammonia – freshwater. Washington, DC.

U.S. Federal Highway Association 2017. Ground modification methods reference manual – Volume I (No. FHWA-NHI-16-027).

U.S. Federal Highway Association, Berg R.R., Collin J.G., DiMaggio J.A., Filz G.M., Bruce D.A., and Ayala D. 2017. Ground modification methods reference manual – Volume II (No. FHWA-NHI-16-028).

van Ballegooy S., Malan P., Lacrosse V., Jacka M.E., Cubrinovski M., Bray J.D., O'Rourke T.D., Crawford S.A., and Cowan H. 2014. Assessment of liquefaction-induced land damage for residential Christchurch. *Earthquake Spectra* 30 (1), 31–55. https://doi.org/10.1193/031813EQS070M

van Paassen L.A. 2011. Bio-mediated ground improvement: from laboratory experiment to pilot applications *Geo-Frontiers 2011*, Proceedings. American Society of Civil Engineers, Dallas, Texas, United States, 4099–4108. https://doi.org/10.1061/41165(397)419

van Paassen L.A. 2009. Biogrout: ground improvement by microbially induced carbonate precipitation. (PhD Dissertation). Delft University of Technology, Delft, Netherlands.

van Paassen L.A., Daza C.M., Staal M., Sorokin D.Y., van der Zon W., and van Loosdrecht Mark.C.M. 2010a. Potential soil reinforcement by biological denitrification. *Ecological Engineering*, Special Issue: BioGeoCivil Engineering 36 (2), 168–175. https://doi.org/10.1016/j.ecoleng.2009.03.026

van Paassen L.A., Ghose R., van der Linden T.J.M., van der Star W.R.L., and van Loosdrecht M.C.M. 2010b. Quantifying biomediated ground improvement by ureolysis: large-scale biogrout experiment. *J. Geotech. Geoenviron. Eng.* 136 (12), 1721–1728. https://doi.org/10.1061/(ASCE)GT.1943-5606.0000382

van Paassen L.A., Harkes M.P., and van Zwieten G.A. 2009. Scale up of biogrout: a biological ground reinforcement method 6.

van Paassen L.A., Hemert W.J. van, Star W.R.L. van der, Zwieten G. van, and Baalen L. van 2012. Direct shear strength of biologically cemented gravel *GeoCongress 2012*. American Society of Civil Engineers, Oakland, California, United States, 968–977. https://doi.org/10.1061/9780784412121.100

van Paassen L.A., Pham V., Mahabadi N., Hall C., Stallings E., and Kavazanjian E. 2018. Desaturation via biogenic gas formation as a ground improvement technique 244–256. https://doi.org/10.1061/9780784481677.013

van Tittelboom K., De Belie N., De Muynck W., and Verstraete W. 2010. Use of bacteria to repair cracks in concrete. *Cement and Concrete Research* 40 (1), 157–166. https://doi.org/10.1016/j.cemconres.2009.08.025

Vatsala A., Nova R., and Murthy B.R.S. 2001. Elastoplastic model for cemented soils. *Journal of Geotechnical and Geoenvironmental Engineering* 127 (8), 679–687. https://doi.org/10.1061/(ASCE)1090-0241(2001)127:8(679)

Vaunat J., and Gens A. 2003. Bond degradation and irreversible strains in soft argillaceous rock *Soil mechanics and geotechnical engineering*. 479–484.

Vego I., Ceccato F., Simonini P., Frost J.D., Mallett S.D., and Cola S. 2021. Numerical investigation of failure mechanism during pullout of root inspired anchorages *IACMAG 2021: Challenges and Innovations in Geomechanics*. Springer, Cham, 111–118. https://doi.org/10.1007/978-3-030-64518-2_14

Wadell H. 1935. Volume, shape, and roundness of quartz particles. *The Journal of Geology* 43 (3), 250–280. https://doi.org/10.1086/624298

Wadell H. 1933. Sphericity and roundness of rock particles. *The Journal of Geology* 41 (3), 310–331. https://doi.org/10.1086/624040

Wadell H. 1932. Volume, shape, and roundness of rock particles. *The Journal of Geology* 40 (5), 443–451. https://doi.org/10.1086/623964

Wang L., Chu J., Wu S., and Wang H. 2021. Stress–dilatancy behavior of cemented sand: comparison between bonding provided by cement and biocement. *Acta Geotech.* 16 (5), 1441–1456. https://doi.org/10.1007/s11440-021-01146-4

Wang Y., Soga K., DeJong J.T., and Kabla A.J. 2019. Microscale visualization of microbial-induced calcium carbonate precipitation processes. *J. Geotech. Geoenviron. Eng.* 145 (9), 04019045. https://doi.org/10.1061/(ASCE)GT.1943-5606.0002079

Wang Y.-H., and Leung S.-C. 2008. A particulate-scale investigation of cemented sand behavior. *Can. Geotech. J.* 45 (1), 29–44. https://doi.org/10.1139/T07-070

Warthmann R., van Lith Y., Vasconcelos C., McKenzie J.A., and Karpoff A.M. 2000. Bacterially induced dolomite precipitation in anoxic culture experiments 4.

Weatherburn M.W. 1967. Phenol-hypochlorite reaction for determination of ammonia. *Anal. Chem.* 39 (8), 971–974. https://doi.org/10.1021/ac60252a045

Weaver T.J., Burbank M., Lewis A., Lewis R., Crawford R., and Williams B. 2011. Bio-induced calcite, iron, and manganese precipitation for geotechnical engineering applications *Geo-Frontiers 2011*. American Society of Civil Engineers, Dallas, Texas, United States, 3975–3983. https://doi.org/10.1061/41165(397)406

Weil M.H., DeJong J.T., Martinez B.C., and Mortensen B.M. 2011. Seismic and resistivity measurements for real-time monitoring of microbially induced calcite precipitation in sand. *Geotechnical testing journal* 35 (2), 1–12. https://doi.org/10.1520/GTJ103365

Whiffin V.S. 2004. Microbial caco3 precipitation for the production of biocement (phd). *Whiffin, Victoria S. <https://researchrepository.murdoch.edu.au/view/author/Whiffin, Victoria.html> (2004) Microbial CaCO3 precipitation for the production of biocement. PhD thesis, Murdoch University.* Murdoch University, Perth, Australia.

Whiffin V.S., Paassen L.A. van, and Harkes M.P. 2007. Microbial carbonate precipitation as a soil improvement technique. *Geomicrobiology Journal* 24 (5), 417–423. https://doi.org/10.1080/01490450701436505

Williams K.H., Kemna A., Wilkins M.J., Druhan J., Arntzen E., N'Guessan A.L., Long P.E., Hubbard S.S., and Banfield J.F. 2009. Geophysical monitoring of coupled microbial and geochemical processes during stimulated subsurface bioremediation. *Environ. Sci. Technol.* 43 (17), 6717–6723. https://doi.org/10.1021/es900855j

Wilson W.W., Wade M.M., Holman S.C., and Champlin F.R. 2001. Status of methods for assessing bacterial cell surface charge properties based on zeta potential measurements. *Journal of*

Microbiological Methods 12. https://doi.org/10.1016/S0167-7012(00)00224-4

Wu S., Li B., and Chu J. 2021. Stress-dilatancy behavior of MICP-treated sand. *Int. J. Geomech.* 21 (3), 04020264. https://doi.org/10.1061/(ASCE)GM.1943-5622.0001923

Wu S., Li B., and Chu J. 2019. Large-scale model tests of biogrouting for sand and rock. *Proceedings of the Institution of Civil Engineers - Ground Improvement* 1–10. https://doi.org/10.1680/jgrim.18.00074

Wu Y., Hubbard S., Williams K.H., and Ajo-Franklin J. 2010. On the complex conductivity signatures of calcite precipitation. *J. Geophys. Res.* 115 (G2), n/a-n/a. https://doi.org/10.1029/2009JG001129

Xiao P., Liu H., Stuedlein A.W., Evans T.M., and Xiao Y. 2019. Effect of relative density and biocementation on cyclic response of calcareous sand. *Can. Geotech. J.* 56 (12), 1849–1862. https://doi.org/10.1139/cgj-2018-0573

Xiao P., Liu H., Xiao Y., Stuedlein A.W., and Evans T.M. 2018. Liquefaction resistance of bio-cemented calcareous sand. *Soil Dynamics and Earthquake Engineering* 107, 9–19. https://doi.org/10.1016/j.soildyn.2018.01.008

Xiao Y., Stuedlein A.W., Pan Z., Liu H., Matthew Evans T., He X., Lin H., Chu J., and van Paassen L.A. 2020. Toe-bearing capacity of precast concrete piles through biogrouting improvement. *J. Geotech. Geoenviron. Eng.* 146 (12), 06020026. https://doi.org/10.1061/(ASCE)GT.1943-5606.0002404

Xiao Y., Wang Y., Wang S., Evans T.M., Stuedlein A.W., Chu J., Zhao C., Wu H., and Liu H. 2021a. Homogeneity and mechanical behaviors of sands improved by a temperature-controlled one-phase MICP method. *Acta Geotech.* 16 (5), 1417–1427. https://doi.org/10.1007/s11440-020-01122-4

Xiao Y., Xiao W., Ma G., He X., Wu H., and Shi J. 2022. Mechanical performance of biotreated sandy road bases. *J. Perform. Constr. Facil.* 36 (1), 04021111. https://doi.org/10.1061/(ASCE)CF.1943-5509.0001671

Xiao Y., Zhang Z., Stuedlein A.W., and Evans T.M. 2021b. Liquefaction modeling for biocemented calcareous sand. *Journal of Geotechnical and Geoenvironmental Engineering* 147 (12), 04021149. https://doi.org/10.1061/(ASCE)GT.1943-5606.0002666

Yanez V.R. 2021. Effect of microbially induced calcite precipitation in carbonate rich soils (Master's Thesis). University of California, Davis, Davis, CA.

Yanez V.R., San Pablo A.C.M., Graddy C.M.R., DeJong J.T., Gomez M.G., and Nelson D.C. 2022. Bio-stimulated MICP soil improvement in marine and brackish environments.*To Be Submitted.*

Yang C., Cui Y.J., Pereira J.M., and Huang M.S. 2008. A constitutive model for unsaturated cemented soils under cyclic loading. *Computers and Geotechnics* 35 (6), 853–859. https://doi.org/10.1016/j.compgeo.2008.08.005

Yang M., Défossez P., Danjon F., and Fourcaud T. 2018. Analyzing key factors of roots and soil contributing to tree anchorage of Pinus species. *Trees* 32 (3), 703–712. https://doi.org/10.1007/s00468-018-1665-4

Yang P. 2018. Discrete element modeling of the mechanical response of cemented granular materials (PhD Dissertation). Arizona State University, Tempe, Arizona.

Yang P., Kavazanjian E., and Neithalath N. 2019. Particle-scale mechanisms in undrained triaxial compression of biocemented sands: Insights from 3D DEM simulations with flexible boundary. *Int. J. Geomech.* 19 (4), 04019009. https://doi.org/10.1061/(ASCE)GM.1943-5622.0001346

Yang P., O'Donnell S., Hamdan N., Kavazanjian E., and Neithalath N. 2017. 3D DEM simulations of drained triaxial compression of sand strengthened using microbially induced carbonate precipitation. *Int. J. Geomech.* 17 (6), 04016143. https://doi.org/10.1061/(ASCE)GM.1943-5622.0000848

Yu H.S., Tan S.M., and Schnaid F. 2007. A critical state framework for modelling bonded geomaterials. *Geomechanics and Geoengineering* 2 (1), 61–74. https://doi.org/10.1080/17486020601164275

Yu T., Souli H., Pechaud Y., and Fleureau J.-M. 2021. Review on engineering properties of MICP-treated soils. *Geomechanics and Engineering* 27 (1), 13–30. https://doi.org/10.12989/GAE.2021.27.1.013

Zamani A., and Montoya B.M. 2019. Undrained cyclic response of silty sands improved by microbial induced calcium carbonate precipitation. *Soil Dynamics and Earthquake Engineering* 120, 436–448. https://doi.org/10.1016/j.soildyn.2019.01.010

Zamani A., and Montoya B.M. 2018. Undrained monotonic shear response of MICP-treated silty sands. *J. Geotech. Geoenviron. Eng.* 144 (6), 04018029. https://doi.org/10.1061/(ASCE)GT.1943-5606.0001861

Zamani A., Montoya B.M., and Gabr M.A. 2019. Investigating challenges of in situ delivery of microbial-induced calcium carbonate precipitation (MICP) in fine-grain sands and silty sand. *Can. Geotech. J.* 56 (12), 1889–1900. https://doi.org/10.1139/cgj-2018-0551

Zamani A., Phradichith C., Graddy C.M.R., DeJong J.T., Nelson D.C., and Parales R.E. 2022. Control of biofilm permeability reduction in sand columns by varying the treatment delivery system.*To Be Submitted.*

Zamani A., Xiao P., Baumer T., Carey T.J., Sawyer B., DeJong J.T., and Boulanger R.W. 2021. Mitigation of liquefaction triggering and foundation settlement by MICP treatment. *J. Geotech. Geoenviron. Eng.* 147 (10), 04021099. https://doi.org/10.1061/(ASCE)GT.1943-5606.0002596

Zambare N.M., Naser N.Y., Gerlach R., and Chang C.B. 2020. Mineralogy of microbially induced calcium carbonate precipitates formed using single cell drop-based microfluidics. *Sci Rep* 10 (1), 17535. https://doi.org/10.1038/s41598-020-73870-y

Zeng C., Veenis Y., Hall C.A., Young E.S., van der Star W.R.L., Zheng J., and van Paassen L.A. 2021. Experimental and numerical analysis of a field trial application of microbially induced calcite precipitation for ground stabilization. *J. Geotech. Geoenviron. Eng.* 147 (7), 05021003. https://doi.org/10.1061/(ASCE)GT.1943-5606.0002545

Zhang A., Dafalias Y.F., and Jiang M. 2021. A bounding surface plasticity model for cemented sand under monotonic and cyclic loading. *Géotechnique* 1–18. https://doi.org/10.1680/jgeot.20.P.275

Zhang F., Wang C., Chang J., and Feng H. 2022. DEM analysis of cyclic liquefaction behaviour of cemented sand. *Computers and Geotechnics* 142, 104572. https://doi.org/10.1016/j.compgeo.2021.104572

Zhang G., Robertson P.K., and Brachman R.W.I. 2004. Estimating liquefaction-induced lateral displacements using the standard penetration test or cone penetration test. *J. Geotech. Geoenviron. Eng.* 130 (8), 861–871. https://doi.org/10.1061/(ASCE)1090-0241(2004)130:8(861)

Zhang G., Robertson P.K., and Brachman R.W.I. 2002. Estimating liquefaction-induced ground settlements from CPT for level ground. *Can. Geotech. J.* 39 (5), 1168–1180. https://doi.org/10.1139/t02-047

Zhang X., Chen Y., Liu H., Zhang Z., and Ding X. 2020. Performance evaluation of a MICP-treated calcareous sandy foundation using shake table tests. *Soil Dynamics and Earthquake Engineering* 129, 105959. https://doi.org/10.1016/j.soildyn.2019.105959

Zhang X., Knappett J.A., Leung A.K., Ciantia M.O., Liang T., and Nicoll B.C. 2022. Centrifuge modelling of root-soil interaction of laterally loaded trees under different loading conditions. *Géotechnique* 1–39. https://doi.org/10.1680/jgeot.21.00088

Zhao Q., Li L., Li C., Li M., Amini F., and Zhang H. 2014. Factors affecting improvement of engineering properties of MICP-treated soil catalyzed by bacteria and urease. *Journal of Materials in Civil Engineering* 26 (12), 04014094. https://doi.org/10.1061/(ASCE)MT.1943-5533.0001013

Zheng J., and Hryciw R.D. 2015. Traditional soil particle sphericity, roundness and surface roughness by computational geometry. *Géotechnique* 65 (6), 494–506. https://doi.org/10.1680/geot.14.P.192

Ziotopoulou K., and Boulanger R.W. 2016. Plasticity modeling of liquefaction effects under sloping ground and irregular cyclic loading conditions. *Soil Dynamics and Earthquake Engineering* 84, 269–283. https://doi.org/10.1016/j.soildyn.2016.02.013